Neuronal coding and metabolic cost of information

Tomáš Bárta

FIRST FACULTY
OF MEDICINE
Charles University

SORBONNE
UNIVERSITÉ

Doctoral thesis

Tomáš Bárta

Neuronal coding and metabolic cost of information

Laboratory of Computational Neuroscience, Institute of Physiology CAS

Department of Sensory Ecology, Institute of Ecology
and Environmental Sciences - Paris

Supervisors of the doctoral thesis:	Lubomír Košťál (IPhys CAS) Philippe Lucas (iEES - Paris)
Study programmes:	Doctoral Studies in Biomedicine (CU) DS Brain Cognition Behavior (SU)
Study branch:	Biomedical informatics (CU) Neuroscience (SU)

March 2023, Prague

I declare that I carried out this master thesis independently, and only with the cited sources, literature and other professional sources.

I understand that my work relates to the rights and obligations under the Act No. 121/2000 Sb., the Copyright Act, as amended, in particular the fact that the Charles University in Prague has the right to conclude a license agreement on the use of this work as a school work pursuant to Section 60 subsection 1 of the Copyright Act.

In ..... date ..... signature of the author

BÁRTA, Tomáš. Neuronal coding and metabolic cost of information. Prague, 2023. 72 pages, 6 attachments. Disertation thesis. Charles Universtiy, First Faculty of Medicine and Czech Academy of Sciences, Institute of Physiology, Laboratory of Computational Neuroscience, en cotutelle with Sorbonne University, Doctoral School Brain, Cognition, Behavior and National Research Institute for Agriculture, Food and the Environment, Institute of Ecology and Environmental Sciences - Paris, Department of Sensory Ecology. Supervisors: KOŠŤÁL, Lubomír and LUCAS, Philippe.

Abstract: For most neurons, the information the neuron passes on is contained within the times of sending out electrical pulses - so-called action potentials. It is still not fully understood how to read this „neural code“. The efficient coding hypothesis proposes that due to evolutionary pressures sensory systems evolved to transmit and process information in the most efficient way possible. However, the notion of efficiency seems to be different in different sensory systems. Cortical neurons keep their firing rates low to minimize metabolic expenses. So do insect olfactory receptor neurons (ORNs, the first layer of the olfactory system). Neurons in the insect antennal lobe (the second layer of the olfactory system), on the other hand fully use the space of possible firing rates to encode the maximum information about the odor. In my thesis, I studied how can single cortical neurons and their populations transmit and process information, while keeping metabolic expenses low, and also how the insect olfactory system encodes information about odors encountered in the air.

In the part of my thesis about metabolically efficient information transmission I focused mainly on the role of inhibitory neurons in efficient information transmission. Through mathematical analysis and Monte Carlo simulations of spiking neuronal models, I show how can the input from pre-synaptic inhibitory neurons decrease the trial-to-trial variability of the post-synaptic neuron, and by generalizing these results to a recurrent neural network I illustrated how the trial-to-trial variability can decrease with a stimulus-onset, phenomenon known as neural variability quenching. However, an information-theoretical analysis showed that the input from inhibitory neurons in the form of inhibitory feedback with a stimulus onset will only yield significant improvements in metabolically efficient information transmission if the information is being transmitted by a population of recurrently connected neurons, rather than a single neuron.

To understand the general principles governing neural coding, I next focused on the neural activity of the insect olfactory system. I analyzed the local field potentials (LFPs) and firing activity of insect ORNs stimulated with a novel odor-delivery device, capable of temporally precise stimulus delivery. These novel recordings showed that moth ORNs are much more capable of encoding the stimulus duration than previously thought. The properties of moth ORNs were revealed to be very similar to the properties of the majority of Drosophila ORNs, which allows the unification of the research on those species. Using the recordings of the LFPs I constructed a minimal model of the moth ORN, which reliably describes the firing activity while using only several interpretable parameters.

A simple and transferable model, that can describe the firing activity of the ORNs is essential for building an integrative model of the insect olfactory system. Such a model could be used to study the information-metabolic efficiency of the whole system and analyze if under certain conditions the high firing rates in the antennal lobe actually aid the information-metabolic efficiency. Therefore, the results of my thesis are a step forward to understanding the general principles governing the neural code.

Keywords: Neuron, coding, olfaction

Abstrakt: U většiny neuronů je informace, kterou neuron předává, obsažena v časech vysílání elektrických impulzů - tzv. akčních potenciálů. Dosud není zcela jasné, jak tento "neuronový kód" číst. Hypotéza efektivního kódování předpokládá, že v důsledku evolučních tlaků se smyslové systémy vyvinuly tak, aby přenášely a zpracovávaly informace co nejefektivnějším způsobem. Zdá se však, že pojem efektivity se v různých smyslových systémech liší. Kortikální neurony udržují nízkou frekvenci vysílání akčních potentiálů, aby minimalizovaly metabolické náklady. Podobně to dělají i hmyzí čichové receptorové neurony (ORN, první vrstva čichového systému). Neurony v hmyzím tykadlovém laloku (druhá vrstva čichového systému) naopak plně využívají prostor možných frekvencí, aby zakódovaly maximum informací o pachu. Ve své diplomové práci jsem se zabýval tím, jak mohou jednotlivé korové neurony a jejich populace přenášet a zpracovávat informace při zachování nízkých metabolických nákladů a také tím, jak hmyzí čichový systém kóduje informace o paších, které se vyskytují ve vzduchu.

V části své práce věnující se metabolicky efektivnímu přenosu informace jsem se zaměřil především na roli inhibičních neuronů v efektivním přenosu informace. Pomocí matematické analýzy a simulací Monte Carlo modelů spikujících neuronů jsem ukázal, jak může vstup z pre-synaptických inhibičních neuronů snížit variabilitu post-synaptického neuronu přes jednotlivé pokusy, a zobecněním těchto výsledků na rekurentní neuronovou síť jsem ilustroval, jak může variabilita přes pokusy klesat s nástupem podnětu, což je jev známý jako zhášení neuronové variability. Informačně-teoretická analýza však ukázala, že vstup z inhibičních neuronů v podobě inhibiční zpětné vazby s nástupem podnětu přinese významné zlepšení metabolicky účinného přenosu informace pouze tehdy, pokud je informace přenášena populací rekurentně propojených neuronů, nikoliv jediným neuronem.

Abych pochopil obecné principy, kterými se řídí nervové kódování, zaměřil jsem se na nervovou aktivitu čichového systému hmyzu. Analyzoval jsem lokální polní potenciály (LFP) a aktivitu spikování hmyzích ORN stimulovaných novým zařízením pro doručování pachů, které je schopné časově přesně doručit podnět. Tyto nové záznamy ukázaly, že ORN můry jsou mnohem schopnější kódovat délku trvání podnětu, než se dosud předpokládalo. Ukázalo se, že vlastnosti ORN můry jsou velmi podobné vlastnostem většiny ORN octomilky, což umožňuje sjednotit výzkum na těchto druzích. Na základě záznamů LFP jsem zkonstruoval minimální model ORN můry, který spolehlivě popisuje její aktivitu, přičemž využívá pouze několik interpretovatelných parametrů.

Jednoduchý a přenositelný model, který dokáže popsat aktivitu ORN, je nezbytný pro vytvoření integrativního modelu čichového systému hmyzu. Takový model by mohl být využit ke studiu informační metabolické účinnosti celého systému a k analýze, zda za určitých podmínek vysoká frekvence akčních potenciálů v anténním laloku skutečně napomáhá informačně-metabolické účinnosti. Výsledky mé práce jsou tedy krokem vpřed k pochopení obecných principů řídících nervový kód.

Klíčová slove: Neuron, kódování, čich

Résumé: Pour la plupart des neurones, l'information qu'ils transmettent est contenue dans le décours temporel d'émission de leurs impulsions électriques, appelées potentiels d'action. On ne sait pas encore bien décrypter ce "code neuronal". L'hypothèse du codage efficace propose que, sous l'effet de la pression évolutive, les systèmes sensoriels ont évolué pour transmettre et traiter l'information de la manière la plus efficace possible. Toutefois, la notion d'efficacité semble varier selon les systèmes sensoriels. Les neurones corticaux maintiennent une faible fréquence d'émission de potentiels d'action pour minimiser les dépenses métaboliques. Il en va de même pour les neurones récepteurs olfactifs des insectes (NRO, première couche du système olfactif). Les neurones du lobe antennaire des insectes (deuxième couche du système olfactif), en revanche, utilisent pleinement la gamme possible d'activité d'émission de potentiels d'action pour optimiser le codage olfactif. Dans ma thèse, j'ai étudié comment des neurones corticaux uniques et leurs populations peuvent transmettre et traiter des informations, tout en maintenant des dépenses métaboliques faibles, et aussi comment le système olfactif des insectes encode les informations sur les odeurs détectées dans l'air.

Dans la partie de ma thèse consacrée à la transmission métabolique efficace de l'information, j'ai principalement analysé la contribution des neurones inhibiteurs. En généralisant ces résultats à un réseau de neurones récurrents, j'ai illustré comment la variabilité d'un essai à l'autre peut diminuer avec l'apparition d'un stimulus, un phénomène connu sous le nom de "neural variability quenching" (atténuation de la variabilité neuronale). Toutefois, une analyse théorique de l'information a montré que l'apport des neurones inhibiteurs sous la forme d'une rétroaction inhibitrice lors de l'apparition d'un stimulus n'améliore significativement la transmission métabolique efficace de l'information que si cette information est transmise par une population de neurones connectés de manière récurrente, plutôt que par un seul neurone.

Pour comprendre les principes généraux régissant le codage neuronal, je me suis ensuite focalisé sur l'activité neuronale du système olfactif des insectes. J'ai analysé les potentiels de champ locaux (LFP) et l'activité d'émission de potentiels d'action de NRO d'insectes stimulés avec un nouveau dispositif capable de délivrer des stimuli temporellement précis. L'utilisation de ce stimulateur a permis de démontrer que les NRO des papillons de nuit encodent mieux la durée du stimulus que ce qui était admis jusqu'à présent. Les propriétés des NRO de papillon de nuit se sont révélées très similaires à celles de la majorité des NRO de drosophile, ce qui permet d'unifier les recherches sur ces espèces. En utilisant les enregistrements des LFP, j'ai construit un modèle minimal du NRO du papillon de nuit qui décrit de manière fiable l'activité d'émission de potentiels d'action tout en utilisant seulement quelques paramètres interprétables.

Un modèle simple et transférable, capable de décrire la réponse des NRO, est essentiel pour construire un modèle intégratif du système olfactif des insectes. Un tel modèle pourra être utilisé pour étudier l'efficacité métabolique du codage de l'information par l'ensemble du système olfactif et analyser si, dans certaines conditions, les taux d'excitation élevés des neurones du lobe antennaire favorisent réellement cette efficacité. Les résultats de ma thèse constituent donc un pas en avant vers la compréhension des principes généraux régissant le code neuronal.

Mots clés: Neuron, codage, olfaction

First and foremost, I would like to thank my thesis supervisors, Lubomír Košťál and Philippe Lucas, without whom this thesis would never see the light of day. Lubomír Košťál introduced me to the field of computational neuroscience and I am indebted to him for his patience and encouragement during the ups and downs of my research. The scientific enthusiasm and curiosity of Philippe Lucas are what inspired me to continue in the pursuit of an academic career.

I want to thank my colleagues from the Laboratory of Computational Neuroscience in Prague and the Department of Sensory Ecology in Versailles. The pursuit of a doctoral degree can be a mentally challenging endeavor, but having Rimjhim Tomar as a colleague and a friend helped me stay sane throughout the years. I am incredibly thankful to Christelle Monsempès and Elodie Demondion for performing the experiments for my thesis and to Abhishek Chatterjee who has been very helpful not only with his scientific input but also provided me with lots of career advice. I also want to extend my thanks to the rest of my colleagues for creating such a friendly environment.

I thank the members of my thesis committee, Renaud Jolivet and Jürgen Reingruber, for their time and valuable suggestions, and to people with whom I discussed or who provided comments on my manuscripts, namely Ryota Kobayashi, Vincent Jacob, and Claude Collet.

Last but not least, I cannot describe how thankful I am to my family. They were incredibly understanding and supportive. I knew they would always be there for me if any problem would come about and I could always rely on them.

Contents

1. Introduction

Neurons are cells that process and transmit information. They contain an excess of negatively charged ions compared to their surroundings, which makes the neuronal membrane polarized. An external signal (received, e.g., from other neurons or from a sensory stimulus) then opens ion channels in the neuronal membrane, allowing an exchange of ions between the neuron and its surroundings. Thus the external signal translates into a graded change of the neuron's membrane potential. If certain conditions are met (the membrane potential has to reach a threshold value), the neuron produces its own electrical signal, called an action potential (or a spike), which then propagates through the neuron's axon and can, e.g., excite or inhibit other neurons it connects to by synapses. For most neurons, an action potential is the only way for a neuron to communicate information further (Dayan and Abbott, 2005).

The shape of the action potentials typically does not differ much for a single neuron (Fig. 1A,B). Moreover, their duration (commonly 1 ms to 4 ms) is relatively short compared to other timescales of the system. Therefore, to analyze the information that the neuron is sending further on, it is sufficient to limit ourselves to the timings of individual action potentials - the communicated information has to be encoded in the neuron's "spike train": a sequence of times when an action potential was sent, or "fired", (Fig. 1C).

It is unknown how the information should be "read out" from the spike trains, and this clearly depends on the system. However, a classical hypothesis is the rate coding hypothesis, dating back to the early experiments of Adrian and Zotterman (Adrian, 1926; Adrian and Zotterman, 1926a,b; Adrian, 1954), who showed that the number of action potentials from sensory nerves innervating a muscle increased with the force the muscle was delivering. It was then observed in most sensory systems that the number of spikes increases with the stimulus intensity (Kandel et al., 2013).

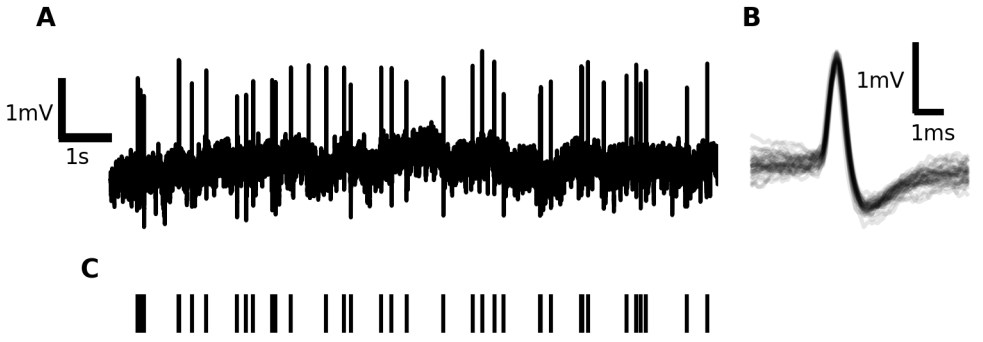

Figure 1: The neural code. A: Extracellular recording of the membrane potential of the olfactory receptor neuron of the noctuid moth *Agrotis ipsilon*. The electrical pulses (apparent as vertical lines) are the action potentials. **B**: All action potentials from **A** plotted over each other. The shape of the action potential does not vary significantly. **C**: The spike train. Since the shape of the action potential does not carry any information, the neuronal output can be reduced to a sequence of times when the action potential was fired.

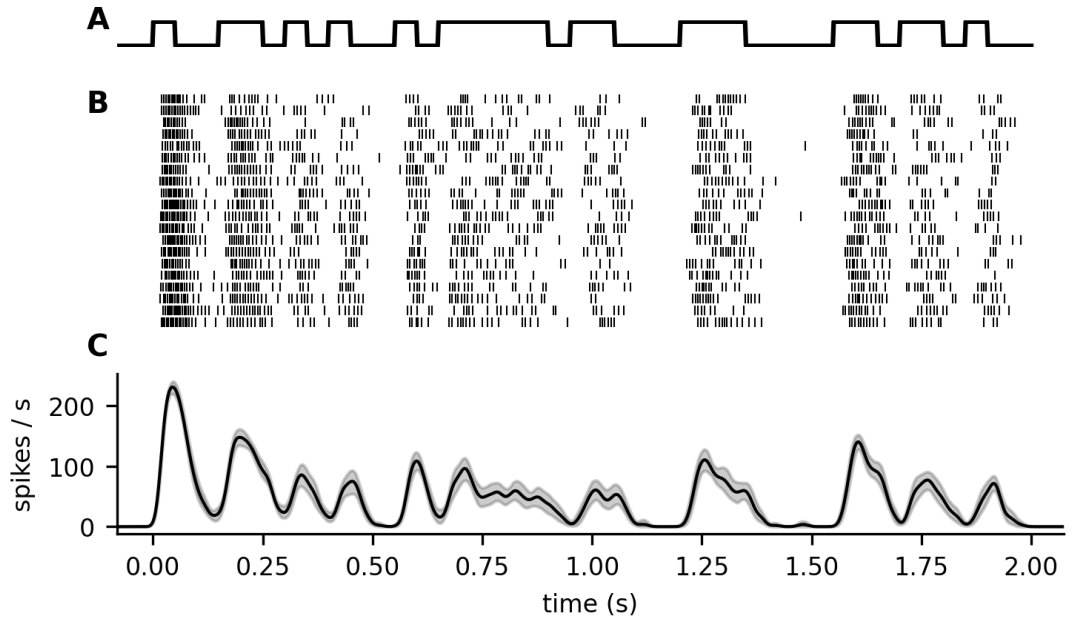

Figure 2: Variability of neural response. The spiking activity of a single ORN of *Agrotis ipsilon*. The ORN was presented with the same stimulus many times (**A**, ON/OFF delivery of pheromone). The neuron's response is different in each trial (**B**, raster plots, each row represents a trial, each line represents a spike). The precise timing of spikes is not maintained over the trials, but the time course of the activity can be captured by a time-dependent firing rate (**C**, estimated with kernel density estimation, as described in the Section 2.2.3, Eq. 2.9, bw = 10 ms). The shaded area represents a 95% confidence interval of the mean firing rate, estimated by bootstrapping.

According to the rate coding hypothesis, the information is encoded in the mean firing rate of the neuron, with the mean firing rate of a neuron defined as the number of spikes fired by the neuron, averaged over some time window, specified by the experimenter. Therefore, within this time window, all information possibly contained in the precise timing of the spikes is not considered (Stein et al., 2005). In contrast to the rate code, a cell is considered to use temporal code if the precise pattern of spike firing contains essential information about the stimulus (Dayan and Abbott, 2005).

The great benefit of rate code is its robustness towards noise. Efficient information transmission with temporal code requires precise timing of spikes over multiple trials of presentation of the same stimulus. Although some neurons might exhibit such behavior for certain stimuli (Mainen and Sejnowski, 1995), neurons typically exhibit a significant trial-to-trial variability, and their behavior is better described by an average firing rate. Fig. 2 shows the response of an ORN to a repeated presentation of an identical stimulus. The precise timings of spikes are not maintained over subsequent trials, but a time-dependent firing rate can describe the activity.

Understanding how the information about the stimulus is encoded is essential for understanding the evolutionary pressures on the neural system. The efficient coding hypothesis asserts that neurons, under strong evolutionary pressure, are

adapted to process the information from their natural surroundings efficiently (Barlow, 1961). A popular approach to evaluating the efficiency of information processing is using Shannon's information theory (Shannon, 1948). Recordings from the retina of the blow fly showed that the stimulus-response relationship of the neurons (stimulus: contrast of the visual scene, response: firing rate) is such that the entropy of the response is maximized by a stimulus distribution which is very close to the contrast distribution observed in its natural environment. Similar entropy maximization principle has been observed in the *Drosophila* antennal lobe, the secondary layer of olfactory signal processing in insects (Bhandawat et al., 2007; Abbott and Luo, 2007; Kadakia and Emonet, 2019).

The entropy of the output distribution corresponds to the maximum amount of information that can be encoded in the output (Shannon, 1948). However, due to the noise in the system, this is not necessarily equivalent to the maximum amount of information that the system can transmit. It is, therefore, essential to understand the trial-to-trial variability of the system. A number of studies, therefore, analyzed both theoretically and experimentally the trial-to-trial variability in various neurons and neuronal models, showing that the trial-to-trial variability can be in a large portion of neurons described by a Poisson-like activity with a Fano factor close to one (Tuckwell, 1988; Gur et al., 1997; Geisler and Albrecht, 1997; Shadlen and Newsome, 1998; Brunel, 2000). Interestingly, experimental studies also showed that the trial-to-trial variability may decrease after the stimulus onset (Monier et al., 2003; Churchland et al., 2010), a phenomenon which we studied theoretically (Barta and Kostal (2021), Attachment I the attached report Attachment II).

Taking the trial-to-trial variability into account, the entropy maximization principle can be substituted by the mutual information maximization principle (Stein, 1967; Borst and Theunissen, 1999; Ikeda and Manton, 2009; McDonnell et al., 2011). However, neither entropy maximization of the output distribution nor mutual information maximization principle is observed in the *in-vivo* recordings of cortical neurons. Instead, their post-synaptic firing rates concentrate mainly at lower values (Treves et al., 1999).

This points towards a balance between information transmission and energy consumption (de Polavieja, 2002, 2004; Balasubramanian et al., 2001; Levy and Baxter, 1996). Neurons need a significant amount of energy to process and transmit information. It is estimated that in children, the brain accounts for up to 50% of the resting body's total oxygen consumption (Sokoloff, 1996). Given that the brain's energy budget is limited (Attwell and Laughlin, 2001), it is likely that neurons have to balance between transmitting as much information as possible and being economical.

Based on the observation in cortical neurons, suggesting that the cortex maximizes transmitted information with constraints on the metabolic expenses, a number of studies investigated the maximization of information-per-cost in single neurons (Kostal and Kobayashi, 2015; Suksompong and Berger, 2010; Sengupta et al., 2013; Xing et al., 2015; Sungkar et al., 2016, 2017). Sengupta et al. (2013) showed that the balance between excitatory and inhibitory synaptic currents observed in *in-vivo* recordings of the cortex (Destexhe et al., 2003; Paré et al., 1998) maximizes the information-per-cost in neurons using temporal code. This study, however, only considered a constant intensity input and did not analyze the

effects of the external stimulus and the effect of its randomness on the trial-to-trial variability of the neuron and how the external stimulus is encoded.

In (Barta and Kostal (2019), Attachment III), we modeled information transmission by single neurons, with spontaneous activity generated by the background input with balanced excitatory and inhibitory synaptic currents as in (Sengupta et al., 2013), but receiving an additional stimulus signal on top of this background input and studied the effect of different model parameters on the mutual information between the stimulus and the response with metabolic constraints. The stimulus increased both the excitatory and inhibitory input to the neurons, as observed in *in-vivo* recordings after stimulus presentation (Monier et al., 2003). Among other parameters, we studied how the stimulus-associated inhibition affects metabolically efficient information transmission by the neurons and found that compared to other parameters, such as spontaneous activity, the stimulus-associated inhibition has only a minor effect.

The inhibitory input is, however, likely to be much more important in neural networks. The information about the stimulus is in some cases expected to be carried by the averaged firing rate of the population instead of the firing rate of a single neuron, which decreases the trial-to-trial variability of the response (Shadlen and Newsome, 1998). The magnitude of the decrease of the trial-to-trial variability is however affected by correlations between the neurons. Neural correlations are typically classified as signal correlations and noise correlations (Averbeck et al., 2006). While signal correlations are related to the encoded stimulus and are important for discriminating between different stimuli, noise correlations are a shared trial-to-trial variability among the neurons, which is detrimental to the information transmission by the averaged population activity (Abbott and Dayan, 1999).

In recurrent neural networks, the inhibition associated with the external stimulus emerges due to the recurrent connectivity of the network. This inhibitory feedback then decreases the noise correlations (Renart et al., 2010; Tetzlaff et al., 2012; Bernacchia and Wang, 2013) and thus improves the information transmission capabilities of the network. In (Barta and Kostal, 2019) we showed that the inhibition associated with the stimulus increases the cost of the neural activity. This raises the question, of whether the decreased noise correlations offer sufficient improvement in information transmission to justify the increased metabolic expenses. To better understand this balance, we analyzed the trade-off in a population consisting of recurrently connected excitatory and inhibitory neurons, representing a small area in the sensory cortex (Barta and Kostal (2023), Attachment IV).

Studying the amount of transferred information about the external stimulus and the associated metabolic expenses only makes sense if we understand what information about the stimulus is actually being transmitted. In (Barta and Kostal, 2019) and (Barta and Kostal, 2023) we assumed that the system is encoding the intensity of the stimulus, such as contrast intensity in a visual scene, sound intensity or the intensity of mechanical simulation and we assumed that the information is carried by the number of fired action potentials. However, the stimulus might be encoded in a more complex manner, e.g., in the time course of the response. A popular method of estimating the transmitted information is then attempting to decode the stimulus from the response and calculating the mutual information between the decoded stimulus and the real stimulus and thus

obtaining the lower bound on the mutual information (Borst and Theunissen, 1999; Geffen et al., 2009). However, we still need to make assumptions about which parts of the stimulus are being encoded and what is their importance.

For insects using the olfactory signal for navigation, encoding the temporal structure of the signal becomes crucial (Baker et al., 2018; Murlis et al., 1992; Mafra-Neto and Cardé, 1994; Martinez et al., 2013; Cardé, 2021). However, it is not yet fully understood which temporal features are encoded by the olfactory system and how is the olfactory system adapted to encode these features. Moreover, different insect species encode the olfactory signal differently, which could be the result of different environments and behavioral strategies of the different species.

Among insects, male moths are considered to be the most efficient navigators. They are able to locate a conspecific female emitting a pheromone plume over hundreds of meters (Cardé and Charlton, 1984; Elkinton et al., 1987; Shorey, 1976; Wall and Perry, 1987) and their olfactory system is expected to be highly tuned for this task and understanding how they respond to different stimuli will help us understand what features in the olfactory signal are important for odor-guided navigation in turbulent environments. However, studying the response dynamics of moth ORNs to pheromone stimulation is complicated due to difficulties with the precise delivery of odor molecules with low volatility, such as pheromones (Gorur-Shandilya et al., 2019). We built a new odor delivery device that solved the previously encountered issues and studied the responses of male moth ORNs to pheromone stimulation (Barta et al. (2022), Attachment V and Attachment VI).

Previous studies showed that the ORNs respond phasi-tonically to a stimulus, with an intense response to stimulus onset and a gradual adaptation to a steady state activity (Fig. 3). The ORNs, therefore, seem to put more emphasis on encoding the stimulus onset, which correlates with the observed behavior of moths. Upon odor encounter, moths start an upwind flight (Mafra-Neto and Cardé, 1994). Similarly, moths are observed to cease the upwind flight and start a movement called zig-zag casting after losing the odor plume. We could therefore expect that similar emphasis is put on detecting the stimulus offset. Some *Drosophila* ORNs have been known to encode the stimulus offset by a transient inhibition following the stimulus offset (Kim et al., 2011, 2015; Nagel and Wilson, 2011; Martelli et al., 2013) (Fig. 3). However, moth ORNs were typically observed to show little change in their firing activity after the stimulus offset and the duration of their responses long exceeded the duration of the stimulus (Kaissling et al., 1989; Jarriault et al., 2010; Grémiaux et al., 2012; Rospars et al., 2014) (Fig. 3) and the detection of the stimulus offset was assumed to take place in the antennal lobe (AL), the second olfactory signal processing layer in the insect olfactory signal. The duration of the response of the AL neurons, however, still exceeded the duration of the stimulus (Jarriault et al., 2009, 2010). With our new odor delivery device, we were able to show that the responses of moth ORNs actually closely resemble the responses of *Drosophila* ORNs by encoding the stimulus offset by a transient inhibition (Barta et al., 2022).

To understand how a neuron integrates the stimulus and what features it extracts, linear-nonlinear models are often employed (Geffen et al., 2009; Nagel and Wilson, 2011; Martelli et al., 2013; Jacob et al., 2017). These robust models consisting of a linear kernel and a static nonlinearity provide insight into the

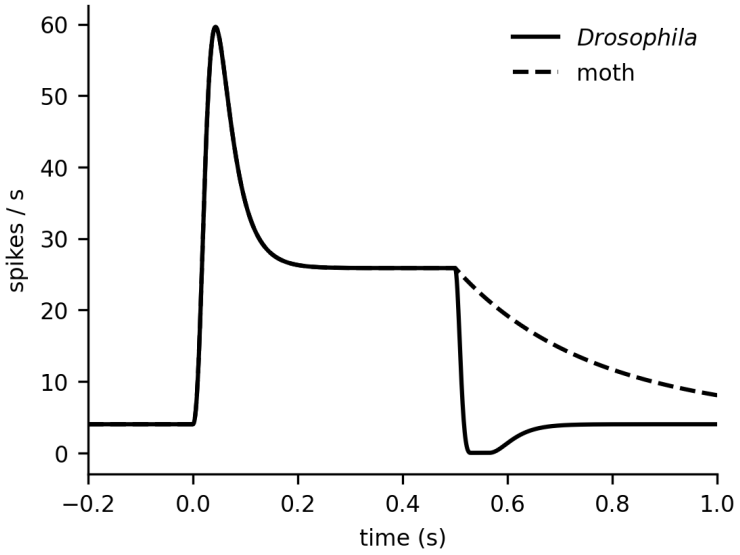

Figure 3: Stimulus offset detection by *Drosophila* and moths.
Illustration of time-dependent firing rates in a response to a 500 ms stimulus. The onset is detected by a rapid rise of the firing rate, which then gradually decays to a steady state. While immediate termination of spike firing activity and a transient inhibition typically marks the end of stimulus in *Drosophila* ORNs, the response of moth ORNs to pheromone is long-lasting. Here the offset for the moth response is modeled as an exponential decay with a time constant 384 ms, as in (Tuckman et al., 2021b,a).

temporal integration of the stimulus and can predict well the firing rate of a neuron. However, classical approaches to fitting these models have drawbacks, such as high-frequency oscillations of the linear kernel and acausality of the linear kernel that complicate the interpretability of the model. We proposed a new method of fitting the linear kernel which circumvents these issues and successfully applied it to identify the time scales of integration and adaptation of the moth ORNs (Barta et al., 2022).

Although temporal code is assumed to play a role in odor identification (Wehr and Laurent, 1996; Laurent, 1997, 2002; Stopfer et al., 2003; Wilson and Laurent, 2005; Wilson et al., 2017; Kadakia and Emonet, 2019), studies focusing on the encoding of the temporal information focus on the time-dependent firing rate in relation to the stimulus and the spike firing patterns of the activity are ignored or are modeled as inhomogeneous Poisson processes (Lee et al., 2023; Rapp and Nawrot, 2020; Betkiewicz et al., 2020; Tuckman et al., 2021b,a). However, we observed that this assumption is typically not satisfied in the ORN activity, proposed a statistical model for its description, and discussed the possible origin of the firing pattern and the effects on downstream neurons in the antennal lobe (Attachment VI).

In the following chapters, I first provide a brief theoretical introduction to insect olfaction, mathematical models of neural activity, and methods used in this work. The chapter provides a general overview, more detailed information about the used methods is provided in the attached manuscripts and reports. In the Chapter 3 I provide a short summary of the main results and a discussion of each

attached work.

2. Theory and methods

2.1 Insect olfactory system

Olfaction is essential for insects to locate food sources, mating partners, and oviposition sites. The high efficiency of the insect olfactory system, paired with its relative simplicity, compared, e.g., to the sensory systems in mammals, makes it ideal for studying the principles of efficient neural coding.

In my thesis, I focus on early information processing, i.e., on the ORNs, stimulated directly by the odor molecules in the air and on the antennal lobe (AL), the primary olfactory brain area in insects, consisting of projection neurons (PNs), local neurons (LNs), and ORN terminals (the AL is the equivalent of the olfactory bulb in vertebrates).

2.1.1 Olfactory receptor neurons

ORNs can be divided into functional types based on what odor receptor they express. The expressed type of odor receptor defines to which odor molecules the neuron responds. Some odor receptors are broadly tuned (responding to many different odors), and some are narrowly tuned (responding only to one or few different odor molecules) (de Fouchier et al., 2017). Typically, receptors sensitive to social odors (e.g., pheromones) are narrowly tuned. Narrowly tuned moth ORNs responding to a sex pheromone are the main focus of the olfaction-focused part of the thesis.

The dendrite and soma of the ORN are located inside a sensillum, a porous, hair-like structure on the insect antenna (Fig. 4A). The sensillum contains three auxiliary cells, tightly wrapping the soma and effectively separating the ORN into two parts with different extracellular ionic environments - the outer dendrite is bathing the sensillar lymph, and the inner dendrite, soma, and axon in the hemolymph (Jacquin-Joly and Lucas, 2005; Kaissling, 2014; Chertemps, 2017).

When the odor molecules enter the sensillar lymph and bind to their cognate odor receptors on the dendrite, receptor ion channels open, and the dendrite becomes depolarized. Knowledge of the transduction process, from odor molecules entering the sensillar lymph to receptor channels opening (and eventually closing), is essential for modeling the response of the ORN to an odor encounter. Classically, the transduction process can be described by a set of chemical kinetic equations (Kaissling, 2001, 2004):

$$L_{\text{air}} \xrightarrow{k_i} L \tag{2.1}$$

$$nL + R \underset{k_1}{\overset{k_{-1}}{\rightleftharpoons}} R_L \underset{k_2}{\overset{k_{-2}}{\rightleftharpoons}} R_L^* \tag{2.2}$$

$$L + N \underset{k_3}{\overset{k_{-3}}{\rightleftharpoons}} N_L \xrightarrow{k_4} P + N \tag{2.3}$$

Here L_{air} represents the number of odor molecules (ligands) in the air surrounding the sensillum, L is the number of molecules that enter the sensillum, R is the number of free receptors, n is the number of molecules required to activate the receptor, R_L the number of bound receptors and R_L^* number of activated receptors.

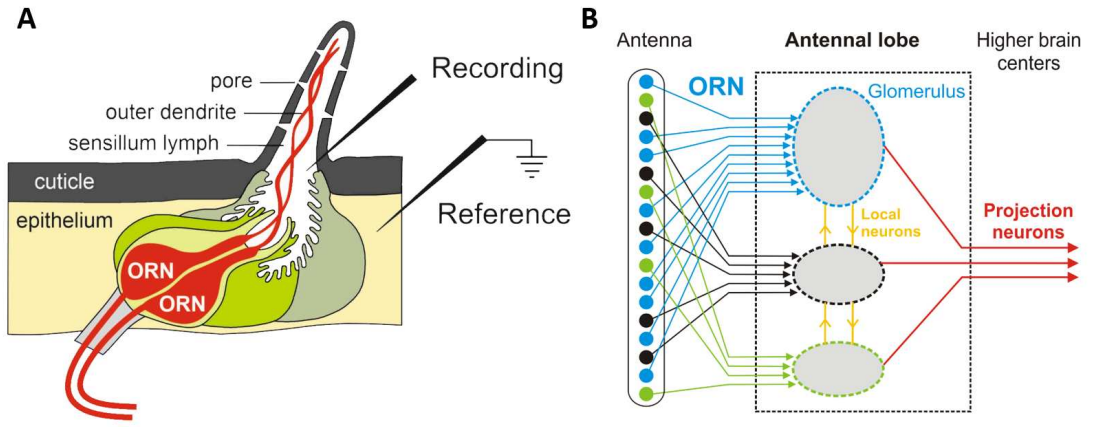

Figure 4: Insect olfactory system. A: The ORN is located in a hair-like structure called the sensillum. The pores in the cuticle allow the entry of odor molecules into the sensillar lymph, where they can bind to the receptors on the dendrite of the ORN. One sensillum can contain more than one ORN. The neuron's soma is surrounded by three auxiliary cells (thecogen, trichogen, and tormogen) that delimit the sensillar compartment and control its ionic composition. The electrodes illustrate their placement during single sensillar recording (SSR). Note that the placement of the recording is different for tip SSR. **B:** ORNs on the antenna express different odor receptors (color-coded in black, green, and blue). All ORNs expressing the same type of receptor converge into the same glomerulus in the antennal lobe (AL), where their axons connect to the dendrites of projection neurons (PNs) and local neurons (LNs). LNs provide lateral connections between the glomeruli and inhibit the PNs. The axons of the PNs project to higher brain centers of the insect.

R_L^* is the number that specifies the number of open ionic channels, therefore, the conductance between the dendrite and the sensillar lymph. The last equation then describes the degradation of the ligands. N is the number of degrading enzymes, N_L the number of bound enzymes and P the number of inactivated ligands. k_x describe the reaction rates. The Eqs. (2.1-2.3) are a simplification of a more complicated process, yet they can be used to build an ORN model with a good predicting power (Levakova et al., 2019). The transduction process can also be simplified by leaving out some intermediate steps or generalized by including the spontaneous opening of the receptor channels (Nagel and Wilson, 2011; Gorur-Shandilya et al., 2017):

$$R \underset{k_{-1}}{\overset{k_1[L_{\text{air}}]}{\rightleftharpoons}} R_L \underset{k_{-2}}{\overset{k_2}{\rightleftharpoons}} R_L^*, \tag{2.4}$$

$$R \underset{k_{-3}}{\overset{k_3}{\rightleftharpoons}} R^* \underset{k_{-4}}{\overset{k_4[L_{\text{air}}]}{\rightleftharpoons}} R_L^*. \tag{2.5}$$

Here the ligand dependence was moved into reaction rates that depend on the ligand concentration in the air $[L_{\text{air}}]$, R^* represents receptors activated without any ligand, responsible for the spontaneous activity.

2.1.2 Antennal lobe

The axons of ORNs expressing the same receptor type converge into the same glomerulus in the AL, where they connect by synapses onto the dendrites of the PNs and LNs (Kay and Stopfer, 2006; Wilson, 2013). PNs excite other PNs and LNs within the glomerulus (Fig. 4B). The convergence of the ORNs ensures a rapid response of the PNs to the odorant and reduction of the trial-to-trial variability exhibited by individual ORNs when exposed to the same stimulus over multiple trials (Rospars et al., 2014).

The LNs provide a lateral connection to other glomeruli in the AL. The lateral input to PNs is generally inhibitory. Therefore the LNs are responsible for odor-evoked inhibition. The lateral inhibition acts both presynaptically at the ORN axon terminal (thus mediating a gain control in the synapse (Olsen and Wilson, 2008)) and synaptically, directly hyperpolarizing the PNs (Wilson and Laurent, 2005). The lateral inhibition is responsible, e.g., for narrowing the tuning of PNs or for shaping their response profile by intensifying their response to the onset of the stimulus (Olsen et al., 2010).

2.2 Experimental methods and data analysis

2.2.1 Single sensillum recordings

Each sensillum contains one or multiple ORN dendrites. By extracellularly recording from a single sensillum, it is possible to record the activity of these ORNs. The activity of these ORNs can be discriminated by their spike amplitude and shape. In the trichoid sensilla of *Agrotis ipsilon*, containing neurons sensitive to the main compound of their sex pheromone, (Z)-7-dodecenyl acetate (Z7-12:Ac), typically only one amplitude of action potentials is observed (see Appendix A for cases with two different spike amplitudes). After recording the electrical signal from the sensillum, the spiking activity needs to be extracted from the electrical signal. Single sensillum recordings (SSR) and extraction of spiking activity were performed by Christelle Monsempès and Elodie Demondion. In this section, I provide a brief description of the process.

Two electrodes, a recording electrode and a reference electrode are placed into the insect antenna. The recording electrode is placed into the sensillar lymph, while the reference electrode is inserted into an adjacent antennal segment (Fig. 4A). The reference electrode is placed close to the sensillum to avoid contamination of the signal by the activity of ORNs in the neighboring sensilla.

To extract the action potentials, the activity is high-pass filtered (10 Hz) and thresholded (Fig. 5A). From the events that cross the threshold, electrical artifacts and random threshold crossings are separated from the action potentials using principal component analysis in the Spike2 software.

2.2.2 Local field potential and spiking activity

The following methods and electrodes can be used for SSR:

1. Tungsten electrode,

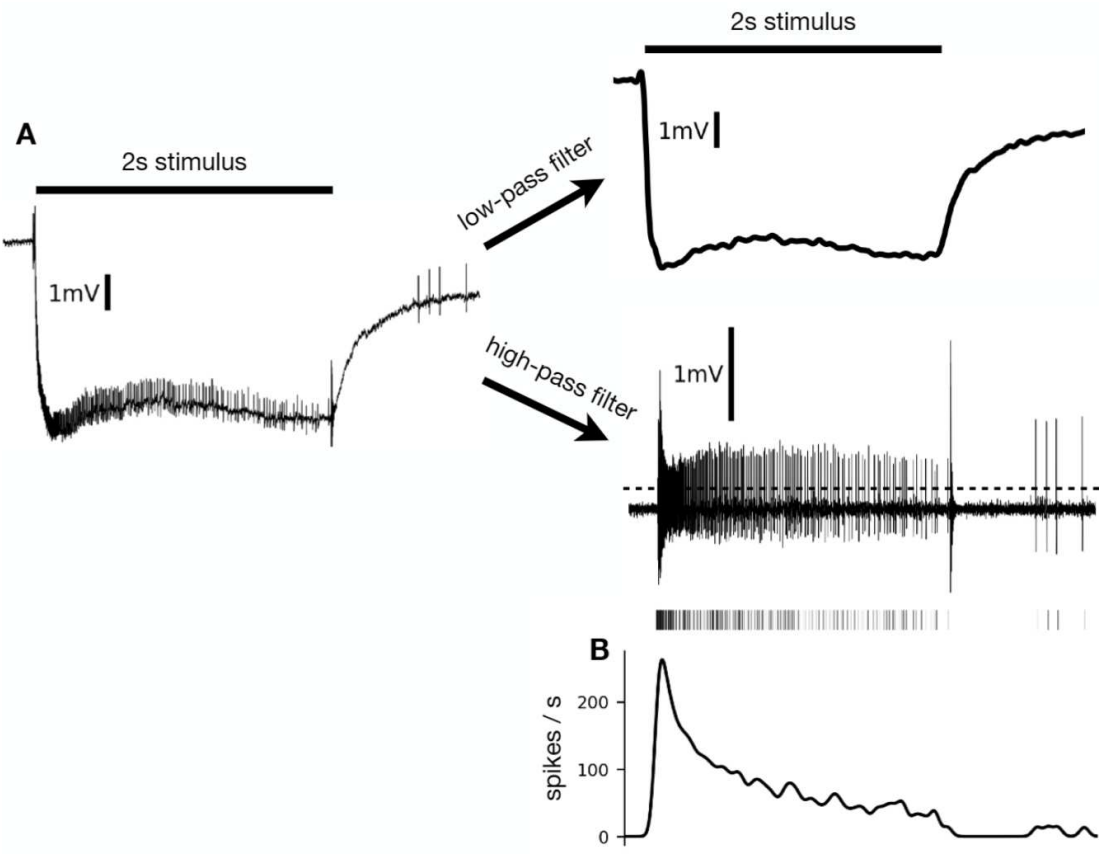

Figure 5: Signal analysis and firing rate estimation.A: Recording with a glass electrode can be low-pass filtered to obtain the LFP or high-pass filtered to isolate the firing activity. The high-pass filtered activity can be thresholded (dashed line) to obtain the spike train. Note that the vertical line at the beginning and end of the stimulus is an artifact, a signal from the electrovalve controlling the stimulus. **B:** The estimated firing rate. Replacing each spike with a normal distribution results in an estimate of time-dependent firing rate.

2. Glass electrode with a silver wire inserted in the base of the sensillum,

3. Glass electrode with a silver wire placed over the sensillum with a tip cut off (tip recording).

Due to the sharpness of the electrode, recordings with the tungsten electrode are the least invasive and it is possible to obtain long and stable recordings. However, the signal tends to drift away from its baseline due to polarization of the electrode and therefore the signal has to be high-pass filtered during the recording and we can only obtain the high frequency signal, i.e., the action potentials and their shapes and amplitudes.

Recordings with glass electrodes do not need to be high-pass filtered during the recording, and therefore we can also obtain the low-frequency response, referred to as the local field potential (LFP). During stimulation, positive current flows from the sensillar lymph into the neuron, and we observe a decrease in the potential in the sensillar lymph. To obtain the LFP from the glass electrode recordings, we low-pass filtered the recordings with a 2-pole Butterworth filter (Fig. 5A). The LFP is often used as a proxy for the current flow between the dendrite and the

sensillar lymph (Wilson, 2013; Gorur-Shandilya et al., 2017). We showed that in the moth ORNs, the relationship between the current I_d and LFP can be approximately expressed as (Barta et al., 2022):

$$\mathrm{LFP}(t) = (I_d * g)(t) \tag{2.6}$$

$$g(t) = \begin{cases} 0 & \text{for } t \leq 0, \\ -\frac{\beta}{\tau_{\mathrm{LFP}}} \exp(-t/\tau_{\mathrm{LFP}}) & \text{for } t > 0, \text{ with } \tau_{\mathrm{LFP}} = 10\,\mathrm{ms}, \end{cases} \tag{2.7}$$

where β is a scaling constant.

The recordings with the glass electrode are more invasive than the recordings with the tungsten electrode, and we observed that after some time of recording, the properties of the ORNs were often modified. This happened considerably sooner with the tip recording technique, therefore, all recordings of the LFP were done with the glass electrode inserted in the base of the sensilla.

2.2.3 Firing rate estimation

The time-dependent firing rate $\nu(t)$ of a neuron is defined as:

$$\nu(t) = \lim_{\Delta t \to 0^+} \frac{\mathrm{E}[N(t, t+\Delta t)]}{\Delta t}, \tag{2.8}$$

where $N(t, t+\Delta t)$ is the number of action potentials observed in the time window t to $t+\Delta t$ and E signifies the mean value across independent trials. To estimate the firing rate from a single trial, we used the kernel density estimation method with a Gaussian kernel (Fig. 5B):

$$\hat{\nu}(t) = \sum_{\{t_k\}} \mathcal{N}(t_k, \mathrm{bw}(t)^2), \tag{2.9}$$

where the sum goes over all spike times t_k, $\mathcal{N}(\mu, \sigma^2)$ is the normal distribution with mean μ and variance σ^2 and bw is the (possibly time-dependent) bandwidth of the kernel.

2.2.4 Trial-to-trial variability quantification

When comparing the trial-to-trial variability of two neurons (or the same neuron in different conditions) with the same mean activity $\mathrm{E}[N(t, t+\Delta t)]$, where $N(t, t+\Delta t)$ is the number of observed action potentials in a time window $(t, t+\Delta t)$, we can directly compare the variance of the number of observed action potentials $\mathrm{Var}[N(t, t+\Delta t)]$. However, sometimes it is beneficial to scale the variance relative to the mean number of action potentials and obtain the Fano factor:

$$\mathrm{FF} = \frac{\mathrm{Var}[N(t, t+\Delta t)]}{\mathrm{E}[N(t, t+\Delta t)]}. \tag{2.10}$$

The Fano factor of a Poisson process is equal to one, therefore, calculating the Fano factor lets us compare the trial-to-trial variability to a Poisson process.

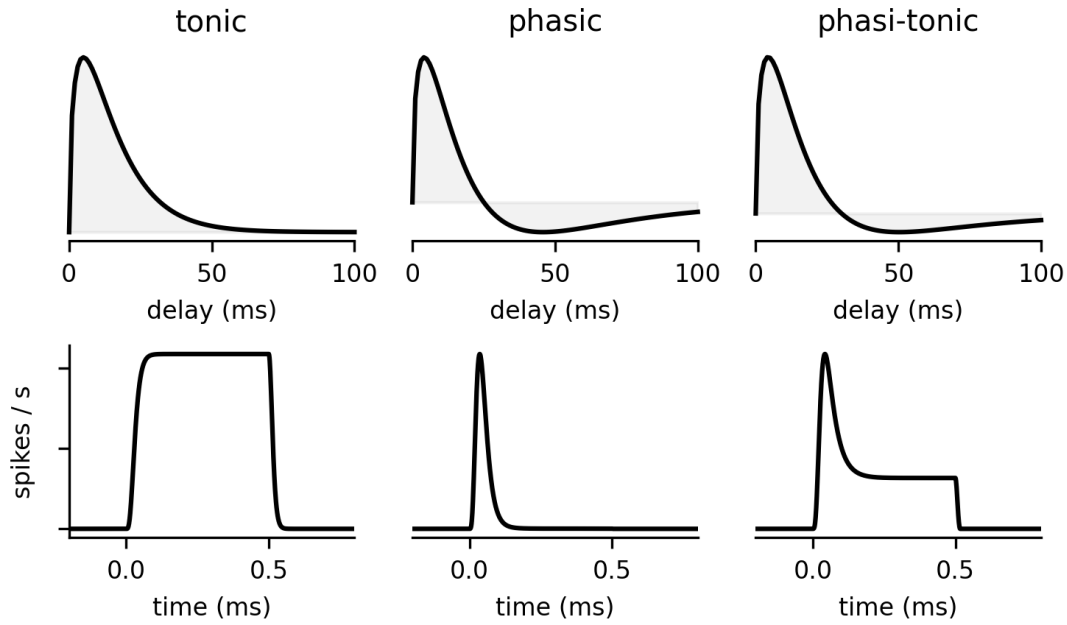

Figure 6: Linear filters and response profiles. The top row shows different linear filters and the bottom row the firing responses obtain with the filter convolved with a rectangular stimulus and passed through a static nonlinearity. The shaded area illustrates the positive and negative parts of the linear filter.

We can also estimate the trial-to-trial variability from the inter-spike intervals (ISIs) of a steady-state spike train with a coefficient of variation:

$$\mathrm{CV} = \frac{\sqrt{\mathrm{Var}[\tau_i]}}{\mathrm{E}[\tau_i]}, \tag{2.11}$$

where τ_i are the interspike intervals. Then

$$\mathrm{FF}_0 = \mathrm{CV}^2, \tag{2.12}$$

where FF_0 is the Fano factor calculated from infinite-length time window ($\Delta t \to +\infty$).

2.3 Mathematical models of neural activity

2.3.1 Linear-nonlinear models

A common approach to predicting the firing rate from the time-dependent stimulus $s(t)$ are linear-nonlinear models. Linear-nonlinear models consist of a linear kernel K and a static non-linearity f:

$$\nu(t) = f((K * s)(t)). \tag{2.13}$$

In the case of an excitatory stimulus, the kernel K can be decomposed into an excitatory component K_{exc} ($K_{\mathrm{exc}}(t) > 0\ \forall t$) representing the integration of the stimulus and an adaptation component K_{SFA} ($K_{\mathrm{SFA}} < 0\ \forall t$). Depending on the kernel shape, the convolution $K * s$ can then produce different firing rate profiles (Fig. 6):

- Tonic response: single-lobed kernel,
- Phasic response: bi-lobed kernel, $\int K(t)\,\mathrm{d}t = 0$,
- Phasi-tonic response: bi-lobed kernel, $\int K(t)\,\mathrm{d}t > 0$.

Typical choices for the static nonlinearity f are the Hill function

$$\nu = \frac{1}{1 + (H/\nu_{\text{lin}})^n}, \tag{2.14}$$

where H is the half maximum, n is the hill coefficient and $\nu_{\text{lin}} = K * s$; or a rectifier function

$$\nu(t) = \begin{cases} 0 & \text{for } t \leq 0, \\ \nu_{\text{lin}}(t) & \text{for } t > 0. \end{cases} \tag{2.15}$$

Fitting the linear-nonlinear model to neural data allows us to understand the time scales of input integration and adaptation.

Estimation of the linear kernel

Two common approaches exist for estimating the linear kernel K (Dayan and Abbott, 2005):

1. Estimation in the frequency domain (Wilson, 2013),
2. Estimation using the variation calculus (Geffen et al., 2009; Martelli et al., 2013; Jacob et al., 2017).

The linear kernel should only be defined for $t > 0$ (positive delays) so that the model predicts the response only based on the past stimulus. A common issue with filters estimated in the frequency domain is that unless the stimulus has a flat power spectrum, the domain of the filter spans also to negative values of the delay and the filter is therefore acausal. Such filters cannot be considered biologically plausible and are difficult to interpret.

In the case of odor delivery, although it is possible to deliver a stimulus with a flat power spectrum (up to a cut-off frequency), the LFP does not have a flat power spectrum anymore and therefore we cannot estimate a causal LFP-to-firing rate linear filter in the frequency domain. Therefore, in the following paragraphs I focus on the variation calculus method.

In (Barta et al., 2022) we proposed an approach to linear filter estimation closely related to the approach using variation calculus. Here I will first describe the variation calculus approach and then the approach we used in (Barta et al., 2022). Benefits of our new approach are discussed in the Section 3.5.

The goal is to estimate such linear filter K that the squared error between the prediction $(K * s)(t)$ and the response $\nu(t)$ is minimized:

$$E = \int_0^T \left(\int_0^{+\infty} K(t')s(t - t')\,\mathrm{d}t - \nu(t) \right)^2 \mathrm{d}t. \tag{2.16}$$

To calculate the shape of the filter numerically, we may discretize the time, and the problem may be solved as a least squares optimization problem. We construct a

time shifted stimulus matrix $\mathbf{S}$, $S_{ji} = s(t-(i+j)\Delta t)$. With $\mathbf{k} = (k_1, \ldots, k_N)^T$ as the kernel vector (time delay ranging from 0 to $N\Delta t$) and $\boldsymbol{\nu} = (\nu((N+1)\Delta t), \nu((N+2)\Delta t), \ldots, \nu(T))^T$ as the response vector, the problem can be formulated as:

$$\mathbf{k} = \arg\min_{\mathbf{k}'}(\|\mathbf{r} - \mathbf{S}\mathbf{k}'\|). \tag{2.17}$$

Elastic-net regularization is often implemented to avoid overfitting on small data sets (Zou and Hastie, 2005; Martelli et al., 2013; Jacob et al., 2017; Lever et al., 2016):

$$\mathbf{k} = \arg\min_{\mathbf{k}'}(\|\mathbf{r} - \mathbf{S}\mathbf{k}'\| + \lambda\|\mathbf{k}'\|^2 + \mu\|\mathbf{k}'\|_1), \tag{2.18}$$

where λ and μ are regularization coefficients, $\|\mathbf{v}\| = \sqrt{\sum |v_i|^2}$ is the L2 norm and $\|\mathbf{v}\|_1 = \sum |v_i|$ the L1 norm of a vector.

In (Barta et al., 2022), we modified the time-shifted stimulus matrix $\mathbf{S}$. Instead of the i-th row representing a stimulus segment of length $N\Delta t$, shifted by $i\Delta t$, each column can be thought of as a convolution of the past stimulus with a gamma distribution with time constant τ and shape parameter α:

$$p_\gamma(x; \tau, \alpha) = \frac{1}{\Gamma(\alpha)\tau^\alpha} x^{\alpha-1} e^{-x/\tau}. \tag{2.19}$$

The coefficient vector $\boldsymbol{\theta} = (\theta_{\tau_1,\alpha_1}, \theta_{\tau_2,\alpha_1}, ...)^T$ then contains coefficients corresponding to different time constants and shapes. We used lasso regression to estimate the coefficients for a grid of (τ, α) pairs:

$$\boldsymbol{\theta} = \arg\min_{\boldsymbol{\theta}'}(\|\mathbf{r} - \mathbf{S}_{\boldsymbol{\tau},\boldsymbol{\alpha}}\boldsymbol{\theta}'\| + \mu\|\boldsymbol{\theta}'\|_1). \tag{2.20}$$

The delay-dependent kernel is then expressed as:

$$K(t) = \sum_{\boldsymbol{\tau}} \sum_{\boldsymbol{\alpha}} \theta_{\tau,\alpha}(p_\gamma(x; \tau, \alpha) * s)(t). \tag{2.21}$$

2.3.2 Spiking neural models

The linear-nonlinear model belongs to a class of models that only predict the firing rate of a neuron. But sometimes, a model generating action potential is desirable. Apart from exploring coding by precise spike timing, spiking models may help us investigate the trial-to-trial variability of neural systems. Here I first describe how the membrane potential of neurons is modeled without any spike-generating mechanism and then discuss different ways of extending the membrane potential model with a spike-generating mechanism.

Subthreshold membrane potential

Neurons are commonly modeled as electrical circuits (Dayan and Abbott, 2005). In the absence of any ion-transporting proteins, the neural membrane is impermeable to electrically charged ions and acts as a capacitor with capacitance C. Here I only consider models where we assume that charge and ions are distributed evenly across the neuron without any delay and thus neglect the effect of the neuron's morphology.

Ion pumps are proteins that actively use energy to move ions across the membrane, make the neuron negatively charged, and create an electrical gradient between the inside and outside of the neuron. Certain proteins, ion channels, let specific ions pass through the membrane. These channels allow the flow of electrical current and can therefore be described as conductances in an electrical circuit.

The combination of active ion transport by ion pumps and passive transport by ion channels leads not only to an electrical gradient but also to different concentration gradients for different ion types. An equilibrium potential exists for each ion channel type, at which the diffusion, driving the ions across the membrane due to the concentration gradient, is in balance with the electrical forces. An RC circuit equation can then describe the membrane potential V:

$$C\frac{\mathrm{d}V}{\mathrm{d}t} = -\sum_X g_X(t)(V - E_X), \tag{2.22}$$

where the sum goes over different ion channel types X, $g_X(t)$ are their (possibly time dependent) conductances and E_X are their equilibrium potentials.

The conductance of some ion channels can be considered constant over time. These channels are grouped as leaky channels with leak equilibrium potential E_L (typically between $-80\,\mathrm{mV}$ and $-70\,\mathrm{mV}$) and conductance g_L.

Neurons receive external input, which causes the temporary opening of different ion channels. These channels are either excitatory (equilibrium potential $E_{\mathrm{exc}} > V$), and their opening depolarizes the neuron, or inhibitory (equilibrium potential E_{inh}) and their opening hyperpolarizes the neuron. A simple model of a cell receiving excitatory and inhibitory external input is then

$$C\frac{\mathrm{d}V}{\mathrm{d}t} = -g_L(V - E_L) + I_{\mathrm{ext}}(t) \tag{2.23}$$

$$I_{\mathrm{ext}}(t) = -g_{\mathrm{exc}}(t)(V - E_{\mathrm{exc}}) - g_{\mathrm{inh}}(t)(V - E_{\mathrm{inh}}) \tag{2.24}$$

Hodgkin-Huxley model

Neurons usually communicate by electrical impulses called action potentials (or spikes). Action potentials are triggered by the depolarization of the membrane and are shaped by a complex interplay of ion channels with membrane potential (voltage)-dependent conductances. Sodium-based action potential stem from voltage-gated sodium channels. Calcium-based action potentials, stemming from voltage-gated calcium channels, also occur in some neurons. However, in this work, I focus only on sodium-based action potentials, which propagate along the neuron's axon and pass the signal to neurons downstream. Therefore, in this text, action potential, or spike, refers to a sodium-based action potential.

The interplay of the ion channels can be described by the Hodgkin-Huxley model (Hodgkin and Huxley, 1952; Destexhe and Paré, 1999), describing the dynamics of the voltage-gated sodium and voltage-gated potassium channels:

$$C\frac{\mathrm{d}V}{\mathrm{d}t} = -g_L(V - E_L) - g_{\mathrm{Na}}m^3h(V - E_{\mathrm{Na}}) - g_{\mathrm{K}}n^4(V - E_{\mathrm{K}}) + I_{\mathrm{ext}}(t), \tag{2.25}$$

where I_{ext} describes the external input (e.g., as in Eq. 2.23), g_{Na} and g_{K} are maximum conductances of sodium and potassium channels, respectively, E_{Na} and

E_{K} the corresponding reversal potentials and m, h, n are voltage-dependent gating variables ($0 \leq x \leq 1$ for $x \in \{m, h, n\}$). The gating variables obey the kinetic equations

$$\frac{\mathrm{d}x}{\mathrm{d}t} = \alpha_x(V)(1-x) - \beta_x(V)x, \tag{2.26}$$

where α_x, β_x are the opening and closing rates, $0 \leq x \leq 1$. Equivalently

$$\tau_x(V)\frac{\mathrm{d}x}{\mathrm{d}t} = -[x - x_\infty(V)], \tag{2.27}$$

where $x_\infty(V)$ is the steady state and $\tau_x(V)$ the corresponding time constant.

A possible dependence of τ_x and x_∞ on V is shown in Fig. 7 (Destexhe and Paré, 1999), the mathematical form of the dependences is in the Appendix B. The action potential is initiated when depolarization of the membrane potential triggers further depolarization by opening the m-gates with a short time constant. The action potential is terminated by slower inactivation of the h-gates and activation of the n-gates, gating the hyperpolarizing potassium channels.

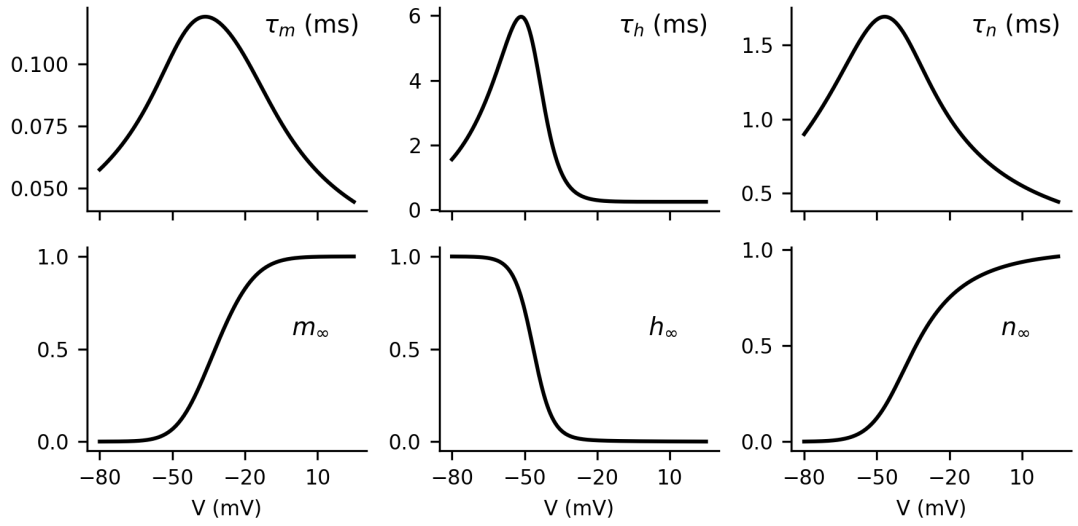

Figure 7: Dependence of gating variables of the Hodgkin-Huxley model on the membrane potential. The dependence of the time constants and steady-state values, as in Eqs. (2.27), on the membrane potential is shown for the gating variables m, h, n.

Exponential leaky integrate-and-fire models

The Hodgkin-Huxley model can be simplified by only modeling the onset of the action potential. During the initiation phase of the action potential, we can assume that

$$\frac{\mathrm{d}h}{\mathrm{d}t} = \frac{\mathrm{d}n}{\mathrm{d}t} = 0. \tag{2.28}$$

Further, due to τ_m being very short, we can assume

$$m(V) = m_\infty(V). \tag{2.29}$$

In the range of membrane potentials where action potentials are initiated, we can model $g_{\mathrm{Na}}m^3(V)$ as an exponential function instead and obtain the exponential leaky integrate-and-fire model (Fourcaud-Trocmé et al., 2003; Brette and Gerstner, 2005; Platkiewicz and Brette, 2010):

$$C\frac{\mathrm{d}V}{\mathrm{d}t} = -g_L(V - E_L) - g_L k_a \exp\left(\frac{V - V_T}{k_a}\right) + I_{\mathrm{ext}}(t), \tag{2.30}$$

where V_T and k_a characterize the exponential function. When the membrane potential reaches some specific value (e.g., 0 mV), an action potential is recorded, and the membrane potential is reset to a reset value V_r (e.g., $V_r = E_L$).

Leaky integrate-and-fire models

In the limit of $k_a \to 0^+$, we obtain a model where any dynamics below V_T are not affected by the voltage-gated channels and immediately fires an action potential upon reaching V_T. This model, commonly called leaky integrate-and-fire (LIF), while very simple and in some cases analytically tractable, can account for a wide range of properties of single neurons and their networks (Tuckwell, 1989; Dayan and Abbott, 2005; Brunel, 2000).

Spike frequency adaptation

All the models above consisted of two essential parts:

1. Input to the neuron,
2. Spike generating mechanism.

However, neurons express a wide range of ion channels in their membrane, modifying their properties. These properties can be implemented in the models above by including the additional ion channels in the Eq. (2.22) or modifying their properties. An important property missed by the models above is spike frequency adaptation (SFA) (Benda and Herz, 2003; Benda, 2021). SFA is a mechanism that makes action potential firing more difficult. The onset of SFA is delayed to the onset of the firing response. After the stimulus onset, neurons respond with a firing response decreasing in its intensity with time during the stimulus. SFA is a widespread neuronal property present in different animals, different brain areas, and different sensory systems (including ORNs, Fig. 5B). LIF models extended with various mechanisms of SFA can be fit to precisely predict a large variety of neural responses, including precise spike timing (Jolivet et al., 2006, 2008; Kobayashi et al., 2009; Yamauchi et al., 2011; Teeter et al., 2018).

The mechanisms of SFA can be grouped into two categories (Benda and Herz, 2003; Gutkin and Zeldenrust, 2014):

1. Inactivation of depolarizing currents,
2. Activation of hyperpolarizing currents.

Further, the (in)activation can be either

1. Spike dependent,
2. Voltage-dependent.

Dynamic threshold models. Inactivation of depolarizing currents typically means that the voltage-gated sodium channels are inactivated and, therefore, cannot activate to generate an action potential. If the inactivation occurs only at high membrane potential values, it can be considered spike dependent. Otherwise, the inactivation is voltage-dependent or a combination of both if the inactivation happens faster at high membrane potential values, as observed, for example, in Fig. 7.

Inactivation of the sodium channels leads to a dynamic threshold V_T in the LIF model. Classically, the threshold is modeled as spike dependent, increasing by ΔV_T with every fired action potential and then decreasing to its original value (Platkiewicz and Brette, 2010; Benda et al., 2010; Kobayashi et al., 2009; Yamauchi et al., 2011; Kobayashi and Kitano, 2016; Levakova et al., 2019).

In the MAT model (Kobayashi et al., 2009), the threshold V_T decays exponentially to its steady state ω on several different time scales:

$$V_T(t) = \sum_k H(t - t_k) + \omega, \tag{2.31}$$

$$H(t) = \sum_{j=1}^{L} \alpha_j \exp(-t/\tau_j), \tag{2.32}$$

where t_k are the previous spikes of the neuron, L is the number of threshold components, α_j is the increase of j-th component upon spike firing, which then decays to zero exponentially with a time constant τ_j. This model, in particular, is very effective in precisely predicting spike firing times and spike firing patterns (Kobayashi et al., 2009; Jahangiri and Gerling, 2011; Lee et al., 2023).

In models without a clear threshold, such as the exponential leaky integrate-and-fire, the dynamic threshold may be implemented by modifying the inactivation properties of the sodium channels (Fleidervish et al., 1996; Martina and Jonas, 1997; Edman et al., 1987; Benda and Herz, 2003; Benda et al., 2010). A common extension is an additional gating variable s (governed by the Eq. 2.26) inactivating during depolarization:

$$C\frac{\mathrm{d}V}{\mathrm{d}t} = -g_L(V - E_L) - g_{\mathrm{Na}}m^3hs(V - E_{\mathrm{Na}}) - g_{\mathrm{K}}n^4(V - E_{\mathrm{K}}) + I_{\mathrm{ext}}(t), \tag{2.33}$$

where τ_s (Eq. 2.27) is on the time scales of several hundred ms.

Hyperpolarizing currents. Hyperpolarizing currents lower the rate of depolarization by the stimulus and therefore attenuate the neuron's spike-firing response. These currents can be activated by depolarization of the neuron or by processes resulting from firing an action potential, such as the influx of calcium ions, activating hyperpolarizing potassium channels.

A common example of voltage-activated SFA through hyperpolarizing currents is the M-current adaptation. The Hodgkin-Huxley model with M-current adaptation can be expressed as:

$$\begin{aligned} C\frac{\mathrm{d}V}{\mathrm{d}t} = &-g_L(V - E_L) - g_{\mathrm{Na}}m^3h(V - E_{\mathrm{Na}}) - \\ &-g_{\mathrm{K}}n^4(V - E_{\mathrm{K}}) - g_M p(V - E_{\mathrm{K}}) + I_{\mathrm{ext}}(t), \end{aligned} \tag{2.34}$$

where p is another gating variable following the Eqs. (2.26–2.27). The voltage dependence of the activation and inactivation rates is given in the Appendix B.

After-hyperpolarization (AHP) currents are currents triggered by calcium influx into the neuron during an action potential. It is, therefore, a spike-dependent SFA. Proper modeling of AHP involves describing the calcium influx, calcium extrusion, and calcium-dependent potassium channel activation. However, a more straightforward approach is often implemented for LIF or exponential LIF models. Additional potassium conductance that increases with every action potential and decays exponentially to zero is added:

$$C\frac{\mathrm{d}V}{\mathrm{d}t} = -g_L(V - E_L) - g_L k_a \exp\left(\frac{V - V_T}{k_a}\right) - g_{\mathrm{AHP}}(t)(V - E_{\mathrm{K}}) + I_{\mathrm{ext}}(t), \tag{2.35}$$

$$\frac{\mathrm{d}g_{\mathrm{AHP}}}{\mathrm{d}t} = -\frac{g_{\mathrm{AHP}}}{\tau_{\mathrm{AHP}}} + \sum_k \Delta_{\mathrm{AHP}}\delta(t - t_k), \tag{2.36}$$

where τ_{AHP} is the time constant of the hyperpolarizing conductance decay, Δ_{AHP} the increase in the conductance with every action potential fired, and t_k are the action potentials fired by the modeled neuron.

Models of external input

Neurons connect with synapses. At the synapse, the pre-synaptic neuron (connecting with a synapse onto the studied, post-synaptic, neuron) releases neurotransmitters which are then bound by the synaptic receptors of the post-synaptic neuron. In turn, ion channels are temporarily open. In the models above, the conductances of these channels were represented by g_{exc} and g_{inh} and the total currents as $g_{\mathrm{exc}}(E_{\mathrm{exc}} - V)$ for the excitatory and $g_{\mathrm{inh}}(E_{\mathrm{inh}} - V)$. In the following, I will summarize different approaches to modeling the time course of the conductances and the synaptic currents used in this work.

We assume that the release of neurotransmitters and their uptake by the receptors is fast, and the conductances of the synaptic channels then increase discontinuously when the pre-synaptic neuron fires an action potential. Further, we assume that there is a large number of these receptors that are activated after pre-synaptic action potentials, and they start closing randomly and independently, resulting the the time course of the conductances described by:

$$\frac{\mathrm{d}g_{\mathrm{exc}}}{\mathrm{d}t} = -\frac{g_{\mathrm{exc}}}{\tau_{\mathrm{exc}}} + \sum_{t_k \in \mathcal{T}_{\mathrm{exc}}} \Delta_{\mathrm{exc}}\delta(t - t_k), \tag{2.37}$$

$$\frac{\mathrm{d}g_{\mathrm{inh}}}{\mathrm{d}t} = -\frac{g_{\mathrm{exc}}}{\tau_{\mathrm{inh}}} + \sum_{t_k \in \mathcal{T}_{\mathrm{inh}}} \Delta_{\mathrm{inh}}\delta(t - t_k), \tag{2.38}$$

where τ_{exc}, τ_{inh} are the inverse of the closing rates, Δ_{exc} and Δ_{inh} are the conductance increases and $\mathcal{T}_{\mathrm{exc}}$, $\mathcal{T}_{\mathrm{inh}}$ are the pre-synaptic action potentials from excitatory and inhibitory neurons.

This model can be further simplified, commonly with one or both of the following assumptions:

1. Reversal potentials E_{exc} and E_{inh} are ignored and the differences $(E_{\text{exc}} - V)$ and $(E_{\text{inh}} - V)$ are considered constant,

2. Synaptic filtering is ignored, meaning that $\tau_x \to 0^+$ while $\frac{\Delta_x}{\tau_x}$ remains constant $(x \in \{\text{exc}, \text{inh}\})$.

If synaptic filtering is ignored, a pre-synaptic action potential evokes an immediate discontinuous increase of the membrane potential of the post-synaptic neuron. If reversal potentials are considered, this increase is proportional to $(E_{\text{exc}} - V)$ or $(E_{\text{inh}} - V)$, depending on whether the pre-synaptic neuron is excitatory or inhibitory.

If only the reversal potentials are ignored, the external current I_{ext} can be described as

$$I_{\text{ext}} = I_{\text{exc}} + I_{\text{inh}}, \tag{2.39}$$

$$\frac{\mathrm{d}I_{\text{exc}}}{\mathrm{d}t} = -\frac{I_{\text{exc}}}{\tau_{\text{exc}}} + \sum_{t_k \in \mathcal{T}_{\text{exc}}} A_{\text{exc}} \delta(t - t_k), \tag{2.40}$$

$$\frac{\mathrm{d}I_{\text{inh}}}{\mathrm{d}t} = -\frac{I_{\text{inh}}}{\tau_{\text{inh}}} + \sum_{t_k \in \mathcal{T}_{\text{inh}}} A_{\text{inh}} \delta(t - t_k), \tag{2.41}$$

where $A_{\text{exc}} > 0$ and $A_{\text{inh}} < 0$ are discontinuous changes in the synaptic current upon arrival of the post-synaptic action potential.

Diffusion approximation The diffusion approximation simplifies analytical tractability and computer simulations by expressing the input in terms of Gaussian noise. To apply the diffusion approximation, we make the following assumptions:

1. The arrival times of pre-synaptic spikes are described by Poisson processes with intensities λ_{exc} and λ_{inh},

2. The increments Δ_{exc} and Δ_{inh} are infinitesimally small, while λ_{exc} and $\lambda_{\text{inh}} \to \infty$ and $\Delta_{\text{exc}}\lambda_{\text{exc}}$, $\Delta_{\text{inh}}\lambda_{\text{inh}}$ remain constant.

The conductances can then be described by the Ornstein-Uhlenbeck process (Uhlenbeck and Ornstein, 1930):

$$\frac{\mathrm{d}g_{\text{exc}}}{\mathrm{d}t} = -\frac{g_{\text{exc}} - \mu_{\text{exc}}}{\tau_{\text{exc}}} + \sqrt{2\tau_{\text{exc}}}\sigma_{\text{exc}}\eta_{\text{exc}}(t), \tag{2.42}$$

$$\frac{\mathrm{d}g_{\text{inh}}}{\mathrm{d}t} = -\frac{g_{\text{inh}} - \mu_{\text{inh}}}{\tau_{\text{inh}}} + \sqrt{2\tau_{\text{inh}}}\sigma_{\text{inh}}\eta_{\text{inh}}(t), \tag{2.43}$$

where ν_{exc} and ν_{inh} are white noise realizations and

$$\mu_{\text{exc}} = \Delta_{\text{exc}}\lambda_{\text{exc}}\tau_{\text{exc}}, \tag{2.44}$$

$$\sigma_{\text{exc}} = \sqrt{\frac{\tau_{\text{exc}}\lambda_{\text{exc}}\Delta_{\text{exc}}^2}{2}}, \tag{2.45}$$

representing the mean and standard deviation of the excitatory conductance, with corresponding expressions for μ_{inh} and σ_{inh}. Conductances modeled in this manner reproduce well the realistic properties of the neuronal membrane potential (Destexhe et al., 2001).

Spiking neural networks

Neurons create complex recurrent networks. The connectivity of a group of neurons can be described by a connectivity matrix $\mathbf{W}$ containing the synaptic weights. The membrane potential of an i-th neuron in a network of N neurons, with neurons $1, \ldots, N_{\text{exc}}$ being excitatory and $N_{\text{exc}}, \ldots, N$ being inhibitory, can then be described by:

$$C\frac{\mathrm{d}V_i}{\mathrm{d}t} = -g_L(V_i - E_L) + I^i_{\text{ext}}, \tag{2.46}$$

$$I^i_{\text{ext}} = -g^i_{\text{exc}}(V_i - E^i_{\text{exc}}) - g^i_{\text{inh}}(V_i - E^i_{\text{inh}}), \tag{2.47}$$

$$\frac{\mathrm{d}g_{\text{exc}}}{\mathrm{d}t} = \frac{g_{\text{exc}}}{\tau_{\text{exc}}} + \sum_{j=1}^{N_{\text{exc}}} \sum_{t_s \in \mathcal{T}_j} w_{ji}\delta(t - t_s), \tag{2.48}$$

$$\frac{\mathrm{d}g_{\text{inh}}}{\mathrm{d}t} = \frac{g_{\text{inh}}}{\tau_{\text{inh}}} + \sum_{j=N_{\text{exc}}+1}^{N} \sum_{t_s \in \mathcal{T}_j} w_{ji}\delta(t - t_s), \tag{2.49}$$

where w_{ij} is the strength of the synapse from the j-th neuron to the i-th neuron, $\mathcal{T}_j$ are the times of action potentials fired by the j-th neuron. Extending the Eq. (2.46) with additional properties, such as SFA, is straightforward.

2.4 Metabolic cost of neural activity

The main component of the cost of neural activity is the cost to reverse the ionic currents to maintain homeostasis, most importantly the reversal of the sodium currents (Attwell and Laughlin, 2001). The sodium-potassium pump uses one ATP molecule to pump 3 Na^+ ions outside of the neuron and two K^+ ions inside the neuron. Therefore in order to estimate the cost of the neural activity, we need to consider the events leading to the entry of Na^+ ions and estimate the number of Na^+ ions that enter the neuron.

The main events that contribute to the influx of Na^+ ions are:

- Action potentials,
- Excitatory synaptic currents,
- Na^+ influx through leakage channels.

Attwell and Laughlin (2001) estimated that the extrusion of Na^+ ions from a neuron costs 0.384×10^9 ATP per produced action potential. Their calculations can be tailored to a specific neuronal model, as we have done in (Barta and Kostal, 2023).

We assume that the excitatory synaptic current is carried by Na^+ and K^+ ions. For the excitatory reversal potential E_{exc} and total excitatory conductance g_{exc} it then holds (Harris et al., 2015):

$$E_{\text{exc}} = \frac{g^{\text{exc}}_{\text{K}} E_{\text{K}} + g^{\text{exc}}_{\text{Na}} E_{\text{Na}}}{g^{\text{exc}}_{\text{K}} + g^{\text{exc}}_{\text{Na}}}, \tag{2.50}$$

$$g_{\text{exc}} = g^{\text{exc}}_{\text{K}} + g^{\text{exc}}_{\text{Na}}, \tag{2.51}$$

where $g_{\mathrm{K}}^{\mathrm{exc}}$ and $g_{\mathrm{Na}}^{\mathrm{exc}}$ are the sodium and potassium conductances associated with the excitatory synapses. We may calculate the Na^+ current as

$$I_{\mathrm{Na}}(t) = g_{\mathrm{Na}}^{\mathrm{exc}}(t)(V(t) - E_{\mathrm{Na}}), \tag{2.52}$$

$$g_{\mathrm{Na}} = \frac{E_{\mathrm{exc}} - E_{\mathrm{K}}}{E_{\mathrm{Na}} - E_{\mathrm{K}}}. \tag{2.53}$$

and the rate of Na^+ ions entry as I_{Na}/e, where e is the elementary charge. Similarly, we may estimate the influx of Na^+ ions through the leakage channels with reversal potential E_L ($w_{\mathrm{rest}} = 0.342 \times 10^9$ ATP per second according to Attwell and Laughlin (2001)).

An action potential also causes depolarization of other, post-synaptic neurons. If the activity of a single neuron is being calculated (Barta and Kostal, 2019), the costs associated with the subsequent excitatory synaptic currents of its post-synaptic neurons should also be included. This cost was estimated at additional 0.328×10^9 ATP per action potential adding up to the total cost of action potential $w_{\mathrm{spike}} = 0.71 \times 10^9$ ATP (Attwell and Laughlin, 2001). Note that this cost does not need to be calculated when the cost for the entire network is being calculated, since this cost is included in the costs of synaptic currents of individual neurons (Barta and Kostal, 2023).

The cost of activity w for a duration of ΔT associated with a stimulus s can be then calculated as

$$w(s) = \Delta T(w_{\mathrm{rest}} + w_{\mathrm{exc}} + \nu \cdot w_{\mathrm{spike}}), \tag{2.54}$$

where ν is the firing rate of the neuron.

2.5 Measuring the transmitted information

2.5.1 Entropy and mutual information

Although the models presented in this chapter are deterministic, their input is often treated as random. Many variables affect for example the binding of ligands to receptors and the activity of pre-synaptic neurons and a coarse-grain description then describes the receptor activity or the pre-synaptic spike trains as random processes.

Due to the randomness in the input, presenting the same stimulus repeatedly results in a different output of the neuron over the trials. If we denote the input as $\mathbf{x}$ and the response as $\mathbf{y}$, we may describe the stimulus-response relationship by a conditional probability distribution $f(\mathbf{y}|\mathbf{x})$, i.e., the probability of observing the response $\mathbf{y}$, given the stimulus $\mathbf{x}$.

In the following, I will focus on one-dimensional stimulus x, described by a random variable X, representing the stimulus intensity, and one-dimensional response y, described by a random variable Y, representing the number of action potentials observed in a time window ΔT.

With the knowledge of the input probability distribution $p(x)$, we can calculate marginal output distribution:

$$q_p(y) = \int_{x_{\mathrm{min}}}^{x_{\mathrm{max}}} p(x) f(y|x)\,\mathrm{d}x, \tag{2.55}$$

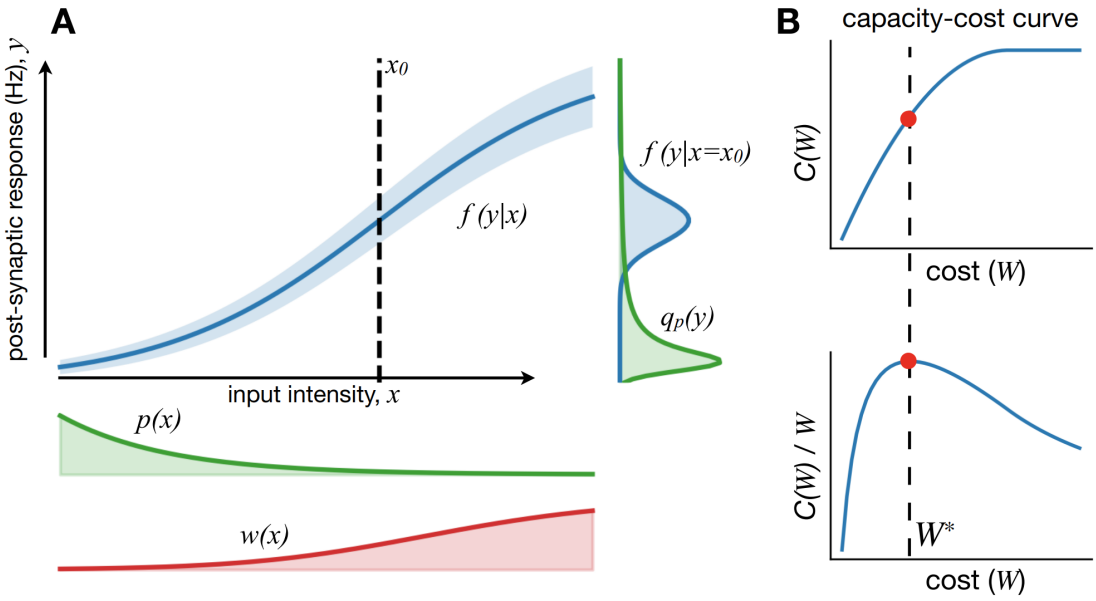

Figure 8: Stimulus-response relationship and information-metabolic efficiency. A: The stimulus-response relationship. The mean response to a stimulus x is signified by a blue line, while the shaded area represents the noise (standard deviation). The probability distribution of the response for a given stimulus x_0 is shown on the side. If we know the input probability distribution $p(x)$, we can calculate the marginal output distribution of the responses using the stimulus-response relationship (Eq. 2.55). Each input x is associated with a metabolic cost $w(x)$. Stronger input implies a higher cost. **B:** The capacity cost function (Eq. 2.60) and the ratio $\frac{C(W)}{W}$ with the information-metabolic efficiency (Eq. 2.62) highlighted.

where $x_{\min}$ and $x_{\max}$ define the boundaries of the input.

The maximal amount of information that can be encoded in $q_p(y)$ is given by the entropy of the distribution:

$$H(Y) = -\sum_{y=0}^{+\infty} q_p(y) \log_2 q_p(y). \tag{2.56}$$

However, the mutual information between the stimulus and the response $I(X;Y)$ is limited by the noise (Shannon, 1948; Gallager, 1968; Thomas M. Cover, 2006):

$$I(X;Y) = H(Y) - H(Y|X), \tag{2.57}$$

where $H(Y|X)$ is the average noise entropy:

$$H(Y|X) = \int_{x_{\min}}^{x_{\max}} p(x) H(Y|x)\, \mathrm{d}x, \tag{2.58}$$

$$H(Y|x) = -\sum_{y=0}^{+\infty} f(y|x) \log_2 f(y|x). \tag{2.59}$$

The mutual information sets the upper limit on the information the neuron can reliably transmit, assuming a rate coding scheme with a counting time window ΔT.

2.5.2 Information capacity, capacity-cost function and information-metabolic efficiency

The Eqs. (2.55-2.59) allow us to calculate the mutual information $I(X;Y)$ when the input probability distribution is known. However, it is possible to reverse the problem and search for such $p(x)$ that maximizes the mutual information. The maximum over all possible input distributions is called the information capacity. Moreover, we can put constraints on the average metabolic cost of the neural activity to obtain the capacity-cost function (Fig. 8B):

$$C(W) = \max_{\substack{p(x) \\ W_p<W}} I(X;Y), \tag{2.60}$$

where W_p is the average cost of the activity associated with the input probability distribution $p(x)$:

$$W_p = \int_{x_{\min}}^{x_{\max}} p(x)w(x)\,\mathrm{d}x. \tag{2.61}$$

The ratio $\frac{C(W)}{W}$ provides the limit on transmitted information per unit of cost (ATP molecule). The information-metabolic efficiency, the maximum of this ratio, is then the upper limit on information per unit of cost that the neuron can transmit:

$$E = \frac{C(W^*)}{W^*}, \tag{2.62}$$

$$W^* = \arg\max_W \frac{C(W)}{W}. \tag{2.63}$$

Typically, the distribution maximizing the mutual information at a given average cost has to be found numerically. The classical algorithm for this maximization is the Blahut-Arimoto algorithm (Blahut, 1972). It is also possible to skip the step of obtaining the capacity cost function $C(W)$ and obtain the information-metabolic efficiency E with the Jimbo-Kunisawa algorithm (Jimbo and Kunisawa, 1979; Suksompong and Berger, 2010) directly.

3. Results

3.1 The stabilizing effect of inhibition

Attachment I

Upon stimulus presentation, cortical neurons receive both excitatory and inhibitory input (Monier et al., 2003). Each neuron typically receives input from many pre-synaptic neurons, and the timing of the pre-synaptic action potentials will differ in each trial with the same stimulus. Such noise in the input to the neuron leads to noise in the output of the neuron (Stein et al., 2005). Comparing a situation where a neuron is excited only by the excitatory input with a situation where the neuron is excited to the same level by combined excitatory and inhibitory input, in the latter case, more pre-synaptic action potentials are necessary to excite the neuron, which implies higher input noise. Intuitively, the higher input noise should lead to higher trial-to-trial variability of the output.

Monier et al. (2003) observed that the fluctuation of the membrane potential in the neurons in the cat visual cortex decreased after stimulus onset, even when the mean membrane potential of the neuron remained unchanged. This is counter-intuitive due to the higher input noise associated with the inhibitory input. We analyzed this problem theoretically and showed that if the synaptic input to a neural model is modeled with either of the two simplifying assumptions discussed in the Section 2.3.2 (reversal potentials or synaptic filtering are neglected), the stronger input noise leads to higher membrane potential fluctuations. However, if neither of the two assumptions is considered, decreased membrane potential fluctuations may be observed (Fig. 9).

The equation describing the membrane potential (Eq. 2.23) can be rewritten as

$$C\frac{\mathrm{d}V}{\mathrm{d}t} = -g_{\mathrm{tot}}(t)(V - E_0(t)), \tag{3.1}$$

where g_{tot} is the total conductance and $E_0(t)$ the effective reversal potential:

$$g_{\mathrm{tot}}(t) = g_L + g_{\mathrm{exc}}(t) + g_{\mathrm{inh}}(t), \tag{3.2}$$

$$E_0(t) = \frac{g_L E_L + g_{\mathrm{exc}}(t)E_{\mathrm{exc}} + g_{\mathrm{inh}}(t)E_{\mathrm{inh}}}{g_L + g_{\mathrm{exc}}(t) + g_{\mathrm{inh}}(t)}. \tag{3.3}$$

Simultaneously increasing the conductances g_{exc} and g_{inh} while keeping the mean membrane potential constant, leads to the membrane potential V following the effective reversal potential $E_0(t)$ more closely. Therefore, if fluctuations of $E_0(t)$ decrease, membrane potential fluctuations may also decrease. We showed asymptotically that $\mathrm{Var}[E_0(t)] \to 0$ as long as the fluctuations of the conductances scale sub-linearly with the mean conductance value ($\mathrm{Var}[g_X] = O(g_X^p)$, $p < 2$, X stands for exc and inh). This is naturally satisfied if the input is modeled as a Poisson spike train and increasing the input intensity is modeled as increasing the intensity of the Poisson process. Then $\mathrm{Var}[g_X] = O(E[g_X])$.

The stimulus onset has been shown to decrease not only the trial-to-trial variability of the membrane potential but also the trial-to-trial variability of the firing activity (Churchland et al., 2010) as measured by the Fano factor (Eq. 2.10), a phenomenon known as neural variability quenching. We analyzed whether this

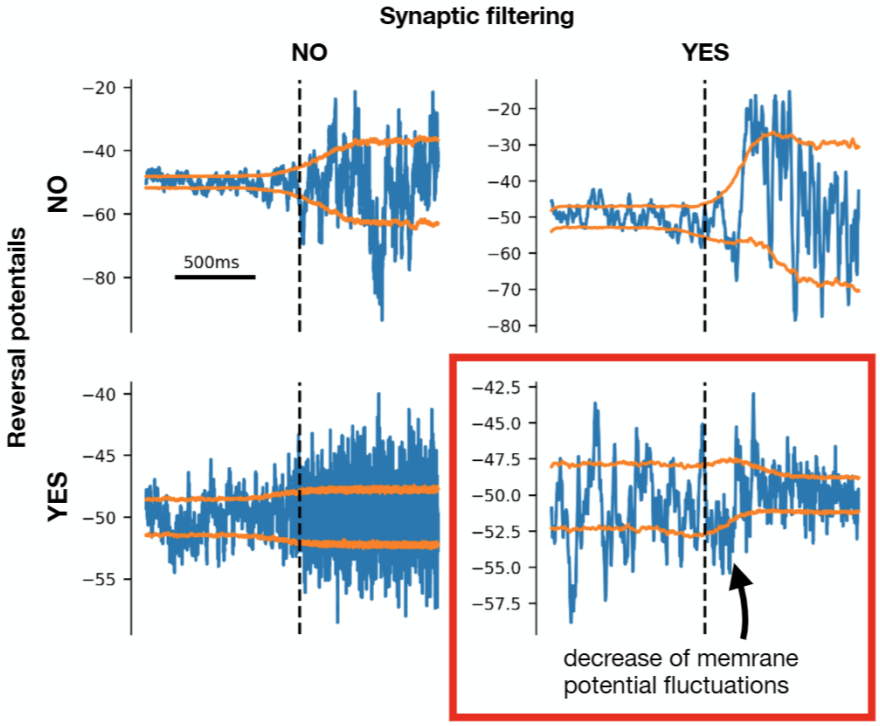

Figure 9: The stabilizing effect of inhibition. During a 2 s long simulation the intensity of inhibitory input increases from 0 kHz to 20 kHz. The pre-synaptic spike trains are modeled as Poisson point processes. The intensity of the excitatory input is increased simultaneously with the inhibition to keep the mean membrane potential constant. This increases synaptic current fluctuations and subsequently increases membrane potential fluctuations unless both synaptic filtering and reversal potentials are considered. The orange lines signify the mean value ± the standard deviation.

might be caused by the decreased membrane potential fluctuations associated with the stimulus onset. We found that the effect of the increased inhibitory input depends on the spike frequency adaptation mechanism of the neuron. Models with M-current or AHP current showed an increased trial-to-trial variability with the increased inhibitory input. In contrast, models with dynamic threshold showed decreased trial-to-trial variability (Fig. 10).

Our results illustrate the importance of considering synaptic filtering and reversal potentials in neural modeling and extend our understanding of the effects of using different SFA mechanisms on the input-output properties of neural models (Benda et al., 2010). Moreover, we theoretically explain the experimentally observed decrease of membrane potential fluctuations and provide a possible mechanism of decreased Fano factor with the stimulus onset. Results of our study were published in the journal *Physical Review E* (Barta and Kostal, 2021). A reprint of the manuscript is enclosed with this thesis (Attachment I).

3.2 Neural variability quenching in networks

Attachment II

In our published work, we studied the properties of single neurons and simulated

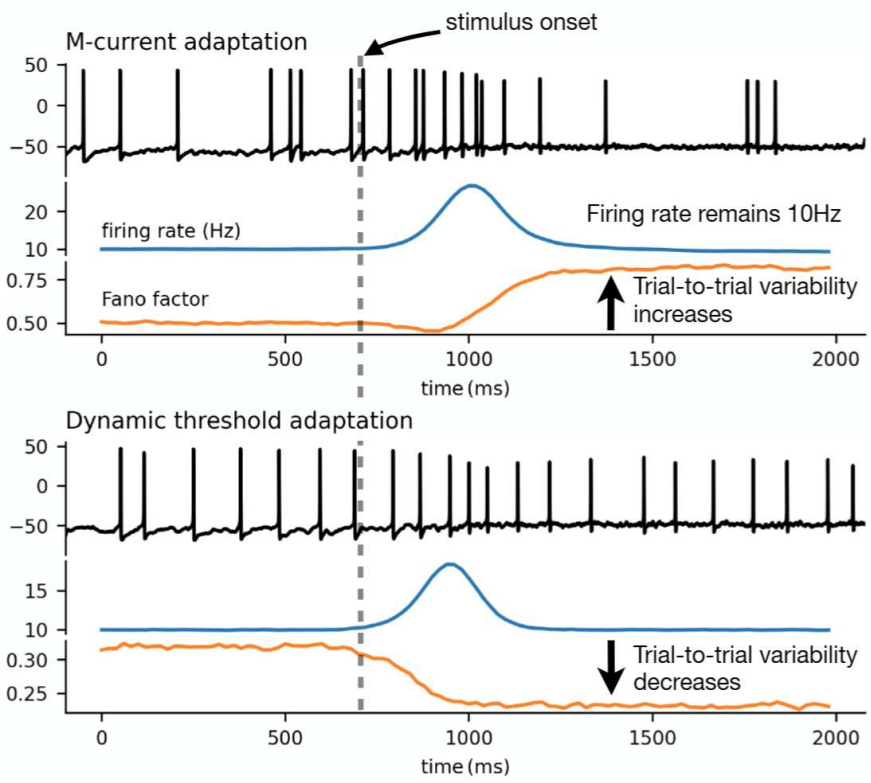

Figure 10: Changes in Fano factor with stimulus onset. During a 2 s long simulation the intensity of inhibitory input increases from 0 kHz to 20 kHz. The intensity of the excitatory activity is increased simultaneously to keep the steady-state post-synaptic firing rate at approximately 10 Hz (blue trace). The pre-synaptic spike trains are modeled as Poisson processes. The Fano factor (orange trace) decreases with the addition of inhibition to the input in the model with spike-firing adaptation by M-currents. However, the model with the dynamic threshold shows a clear increase in regularity with the added inhibitory input. The Fano factor was calculated with a 100 ms sliding window from multiple trials.

the stimulus onset as a simultaneous increase in the excitatory and inhibitory input at different ratios. To understand better the neurons' behavior with stimulus onset, it is beneficial to study the single neuron behavior in the context of a recurrent neural network in the sensory cortex with different neurons having different stimulus preferences and thus reproduce the experimental conditions as in (Monier et al., 2003) and (Churchland et al., 2010). The stimulus would be represented by an increased input intensity from thalamocortical synapses, with the increase dependent on the preferred stimulus and the associated increase in inhibitory input given by the network properties. Thus, we can reproduce the variability quenching effect with stimulus onset.

We started extending the published results in this direction. We considered a recurrent neural network of 10000 neurons, with 7500 neurons excitatory and 2500 inhibitory. Each neuron was modeled as an exponential leaky integrated-and-fire neuron, and the probability of a connection from one neuron to another was set to 5% (Zerlaut et al., 2017). We compared three types of networks, specified by two types of spike frequency adaptation (SFA) of the neurons:

1. SFA through after-hyperpolarization currents (AHP),

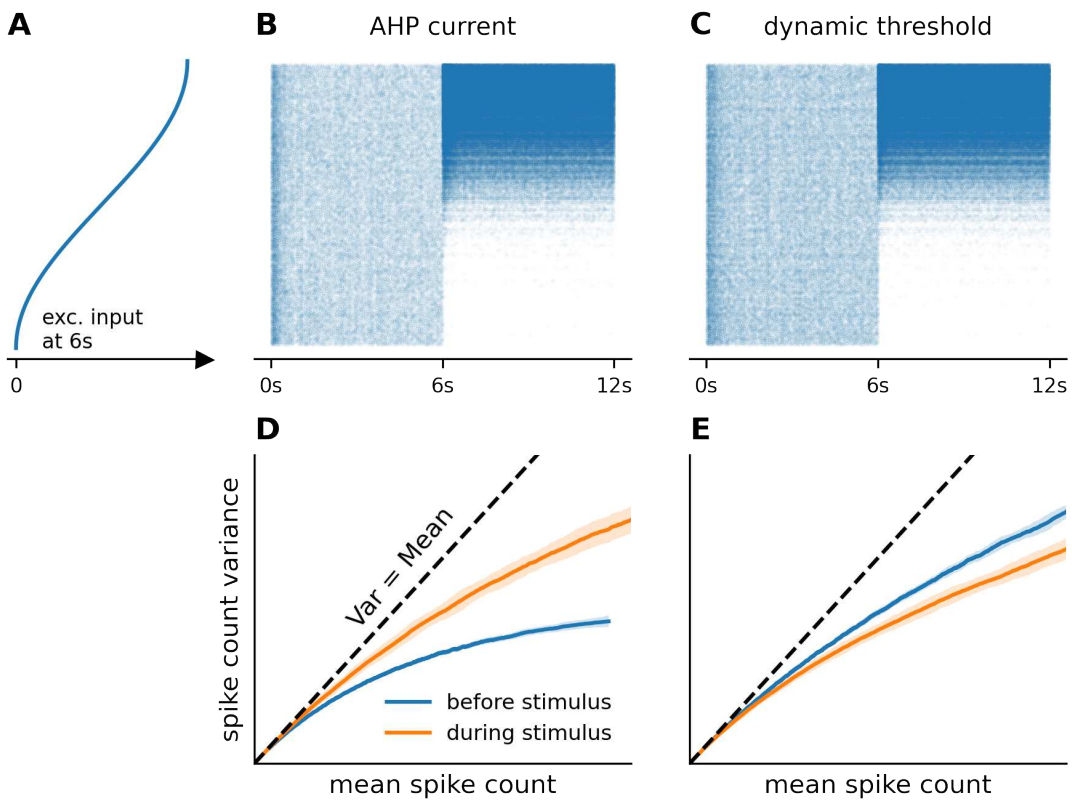

Figure 11: Neural variability quenching in recurrent neural networks. **A:** All neurons receive a background input throughout the 12 s simulation. After the stimulus onset at 6 s, each neuron receives a different additional input due to their different stimulus preference, representing the input from the thalamocortical synapses. Neurons are organized vertically, neurons at the bottom do not receive any thalamic input, and neurons at the top receive the strongest thalamic input. **B-C:** Raster plots of the 7500 excitatory neurons with different spike frequency adaptation mechanisms (SFA): after-hyperpolarization (AHP) current (**B**) and dynamic threshold (**C**). In both cases, the neurons receiving a strong input increase their firing activity, while neurons receiving weak or no input decrease their firing activity. **D-E:** With fixed network connectivity, we repeated the simulation 3600 times. For each neuron, we plotted the variance of the response across the 3600 trials against its mean response. Neurons with AHP SFA (**D**) increased their trial-to-trial variability after the stimulus onset. In contrast, neurons with dynamic threshold SFA decreased their trial-to-trial variability after the stimulus onset (**E**).

2. SFA through dynamic firing threshold.

Each neuron was receiving a background input before being presented with a stimulus on top of this background input. Regardless of the SFA mechanism, the neurons receiving strong input responded with an increased firing activity, while neurons receiving only a weak input decreased their firing activity due to increased inhibitory input from the network activity (Fig. 11B-C).

For fixed network connectivity, we ran the simulation 3600 times to obtain the trial-to-trial variability of each neuron before and after the stimulus. We

plotted the variance of the response of each neuron against the mean response. Neurons with the AHP-mediated SFA increased their trial-to-trial variability after the stimulus onset. In contrast, neurons with the SFA mediated by a dynamic threshold decreased their trial-to-trial variability after the stimulus onset (Fig. 11).

This model clearly illustrates a possible mechanism of decrease in trial-to-trial variability with stimulus onset. To develop this work further, we will consider more realistic, proximity-based probabilities of synaptic connections between neurons. Particularly, neurons with a peak response to a similar stimulus should be connected with a higher probability than neurons responding to very different stimuli. The preliminary results of the study are enclosed with this thesis in the form of a short report (Attachment II).

3.3 Efficient coding by individual cortical neurons

Attachment III

Given that all the information a neuron passes on is contained within its output spike train, a model reproducing the neuron's response to a stimulus can be a proxy for conducting experiments. This is especially useful for evaluating the information transmission capabilities of neurons because such studies require large amounts of data, which are costly and lengthy to obtain experimentally. Numerous studies used mathematical neuronal models to evaluate the theoretical limits on information transmission. However, these studies typically dealt with simplified models with simplified inputs, which do not represent well the true behavior of neurons (Stein, 1967; de Polavieja, 2002, 2004; Suksompong and Berger, 2010; Xing et al., 2015; Sungkar et al., 2016, 2017) or with biophysical models, which are difficult to generalize (Kostal and Kobayashi, 2015).

A gap between those model types was somewhat filled by the Multi-timescale Adaptive Threshold (MAT) model (Kobayashi et al., 2009) (Eqs. 2.31-2.32). Kobayashi et al. (2009) showed that if the SFA is modeled at two separate timescales: 10 ms and 200 ms, the MAT model can precisely predict the timings of individual spikes of cortical neurons (Kobayashi et al., 2009; Gerstner and Naud, 2009; Jahangiri and Gerling, 2011; Kobayashi and Kitano, 2016). The great benefit of this model is its modest number of free parameters, which greatly simplifies its fitting to neural recordings. We used this model to evaluate the limits of metabolically efficient information transmission by neurons and to investigate the effect of changing the free parameters, which can be directly related to the neurons' properties. An "optimal regime" can then be found for any neuron that can be fitted by the MAT model, making the model the perfect tool for comparing real neuronal responses with predictions based on efficient coding arguments.

In accordance with some of the previous studies, we assumed that the "optimal regime" is such that it allows the transmission of as much information as possible per unit of energy (molecule of ATP). Previous studies typically considered the metabolic expenses of the neuron to be equivalent to its output firing rate. However, the synaptic input to the neuron is responsible for a large portion of the metabolic expenses (Harris et al., 2012) (in our study, possibly more than 50%, depending

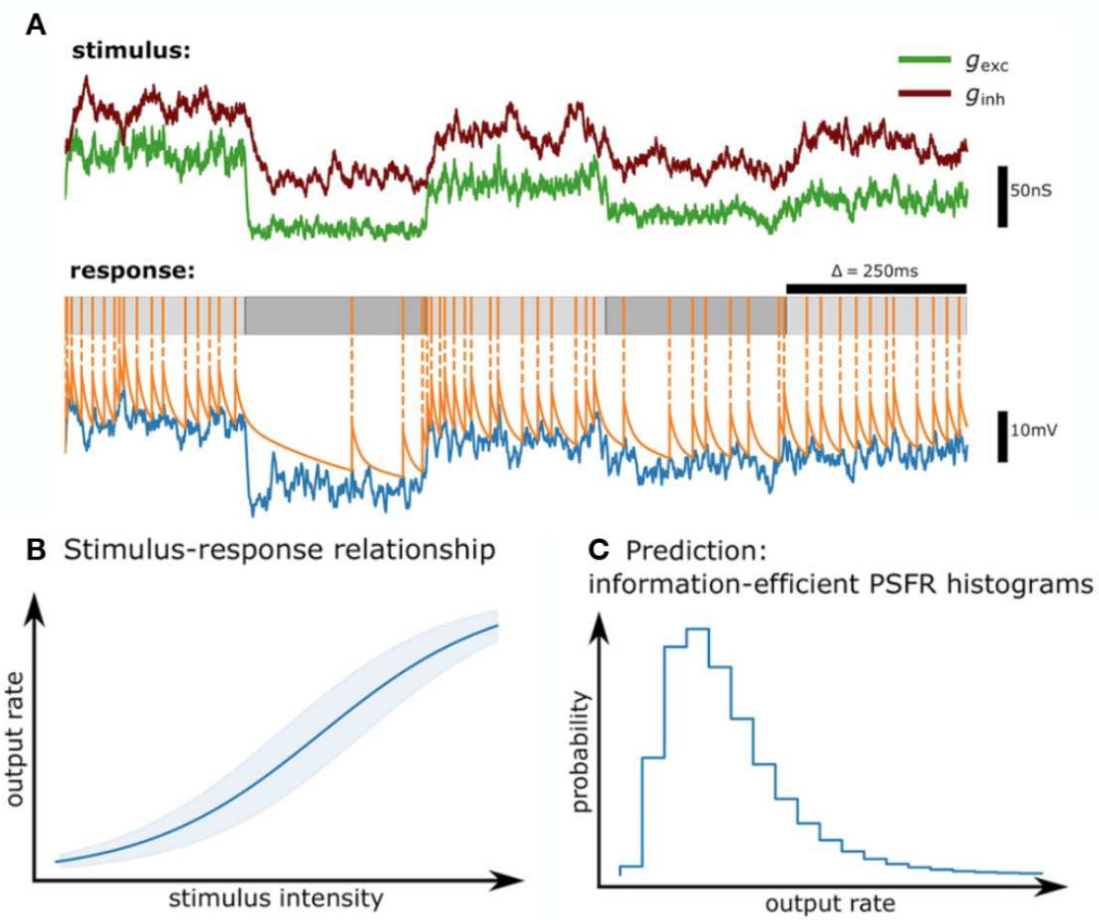

Figure 12: Simulation schematics. A: We record the response of the neural model to a time-varying stimulus. The output of the neuron is the number of spikes in a time window Δ (here 250 ms). **B:** The output of the neuron to the same stimulus is random due to the randomness of the stimulus. The stimulus-response relationship then has to describe the complete output probability distribution for each input. Here thick lines signify the mean response and the shaded area the standard deviation. **C:** Maximization of mutual information provides a prediction in the form of post-synaptic firing rate histograms, which can be compared to *in-vivo* recordings.

on the input and output, see Fig. 5A in (Barta and Kostal, 2019)).

With the knowledge of the stimulus-response relationship and the cost of the neural activity, the information-metabolic efficiency can be calculated. However, the adaptation properties of the neurons introduce memory to the neuron. The Jimbo-Kunisawa algorithm cannot be directly applied to calculate the information-metabolic efficiency of such channels. Therefore, we had to extend the Jimbo-Kunisawa algorithm to take the adaptation properties into account (S5 Appendix in (Barta and Kostal, 2019)).

We then studied the effect of the following neuronal and coding properties on the information-metabolic efficiency:

- Spike firing patterns,
- Stimulus-associated inhibitory input,

- Coding time window Δ,
- Spontaneous activity of the neuron.

We found that while the information-metabolic efficiency (Eq. 2.62) was robust towards the changes in the inhibition excitation balance and to the change in model parameters responsible for the spike firing patterns (Figure 4 in (Barta and Kostal, 2019)), the coding time window and spontaneous activity of the neuron had significant effects on the information-metabolic efficiency. Neurons with the lowest spontaneous activity had the highest values of information-metabolic efficiency, and shorter coding time windows led to higher information-metabolic efficiency.

We showed that it holds from the information-theoretic principles that shorter time windows cannot decrease the mutual information if the neuron is considered to be a memoryless information channel. However, with a shorter coding time window, the response of the neuron is more affected by the previous stimulus than in the case of a longer coding time window, decreasing its signal-to-noise ratio, as the stimulus history introduced another source of stochasticity (Figure 8B in (Barta and Kostal, 2019)). We found that despite the additional source of variability in the stimulus history, shorter coding time windows led to higher information-metabolic efficiency (Figure 8E in (Barta and Kostal, 2019)).

We used 34 sets of parameters obtained by fitting 34 neurons from layers 2/3 and 5 of the rat motor cortex (Kobayashi et al., 2009; Isomura et al., 2009) (provided by professor Ryota Kobayashi) to investigate the role of different parameters on the efficiency of information transmission. For a fixed coding time window, the information-metabolic efficiency was given mainly by the neurons' spontaneous firing rate due to the background network activity (Destexhe et al., 2001, 2003), which is in turn given by the neurons' long-term adaptation properties and their resting threshold for action potential initiation. More detailed properties (e.g., the tendency to burst - fire rapidly many action potentials during a short period) turned out to be of lesser importance (Figure 9 in (Barta and Kostal, 2019)).

The results of our study were published in the journal PLoS Computational Biology (Barta and Kostal, 2019). The reprint of the manuscript is enclosed with this work (Attachment III).

3.4 Efficient coding by populations cortical neurons

Attachment IV

In the above-discussed study, among other parameters, we analyzed the effect of the stimulus-associated inhibitory input on metabolically efficient information transmission. While we observed that in some cases higher inhibition-to-excitation ratio may decrease the trial-to-trial variability of the response (see also (Barta and Kostal, 2021)), this decrease was not sufficient to balance out the increased costs of synaptic currents and decreased coding range of the neurons. Yet, an increase in excitatory input intensity due to an external stimulus is typically accompanied by a simultaneous increase in the inhibitory input due to the excitation of inhibitory neurons (Monier et al., 2003), and it is unclear if and how the inhibition aids metabolically efficient information transmission.

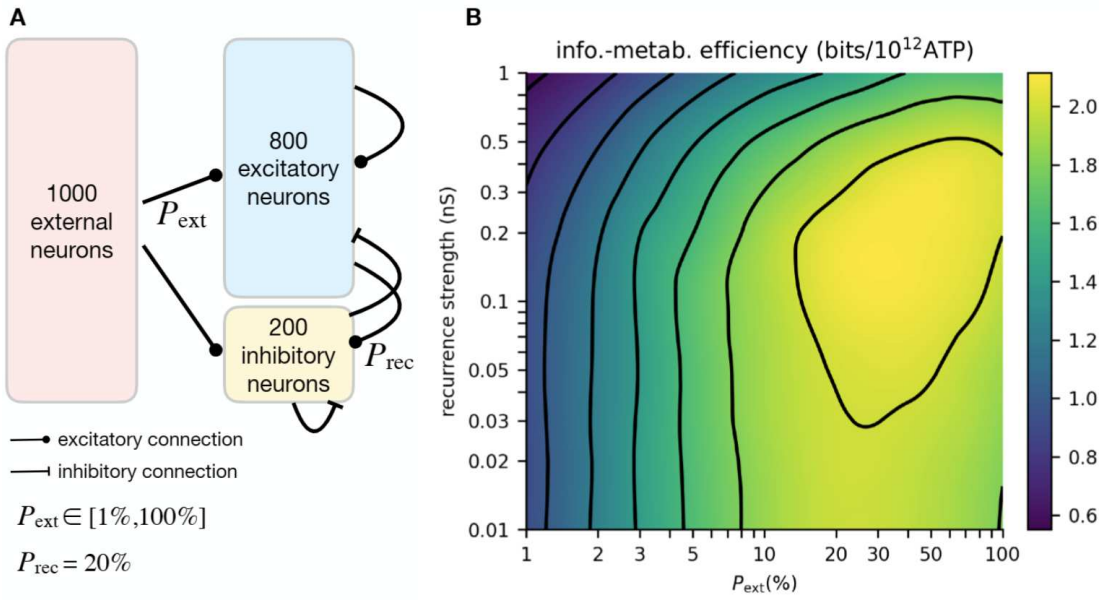

Figure 13: Metabolically efficient information transmission by a recurrent neural network. A: Schematic illustration of a network used to study the role of inhibition in metabolically efficient encoding by neural populations. Neurons from an external population make random excitatory connections on neurons in the excitatory and inhibitory populations. The connection probability P_{ext} was varied for different simulations between 1% and 100%, leading to different pair-wise correlations between the post-synaptic neurons. The probability of recurrent connections (ext to exc, ext to inh, inh to inh, inh to exc) was set to 20%, but the strength of those connections was varied. **B:** Contour plot of the information-metabolic efficiency for different values of P_{ext} and recurrence strength. The information-metabolic efficiency is the highest for P_{ext} between 20% and 50% and recurrence strength of approximately 0.2 nS, or 20% of the synapse strength from the external population.

However, inhibition is likely to play a much more important role on the level of whole neural populations instead of individual neurons. Inhibitory feedback can decrease the noise correlations and subsequently the trial-to-trial variability of the total population activity (Abbott and Dayan, 1999; Averbeck et al., 2006; Renart et al., 2010; Tetzlaff et al., 2012; Bernacchia and Wang, 2013).

To analyze the impact of the inhibitory feedback on the rate coding capabilities of neural populations, we modeled a recurrent spiking neural network with 800 excitatory and 200 inhibitory neurons, representing a small cortical area (Fig. 13A). Similarly, as in the above-discussed study, the neurons were receiving a balanced excitatory and inhibitory input, representing the input from neighboring cortical areas and an external input representing the excitatory input from the thalamocortical synapses. We modeled the thalamic input by considering an external population of 1000 excitatory neurons, making random connections onto the 800 excitatory and 200 inhibitory neurons. In our simulation, the inhibitory neurons provided the inhibitory feedback, and we varied the strength of the feedback by varying the strength of the recurrent connections.

We treated the whole population of 800 excitatory and 200 inhibitory neurons

as a single information channel. We defined the output of this channel as the total number of post-synaptic action potentials observed in a time window $\Delta = 1\,\mathrm{s}$. Adding together the activity of many neurons can lead to a significant decrease in the trial-to-trial variability. However, noise correlations are induced by neurons sharing input from the same neurons in the external population. In the presence of noise correlations, the decrease in the signal-to-noise ratio will be lower (Abbott and Dayan, 1999). We varied the noise correlations between neurons by varying the connection probability P_{ext} from the external neurons to the excitatory and inhibitory populations. High values of P_{ext} meant high noise correlations.

We considered the costs of the whole system. Therefore, on top of the costs of the excitatory and inhibitory subpopulations (the cost of synaptic currents and action potentials), we also considered the cost of the action potentials from the external population. With higher P_{ext}, more neurons are involved in exciting any neuron from the excitatory or inhibitory subpopulation. Therefore, the total activity of the external population can be lower to reach the same post-synaptic firing rate.

On the other hand, increasing the inhibitory feedback by increasing the strength of the recurrent connections decreases the post-synaptic firing rate of the network, and stronger synaptic currents and stronger external input are needed to reach the same post-synaptic firing rate, compared to a network with weaker inhibitory feedback. Therefore, the cost of the neural activity of a network with stronger recurrent connections is higher.

In our work, we studied the balance between mutual information in metabolic costs. We found that high values of P_{ext} typically increase the information-metabolic efficiency of the system. With high values of P_{ext}, the information-metabolic efficiency can be further improved by strengthening the inhibitory feedback (Fig. 13B). Moreover, we showed that the neural system can decrease its energy consumption by decreasing the strength of the synaptic weights, a phenomenon observed experimentally in food-restricted mice (Padamsey et al., 2022).

Results of our study are currently published in *bioRxiv*. The preprint is enclosed with this report (Attachment IV).

3.5 Temporal features encoding by moth olfactory receptor neurons

Attachment V

Studying insect olfaction is, in certain aspects, the ideal system to study how evolution shapes neural systems to adapt to their environment. The olfactory system is relatively simple, and specifically, moth ORNs need to be highly adapted to encode the temporal features of the pheromone plume. However, a lot is still unknown about what temporal features the system actually encodes, and studying the dynamics of the ORN response has been difficult in moths due to difficulties with delivering odor stimulus with a sharp onset and offset, such as the moth might encounter in nature.

We developed a new odor-delivery device that can deliver sharp stimulus pulses even with odors with low volatility. We tested the precision of the odor delivery

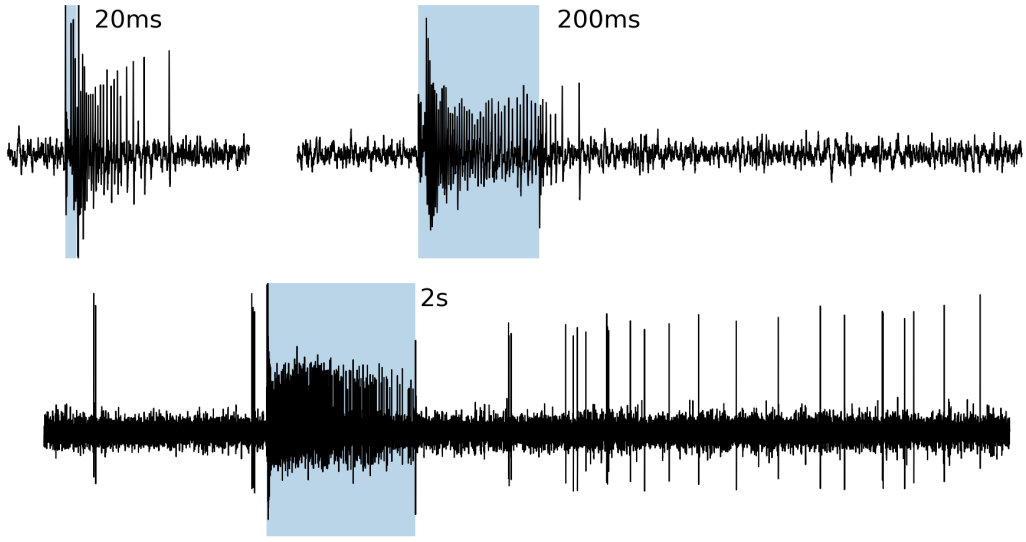

Figure 14: Spiking responses to constant stimuli of different durations. After the short stimulus (20 ms) the ORN continues to fire for approximately 100 ms after the stimulus offset. After the 2 s stimulation, the stimulus offset is immediately followed by a transient inhibition.

device with molecules detectable by a photo-ionization detector (PID). Although the recorded stimulus became less sharp with less volatile odors, such as linalool, we showed that the slow dynamics arise primarily from the properties of the PID rather than from the delivered stimulus (Figure 3 in (Barta et al., 2022)).

Previous studies showed that the moth ORNs clearly detect the onset of the stimulus by responding to the sudden increase in odor concentration, but also observed a sustained response even after the stimulus offset (Kaissling et al., 1989; Jarriault et al., 2010; Grémiaux et al., 2012; Rospars et al., 2014). Such observations were surprising since it complicates the detection of the odor offset, a feature which was then thought to be performed in the AL (Jarriault et al., 2009, 2010; Rospars et al., 2014; Tuckman et al., 2021b,a). With the new odor delivery device we observed that the moth ORNs can, in fact, detect the odor offset by a transient inhibitory phase, provided that the stimulus is sufficiently long (Fig. 14). Moreover, we showed that the response shape is independent of the stimulus concentration, which has important implications for odor identity discrimination (Martelli et al., 2013) (Figure 5 in (Barta et al., 2022)).

For brief stimuli, the response of the ORNs continued after the stimulus offset. For pulses of duration below 200 ms the firing response continued for approximately 100 ms after the stimulus offset (Fig. 14). Previous studies showed that even though the response of ORNs is sustained after the stimulus offset, the PNs do exhibit the transient inhibition marking the stimulus offset, albeit with a delay of more than 100 ms (Jarriault et al., 2009). We were therefore interested in whether the encoding of the stimulus offset is further sharpened at the AL level. We used the ORN firing rates as an input to a moth antennal lobe model (Tuckman et al., 2021b,a) and did not observe any improvement in stimulus offset detection. Although recordings from the antennal lobe neurons will be necessary to show that the stimulus offset detection is not improved, we hypothesize that

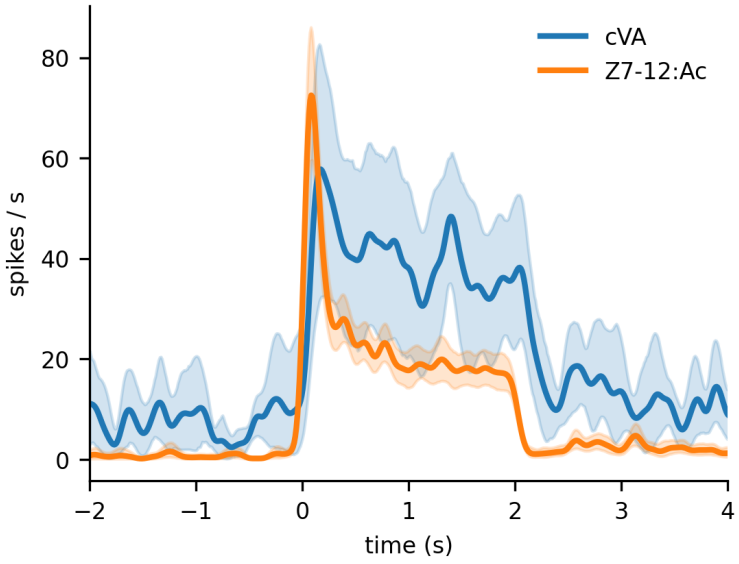

Figure 15: Comparison of moth and *Drosophila* ORN response to their respective pheromones. A constant stimulus (10 pg of Z7-12:Ac for the moth ORN, 10 µg of cVA for the *Drosophila* ORN) was presented between 0 s and 2 s. The response of the moth ORN shows a phasi-tonic pattern with an intense firing response to the stimulus onset and a gradual decrease to steady-state activity. Response of the *Drosophila* ORN to cVA is rather tonic and does not show any significant adaptation throughout the 2 s stimulus. Firing rate profiles of individual neurons were estimated with kernel density estimation (Eq. 2.9, bw = 50 ms). The shaded area represents a 95% confidence interval of the mean estimated by bootstrapping the firing rate profiles of individual neurons (8 *Drosophila* neurons, 57 moth neurons).

the stimulus offset detection is not necessary for very brief encounters with the odor. This correlates with the observed behavior of flying insects. Moths were shown to continue flying in a straight line towards the source when presented with a pulsating stimulus (Willis and Baker, 1984; Kennedy et al., 1980; Mafra-Neto and Cardé, 1994). Particularly, Mafra-Neto and Cardé studied the behavior of the almond moth *Cadra cautella* and observed that the best navigation performance was achieved with a pulse duration of 130 ms and a gap between pulses of 83 ms. Instead, the prolonged response to very brief odor encounters might help the insect to register those encounters.

The transient inhibition marking the stimulus offset has also been observed in some *Drosophila* ORNs (Nagel and Wilson, 2011; Kim et al., 2011). The absence of transient inhibition with some odors was attributed to imprecise odor delivery (Martelli et al., 2013; Gorur-Shandilya et al., 2019). We recorded the activity of *Drosophila* ORNs expressing the receptor OR67d sensitive to 11-*cis*-vaccenyl acetate (cVA), an odor of low volatility with which precise odor delivery with classical odor delivery devices is difficult. However, we still observed that the recorded response did not exhibit the phasicity and transient inhibition as the other ORNs. We also expressed the receptor sensitive to the main component of the *A. ipsilon* pheromone (Z7-12:Ac) and observed that the response shape remained the same as with cVA with no transient inhibition at stimulus offset.

These observations suggest that:

- The lack of transient inhibition and phasicity in response to cVA are properties of the ORN and not due to imprecise odor delivery,
- Phasicity and transient inhibition in moth ORNs are a property of the spike-generating mechanism of the ORN.

Interestingly, *Drosophila* does not use cVA for navigation, only at short distance for recognizing whether mating partners are virgins. The staggering difference between the response shapes of cVA-sensitive neurons and those responsible for navigation (both in *Drosophila* and moths) suggests that the phasi-tonic response shape evolved to aid navigation. The experiments in *Drosophila* ORNs are not included in the attached version of the manuscript and will be part of its next version.

It has been known that the phasi-tonic response shape of ORNs originates from the adaptation processes in the spike-generating mechanism (Kaissling et al., 1987). However, the molecular origins of this adaptation are still unknown (Brandão et al., 2021). Low ratio of Na^+ to K^+ channels may make a neuron respond more phasically (Lundstrom et al., 2008), and it was hypothesized that the phasicity on *Drosophila* ORNs is due to this mechanism (Nagel and Wilson, 2011). With a linear-nonlinear model, we identified that in the moth ORNs, the firing response is shaped by adaptation processes in the soma at time scales of approximately 31 ms and 635 ms, which are longer than the common adaptation time scales of Na^+ channels in insect ORNs (approximately 5 ms (Kadala et al., 2011)). Slower adaptation of the Na^+ channels, close to either 31 ms or 635 ms, would be necessary to partially explain the observed responses. Further experiments focused on identifying possible adaptation of insect ORN Na^+channels at longer timescales should be performed to understand better whether the hypothesis proposed by Nagel and Wilson (2011) is correct.

We proposed a new approach to fitting linear-nonlinear models to neural activity (described in the Section 2.3.1 of this thesis). As discussed in the previous paragraph, this approach provides insight into the time scales of the physiological processes responsible for the adaptation of the ORNs. Moreover, this approach overcomes issues imposed by elastic net regularization, commonly employed for fitting linear-nonlinear models (Martelli et al., 2013; Jacob et al., 2017) by enforcing a continuous linear filter without oscillations while allowing high-frequency components in the linear filter.

The two separate adaptation time scales also explain the prolonged response to brief stimuli. During the short stimulus, the slow adaptation does not activate sufficiently to rapidly terminate the response.

Studies using ORN firing rates as an input to models of higher brain centers typically model the ORN input as piece-wise exponential functions with slow firing rate decay after the stimulus offset (Belmabrouk et al., 2011; Tuckman et al., 2021b,a). By combining our linear-nonlinear model with a simple transduction model (Eq. 2.4), we created a reliable odor-to-firing rate model containing only a small number of parameters that can be easily transferred to be used in such studies and also incorporates the newly discovered properties of moth ORNs (Fig. 16).

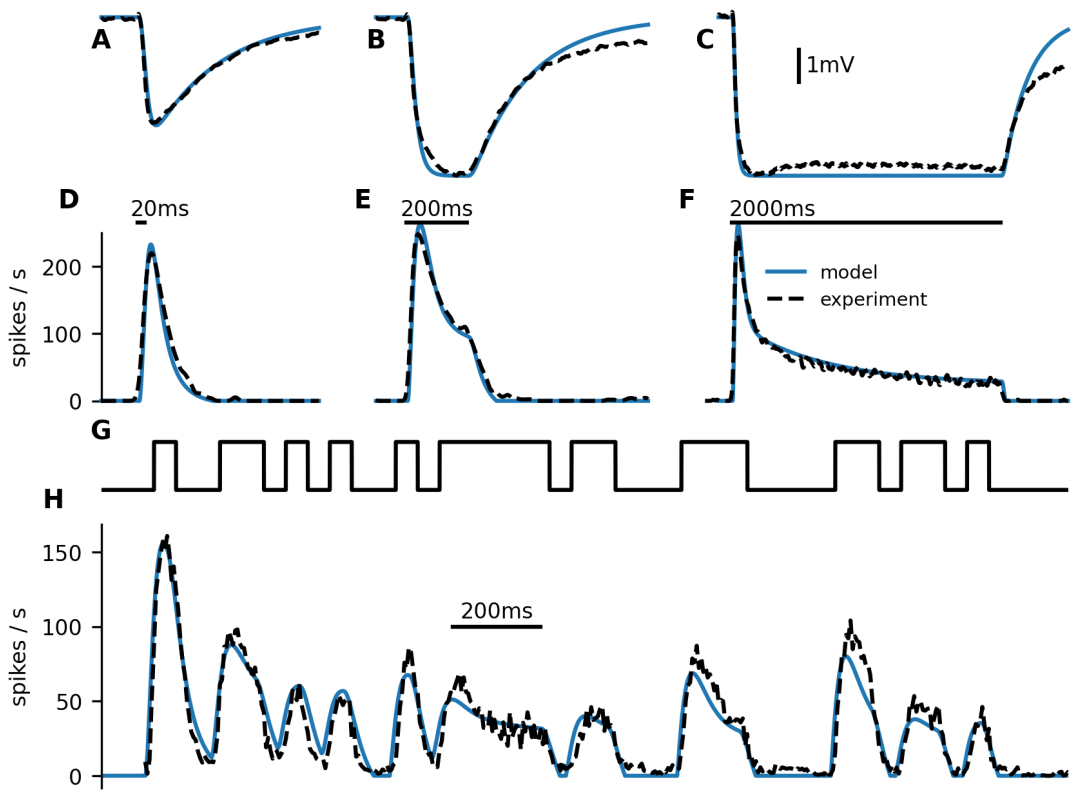

Figure 16: Odor-to-firing rate model. A-C: Prediction of LFP responses to stimuli of different durations. The blue line shows the transduction model prediction, dashed black line is the average LFP observed from SSR. **D-F:** Combining the transduction model with the linear-nonlinear model leads to an odor-to-firing rate model, which accurately predicts firing responses to the different stimulus durations. **G-H:** The odor-to-firing rate model also reliably predicts the firing rate in response to a fluctuating stimulus. **G** shows the stimulus being switched between ON and OFF with a constant odor concentration.

3.6 Spike firing patterns of olfactory receptor neurons

Attachment VI

The literature so far has paid attention mainly to the time course of firing rates in ORNs and not so much to the spike firing patterns and the subsequent trial-to-trial variability of the response. A common assumption is that the spike firing activity can be described by an inhomogeneous Poisson process (Belmabrouk et al., 2011; Rapp and Nawrot, 2020; Betkiewicz et al., 2020; Tuckman et al., 2021b,a). Such an approach may be justified in some cases since the pooled activity of all neurons could be approximated by an inhomogeneous Poisson process. However, synapses from ORNs to the projection neurons in the antennal lobe (PNs) are known to undergo short-term synaptic depression. Temporal correlations in the spike trains are known to affect signal processing by such depressing synapses (Bird and Richardson, 2018), and temporal correlations in the ORN firing activity may, therefore, significantly affect how the signal is passed on from the ORNs to the PNs. Consequently, a good statistical description of the spike firing patterns

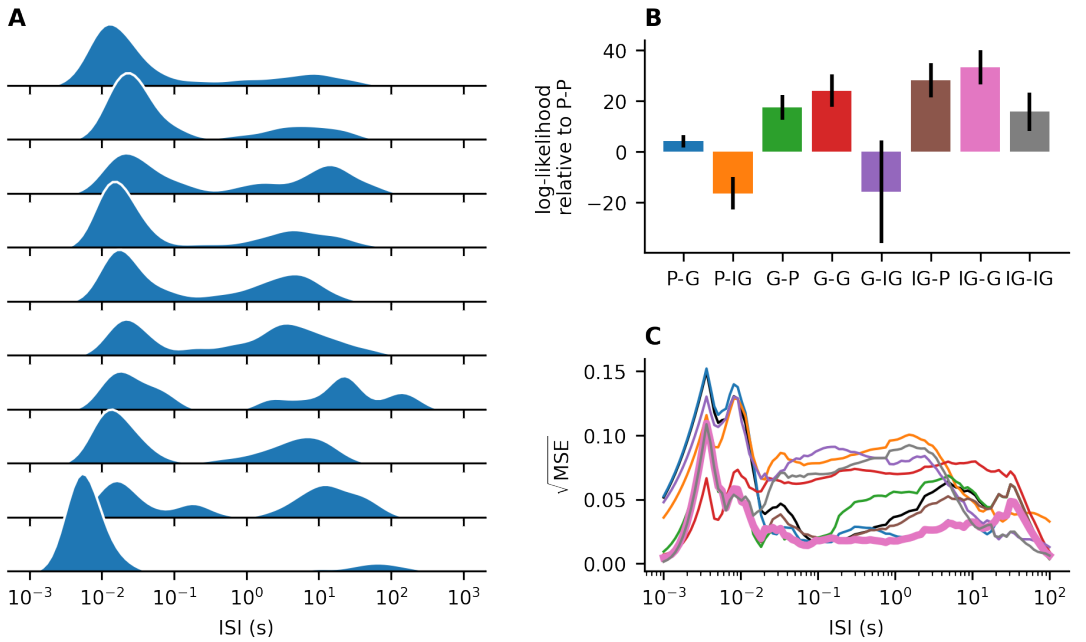

Figure 17: Statistical description of spontaneous activity of moth ORNs. A: Distributions of ISIs for 10 different ORNs. The distributions have two modes, one corresponding to ISIs within a burst and the second to ISI between two bursts. **B:** We fit mixtures of two distributions to the ISIs by the maximum likelihood method. The shown values are average log-likelihood values relative to the exponential-exponential distribution. P - exponential distribution, G - gamma distribution, IG - inverse Gaussian distribution. The vertical bar indicates the standard error. The best fit was a mix of inverse Gaussian distribution for the bursts and gamma distribution for the inter-burst intervals. **C:** Root of the square error between the cumulative distribution function of the fitted distribution and the empirical cumulative distribution function, averaged over the neurons. The colors correspond to **B**, the IG-G model is in bold, and the P-P model is in black.

is needed to understand the effect of these patterns on information transmission from the ORNs to the PNs.

We analyzed the trial-to-trial variability and spike firing patterns of moth ORNs. We found that most ORNs exhibit a bursting spike firing pattern, as seen in inter-spike interval (ISI) histograms on a logarithmic scale (Fig. 17A). We could describe the short ISIs within a burst by the inverse Gaussian distribution, while the inter-burst intervals (IBIs) could be described with a gamma distribution (Fig. 17B-C).

The moth ORNs show an elevated spontaneous activity following the transient inhibition after the stimulus offset (rebound activity). The elevated activity slowly returns to its original level on the time scale of minutes. This activity also clearly shows two modes of ISIs which can again be described by inverse Gaussian and gamma distributions. We applied the time rescaling theorem (Brown et al., 2002; Barbieri et al., 2001b,a) to fit a double exponential decay of the firing rate to the rebound activity. The mixture of inverse Gaussian and gamma distributions with time-dependent intensities provides a good fit to the rebound activity, as

illustrated in the attached report.

We showed that the activity of moth ORNs can be described by a mixture of two stochastic point processes with inverse Gaussian and gamma distributions. We were able to fit well the spontaneous activity and the rebound activity. Whether a similar model can describe the response during stimulation remains to be analyzed. If we can describe the full behavior or an ORN with an inhomogeneous point process, we can use it to extend the linear-nonlinear models with a spiking activity, simulate realistic spike trains and thus obtain a spiking odor-to-firing rate model. Such a model could then be used as an input to AL models to understand the role of the observed spike firing patterns in signal transmission.

SSR recordings (Barta et al., 2022) indicate that the inactivation of the receptor current is slow, which should lead to temporal correlations of the receptor current. We extended the multi-compartmental model from (Barta et al., 2022) by adding voltage-gated sodium and potassium channels in the somatic compartment to simulate a spiking ORN. We described the receptor current as an Ornstein-Uhlenbeck process to create temporal correlations. The firing pattern of this neuron can then resemble the firing patterns observed in moth ORNs. However, the average action potential observed in the extracellular recording should lie within a valley, resembling an elementary action potential (Kaissling, 1986; Minor and Kaissling, 2003; Pézier et al., 2007; Kaissling, 2013), which is not observed in the *A. ipsilon* SSR. Further investigation is therefore needed to understand the origin of the spontaneous activity and of the bursting firing patterns.

These results are not yet ready for publication. However, a brief report is attached with this thesis (Attachment VI).

Conclusion

In my thesis, I studied the encoding of neural information by different systems and conditions and the information-metabolic efficiency of the encoding. I showed that while inhibitory feedback does not help increase the efficiency of encoding by single neurons, it may improve the information-metabolic efficiency of neural populations. I showed that the information-metabolic efficiency is crucially affected by the spontaneous activity of the neuron and its cost.

Such observation inspires questions about the importance of the spontaneous activity. In the higher brain areas, the spontaneous activity can be important, for example, for memory consolidation (Fukai, 2022). Such function is unlikely, for example, in the periphery of the insect olfactory system. Accordingly, the spontaneous activity of the pheromone-sensitive moth ORNs is very low (Pézier et al., 2007; Jarriault et al., 2010; Barta et al., 2022). However, this is not always the case across all ORN types and insect species. For example, moth ORNs sensitive to plant volatile compounds and *Drosophila* ORNs may exhibit much higher spontaneous firing rates (Hallem et al., 2004). The ORNs responding to plant volatile compounds typically respond to a broad range of odors, and the odor's identity is then encoded by the combinatorial code (one ORN recognizes multiple odor molecules, and one odor molecule is recognized by multiple ORNs) (Malnic et al., 1999). Although most ORN-odor combinations result in excitation of the ORN, some ORN-odor combinations decrease the spontaneous activity, helping discriminate different odors (Hallem et al., 2004; Cao et al., 2017). The metabolic importance of keeping the spontaneous activity low might be why the spontaneous activity is not even higher and odor-induced inhibition not more common. Pheromone-sensitive ORNs, on the other hand, do not need to encode the odor identity, and higher spontaneous activity might not be beneficial for stimulus encoding.

In the analysis of metabolically efficient neural coding, I focused predominantly on models of cortical neurons and neural networks. The proposed model of ORN is a step towards conducting similar studies in the moth olfactory system. Although models of moth ORNs and PNs reproducing the firing rates of the neurons and their heterogeneity have been proposed (Jacob et al., 2017; Levakova et al., 2019), these models focused only on the firing rates and although the model by Levakova et al. (2019) is a spiking model, it does not aim to reproduce the spiking patterns of the ORNs and their trial-to-trial variability, properties essential for understanding the efficiency of information encoding and effect on neurons downstream. The model by Jacob et al. (2017) could be extended to take into account the trial-to-trial variability of the neurons in the same way as the linear-nonlinear model proposed in this thesis. However, the portability of this model is limited, as the knowledge of the full time course of the filters (or the time course of their principal components) is necessary to replicate the results.

Firing profiles of the ORN responses and behavior of the insects suggest that greater emphasis is put on encoding the odor onset and odor offset when encoding the information about the stimulus. Further downstream, PNs are less sensitive to differences in odor concentration than ORNs (Jarriault et al., 2010; Stevens, 2016; Olsen et al., 2010). Therefore we can assume that the goal of the olfactory

system is not to transmit as much information as possible about the stimulus to the higher brain areas. Instead, the ORNs and the neurons in the AL clearly select which information should be passed on. An alternative approach is then to evaluate the encoding efficiency of the specific features of the stimulus, such as the durations of blanks between two subsequent odor encounters (Levakova et al., 2018).

Ultimately, however, the goal of the insect in the navigation problem is to locate the source. The efficiency of the olfactory system should therefore be evaluated as the efficiency in locating the source. Simulations of insect behavior based on olfactory system activity have been shown to be useful in comparing different navigation strategies (Voges et al., 2014; Liberzon et al., 2018; Jayaram et al., 2022) and in testing how properties of the olfactory system affect the navigation efficiency (Jayaram et al., 2022; Kadakia et al., 2022). Having a reliable model of the olfactory system is essential for such studies. Enforcing metabolic constraints on the navigation task could then help explain from the first principles why PNs seem to maximize the entropy of their output while ORN firing rates remain low.

Appendix

Appendix A

Multiple spike amplitudes in the trichoid sensillum of *A. ipsilon*

Here we analyze a single recording in which two different spike amplitudes are clearly visible, both showing a stable behavior during 30 min recording with tungsten electrodes. The ORN was first recorded for 15 min, then presented with a 2 s stimulus and then recorded for additional 15 min. The recording was high-pass filtered with a Butteworth 2-pole filter at the frequency of 200 Hz. We selected two thresholds: $\theta_1 = 0.5\,\text{mV}$ and $\theta_2 = 1.2\,\text{mV}$. Small spikes had an amplitude $> \theta_1$ but $< \theta_2$, large spikes had an amplitude $> \theta_2$ (Fig. 18A).

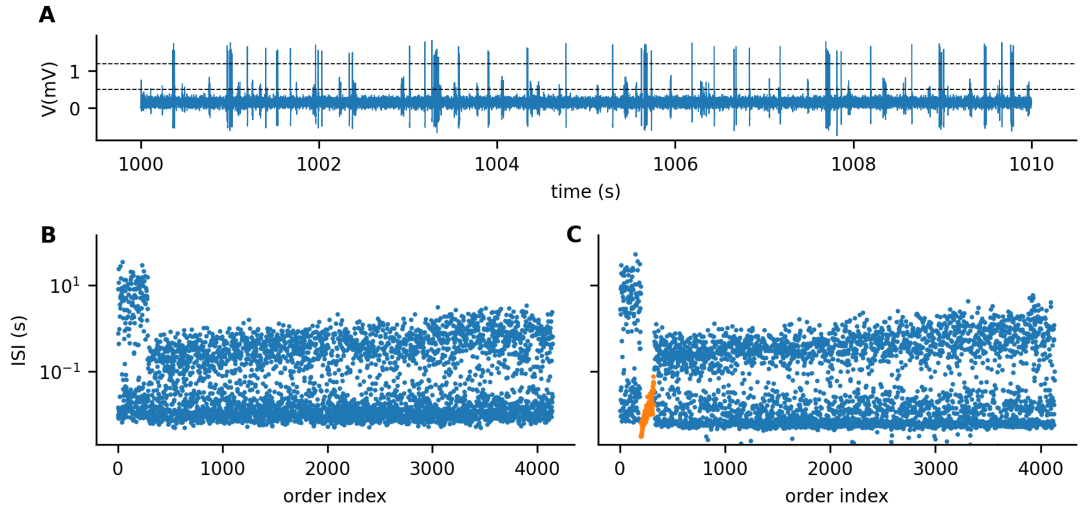

Figure 18: Recording with different spike amplitudes. A: The high-pass filtered recording in the interval 1000 s to 1010 s. Note that the stimulus was presented between 900 s and 902 s. The dashed horizontal lines represent the thresholds for spike detection, $\theta_1 = 0.5\,\text{mV}$ and $\theta_2 = 1.2\,\text{mV}$. **B-C:** Inter-spike intervals (ISIs) in chronological order for the large spikes (**B**) and the small spikes (**C**). Orange points represent the ISIs that occured during the stimulus.

Firing of both spike amplitudes was more intense after the stimulus onset (ISIs were shorter), indicating a rebound activity. Although we couldn't see both spike amplitudes during the response (small spike amplitudes were probably too small to be distinguishable), we can assume that both neurons responded to the pheromone stimulus. Therefore, either the sensilla contains two pheromone sensitive ORNs, or the small amplitude corresponds to an ORN from a neighboring sensilla.

Appendix B

Gating variables of the Hodgkin-Huxley model

An example of the functional form of the gating variables of the Hodgkin-Huxley model (Destexhe and Paré, 1999):

$$\alpha_m = -0.32 \frac{V - V_T - 13}{\exp(-(V - V_T - 13)/4) - 1}, \tag{3.4}$$

$$\beta_m = 0.28 \frac{V - V_T - 40}{\exp((V - V_T - 40)/5) - 1}, \tag{3.5}$$

$$\alpha_h = 0.128 \exp(-(V - V_T - V_S - 17)/18), \tag{3.6}$$

$$\beta_h = \frac{4}{1 + \exp(-(V - V_T - V_S - 40)/5)}, \tag{3.7}$$

$$\alpha_n = -0.032 \frac{V - V_T - 15}{\exp(-(V - V_T - 15)/5) - 1}, \tag{3.8}$$

$$\beta_n = 0.5 \exp(-(V - V_T - 10)/40), \tag{3.9}$$

$$\alpha_p = 0.0001 \frac{V + 30}{1 - \exp(-(V + 30)/9)}, \tag{3.10}$$

$$\beta_p = -0.0001 \frac{V + 30}{1 - \exp((V + 30)/9)}, \tag{3.11}$$

with $V_T = -58\,\mathrm{mV}$ and $V_S = -10\,\mathrm{mV}$. The time constant and steady state activation (Eq. 2.27) can then be obtained as:

$$\tau_x(V) = \frac{1}{\alpha_x(V) + \beta_x(V)}, \tag{3.12}$$

$$x_\infty(V) = \frac{\alpha_x(V)}{\alpha_x(V) + \beta_x(V)}. \tag{3.13}$$

Bibliography

L. F. Abbott and Peter Dayan. The Effect of Correlated Variability on the Accuracy of a Population Code. *Neural Comput.*, 11(1):91–101, 1 1999. ISSN 0899-7667. doi: 10.1162/089976699300016827.

L F Abbott and Sean X Luo. A step toward optimal coding in olfaction. *Nat Neurosci*, 10(11):1342–1343, 11 2007. ISSN 1097-6256. doi: 10.1038/nn1107-1342.

E. D. Adrian. The impulses produced by sensory nerve endings. *J. Physiol.*, 61 (1):49–72, 3 1926. ISSN 00223751. doi: 10.1113/jphysiol.1926.sp002273.

E. D. Adrian. The Basis of Sensation. *BMJ*, 1(4857):287–290, 2 1954. ISSN 0959-8138. doi: 10.1136/bmj.1.4857.287.

E. D. Adrian and Yngve Zotterman. The impulses produced by sensory nerve-endings. *J. Physiol.*, 61(2):151–171, 4 1926a. ISSN 00223751. doi: 10.1113/jphysiol.1926.sp002281.

E. D. Adrian and Yngve Zotterman. The impulses produced by sensory nerve endings. *J. Physiol.*, 61(4):465–483, 8 1926b. ISSN 00223751. doi: 10.1113/jphysiol.1926.sp002308.

David Attwell and Simon B Laughlin. An Energy Budget for Signaling in the Grey Matter of the Brain. *J. Cereb. Blood Flow Metab.*, 21(10):1133–1145, 2001. doi: 10.1097/00004647-200110000-00001.

Bruno B. Averbeck, Peter E. Latham, and Alexandre Pouget. Neural correlations, population coding and computation. *Nat. Rev. Neurosci.*, 7(5):358–366, 5 2006. ISSN 1471-003X. doi: 10.1038/nrn1888.

Keeley L. Baker, Michael Dickinson, Teresa M. Findley, David H. Gire, Matthieu Louis, Marie P. Suver, Justus V. Verhagen, Katherine I. Nagel, and Matthew C. Smear. Algorithms for Olfactory Search across Species. *J. Neurosci*, 38(44): 9383–9389, 10 2018. ISSN 0270-6474. doi: 10.1523/JNEUROSCI.1668-18.2018.

Vijay Balasubramanian, Don Kimber, and Michael J Berry II. Metabolically Efficient Information Processing. *Neural Comput.*, 13(4):799–815, 4 2001. doi: 10.1162/089976601300014358.

Riccardo Barbieri, Loren M. Frank, Michael C. Quirk, Matthew A. Wilson, and Emery N. Brown. Diagnostic methods for statistical models of place cell spiking activity. *Neurocomputing*, 38-40:1087–1093, 6 2001a. ISSN 09252312. doi: 10.1016/S0925-2312(01)00450-7.

Riccardo Barbieri, Michael C Quirk, Loren M Frank, Matthew A Wilson, and Emery N Brown. Construction and analysis of non-Poisson stimulus-response models of neural spiking activity. *J, Neurosci. Methods*, 105(1):25–37, 1 2001b. ISSN 01650270. doi: 10.1016/S0165-0270(00)00344-7.

H B Barlow. Possible Principles Underlying the Transformations of Sensory Messages. In *Sensory Communication*, pages 217–234. The MIT Press, 9 1961. doi: 10.7551/mitpress/9780262518420.003.0013.

Tomas Barta and Lubomir Kostal. The effect of inhibition on rate code efficiency indicators. *PLoS Comput Biol.*, 15(12):e1007545, 12 2019. doi: 10.1371/journal.pcbi.1007545.

Tomas Barta and Lubomir Kostal. Regular spiking in high-conductance states: The essential role of inhibition. *Phys Rev E*, 103(2):022408, 2 2021. ISSN 2470-0045. doi: 10.1103/PhysRevE.103.022408.

Tomas Barta and Lubomir Kostal. Shared input and recurrency in neural networks for metabolically efficient information transmission. 2023.

Tomas Barta, Christelle Monsempès, Elodie Demondion, Abhishek Chatterjee, Lubomir Kostal, and Philippe Lucas. Stimulus duration encoding occurs early in the moth olfactory pathway. *bioRxiv*, page 2022.07.21.501055, 7 2022. doi: 10.1101/2022.07.21.501055.

H. Belmabrouk, T. Nowotny, J.-P. Rospars, and D. Martinez. Interaction of cellular and network mechanisms for efficient pheromone coding in moths. *Proc. Natl. Acad. Sci. U.S.A.*, 108(49), 12 2011. ISSN 0027-8424. doi: 10.1073/pnas.1112367108.

Jan Benda. Neural adaptation. *Curr. Biol.*, 31(3):R110–R116, 2 2021. ISSN 09609822. doi: 10.1016/j.cub.2020.11.054.

Jan Benda and Andreas V. M. Herz. A Universal Model for Spike-Frequency Adaptation. *Neural Comput.*, 15(11):2523–2564, 11 2003. ISSN 0899-7667. doi: 10.1162/089976603322385063.

Jan Benda, Leonard Maler, and André Longtin. Linear Versus Nonlinear Signal Transmission in Neuron Models With Adaptation Currents or Dynamic Thresholds. *J. Neurophysiol*, 104(5):2806–2820, 11 2010. doi: 10.1152/jn.00240.2010.

Alberto Bernacchia and Xiao-Jing Wang. Decorrelation by Recurrent Inhibition in Heterogeneous Neural Circuits. *Neural Comput.*, 25(7):1732–1767, 7 2013. ISSN 0899-7667. doi: 10.1162/NECO{_}a{_}00451.

Rinaldo Betkiewicz, Benjamin Lindner, and Martin P. Nawrot. Circuit and Cellular Mechanisms Facilitate the Transformation from Dense to Sparse Coding in the Insect Olfactory System. *eNeuro*, 7(2):0305–18, 3 2020. ISSN 2373-2822. doi: 10.1523/ENEURO.0305-18.2020.

Vikas Bhandawat, Shawn R Olsen, Nathan W Gouwens, Michelle L Schlief, and Rachel I Wilson. Sensory processing in the Drosophila antennal lobe increases reliability and separability of ensemble odor representations. *Nat Neurosci*, 10 (11):1474–1482, 11 2007. ISSN 1097-6256. doi: 10.1038/nn1976.

Alex D. Bird and Magnus J. E. Richardson. Transmission of temporally correlated spike trains through synapses with short-term depression. *PLoS Comp. Biol.*, 14(6):e1006232, 6 2018. ISSN 1553-7358. doi: 10.1371/journal.pcbi.1006232.

R Blahut. Computation of channel capacity and rate-distortion functions. *IEEE Trans Inf Theory*, 18(4):460–473, 7 1972. doi: 10.1109/tit.1972.1054855.

A Borst and F E Theunissen. Information theory and neural coding. *Nat. Neurosci.*, 2(11):947–957, 11 1999.

Sofia C. Brandão, Marion Silies, and Carlotta Martelli. Adaptive temporal processing of odor stimuli. *Cell Tissue Res.*, 383(1):125–141, 1 2021. ISSN 0302-766X. doi: 10.1007/s00441-020-03400-9.

Romain Brette and Wulfram Gerstner. Adaptive Exponential Integrate-and-Fire Model as an Effective Description of Neuronal Activity. *J. Neurophysiol*, 94(5): 3637–3642, 11 2005. ISSN 0022-3077. doi: 10.1152/jn.00686.2005.

Emery N. Brown, Riccardo Barbieri, Valérie Ventura, Robert E. Kass, and Loren M. Frank. The Time-Rescaling Theorem and Its Application to Neural Spike Train Data Analysis. *Neural Comput.*, 14(2):325–346, 2 2002. ISSN 0899-7667. doi: 10.1162/08997660252741149.

Nicolas Brunel. Dynamics of Sparsely Connected Networks of Excitatory and Inhibitory Spiking Neurons. *J. Comput. Neurosci.*, 8:183–208, 2000. doi: https://doi.org/10.1023/A:1008925309027.

Li-Hui Cao, Dong Yang, Wei Wu, Xiankun Zeng, Bi-Yang Jing, Meng-Tong Li, Shanshan Qin, Chao Tang, Yuhai Tu, and Dong-Gen Luo. Odor-evoked inhibition of olfactory sensory neurons drives olfactory perception in Drosophila. *Nat. Commun.*, 8(1):1357, 11 2017. ISSN 2041-1723. doi: 10.1038/s41467-017-01185-0.

R. T. Cardé and R. E. Charlton. Olfactory sexual communication in Lepidoptera: strategy, sensitivity and selectivity. In T Lewis, editor, *Insect communication*, pages 241–265. Academic press, London, 1984.

Ring T. Cardé. Navigation Along Windborne Plumes of Pheromone and Resource-Linked Odors. *Annu. Rev. Entomol.*, 66(1):317–336, 1 2021. ISSN 0066-4170. doi: 10.1146/annurev-ento-011019-024932.

T. Chertemps. Molecular Basis of Pheromone Detection in Insects. In *Reference Module in Life Sciences*. Elsevier, 2017. doi: 10.1016/B978-0-12-809633-8.04038-3.

Mark M Churchland, Byron M Yu, John P Cunningham, Leo P Sugrue, Marlene R Cohen, Greg S Corrado, William T Newsome, Andrew M Clark, Paymon Hosseini, Benjamin B Scott, David C Bradley, Matthew A Smith, Adam Kohn, J Anthony Movshon, Katherine M Armstrong, Tirin Moore, Steve W Chang, Lawrence H Snyder, Stephen G Lisberger, Nicholas J Priebe, Ian M Finn, David Ferster, Stephen I Ryu, Gopal Santhanam, Maneesh Sahani, and Krishna V Shenoy. Stimulus onset quenches neural variability: a widespread cortical phenomenon. *Nat. Neurosci*, 13(3):369–78, 3 2010. ISSN 1546-1726. doi: 10.1038/nn.2501.

P Dayan and L F Abbott. *Theoretical Neuroscience: Computational and Mathematical Modeling of Neural Systems*. The MIT Press, 2005. ISBN 0262541858.

Arthur de Fouchier, William B. Walker, Nicolas Montagné, Claudia Steiner, Muhammad Binyameen, Fredrik Schlyter, Thomas Chertemps, Annick Maria, Marie-Christine François, Christelle Monsempes, Peter Anderson, Bill S. Hansson, Mattias C. Larsson, and Emmanuelle Jacquin-Joly. Functional evolution of Lepidoptera olfactory receptors revealed by deorphanization of a moth repertoire. *Nat. Commun.*, 8(1):15709, 6 2017. ISSN 2041-1723. doi: 10.1038/ncomms15709.

Gonzalo G de Polavieja. Errors Drive the Evolution of Biological Signalling to Costly Codes. *J. Theor. Biol.*, 214(4):657–664, 2 2002. doi: 10.1006/jtbi.2001.2498.

Gonzalo G de Polavieja. Reliable biological communication with realistic constraints. *Phys Rev E*, 70(6), 12 2004. doi: 10.1103/physreve.70.061910.

A Destexhe, M Rudolph, J M Fellous, and T J Sejnowski. Fluctuating synaptic conductances recreate in vivo-like activity in neocortical neurons. *Neuroscience*, 107(1):13–24, 2001. ISSN 0306-4522.

Alain Destexhe and Denis Paré. Impact of Network Activity on the Integrative Properties of Neocortical Pyramidal Neurons In Vivo. *J. Neurophysiol*, 81(4):1531–1547, 4 1999. doi: 10.1152/jn.1999.81.4.1531.

Alain Destexhe, Michael Rudolph, and Denis Paré. The high-conductance state of neocortical neurons in vivo. *Nat. Rev. Neurosci.*, 4(9):739–751, 9 2003. doi: 10.1038/nrn1198.

A Edman, S Gestrelius, and W Grampp. Analysis of gated membrane currents and mechanisms of firing control in the rapidly adapting lobster stretch receptor neurone. *J. Physiol*, 384(1):649–669, 3 1987. ISSN 00223751. doi: 10.1113/jphysiol.1987.sp016475.

J. S. Elkinton, C. Schal, T. Onot, and R. T. Cardé. Pheromone puff trajectory and upwind flight of male gypsy moths in a forest. *Physiol. Entomol.*, 12(4):399–406, 12 1987. ISSN 0307-6962. doi: 10.1111/j.1365-3032.1987.tb00766.x.

I A Fleidervish, A Friedman, and M J Gutnick. Slow inactivation of Na+ current and slow cumulative spike adaptation in mouse and guinea-pig neocortical neurones in slices. *J. Physiol. (Lond.)*, 493(1), 5 1996. ISSN 00223751. doi: 10.1113/jphysiol.1996.sp021366.

Nicolas Fourcaud-Trocmé, David Hansel, Carl van Vreeswijk, and Nicolas Brunel. How Spike Generation Mechanisms Determine the Neuronal Response to Fluctuating Inputs. *J. Neurosci*, 23(37):11628–11640, 12 2003. ISSN 0270-6474. doi: 10.1523/JNEUROSCI.23-37-11628.2003.

Tomoki Fukai. Computational models of Idling brain activity for memory processing. *Neurosci. Res.*, 12 2022. ISSN 01680102. doi: 10.1016/j.neures.2022.12.024.

Robert G Gallager. *Information Theory and Reliable Communication*. John Wiley & Sons, Inc., New York, NY, USA, 1968. ISBN 0471290483.

Maria N. Geffen, Bede M. Broome, Gilles Laurent, and Markus Meister. Neural Encoding of Rapidly Fluctuating Odors. *Neuron*, 61(4):570–586, 2 2009. ISSN 08966273. doi: 10.1016/j.neuron.2009.01.021.

Wilson S. Geisler and Duane G. Albrecht. Visual cortex neurons in monkeys and cats: Detection, discrimination, and identification. *Vis Neurosci*, 14(5):897–919, 9 1997. ISSN 0952-5238. doi: 10.1017/S0952523800011627.

W Gerstner and R Naud. How Good Are Neuron Models? *Science*, 326(5951): 379–380, 10 2009. doi: 10.1126/science.1181936.

Srinivas Gorur-Shandilya, Mahmut Demir, Junjiajia Long, Damon A Clark, and Thierry Emonet. Olfactory receptor neurons use gain control and complementary kinetics to encode intermittent odorant stimuli. *eLife*, 6:e27670, 2017. doi: https://doi.org/10.7554/eLife.27670.001.

Srinivas Gorur-Shandilya, Carlotta Martelli, Mahmut Demir, and Thierry Emonet. Controlling and measuring dynamic odorant stimuli in the laboratory. *J. Exp. Biol.*, 222(23):jeb207787, 12 2019. ISSN 0022-0949. doi: 10.1242/jeb.207787.

Alexandre Grémiaux, Thomas Nowotny, Dominique Martinez, Philippe Lucas, and Jean-Pierre Rospars. Modelling the signal delivered by a population of first-order neurons in a moth olfactory system. *Brain Res.*, 1434, 1 2012. ISSN 00068993. doi: 10.1016/j.brainres.2011.09.035.

Moshe Gur, Alexander Beylin, and D. Max Snodderly. Response Variability of Neurons in Primary Visual Cortex (V1) of Alert Monkeys. *J. Neurosci*, 17(8): 2914–2920, 4 1997. ISSN 0270-6474. doi: 10.1523/JNEUROSCI.17-08-02914.1997.

Boris Gutkin and Fleur Zeldenrust. Spike frequency adaptation. *Scholarpedia*, 9 (2):30643, 2014. ISSN 1941-6016. doi: 10.4249/scholarpedia.30643.

Elissa A Hallem, Michael G Ho, and John R Carlson. The Molecular Basis of Odor Coding in the Drosophila Antenna. *Cell*, 117(7):965–979, 6 2004. ISSN 00928674. doi: 10.1016/j.cell.2004.05.012.

J J Harris, R Jolivet, and D Attwell. Synaptic energy use and supply. *Neuron*, 75 (5):762–777, 2012.

J J Harris, R Jolivet, E Engl, and D Attwell. Energy-Efficient Information Transfer by Visual Pathway Synapses. *Curr. Biol.*, 25(24):3151–3160, 2015.

A. L. Hodgkin and A. F. Huxley. A quantitative description of membrane current and its application to conduction and excitation in nerve. *J. Physiol*, 117(4): 500–544, 8 1952. ISSN 0022-3751. doi: 10.1113/jphysiol.1952.sp004764.

S Ikeda and J H Manton. Capacity of a single spiking neuron channel. *Neural Comput.*, 21(6):1714–1748, 6 2009.

Yoshikazu Isomura, Rie Harukuni, Takashi Takekawa, Hidenori Aizawa, and Tomoki Fukai. Microcircuitry coordination of cortical motor information in self-initiation of voluntary movements. *Nat. Neurosci.*, 12(12):1586–1593, 11 2009. doi: 10.1038/nn.2431.

Vincent Jacob, Christelle Monsempès, Jean-Pierre Rospars, Jean-Baptiste Masson, and Philippe Lucas. Olfactory coding in the turbulent realm. *PLoS Comput. Biol.*, 13(12):e1005870, 12 2017. ISSN 1553-7358. doi: 10.1371/journal.pcbi.1005870.

E Jacquin-Joly and Philippe Lucas. No Pheromone reception and transduction: mammals and insects illustrate converging mechanisms across phyla. *Curr Top Neurochem.*, 4:75–105, 2005.

Anila F Jahangiri and Gregory J Gerling. A multi-timescale adaptive threshold model for the {SAI} tactile afferent to predict response to mechanical vibration. In *2011 5th International {IEEE}/{EMBS} Conference on Neural Engineering*. IEEE, 4 2011. doi: 10.1109/ner.2011.5910511.

D. Jarriault, C. Gadenne, P. Lucas, J.-P. Rospars, and S. Anton. Transformation of the Sex Pheromone Signal in the Noctuid Moth Agrotis ipsilon: From Peripheral Input to Antennal Lobe Output. *Chem. Senses*, 35(8):705–715, 10 2010. ISSN 0379-864X. doi: 10.1093/chemse/bjq069.

David Jarriault, Christophe Gadenne, Jean-Pierre Rospars, and Sylvia Anton. Quantitative analysis of sex-pheromone coding in the antennal lobe of the moth Agrotis ipsilon: a tool to study network plasticity. *J. Exp. Biol.*, 212(8):1191–1201, 4 2009. ISSN 1477-9145. doi: 10.1242/jeb.024166.

Viraaj Jayaram, Nirag Kadakia, and Thierry Emonet. Sensing complementary temporal features of odor signals enhances navigation of diverse turbulent plumes. *eLife*, 11, 1 2022. ISSN 2050-084X. doi: 10.7554/eLife.72415.

Masakazu Jimbo and Kiyonori Kunisawa. An iteration method for calculating the relative capacity. *Information and Control*, 43(2):216–223, 11 1979. doi: 10.1016/s0019-9958(79)90719-8.

Renaud Jolivet, Alexander Rauch, Hans-Rudolf Lüscher, and Wulfram Gerstner. Predicting spike timing of neocortical pyramidal neurons by simple threshold models. *J. Comput. Neurosci*, 21(1):35–49, 8 2006. ISSN 0929-5313. doi: 10.1007/s10827-006-7074-5.

Renaud Jolivet, Felix Schürmann, Thomas K Berger, Richard Naud, Wulfram Gerstner, and Arnd Roth. The quantitative single-neuron modeling competition. *Biol. Cybern.*, 99(4-5):417–426, 11 2008. doi: 10.1007/s00422-008-0261-x.

Nirag Kadakia and Thierry Emonet. Front-end Weber-Fechner gain control enhances the fidelity of combinatorial odor coding. *eLife*, 8, 6 2019. ISSN 2050-084X. doi: 10.7554/eLife.45293.

Nirag Kadakia, Mahmut Demir, Brenden T. Michaelis, Brian D. DeAngelis, Matthew A. Reidenbach, Damon A. Clark, and Thierry Emonet. Odour motion sensing enhances navigation of complex plumes. *Nature*, 611(7937):754–761, 11 2022. ISSN 0028-0836. doi: 10.1038/s41586-022-05423-4.

Aklesso Kadala, Mercedes Charreton, Ingrid Jakob, Yves Le Conte, and Claude Collet. A use-dependent sodium current modification induced by type I pyrethroid insecticides in honeybee antennal olfactory receptor neurons. *Neurotoxicology*, 32(3):320–330, 6 2011. ISSN 0161813X. doi: 10.1016/j.neuro.2011.02.007.

K Kaissling. Chemo-Electrical Transduction in Insect Olfactory Receptors. *Annu. Rev. Neurosci.*, 9(1), 3 1986. ISSN 0147-006X. doi: 10.1146/annurev.ne.09.030186.001005.

K.-E. Kaissling. Olfactory Perireceptor and Receptor Events in Moths: A Kinetic Model. *Chem. Senses*, 26(2):125–150, 2 2001. ISSN 14643553. doi: 10.1093/chemse/26.2.125.

K.-E. Kaissling. Dose-Response Relationships in an Olfactory Flux Detector Model Revisited. *Chem. Senses*, 29(6):529–531, 7 2004. ISSN 1464-3553. doi: 10.1093/chemse/bjh057.

K. E. Kaissling, C. Z. Strausfeld, and E. R. Rumbo. Adaptation Processes in Insect Olfactory Receptors. *Annals of the New York Academy of Sciences*, 510: 104–112, 11 1987. ISSN 0077-8923. doi: 10.1111/j.1749-6632.1987.tb43475.x.

K. E. Kaissling, L. Z. Meng, and H. J. Bestmann. Responses of bombykol receptor cells to (Z,E)-4,6-hexadecadiene and linalool. *J. Comp. Physiol. A*, 165(2): 147–154, 3 1989. ISSN 0340-7594. doi: 10.1007/BF00619189.

Karl-Ernst Kaissling. Kinetics of olfactory responses might largely depend on the odorant–receptor interaction and the odorant deactivation postulated for flux detectors. *Journal of Comparative Physiology A*, 199(11):879–896, 11 2013. ISSN 0340-7594. doi: 10.1007/s00359-013-0812-z.

Karl-Ernst Kaissling. *Pheromone Reception in Insects: The Example of Silk Moths*. 2014. ISBN 9781466553415.

E R Kandel, T M Jessell, J H Schwartz, S A Siegelbaum, and A J Hudspeth. *Principles of Neural Science, Fifth Edition*. Principles of Neural Science. McGraw-Hill Education, 2013. ISBN 9780071390118.

Leslie M. Kay and Mark Stopfer. Information processing in the olfactory systems of insects and vertebrates. *Semin Cell Dev Biol.*, 17(4):433–442, 8 2006. ISSN 10849521. doi: 10.1016/j.semcdb.2006.04.012.

J. S. Kennedy, A. R. Ludlow, and C. J. Sanders. Guidance system used in moth sex attraction. *Nature*, 288(5790):475–477, 12 1980. ISSN 0028-0836. doi: 10.1038/288475a0.

Anmo J. Kim, Aurel A. Lazar, and Yevgeniy B. Slutskiy. System identification of Drosophila olfactory sensory neurons. *J. Comput. Neurosci.*, 30(1), 2 2011. ISSN 0929-5313. doi: 10.1007/s10827-010-0265-0.

Anmo J Kim, Aurel A Lazar, and Yevgeniy B Slutskiy. Projection neurons in Drosophila antennal lobes signal the acceleration of odor concentrations. *eLife*, 4, 5 2015. ISSN 2050-084X. doi: 10.7554/eLife.06651.

R Kobayashi, Y Tsubo, and S Shinomoto. Made-to-order spiking neuron model equipped with a multi-timescale adaptive threshold. *Front. Comput. Neurosci.*, 3:9, 2009. doi: 10.3389/neuro.10.009.2009.

Ryota Kobayashi and Katsunori Kitano. Impact of slow K+ currents on spike generation can be described by an adaptive threshold model. *J. Comput. Neurosci.*, 40(3):347–362, 4 2016. doi: 10.1007/s10827-016-0601-0.

Lubomir Kostal and Ryota Kobayashi. Optimal decoding and information transmission in Hodgkin-Huxley neurons under metabolic cost constraints. *Biosystems*, 136:3–10, 10 2015. doi: 10.1016/j.biosystems.2015.06.008.

Gilles Laurent. Olfactory processing: maps, time and codes. *Curr. Opin. Neurobiol*, 7(4):547–553, 8 1997. ISSN 09594388. doi: 10.1016/S0959-4388(97)80035-9.

Gilles Laurent. Olfactory network dynamics and the coding of multidimensional signals. *Nat. Rev. Neurosci.*, 3(11):884–895, 11 2002. ISSN 1471-003X. doi: 10.1038/nrn964.

Hayeong Lee, Lubomir Kostal, Ryohei Kanzaki, and Ryota Kobayashi. Spike frequency adaptation facilitates the encoding of input gradient in insect olfactory projection neurons. *Biosyst*, 223:104802, 1 2023. ISSN 03032647. doi: 10.1016/j.biosystems.2022.104802.

Marie Levakova, Lubomir Kostal, Christelle Monsempès, Vincent Jacob, and Philippe Lucas. Moth olfactory receptor neurons adjust their encoding efficiency to temporal statistics of pheromone fluctuations. *PLoS Comput. Biol.*, 14(11): e1006586, 11 2018. doi: 10.1371/journal.pcbi.1006586.

Marie Levakova, Lubomir Kostal, Christelle Monsempès, Philippe Lucas, and Ryota Kobayashi. Adaptive integrate-and-fire model reproduces the dynamics of olfactory receptor neuron responses in a moth. *J R Soc Interface*, 16(157): 20190246, 8 2019. doi: 10.1098/rsif.2019.0246.

Jake Lever, Martin Krzywinski, and Naomi Altman. Model selection and overfitting. *Nat. Methods*, 13(9):703–704, 9 2016. ISSN 1548-7091. doi: 10.1038/nmeth.3968.

William B Levy and Robert A Baxter. Energy Efficient Neural Codes. *Neural Comput.*, 8(3):531–543, 4 1996. doi: 10.1162/neco.1996.8.3.531.

Alexander Liberzon, Kyra Harrington, Nimrod Daniel, Roi Gurka, Ally Harari, and Gregory Zilman. Moth-inspired navigation algorithm in a turbulent odor plume from a pulsating source. *PLoS One*, 13(6):e0198422, 6 2018. ISSN 1932-6203. doi: 10.1371/journal.pone.0198422.

Brian Nils Lundstrom, Sungho Hong, Matthew H. Higgs, and Adrienne L. Fairhall. Two Computational Regimes of a Single-Compartment Neuron Separated by a Planar Boundary in Conductance Space. *Neural Comput.*, 20(5):1239–1260, 5 2008. ISSN 0899-7667. doi: 10.1162/neco.2007.05-07-536.

Agenor Mafra-Neto and Ring T. Cardé. Fine-scale structure of pheromone plumes modulates upwind orientation of flying moths. *Nature*, 369(6476):142–144, 5 1994. ISSN 0028-0836. doi: 10.1038/369142a0.

Z. Mainen and T. Sejnowski. Reliability of spike timing in neocortical neurons. *Science*, 268(5216):1503–1506, 6 1995. ISSN 0036-8075. doi: 10.1126/science.7770778.

Bettina Malnic, Junzo Hirono, Takaaki Sato, and Linda B Buck. Combinatorial Receptor Codes for Odors. *Cell*, 96(5):713–723, 3 1999. ISSN 00928674. doi: 10.1016/S0092-8674(00)80581-4.

C. Martelli, J. R. Carlson, and T. Emonet. Intensity Invariant Dynamics and Odor-Specific Latencies in Olfactory Receptor Neuron Response. *J. Neurosci*, 33(15), 4 2013. ISSN 0270-6474. doi: 10.1523/JNEUROSCI.0426-12.2013.

Marco Martina and Peter Jonas. Functional differences in Na+ channel gating between fast-spiking interneurones and principal neurones of rat hippocampus. *J. Physiol*, 505(3):593–603, 12 1997. ISSN 00223751. doi: 10.1111/j.1469-7793.1997.593ba.x.

Dominique Martinez, Antoine Chaffiol, Nicole Voges, Yuqiao Gu, Sylvia Anton, Jean-Pierre Rospars, and Philippe Lucas. Multiphasic On/Off Pheromone Signalling in Moths as Neural Correlates of a Search Strategy. *PLoS ONE*, 8 (4):e61220, 4 2013. ISSN 1932-6203. doi: 10.1371/journal.pone.0061220.

M D McDonnell, S Ikeda, and J H Manton. An introductory review of information theory in the context of computational neuroscience. *Biol. Cybern.*, 105:55–70, 2011.

A. V. Minor and K.-E. Kaissling. Cell responses to single pheromone molecules may reflect the activation kinetics of olfactory receptor molecules. *Journal of Comparative Physiology A*, 189(3):221–230, 3 2003. ISSN 0340-7594. doi: 10.1007/s00359-003-0394-2.

Cyril Monier, Frédéric Chavane, Pierre Baudot, Lyle J Graham, and Yves Frégnac. Orientation and Direction Selectivity of Synaptic Inputs in Visual Cortical Neurons. *Neuron*, 37(4):663–680, 2 2003. doi: 10.1016/s0896-6273(03)00064-3.

J Murlis, J S Elkinton, and R T Cardé. Odor Plumes and How Insects Use Them. *Annu. Rev. Entomol.*, 37(1):505–532, 1 1992. ISSN 0066-4170. doi: 10.1146/annurev.en.37.010192.002445.

Katherine I Nagel and Rachel I Wilson. Biophysical mechanisms underlying olfactory receptor neuron dynamics. *Nat. Neurosci*, 14(2):208–216, 2 2011. ISSN 1097-6256. doi: 10.1038/nn.2725.

Shawn R. Olsen and Rachel I. Wilson. Lateral presynaptic inhibition mediates gain control in an olfactory circuit. *Nature*, 452(7190):956–960, 4 2008. ISSN 0028-0836. doi: 10.1038/nature06864.

Shawn R. Olsen, Vikas Bhandawat, and Rachel I. Wilson. Divisive Normalization in Olfactory Population Codes. *Neuron*, 66(2):287–299, 4 2010. ISSN 08966273. doi: 10.1016/j.neuron.2010.04.009.

Zahid Padamsey, Danai Katsanevaki, Nathalie Dupuy, and Nathalie L. Rochefort. Neocortex saves energy by reducing coding precision during food scarcity. *Neuron*, 110(2):280–296, 1 2022. ISSN 08966273. doi: 10.1016/j.neuron.2021.10.024.

Denis Paré, Eric Shink, Hélène Gaudreau, Alain Destexhe, and Eric J Lang. Impact of Spontaneous Synaptic Activity on the Resting Properties of Cat Neocortical Pyramidal Neurons In Vivo. *J. Neurophysiol.*, 79(3):1450–1460, 3 1998. doi: 10.1152/jn.1998.79.3.1450.

A. Pézier, A. Acquistapace, M. Renou, J.-P. Rospars, and P. Lucas. Ca2+ Stabilizes the Membrane Potential of Moth Olfactory Receptor Neurons at Rest and Is Essential for Their Fast Repolarization. *Chem. Senses*, 32(4), 5 2007. ISSN 0379-864X. doi: 10.1093/chemse/bjl059.

Jonathan Platkiewicz and Romain Brette. A Threshold Equation for Action Potential Initiation. *PLoS Comput. Biol.*, 6(7):e1000850, 7 2010. ISSN 1553-7358. doi: 10.1371/journal.pcbi.1000850.

Hannes Rapp and Martin Paul Nawrot. A spiking neural program for sensorimotor control during foraging in flying insects. *Proc Natl Acad Sci USA*, 117(45):28412–28421, 11 2020. ISSN 0027-8424. doi: 10.1073/pnas.2009821117.

Alfonso Renart, Jaime de la Rocha, Peter Bartho, Liad Hollender, Néstor Parga, Alex Reyes, and Kenneth D. Harris. The Asynchronous State in Cortical Circuits. *Science*, 327(5965):587–590, 1 2010. ISSN 0036-8075. doi: 10.1126/science.1179850.

Jean-Pierre Rospars, Alexandre Grémiaux, David Jarriault, Antoine Chaffiol, Christelle Monsempès, Nina Deisig, Sylvia Anton, Philippe Lucas, and Dominique Martinez. Heterogeneity and Convergence of Olfactory First-Order Neurons Account for the High Speed and Sensitivity of Second-Order Neurons. *PLoS Comput. Biol.*, 10(12):e1003975, 12 2014. ISSN 1553-7358. doi: 10.1371/journal.pcbi.1003975.

Biswa Sengupta, Simon B Laughlin, and Jeremy E Niven. Balanced Excitatory and Inhibitory Synaptic Currents Promote Efficient Coding and Metabolic Efficiency. *PLoS Comput. Biol.*, 9(10):e1003263, 10 2013. doi: 10.1371/journal.pcbi.1003263.

Michael N Shadlen and William T Newsome. The Variable Discharge of Cortical Neurons: Implications for Connectivity, Computation, and Information Coding. *J. Neurosci.*, 18(10):3870–3896, 5 1998. doi: 10.1523/jneurosci.18-10-03870.1998.

C Shannon. A mathematical theory of communication. *Bell system technical journal*, 27, 1948.

H. H. Shorey. *Animal communication by pheromones*. Academic press, 1976.

L. Sokoloff. Cerebral Metabolism and Visualization of Cerebral Activity. In *Comprehensive Human Physiology*, pages 579–602. Springer Berlin Heidelberg, Berlin, Heidelberg, 1996. doi: 10.1007/978-3-642-60946-6{_}30.

Richard B Stein. The Information Capacity of Nerve Cells Using a Frequency Code. *Biophys. J.*, 7(6):797–826, 11 1967. doi: 10.1016/s0006-3495(67)86623-2.

Richard B Stein, E Roderich Gossen, and Kelvin E Jones. Neuronal variability: noise or part of the signal? *Nat. Rev. Neurosci.*, 6(5):389–397, 5 2005.

Charles F. Stevens. A statistical property of fly odor responses is conserved across odors. *Proc. Natl. Acad. Sci. U.S.A.*, 113(24):6737–6742, 6 2016. ISSN 0027-8424. doi: 10.1073/pnas.1606339113.

Mark Stopfer, Vivek Jayaraman, and Gilles Laurent. Intensity versus Identity Coding in an Olfactory System. *Neuron*, 39(6):991–1004, 9 2003. ISSN 08966273. doi: 10.1016/j.neuron.2003.08.011.

Prapun Suksompong and Toby Berger. Capacity Analysis for Integrate-and-Fire Neurons With Descending Action Potential Thresholds. *IEEE Trans Inf Theory*, 56(2):838–851, 2 2010. doi: 10.1109/tit.2009.2037042.

Mustafa Sungkar, Toby Berger, and William B Levy. Mutual Information and Parameter Estimation in the Generalized Inverse Gaussian Diffusion Model of Cortical Neurons. *IEEE Trans Mol Biol Multiscale Commun*, 2(2):166–182, 12 2016. doi: 10.1109/tmbmc.2017.2656861.

Mustafa Sungkar, Toby Berger, and William B Levy. Capacity achieving input distribution to the generalized inverse Gaussian neuron model. In *2017 55th Annual Allerton Conference on Communication, Control, and Computing (Allerton)*. IEEE, 10 2017. doi: 10.1109/allerton.2017.8262829.

Corinne Teeter, Ramakrishnan Iyer, Vilas Menon, Nathan Gouwens, David Feng, Jim Berg, Aaron Szafer, Nicholas Cain, Hongkui Zeng, Michael Hawrylycz, Christof Koch, and Stefan Mihalas. Generalized leaky integrate-and-fire models classify multiple neuron types. *Nat. Commun*, 9(1):709, 2 2018. doi: 10.1038/s41467-017-02717-4.

Tom Tetzlaff, Moritz Helias, Gaute T. Einevoll, and Markus Diesmann. Decorrelation of Neural-Network Activity by Inhibitory Feedback. *PLoS Comp. Biol.*, 8(8):e1002596, 8 2012. ISSN 1553-7358. doi: 10.1371/journal.pcbi.1002596.

Joy A Thomas Thomas M. Cover. *Elements of Information Theory*. Wiley Series in Telecommunications and Signal Processing. Wiley-Interscience, 2nd ed edition, 2006. ISBN 9780471241959,0471241954.

A Treves, S Panzeri, E T Rolls, M Booth, and E A Wakeman. Firing rate distributions and efficiency of information transmission of inferior temporal cortex neurons to natural visual stimuli. *Neural Comput.*, 11(3):601–632, 4 1999. ISSN 0899-7667.

Harrison Tuckman, Jungmin Kim, Aaditya Rangan, Hong Lei, and Mainak Patel. Dynamics of sensory integration of olfactory and mechanical stimuli within the response patterns of moth antennal lobe neurons. *J. Theor. Biol.*, 509, 1 2021a. ISSN 00225193. doi: 10.1016/j.jtbi.2020.110510.

Harrison Tuckman, Mainak Patel, and Hong Lei. Effects of Mechanosensory Input on the Tracking of Pulsatile Odor Stimuli by Moth Antennal Lobe Neurons. *Front. Neurosci.*, 15, 10 2021b. ISSN 1662-453X. doi: 10.3389/fnins.2021.739730.

Henry C Tuckwell. *Introduction to Theoretical Neurobiology*. Cambridge University Press, 4 1988. doi: 10.1017/cbo9780511623271.

Henry C Tuckwell. *Stochastic Processes in the Neurosciences*. Society for Industrial & Applied, 1989. ISBN 0898712327.

G E Uhlenbeck and L S Ornstein. On the Theory of the Brownian Motion. *Phys. Rev.*, 36(5):823–841, 9 1930. doi: 10.1103/physrev.36.823.

Nicole Voges, Antoine Chaffiol, Philippe Lucas, and Dominique Martinez. Reactive Searching and Infotaxis in Odor Source Localization. *PLoS Comput. Biol.*, 10 (10):e1003861, 10 2014. doi: 10.1371/journal.pcbi.1003861.

C. Wall and J. N. Perry. Range of action of moth sex-attractant sources. *Entomol. Exp. Appl.*, 44(1):5–14, 6 1987. ISSN 00138703. doi: 10.1111/j.1570-7458.1987.tb02232.x.

Michael Wehr and Gilles Laurent. Odour encoding by temporal sequences of firing in oscillating neural assemblies. *Nature*, 384(6605):162–166, 11 1996. ISSN 0028-0836. doi: 10.1038/384162a0.

Mark A. Willis and Thomas C. Baker. Effects of intermittent and continuous pheromone stimulation on the flight behaviour of the oriental fruit moth, Grapholita molesta. *Physiol. Entomol.*, 9(3):341–358, 9 1984. ISSN 0307-6962. doi: 10.1111/j.1365-3032.1984.tb00715.x.

Christopher D. Wilson, Gabriela O. Serrano, Alexei A. Koulakov, and Dmitry Rinberg. A primacy code for odor identity. *Nat. Commun.*, 8(1):1477, 11 2017. ISSN 2041-1723. doi: 10.1038/s41467-017-01432-4.

R. I. Wilson and Gilles Laurent. Role of GABAergic Inhibition in Shaping Odor-Evoked Spatiotemporal Patterns in the Drosophila Antennal Lobe. *J Neurosci.*, 25(40):9069–9079, 10 2005. ISSN 0270-6474. doi: 10.1523/JNEUROSCI.2070-05.2005.

Rachel I. Wilson. Early Olfactory Processing in Drosophila : Mechanisms and Principles. *Annu. Rev. Neurosci*, 36(1):217–241, 7 2013. ISSN 0147-006X. doi: 10.1146/annurev-neuro-062111-150533.

Jie Xing, Toby Berger, Mustafa Sungkar, and William B Levy. Energy Efficient Neurons With Generalized Inverse Gaussian Conditional and Marginal Hitting Times. *IEEE Trans Inf Theory*, 61(8):4390–4398, 8 2015. doi: 10.1109/tit.2015.2444401.

Satoshi Yamauchi, Hideaki Kim, and Shigeru Shinomoto. Elemental Spiking Neuron Model for Reproducing Diverse Firing Patterns and Predicting Precise Firing Times. *Front. Comput. Neurosci.*, 5, 2011. doi: 10.3389/fncom.2011.00042.

Yann Zerlaut, Sandrine Chemla, Frederic Chavane, and Alain Destexhe. Modeling mesoscopic cortical dynamics using a mean-field model of conductance-based networks of adaptive exponential integrate-and-fire neurons. *J. Comput. Neurosci*, 44(1):45–61, 2 2017. ISSN 0929-5313. doi: 10.1007/s10827-017-0668-2.

Hui Zou and Trevor Hastie. Regularization and variable selection via the elastic net. *J R Stat Soc B Biol Sci*, 67(2):301–320, 4 2005. ISSN 1369-7412. doi: 10.1111/j.1467-9868.2005.00503.x.

Attachments

Attachment I Manuscript on decrease in trial-to-trial variability with stimulus onset published in *Physical Review E* (Barta and Kostal, 2021)

Attachment II Report describing an extension of (Barta and Kostal, 2021) to recurrent neural networks

Attachment III Manuscript on information-metabolic efficiency of single neurons published in *PLoS Computational Biology* (Barta and Kostal, 2019)

Attachment IV Manuscript on information-metabolic efficiency of recurrent neural networks, currently published on *bioRxiv* (Barta and Kostal, 2023)

Attachment V Manuscript on stimulus encoding by moth olfactory receptor neurons, currently published on *bioRxiv* (Barta et al., 2022)

Attachment VI Report describing the statistical properties of spontaneous and rebound activity of moth ORNs

Attachment I

Manuscript published in *Physical Review E* **103**, 022408. Published on 18th February 2021, IF 2.707
doi: https://doi.org/10.1103/PhysRevE.103.022408

Regular spiking in high conductance states: the essential role of inhibition

Tomas Barta[1,2,3*], Lubomir Kostal[1**]

1 Institute of Physiology of the Czech Academy of Sciences, Prague, Czech Republic
2 Institute of Ecology and Environmental Sciences of Paris, INRAE, Sorbonne Université, CNRS, IRD, UPEC, Université de Paris, 78000 Versailles, France
3 Charles University, First Medical Faculty, Prague, Czech Republic

* tomas.barta@fgu.cas.cz
** kostal@biomed.cas.cz

Abstract

Strong inhibitory input to neurons, which occurs in balanced states of neural networks, increases synaptic current fluctuations. This has led to the assumption that inhibition contributes to the high spike-firing irregularity observed *in vivo*. We used single compartment neuronal models with time-correlated (due to synaptic filtering) and state-dependent (due to reversal potentials) input to demonstrate that inhibitory input acts to decrease membrane potential fluctuations, a result that cannot be achieved with simplified neural input models. To clarify the effects on spike-firing regularity, we used models with different spike-firing adaptation mechanisms and observed that the addition of inhibition increased firing regularity in models with dynamic firing thresholds and decreased firing regularity if spike-firing adaptation was implemented through ionic currents or not at all. This novel fluctuation-stabilization mechanism provides a new perspective on the importance of strong inhibitory inputs observed in balanced states of neural networks and highlights the key roles of biologically plausible inputs and specific adaptation mechanisms in neuronal modeling.

Introduction

In awake animals, neocortical neurons receive a stream of random synaptic inputs arising from background network activity Matsumura et al. (1988); Rudolph et al. (2007); Steriade et al. (2001). This "synaptic noise" is responsible for the fluctuations in membrane potential and stochastic nature of spike-firing times Shadlen and Newsome (1994); Vreeswijk and Sompolinsky (1996); Shadlen and Newsome (1998); Amit and Brunel (1997); Brunel (2000); Destexhe (2010); Denève and Machens (2016). Since spike-firing times encode the information transmitted by neurons, investigating the properties of neuronal responses to stochastic input, representing pre-synaptic spike arrivals, is of significant interest.

Typically, the total conductance of inhibitory synapses is several-fold higher than that of excitatory synapses Destexhe et al. (2003). This state, commonly referred to as the "high conductance state" has been demonstrated to significantly affect the integrative properties of neurons Bernander et al. (1991); Paré et al. (1998); Mittmann et al. (2005); Wolfart et al. (2005); Rudolph et al. (2007). Concurrently, the high inhibition-to-excitation ratio introduces additional synaptic noise, which should intuitively result in noisier firing. However, studies have demonstrated that the high

ratio of inhibition may lead to more efficient information transmission Sengupta et al. (2013); D'Onofrio et al. (2019); Barta and Kostal (2019). *In vivo* studies have also demonstrated that the onset of stimuli can stabilize the membrane potential without a significant change in its mean value Monier et al. (2003); Churchland et al. (2010). Monier et al. Monier et al. (2003) observed that the decrease in fluctuations was associated with higher evoked inhibition, which may have a shunting effect Fatt and Katz (1953). Nevertheless, a theoretical framework explaining why and under which conditions this shunting effect overpowers the increased synaptic noise is lacking.

Synaptic input can be modelled as temporary opening of excitatory and inhibitory ion channels, which act to either depolarize or hyperpolarize the neural membrane, respectively. Statistical measures of membrane potential can be calculated exactly with the resulting expressions being non-analytic Wolff and Lindner (2010) or they can be approximated in the steady-state with the effective time-constant approximation Richardson (2004); Richardson and Gerstner (2005). For better analytical tractability, the synaptic drive is often simplified with one (or both) of the following assumptions:

A1 The magnitude of the synaptic current elicited by each presynaptic spike is independent of the voltage Lindner and Schimansky-Geier (2001); Brunel et al. (2001); Fourcaud and Brunel (2002); Moreno-Bote and Parga (2004); Schwalger and Schimansky-Geier (2008); Droste and Lindner (2017), or

A2 Time profiles of individual synapses (synaptic filtering) are neglected Brunel (2000); Richardson (2004); Richardson and Gerstner (2006); Lánská et al. (1994); Deger et al. (2012); Droste and Lindner (2017); Sanzeni et al. (2020).

In order to observe the shunting effect of inhibition Monier et al. (2003), reversal potentials have to be considered, which excludes assumption A1. Richardson Richardson (2004) demonstrated that an increase in inhibition could decrease the membrane potential for strongly hyperpolarized membranes in a model of synaptic input with omitted synaptic filtering (assumption A2). However, we demonstrate that if neither of the simplifying assumptions are used, the membrane potential stabilization effect can be observed across the complete range of membrane potentials, despite increased synaptic current fluctuations (Fig 1A,B).

This naturally poses the question if the decreased membrane potential fluctuations lead to more regular firing activity Churchland et al. (2010). To this end, we analyze the effect of membrane potential stabilization on different neuronal models. In particular, we focus on how the effects of inhibition change for different spike-firing adaptation (SFA) mechanisms. SFA is responsible for the decrease of a neuron's firing rate in response to a sustained stimulus and plays a crucial role in all stages of sensory processing (e.g., (Martinez, 2005; Peron and Gabbiani, 2009; Augustin et al., 2013; Ha and Cheong, 2017; Levakova et al., 2019; Betkiewicz et al., 2020)). We compare two distinct SFA mechanisms: adaptation through ionic currents (muscarinic currents, AHP currents) and adaptation through dynamic threshold. We demonstrate that despite their formal similarities (Benda and Herz, 2003; Kobayashi and Kitano, 2016) the effect of inhibition qualitatively differs for these SFA mechanisms (Fig 1C,D). We illustrate the differences on the analytically more tractable generalized leaky integrate-and-fire models (GLIF) followed by the biophysically more plausible Hodgkin-Huxley (HH)-type models.

Methods

Subthreshold membrane potential

In order to analyze the behavior of neurons in the absence of any spike-firing mechanism, we consider a point neuronal model with membrane potential V described by

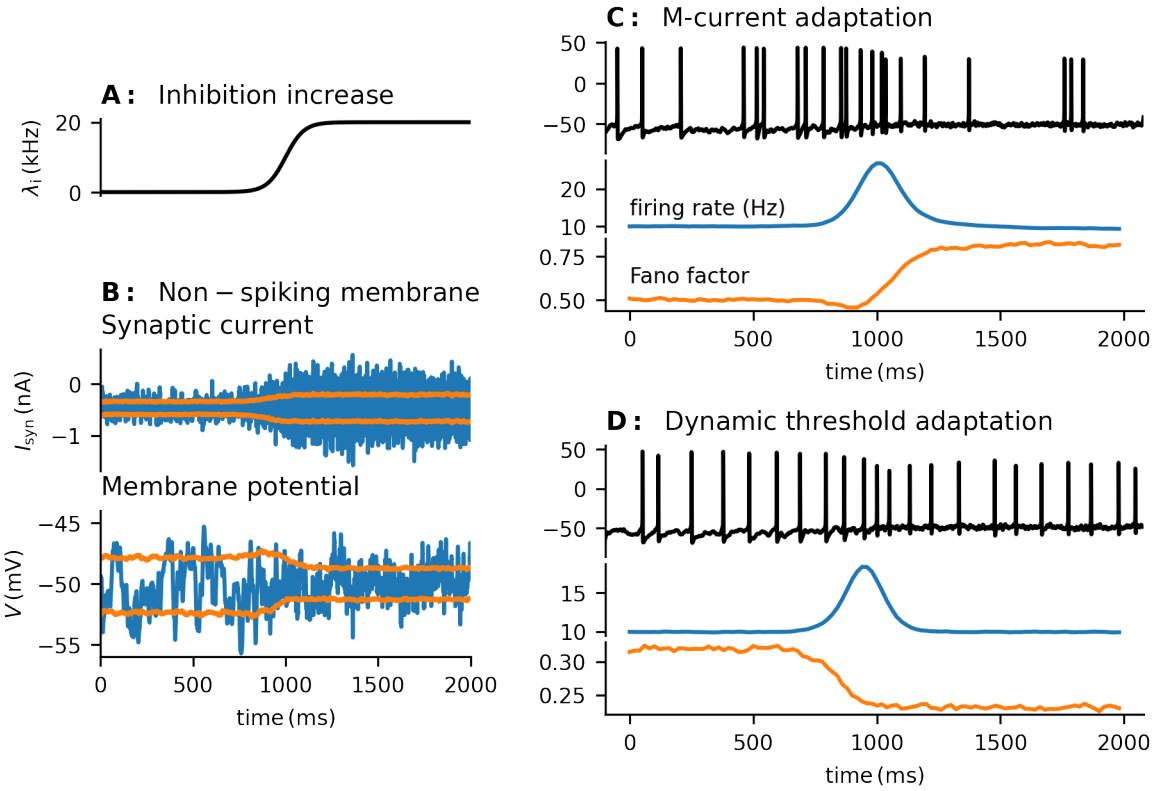

Fig 1. A: During a 2 s long simulation, the intensity of inhibitory input increases from 0 kHz to 20 kHz. The pre-synaptic spike trains are modeled as Poisson point processes. B: The intensity of excitatory input is increased simultaneously with the inhibition in order to maintain the mean membrane potential constant. This increases fluctuations of the synaptic current but decreases fluctuations of the membrane potential. The orange lines signify the mean value ± standard deviation. C and D: The effect of membrane potential stabilization on firing regularity. The intensity of the inhibitory input follows the time course shown in A, and the intensity of the excitatory activity is increased in order to maintain the steady state post-synaptic firing rate at approximately 10 Hz (blue trace). The firing regularity (measured here by the Fano factor, orange trace) decreases with the addition of inhibition to the input in the model with spike-firing adaptation by M currents (C). However, the model with dynamic threshold (D) exhibits a clear increase in regularity with the added inhibitory input. The mean firing rate and Fano factor were calculated by a sliding window of length 100 ms from approximately 10^5 trials.

$$C\frac{\mathrm{d}V(t)}{\mathrm{d}t} = -g_{\mathrm{L}}(V(t) - E_{\mathrm{L}}) + \frac{1}{a}(I_{\mathrm{e}}(t) + I_{\mathrm{i}}(t)), \tag{1}$$

where C is the specific capacitance of the membrane, g_{L} is the specific leak conductance, E_{L} is the leakage potential, $I_{\mathrm{e,i}}$ are the synaptic currents due to stimulation by afferent neurons through excitatory and inhibitory synapses, respectively, and a is the membrane area Tuckwell (1988); Dayan and Abbott (2005). For brevity, we will further use $V \equiv V(t)$. The synaptic currents are described by

$$I_{\mathrm{e,i}}(t) = g_{\mathrm{e,i}}(t)(V - E_{\mathrm{e,i}}), \tag{2}$$

where $g_{\mathrm{e}}(t)$, $g_{\mathrm{i}}(t)$ are the total excitatory and inhibitory conductances, and E_{e}, E_{i} are the respective synaptic reversal potentials.

The total conductances in the Eq (2) are given by

$$g_{\mathrm{e,i}}(t) = \sum_{t_k \in \mathcal{T}_{\mathrm{e,i}}} h_{\mathrm{e,i}}(t - t_k), \tag{3}$$

where $\mathcal{T}_{\mathrm{e,i}}$ are sets of presynaptic spike times modeled as realizations of stochastic point processes and $h_{\mathrm{e,i}}$ are filtering functions (i.e., time profiles of individual excitatory and inhibitory conductances).

Unless stated otherwise, we used the following parameters: $C = 1\,\mu\mathrm{F/cm^2}$, $g_{\mathrm{L}} = 0.045\,\mathrm{mS/cm^2}$, $E_{\mathrm{L}} = -80\,\mathrm{mV}$, $E_{\mathrm{e}} = 0\,\mathrm{mV}$, $E_{\mathrm{i}} = -75\,\mathrm{mV}$, $a = 3.4636 \times 10^{-4}\,\mathrm{cm^2}$ Destexhe et al. (2001).

Spike firing models

GLIF models

We consider three versions of the GLIF model:

1. The classical Leaky Integrate-and-Fire model (LIF),
2. LIF with SFA through ionic (after-hyperpolarization) currents (AHP-LIF),
3. LIF with SFA through dynamic threshold (DT-LIF).

The membrane potential of the LIF model obeys the Eq (1). Whenever $V > \theta$, where θ is a fixed threshold value, a spike is fired, and the membrane potential V is reset to a value V_r. For our simulations, we used $\theta = -55\,\mathrm{mV}$ and $V_r = E_{\mathrm{L}}$.

In the model with AHP current SFA (AHP-LIF), an additional hyperpolarizing conductance g_{AHP} is included in the model, and the membrane potential then obeys the equation Gerstner et al. (2019); Teeter et al. (2018); Benda et al. (2010):

$$C\frac{\mathrm{d}V}{\mathrm{d}t} = -g_{\mathrm{L}}(V - E_{\mathrm{L}}) - g_{\mathrm{AHP}}(t)(V - E_{\mathrm{K}}) + I_{\mathrm{e}}(t) + I_{\mathrm{i}}(t), \tag{4}$$

or equivalently

$$\tau_{\mathrm{ef}}^{\mathrm{AHP}}\frac{\mathrm{d}V}{\mathrm{d}t} = -(V - V_{\mathrm{ef}}^{\mathrm{AHP}}), \tag{5}$$

$$\tau_{\mathrm{ef}}^{\mathrm{AHP}}(t) = \frac{aC}{g_{\mathrm{e}}(t) + g_{\mathrm{i}}(t) + g_{\mathrm{AHP}}(t) + ag_{\mathrm{L}}}, \tag{6}$$

$$V_{\mathrm{ef}}^{\mathrm{AHP}}(t) = \frac{ag_{\mathrm{L}}E_{\mathrm{L}} + g_{\mathrm{e}}(t)E_{\mathrm{e}} + g_{\mathrm{i}}(t)E_{\mathrm{i}} + g_{\mathrm{AHP}}(t)E_{\mathrm{K}}}{g_{\mathrm{e}}(t) + g_{\mathrm{i}}(t) + g_{\mathrm{AHP}}(t) + ag_{\mathrm{L}}}. \tag{7}$$

where E_{K} is the potassium reversal potential, and g_{AHP} is the corresponding conductance which increases by Δg_{AHP} when a spike is fired and otherwise decays exponentially to zero with a time constant τ_{AHP}. $V_{\mathrm{ef}}^{\mathrm{AHP}}$ then represents the effective reversal potential. Note that for simplicity, we omitted the voltage dependence of g_{AHP}.

In the dynamic threshold model (DT-LIF), the threshold increases by $\Delta\theta$ after each spike and then decreases exponentially to θ_0 with time constant τ_θ.

The parameters for the GLIF models are specified in the Tab. 1.

Hodgkin-Huxley models

We adopted HH-type models developed by Destexhe et al. Destexhe and Paré (1999). The membrane potential obeys the equation:

$$\begin{aligned} C\frac{\mathrm{d}V}{\mathrm{d}t} = &- g_{\mathrm{L}}(V - E_{\mathrm{L}}) - g_{\mathrm{Na}}m^3h(V - E_{\mathrm{Na}}) - \\ &- g_{\mathrm{K}}n^4(V - E_{\mathrm{K}}) - g_{\mathrm{M}}p(V - E_{\mathrm{K}}) - \frac{1}{a}I_{\mathrm{syn}}, \end{aligned} \tag{8}$$

Table 1. GLIF models parameters

	LIF	AHP-LIF	DT-LIF
θ, θ_0 (mV)	-50	-50	-50
τ_{AHP} (ms)	-	100	-
Δg_{AHP} (nS)	0	5	0
E_{K} (mV)	-	-100	-
τ_θ (ms)	-	-	100
Δ_θ (mV)	0	0	4

where E_{Na} and E_{K} are the sodium and potassium reversal potentials, respectively; g_{Na}, g_{K}, and g_{M} are peak conductances; and m, h, n, and p are gating variables obeying the equation:

$$\frac{\mathrm{d}x}{\mathrm{d}t} = \alpha_x(V)(1-x) - \beta_x(V)x, \tag{9}$$

or equivalently:

$$\tau_x(V)\frac{\mathrm{d}x}{\mathrm{d}t} = -(x - x_\infty(V)), \tag{10}$$

where x is the respective gating variable, α_x and β_x are the activation and inactivation functions, respectively, and

$$\tau_x(V) = \frac{1}{\alpha_x(V) + \beta_x(V)}, \tag{11}$$

$$x_\infty(V) = \frac{\alpha_x(V)}{\alpha_x(V) + \beta_x(V)}. \tag{12}$$

The activation and inactivation functions are defined as follows:

$$\alpha_m = -0.32\frac{V - V_T - 13}{\exp(-(V - V_T - 13)/4) - 1}, \tag{13}$$

$$\beta_m = 0.28\frac{V - V_T - 40}{\exp((V - V_T - 40)/5) - 1}, \tag{14}$$

$$\alpha_h = A_h \exp(-(V - V_T - V_S - 17)/18), \tag{15}$$

$$\beta_h = \frac{4}{1 + \exp(-(V - V_T - V_S - 40)/5)}, \tag{16}$$

$$\alpha_n = -0.032\frac{V - V_T - 15}{\exp(-(V - V_T - 15)/5) - 1}, \tag{17}$$

$$\beta_n = 0.5\exp(-(V - V_T - 10)/40), \tag{18}$$

$$\alpha_p = 0.0001\frac{V + 30}{1 - \exp(-(V + 30)/9)}, \tag{19}$$

$$\beta_p = -0.0001\frac{V + 30}{1 - \exp((V + 30)/9)}. \tag{20}$$

We set $g_M = 0$ in both the HH-0 and HH-DT models, and $g_M > 0$ in the HH-M model. In order to achieve dynamic threshold behavior, we modified the activation and deactivation functions of the gating variable h, which is responsible for deactivating voltage-gated sodium channels after firing a spike, by changing the parameters A_h and V_S. For more details see the Supplementary Figure 1.

The parameters for the three HH-type models (without SFA (HH-0) / M-current SFA (HH-M) / dynamic threshold SFA (HH-DT)) are specified in the Tab 2.

Table 2. Parameters of the HH models

	HH-0	HH-M	HH-DT
$g_{\mathrm{Na}}\,(\mathrm{mS/cm^2})$	50	50	50
$g_{\mathrm{K}}\,(\mathrm{mS/cm^2})$	5	5	5
$g_{\mathrm{M}}\,(\mathrm{mS/cm^2})$	0	0.5	0
$E_{\mathrm{Na}}\,(\mathrm{mV})$	50	50	50
$E_{\mathrm{K}}\,(\mathrm{mV})$	-90	-90	-90
$V_T\,(\mathrm{mV})$	-58	-58	-58
$V_S\,(\mathrm{mV})$	-10	-10	14
$A_h\,(\mathrm{ms^{-1}})$	0.128	0.128	0.00128

Simulation details

For synapses, we used the exponential filtering function:

$$h_{\mathrm{e,i}}(t) = \begin{cases} A_{\mathrm{e,i}} \exp(-t/\tau_{\mathrm{e,i}}) & t \geq 0 \\ 0 & t < 0 \end{cases} \tag{21}$$

with $A_{\mathrm{e}} = A_{\mathrm{i}} = 0.0015\,\mu\mathrm{S}$, $\tau_{\mathrm{e}} = 3\,\mathrm{ms}$, $\tau_{\mathrm{e}} = 10\,\mathrm{ms}$. Such input parameters with intensities $\lambda_{\mathrm{e}} = 2.67\,\mathrm{Hz}$ and $\lambda_{\mathrm{i}} = 3.73\,\mathrm{kHz}$ provide an input with $g_{\mathrm{e}}^0 = 12\,\mathrm{nS}$, $\sigma_{\mathrm{e}} = 3\,\mathrm{nS}$, $g_{\mathrm{i}}^0 = 57\,\mathrm{nS}$, and $\sigma_{\mathrm{i}} = 6.6\,\mathrm{nS}$, as reported by Destexhe et al. Destexhe et al. (2001).

To ensure stability of the computation, we used the following update rule for the simulations:

$$V_{n+1} = (V_{\mathrm{ef}})_{n+1} + \left(V_n - (V_{\mathrm{ef}})_{n+1}\right) \exp\left(\frac{\Delta t}{\tau_{n+1}}\right), \tag{22}$$

$$V_{\mathrm{ef}} = \frac{\sum_{x \in X} g_x E_x}{\sum_{x \in X} g_x} \tag{23}$$

$$\tau_{\mathrm{ef}} = \frac{C}{\sum_{x \in X} g_x} \tag{24}$$

where X contains all the channel types (synaptic, leak, voltage-gated, and adaptive). The update rule for the synaptic conductances $g_{\mathrm{e,i}}$ was

$$(g_{\mathrm{e,i}})_{n+1} = (g_{\mathrm{e,i}})_n \exp\left(\frac{\Delta t}{\tau_{\mathrm{e,i}}}\right) + N_{\mathrm{e,i}} A_{\mathrm{e,i}}, \tag{25}$$

where $(N_{\mathrm{e,i}})$ is a Poisson random variable with mean $\lambda_{\mathrm{e,i}} \Delta t$.

We used the step size $\Delta t = 0.025\,\mathrm{ms}$.

Evaluating firing rate regularity

A classical measure of the firing regularity of steady spike trains is the coefficient of variation ($\mathrm{C_V}$), defined as follows (e.g., Softky and Koch (1993)):

$$\mathrm{C_V} = \frac{\sigma_{\mathrm{ISI}}}{\mu_{\mathrm{ISI}}}, \tag{26}$$

where μ_{ISI} and σ_{ISI} are the mean and standard deviation of the interspike intervals (ISIs), respectively. Lower $\mathrm{C_V}$ indicates higher firing regularity.

To achieve an accurate estimate of the $\mathrm{C_V}$, we estimated the statistics from approximately 160,000 ISIs for each data point. For a Poisson process ($\mathrm{C_V} = 1$) with this number of ISIs, the estimate of $\mathrm{C_V}$ falls within $[0.995, 1.005]$ in over 95% of cases. Note that the estimation was more accurate for lower values of $\mathrm{C_V}$.

Results

Membrane potential is stabilized with increased input fluctuations

Since the inputs to a neuron consist of pooled spike trains from a large number of presynaptic neurons, according to the Palm-Khintchine theorem Heyman and Sobel (2004), it is sufficient to approximate the excitatory and inhibitory inputs by Poisson processes with intensities λ_e and λ_i, respectively Tuckwell (1988). It has been demonstrated that this condition is not necessarily satisfied for neurons *in vivo* Lindner (2006). However, as we discuss below, this should not affect the conclusions of our analysis. According to Campbell's theorem Kingman (1993), it then holds for the mean $g^0_{\mathrm{e,i}}$ and variance $\sigma^2_{\mathrm{e,i}}$ of the input

$$g^0_{\mathrm{e,i}} = \lambda_{\mathrm{e,i}} \int_0^\infty h_{\mathrm{e,i}}(t)\,\mathrm{d}t, \tag{27}$$

$$\sigma^2_{\mathrm{e,i}} = \lambda_{\mathrm{e,i}} \int_0^\infty h^2_{\mathrm{e,i}}(t)\,\mathrm{d}t. \tag{28}$$

Therefore $\frac{\sigma_{\mathrm{e,i}}}{g^0_{\mathrm{e,i}}} = O\left(\frac{1}{\sqrt{\lambda_{\mathrm{e,i}}}}\right)$ (a well-known property of the Poisson shot noise Tuckwell (1988)).

For the purposes of our analysis, we consider the voltage equations of a membrane without any spike-generating mechanism as:

$$\tau_{\mathrm{ef}}(g_\mathrm{e}(t), g_\mathrm{i}(t))\frac{\mathrm{d}V}{\mathrm{d}t} = -V - V_{\mathrm{ef}}(g_\mathrm{e}(t), g_\mathrm{i}(t)), \tag{29}$$

$$\tau_{\mathrm{ef}}(g_\mathrm{e}, g_\mathrm{i}) = \frac{aC}{ag_\mathrm{L} + g_\mathrm{e} + g_\mathrm{i}}, \tag{30}$$

$$V_{\mathrm{ef}}(g_\mathrm{e}, g_\mathrm{i}) = \frac{ag_\mathrm{L}E_\mathrm{L} + g_\mathrm{e}E_\mathrm{e} + g_\mathrm{i}E_\mathrm{i}}{g_\mathrm{L} + g_\mathrm{e} + g_\mathrm{i}}. \tag{31}$$

For large inputs $\frac{\sigma_{\mathrm{e,i}}}{g^0_{\mathrm{e,i}}} \ll 1$, we can linearize the Eq (31):

$$V_{\mathrm{ef}}(g_\mathrm{e}, g_\mathrm{i}) \doteq E_0 \left(1 - \frac{g^\mathrm{F}_\mathrm{e} + g^\mathrm{F}_\mathrm{i}}{ag_\mathrm{L} + g^0_\mathrm{e} + g^0_\mathrm{i}}\right) + \frac{g^\mathrm{F}_\mathrm{e}E_\mathrm{e} + g^\mathrm{F}_\mathrm{i}E_\mathrm{i}}{ag_\mathrm{L} + g^0_\mathrm{e} + g^0_\mathrm{i}}, \tag{32}$$

where $E_0 = V_{\mathrm{ef}}(g^0_\mathrm{e}, g^0_\mathrm{i})$ and $g^\mathrm{F}_{\mathrm{e,i}} = g_{\mathrm{e,i}} - g^0_{\mathrm{e,i}}$. Since the fluctuating terms in Eq (32) disappear with growing input, evaluating the limits with a fixed inhibition-to-excitation ratio $c = \frac{g^0_\mathrm{i}}{g^0_\mathrm{e}}$ leads to:

$$\lim_{\lambda_\mathrm{e},\lambda_\mathrm{i}\to\infty} \mathrm{E}\left[\mathrm{V_{ef}}\right] = V_\infty(c) \equiv \frac{E_\mathrm{e} + cE_\mathrm{i}}{1+c}, \tag{33}$$

$$\lim_{\lambda_\mathrm{e},\lambda_\mathrm{i}\to\infty} \mathrm{Var}\left[\mathrm{V_{ef}}\right] = 0. \tag{34}$$

$\mathrm{Var}\left[\mathrm{V_{ef}}\right]$ is an upper bound on the variance of V (it follows from the Eq (29) that the membrane potential V is essentially a "low-pass filtered" effective reversal potential V_{ef}). Therefore, it also holds that $\lim_{\lambda_\mathrm{e},\lambda_\mathrm{i}\to\infty} \langle \mathrm{V} \rangle = V_\infty(c) \equiv \frac{E_\mathrm{e}+cE_\mathrm{i}}{1+c}$ and $\lim_{\lambda_\mathrm{e},\lambda_\mathrm{i}\to\infty} \sigma_\mathrm{V} = 0$. This can also be observed from the perturbative approach suggested in Amit and Tsodyks (1992) and further developed in Richardson (2004); Richardson and Gerstner (2005). Therefore, any membrane potential between the reversal potentials E_i, E_e can be asymptotically reached with zero variance, despite the variance of the total synaptic

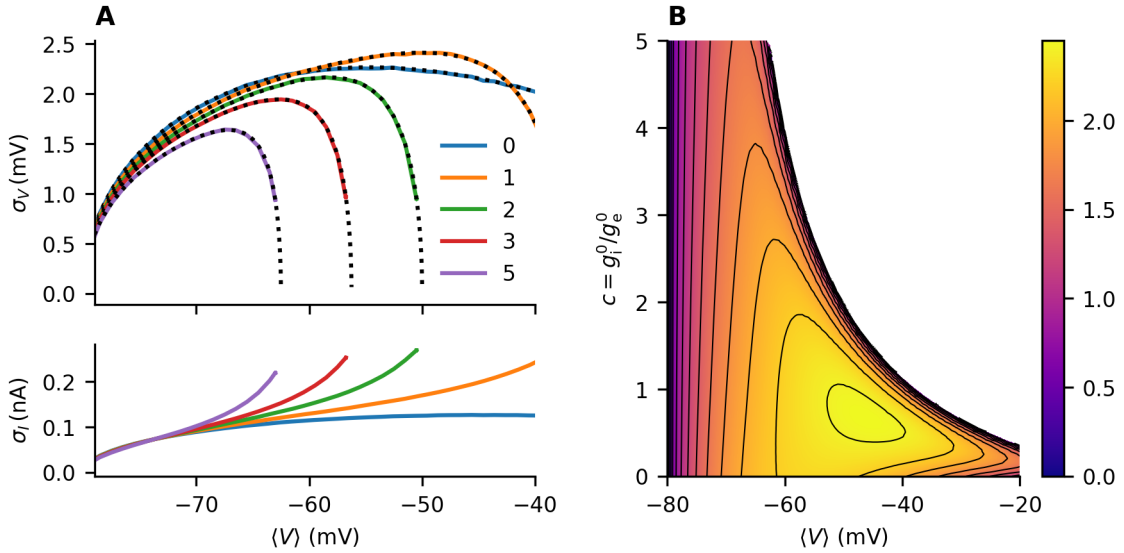

Fig 2. Stabilization of the membrane potential. A, top panel: Membrane potential fluctuations as a function of the mean membrane potential for different values of c. The full lines represent data obtained from simulations with different excitatory input intensities λ_e. The dotted lines represent the effective time-constant approximation (ETA, Appendix A). Bottom panel: The standard deviation σ_I of the total synaptic current $I_{syn} = I_e + I_i$. Note that σ_V decreases with growing c even though σ_I increases. B: Overview of σ_V (color) for all achievable $\langle V \rangle$ (x-axis) at given c (y-axis). $C = 1\,\mu F/cm^2$ and $g_L = 0.045\,mS/cm^2$, approximation of σ_V computed from the ETA. Heatmaps for different values of g_L are provided in the Supplementary Figure 2 and for different values of A_i (Eq. (21)) in the Supplementary Figure 3.

current $I_{syn} = I_e + I_i$ increasing. Note that the Poisson condition can be relaxed, since it is sufficient for this result that $\frac{\sigma_{e,i}}{g^0_{e,i}} \to 0$.

Let $\sigma_V(\langle V \rangle; c)$ be the function specifying the standard deviation of the membrane potential with mean $\langle V \rangle$, parametrized by c. It is a continuous function, with $\sigma_V(E_L; c) = \sigma_V(V_\infty(c); c) = 0$, otherwise $\sigma_V(\langle V \rangle; c) > 0$. Note that lower c leads to higher $V_\infty(c)$. Therefore, given $c_1 > c_2$, there has to be an interval close to $V_\infty(c_1)$ where c_2 results in lower membrane fluctuations. Moreover, simulations indicate that this holds, even in non-limit regimes (Fig 2A, top panel). This result is rather counter-intuitive, since with an increase in c, it is necessary to increase both λ_e and λ_i (if $\langle V \rangle > E_i$), and thus simultaneously increase synaptic current fluctuations (Fig 2A, bottom panel) in order to keep the membrane potential constant. With our choice of parameters, lower c may also result in a slight decrease in membrane potential fluctuations. This is mainly due to the membrane time constant $\tau = \frac{C}{g_L} \doteq 22\,ms$. The shorter the time constant, the closer V follows V_{ef}, and the smaller the region in which decreasing c leads to lower membrane potential variability (see the Supplementary Figure 2).

Effects on firing regularity

The regularity of spike-firing is important for information transmission between neurons Toyoizumi et al. (2006); Kostal et al. (2007); de Ruyter van Steveninck (1997); Strong et al. (1998). In the previous section, we demonstrated that if appropriate synaptic drive is used, higher inhibitory input rates (or equivalently higher

inhibition-to-excitation ratio c) lead to lower membrane potential fluctuations. In this section, we focus on the effects of inhibition on post-synaptic firing regularity, particularly on the regularity of a post-synaptic spike train with a fixed frequency evoked by different stimuli with different levels of inhibition.

Generalized Leaky Integrate-and-Fire models

For our analysis, it is essential to distinguish two different input regimes: 1. Sub-threshold regime: $E_0 \leq \theta$ and 2. Supra-threshold regime: $E_0 > \theta$, where θ is the firing threshold.

In the sub-threshold regime, firing activity is driven by fluctuations in the membrane potential. Therefore, increasing the input rates λ_e, λ_i and simultaneously keeping E_0 constant leads to a decrease in firing rate due to suppressed membrane potential fluctuations (note that an analogous effect was described in the Hodgkin-Huxley model Tiesinga et al. (2000)). In order to maintain the post-synaptic firing rate (PSFR) constant while increasing the input rates, it is necessary to compensate for the decrease in fluctuations by increasing E_0. Therefore, it is not intuitively clear whether the decrease in membrane potential fluctuations will lead to an increase in firing regularity.

In the supra-threshold regime, the firing activity is given by the driving force on the membrane potential $(V - V_{\mathrm{ef}})/\tau_{\mathrm{ef}}$. Fluctuations in the interspike intervals are then given mostly by the fluctuations of V_{ef}. However, lower fluctuations of V_{ef} are associated with lower τ_{ef} and it is necessary to decrease E_0, if one wishes to decrease the fluctuations of V_{ef} and keep the firing rate constant at the same time. Intuitively, the fluctuations of V_{ef} will impact the firing regularity more, if the difference $(V - V_{\mathrm{ef}})$ is lower. Therefore it is again unclear how the increased synaptic fluctuations affect the firing regularity.

In general, we observe that in the suprathreshold regime, the $\mathrm{C_V}$ of ISIs decreases with growing PSFR (Fig 3A,D). Moreover, as we show in the Appendix B:

$$\lim_{\lambda_e, \lambda_i \to \infty} \mathrm{C_V} = 0 \tag{35}$$

However, if the firing rate is held constant, the $\mathrm{C_V}$ increases with growing c. Therefore, an increase in the inhibition-to-excitation ratio decreases firing regularity, despite the stabilizing effect on membrane potential.

With high values of c, the $\mathrm{C_V}$ grows locally with increasing firing rate. This is due to the fact that as E_0 is very close to the threshold and the membrane time constant (Eq (30)) is very low, the neuron fires very rapidly (bursts) when V_{ef} (Eq (29)) exceeds the threshold but is otherwise silent.

For the AHP-LIF model, no improvements are observed in the firing regularity with increasing c (Fig 3B,E). At low firing frequencies, the $\mathrm{C_V}$ of the AHP-LIF model is generally lower than that in the classical LIF model. This is to be expected given the introduction of negative correlations in subsequent ISIs Chacron et al. (2004); Lindner et al. (2005); Farkhooi et al. (2011). However, at higher firing rates, higher c actually leads to a higher $\mathrm{C_V}$ than that observed in the LIF model. This is due to the fact that in regimes where V_{ef} is always above the threshold in the LIF model, the hyperpolarizing M-current drives the time-dependent effective reversal potential $V_{\mathrm{ef}}^{\mathrm{AHP}}$ (Eq (7)) closer to the threshold. This leads to bursting, similar to that observed in the LIF model with E_0 near threshold. This is illustrated in more detail in the Appendix B, where we also demonstrate that if $V_\infty(c) > V_{\mathrm{thr}}$, then $\mathrm{C_V} \to 0$, similar to the LIF model.

In the DT-LIF model, with the limit of infinite conductances, the membrane potential will reach $V_\infty(c)$ immediately after a spike is fired. If $V_\infty(c) \geq \theta_0$, the neuron will fire with exact ISIs

$$T = \tau_\theta \log\left(1 + \frac{\Delta\theta}{V_\infty(c) - \theta_0}\right). \tag{36}$$

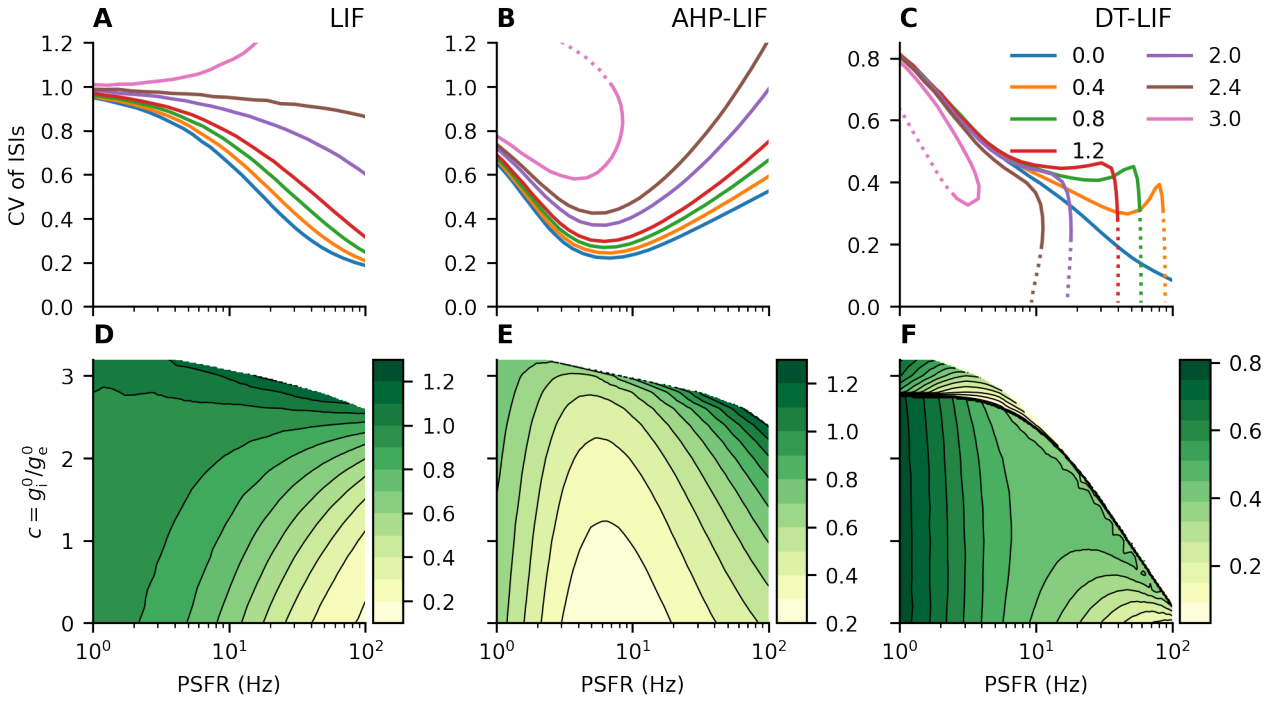

Fig 3. The effect of membrane potential stabilization on spiking regularity in the GLIF models. A-C: Dependence of the C_V of ISIs on the post-synaptic firing rate for different values of c (color-coded). The dotted parts of the curves represent the sections where $\lambda_e > 100\,\text{kHz}$. In the LIF and AHP-LIF model, higher c universally leads to higher C_V. In contrast, in the DT-LIF model, higher c can lead to more regular spike trains, especially if the input intensities are high. If $V_\infty(c) \leq \theta$ (or θ_0 for the DT-LIF model, i.e., $c \geq 2.75$), the firing rate will eventually drop to 0. D-E: Contour plots with color-coded C_V, c on the y-axis. If more than one input can produce the same PSFR with the same c, the lowest possible value of C_V is color-coded, resulting in the discontinuity in F. The data points were obtained from simulations with different input intensities λ_e, λ_i.

Therefore, any firing rate lower than $\left(\tau_\theta \log\left(1 + \frac{\Delta\theta}{V_\infty(c)-\theta_0}\right)\right)^{-1}$ can be asymptotically reached with $C_V = 0$. Thus, firing regularity can always be improved by increasing c, similar to the case of membrane potential variability. However, very high input intensities are necessary to observe such regularization. Further, with biologically realistic input intensities (excitatory input intensity up to 100 kHz), increased regularity with higher c is observed only for post-synaptic firing rates below approximately 20 Hz (Fig 3C,F).

Note that the structure of the contour plot in Fig 3F is very similar to that in Fig 2B, i.e., approximately for $c > 1$, an increase in c stabilizes the membrane potential and increases the spike-firing regularity. The opposite is observed for $c < 1$. Moreover, the structure of the heatmap changes accordingly if the membrane time constant is decreased by increasing g_L (Supplementary Figure 2) or if the inhibitory synaptic connections are strengthened (Supplementary Figure 3).

Hodgkin-Huxley models

Generally, the behavior of the HH models is very similar to that of their GLIF counterparts (Fig 4). Similar "subthreshold" behavior is apparent - for high values of c, the firing rate starts dropping to zero with increasing input intensity.

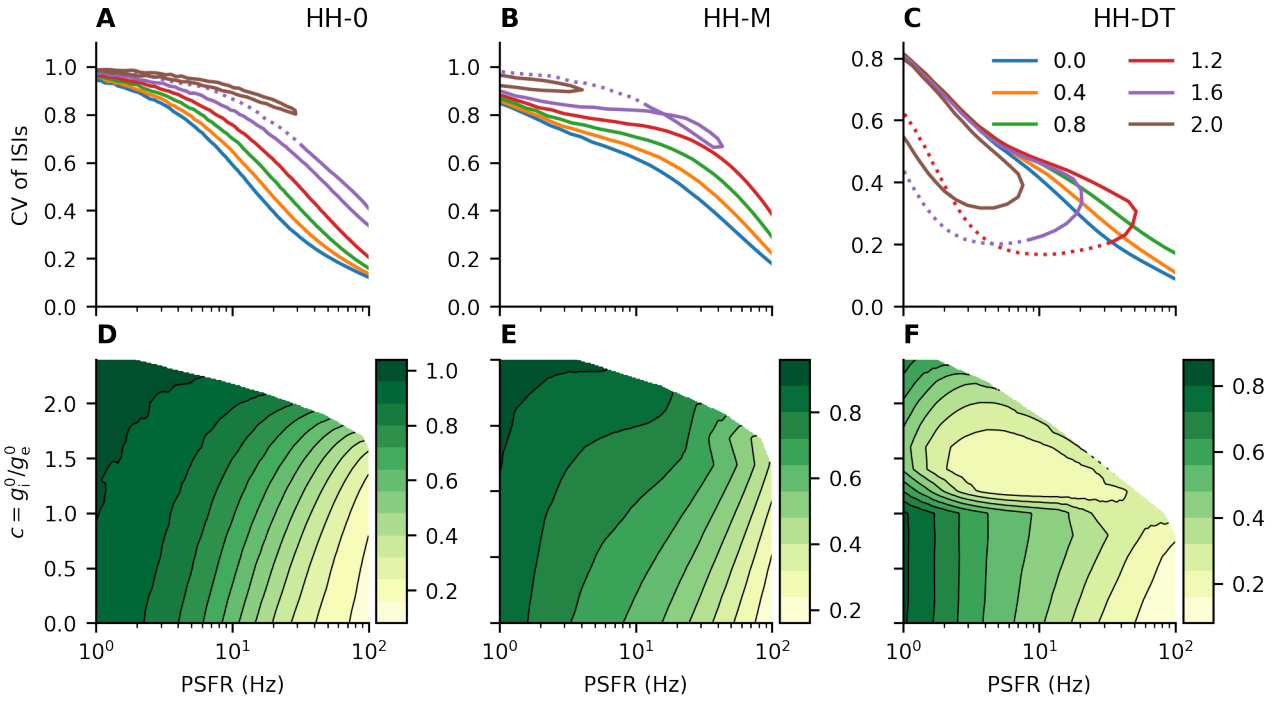

Fig 4. The effect of membrane potential stabilization on spiking regularity in the Hodgkin-Huxley models. A-C: Dependence of the C_V of ISIs on the firing rate for different values of c (color-coded). The dotted parts of the curves represent the sections where $\lambda_e > 100\,\text{kHz}$. In the subthreshold regimes, the output rate reaches its maximum and then starts dropping to zero. For the HH-DT model (C), the C_V decreases at this point, whereas for the HH-0 (A) and HH-M (B) models, no clear improvement is observed. D-F: Contour plots with color-coded C_V, c on the y-axis. If more than one input can produce the same PSFR with the same c, the lowest possible value of C_V is color-coded. Note that there is no discontinuity in F, unlike in Fig. 3F. The transition to the more regular states with growing c is continuous, as is illustrated in Supplementary Figure 4. The data points were obtained from simulations with different input intensities λ_e, λ_i.

Similarly to the GLIF models, no improvements are observed with growing c for the HH-0 (Fig 4A,D) and HH-M (Fig 4B,E) models. For the HH-DT model, lower C_V of ISIs can always be achieved in the subthreshold regime, when the rate starts dropping back to zero due to the strong input (Fig 4C,F).

Increasing c in the HH-DT subthreshold regime decreases the C_V. However, it is important to note that increased c does not imply stronger inhibitory input in this case. In fact, increasing the inhibitory input rate λ_i is almost always beneficial for the spike-firing regularity in the HH-DT model, and this is also the case in the DT-LIF model (Fig 5). From this, we conclude that if a neuron exhibits a dynamic threshold, a stimulus will produce a more regular spike train if it elicits an increase in inhibitory input simultaneously with excitatory input.

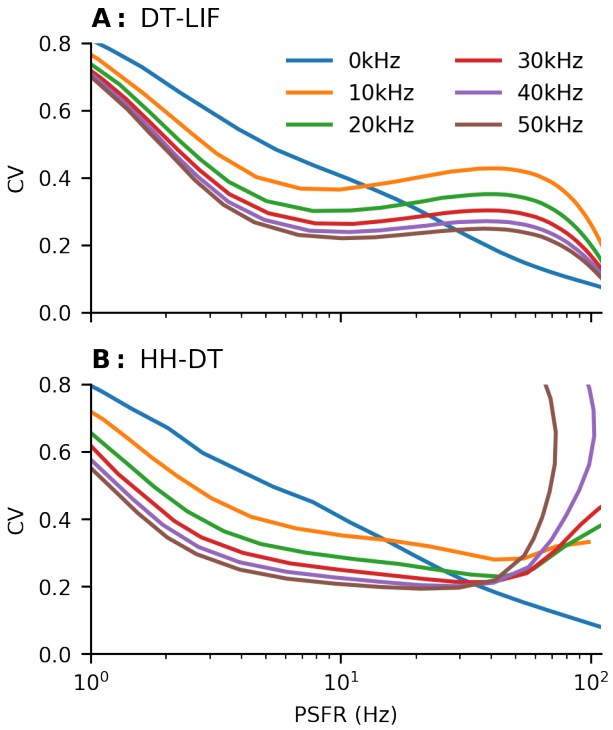

Fig 5. Constant inhibition trajectories for the dynamic threshold models. In both the DT-LIF (A) and HH-DT (B) models, increasing the pre-synaptic inhibitory firing rate (color) is beneficial for the firing regularity (measured by C_V, y-axis) for a wide range of PSFRs (x-axis).

Discussion

Simplified input models

Absence of reversal potentials

If the reversal potentials are not taken into account, the synaptic currents are given by

$$I_{\mathrm{e,i}}(t) = \sum_{t_k \in \mathcal{T}_{\mathrm{e,i}}} H_{\mathrm{e,i}}(t - t_k), \tag{37}$$

where H is again a filtering function. If the two currents are uncorrelated, they will add up to an input current with mean value I_0 and standard deviation σ_I. If the diffusion approximation is employed (the current is modeled as an Ornstein-Uhlenbeck process with a time constant τ_I), the mean and standard deviation of the membrane potential are Lindner and Longtin (2006):

$$\langle V \rangle_I = E_{\mathrm{L}} + \frac{I_0}{g_{\mathrm{L}}}, \tag{38}$$

$$\sigma^2_{V,I} = \sigma^2_I \frac{\tau_I}{a^2 g_{\mathrm{L}}(C + g_{\mathrm{L}}\tau_I)}. \tag{39}$$

In the absence of synaptic reversal potentials, the variance diverges with growing input, and increasing the synaptic current fluctuations by increasing λ_{e} and λ_{i} clearly increases the membrane potential fluctuations, in contrast to the model with synaptic reversal potential.

Absence of synaptic filtering

If synaptic filtering is neglected, $h_{\mathrm{e,i}}$ become δ-functions:

$$h_{\mathrm{e,i}}(t) = Ca_{\mathrm{e,i}}\delta(t), \tag{40}$$

where C is the membrane capacitance, and $a_{\mathrm{e,i}}$ governs the jump in the membrane potential ΔV triggered by a single pulse:

$$\Delta V = (E_{\mathrm{e,i}} - V)(1 - e^{-a_{\mathrm{e,i}}}). \tag{41}$$

This model was studied extensively, e.g., in Lánská et al. (1994); Richardson (2004); Richardson and Gerstner (2006). In Richardson (2004); Richardson and Gerstner (2006), the formulas for the mean membrane potential and its standard deviation are calculated in the diffusion approximation:

$$\langle V\rangle_W = \tau(E_{\mathrm{L}}\tau_L^{-1} + E_{\mathrm{e}}\lambda_{\mathrm{e}}b_{\mathrm{e}} + E_{\mathrm{i}}\lambda_{\mathrm{i}}b_{\mathrm{i}}) \tag{42}$$

$$\sigma^2_{V,W} = \frac{\tau_L}{2}\frac{\lambda_{\mathrm{e}}b_{\mathrm{e}}^2(\langle V\rangle - E_{\mathrm{e}})^2 + \lambda_{\mathrm{i}}b_{\mathrm{i}}^2(\langle V\rangle - E_{\mathrm{i}})^2}{1 + \tau_L\lambda_{\mathrm{e}}b_{\mathrm{e}}(1 - b_{\mathrm{e}}/2) + \tau_L\lambda_{\mathrm{i}}b_{\mathrm{i}}(1 - b_{\mathrm{i}}/2)}, \tag{43}$$

where

$$\tau^{-1} = \tau_L^{-1} + \lambda_{\mathrm{e}}b_{\mathrm{e}} + \lambda_{\mathrm{i}}b_{\mathrm{i}} \tag{44}$$

$$b_{\mathrm{e,i}} = 1 - e^{-a_{\mathrm{e,i}}}. \tag{45}$$

Richardson Richardson (2004) reported that a higher inhibition-to-excitation ratio may lead to a decrease in the membrane potential fluctuations for strongly hyperpolarized membranes. However, the effect of inhibition reverses as the membrane potential depolarizes (Fig 6). Furthermore, the membrane potential does not stabilize within the limit of infinite firing rates. Therefore, the time correlation of synaptic input introduced by synaptic filtering is necessary to observe the shunting effect of inhibitory synapses.

Regular firing in multicompartmental models

The models analyzed in this work are all single-compartmental models, i.e., models in which the charge is distributed infinitely fast across the cell, and the membrane potential is therefore the same everywhere. In reality, neurons receive input predominantly at dendrites, and the spikes are initiated in the soma. To account for this fact, multicompartmental models are typically employed. The soma and dendritic parts can be modeled as two separate compartments (for simplicity, as two identical cylinders) connected through a coupling conductance g_c :

$$C\frac{\mathrm{d}V_S}{\mathrm{d}t} = -g_{\mathrm{L}}(V_S - E_{\mathrm{L}}) - g_c(V_S - V_D) \tag{46}$$

$$\begin{aligned} C\frac{\mathrm{d}V_D}{\mathrm{d}t} = &-g_{\mathrm{L}}(V_D - E_{\mathrm{L}}) - g_c(V_D - V_S) - \\ &- \frac{1}{a_D}(g_{\mathrm{e}}(V_D - E_{\mathrm{e}}) + g_{\mathrm{i}}(V_D - E_{\mathrm{i}})) \end{aligned} \tag{47}$$

where V_S and V_D are the membrane potentials of the somatic and dendritic compartments, respectively; a_D is the dendritic area; and V_S is reset to V_r when the threshold θ is reached.

In the hypothetical case of infinite input rates, $V_D = V_\infty(c)$ and V_S periodically decay to $V_S^0 = \frac{g_{\mathrm{L}}E_{\mathrm{L}} + g_cV_D}{g_{\mathrm{L}} + g_c}$ with a time constant $\tau_2 = \frac{g_{\mathrm{L}} + g_c}{a_SC}$, resulting in regular ISIs

$$T = -\tau_2 \log\left(1 + \frac{V_r - \theta}{V_S^0 - V_r}\right). \tag{48}$$

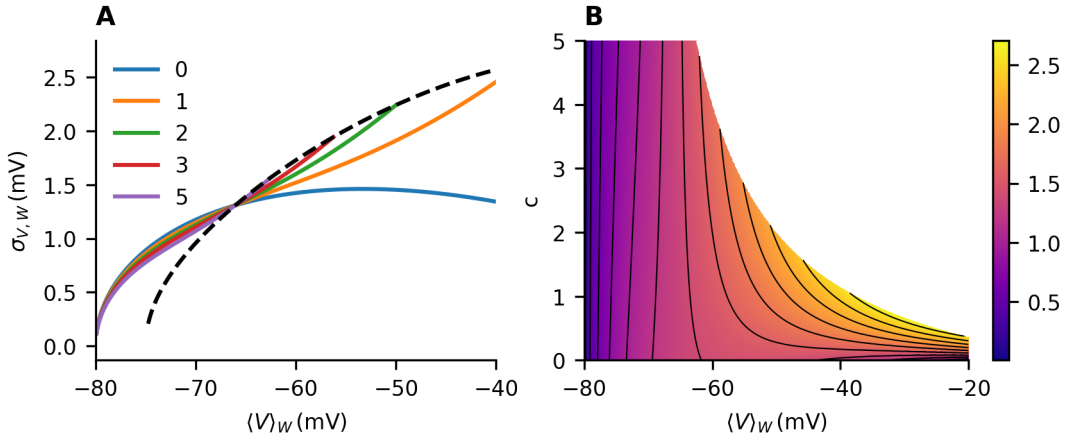

Fig 6. Membrane potential with conductance input without synaptic filtering. A: Membrane potential fluctuations as a function of the mean membrane potential for different values of $c = \frac{\lambda_i b_i}{\lambda_e b_e}$ (color-coded), as calculated from the Eqs (42,43). The dashed line represents the limit $\lim_{\lambda_e, \lambda_i \to \infty} \sigma_{V,W}(\langle V \rangle_W)$. The membrane potential is not stabilized at infinite inputs. Above certain depolarizations, inhibition increases membrane potential fluctuations, contrary to the case of conductance input with synaptic filtering. B: Heatmap with color-coded standard deviation of the membrane potential. Parameters used were $b_e = 0.0045$, $b_i = 0.0150$.

Therefore, it is possible to reach a wide range of firing rates with $C_V = 0$ and decrease C_V while maintaining a constant mean firing rate by increasing c, similar to the case of LIF with a dynamic threshold.

The coupling conductance can be calculated as $g_c = \frac{d}{4R_a l^2}$ Sterratt et al. (2011), where d is the diameter of the cylinder, l is the length, and $R_a = 150\,\Omega\,\mathrm{cm}$ is the longitudinal resistance. If we consider that the original area of the neuron approximately $3.5 \times 10^{-4}\,\mathrm{cm}^2$ is split between the two cylinders and we set $d = l$, we obtain $\tau_2 \approx 4.5\,\mu\mathrm{s}$. It is therefore unlikely that firing rate regularization with biologically relevant post-synaptic firing rates would be observed with biologically plausible inputs.

Conclusion

We demonstrate that a higher inhibition-to-excitation ratio and subsequently higher synaptic current fluctuations lead to a more stable membrane potential if the stimulation is modeled as time-filtered activation of synaptic conductances with reversal potentials. Our analysis thus provides a theoretical context for the experimental observations of Monier et al. (2003). Moreover, our results highlight the importance of incorporating synaptic filtering and reversal potentials into neuronal simulations. The qualitative differences between neurons stimulated with white noise and colored noise current have been reported in the literature Brunel et al. (2001); Fourcaud and Brunel (2002); Moreno-Bote and Parga (2004). However, we demonstrate that realistic synaptic filtering with reversal potentials is responsible for a novel fluctuation-stabilization mechanism which cannot be observed in simplified models.

We analyzed the impact of membrane potential stabilization on spike-firing regularity in GLIF models and HH-type models. We compared the effects of an increased inhibition-to-excitation ratio on two different mechanisms of spike-firing adaptation: adaptation by a hyperpolarizing ionic current (AHP and M-current adaptation) and adaptation implemented as a dynamic firing threshold. Both SFA

mechanisms are biologically relevant and are useful in neuronal modeling Teeter et al. (2018); Benda et al. (2010); Chacron et al. (2000); Kobayashi et al. (2009); Kobayashi and Kitano (2016); Levakova et al. (2019); Gerstner and Naud (2009); Kobayashi et al. (2019). We demonstrated that while an increase in inhibition leads to less regular spike trains in the ionic current adaptation models and models without any spike-firing adaptation, it may enhance the firing regularity in the dynamic threshold models. We observed this effect in both the GLIF models and HH-type models.

High presynaptic inhibitory activity is typical of cortical neurons. In the so called high-conductance state, total inhibitory conductance can be several-fold larger than total excitatory conductance Destexhe et al. (2003). Our findings therefore provide a novel view of the importance of the high-conductance state and inhibitory synapses in biological neural networks.

Acknowledgements

This work was supported by Charles University, project GA UK No. 1042120 and the Czech Science Foundation project 20-10251S.

A Effective time constant approximation

The Eqs (1,2) can be rewritten as:

$$Ca\frac{\mathrm{d}V}{\mathrm{d}t} = -g_0(V-E_0) - g_\mathrm{e}^F(V-E_\mathrm{e}) - g_\mathrm{i}^F(V-E_\mathrm{i}), \tag{49}$$

where $g_0 = ag_\mathrm{L} + g_\mathrm{e}^0 + g_\mathrm{i}^0$, $g_{\mathrm{e,i}}^0$, and $g_{\mathrm{e,i}}^F$ are the mean and fluctuating parts of the conductance input. The input can then be separated into its additive and multiplicative parts:

$$g_\mathrm{e}^F(V-E_\mathrm{e}) = g_\mathrm{e}^F(E_0-E_\mathrm{e}) + g_\mathrm{e}^F(V-E_0). \tag{50}$$

By neglecting the multiplicative part $g_\mathrm{e}^F(V-E_0)$, we obtain the effective time constant approximation (ETA). In the diffusion approximation, the mean and standard deviation of the membrane potential are Richardson (2004); Richardson and Gerstner (2005):

$$\langle V\rangle_\mathrm{ETA} = E_0, \tag{51}$$

$$\begin{aligned}\sigma_{V,\mathrm{ETA}}^2 = &\left(\frac{\sigma_\mathrm{e}}{g_0}\right)^2 (E_\mathrm{e}-E_0)\frac{\tau_\mathrm{e}}{\tau_\mathrm{e}+\tau_0} + \\ &+ \left(\frac{\sigma_\mathrm{i}}{g_0}\right)^2 (E_\mathrm{i}-E_0)\frac{\tau_\mathrm{i}}{\tau_\mathrm{i}+\tau_0},\end{aligned} \tag{52}$$

where $\tau_0 = \frac{aC}{g_0}$ is the effective time constant, and $\sigma_{\mathrm{e,i}}$ are the standard deviations of the excitatory and inhibitory inputs.

B Limit cases of LIF and AHP-LIF models

High conductance limit of the LIF model

If $V_\infty(c) > \theta$, in the case of high input intensities, V_ef is permanently above the threshold, and the effective membrane time constant $\tau(g_\mathrm{e}, g_\mathrm{i})$ approaches zero. Therefore, in the absence of a refractory period, the firing rate $f = \frac{1}{\mu_\mathrm{ISI}}$ diverges (μ_ISI is the average ISI). If the average postsynaptic ISI is much shorter than synaptic

timescales, we can assume that the input remains effectively constant during the entire ISI (corresponding to the adiabatic approximation (Moreno-Bote and Parga, 2004, 2005, 2006; Moreno-Bote et al., 2008; Moreno-Bote and Parga, 2010)). The length of the ISI is then determined solely by the immediate values of the excitatory and inhibitory conductances

$$T(g_\mathrm{e}, g_\mathrm{i}) = -\frac{aC}{ag_\mathrm{L} + g_\mathrm{e} + g_\mathrm{i}} \log\left(\frac{\theta - V_\mathrm{ef}(g_\mathrm{e}, g_\mathrm{i})}{V_r - V_\mathrm{ef}(g_\mathrm{e}, g_\mathrm{i})}\right). \tag{53}$$

Assuming independence of the inputs, the mean ISI and its standard deviation can then be approximated as

$$\mu_\mathrm{ISI} = -\frac{aC}{g_\mathrm{tot}} \log\left(\frac{\theta - E_0}{V_r - E_0}\right), \tag{54}$$

$$\begin{aligned}\sigma^2_\mathrm{ISI} &= \left(\frac{\partial T}{\partial g_\mathrm{e}}\right)^2\Big|_{g_\mathrm{e}=g_\mathrm{e}^0}\sigma^2_\mathrm{e} + \left(\frac{\partial T}{\partial g_\mathrm{i}}\right)^2\Big|_{g_\mathrm{i}=g_\mathrm{i}^0}\sigma^2_\mathrm{i} = \\ &= (aC)^2 g_\mathrm{e}^0 \left[\frac{A_\mathrm{e}\left((E_\mathrm{e}-E_0)(\theta-V_r)+\alpha\right)}{g^4_\mathrm{tot}(\theta-E_0)^2(E_0-V_r)^2} + \right. \\ &\left. + \frac{cA_\mathrm{i}\left((E_\mathrm{i}-E_0)(\theta-V_r)+\alpha\right)}{g^4_\mathrm{tot}(\theta-E_0)^2(E_0-V_r)^2}\right],\end{aligned} \tag{55}$$

$$\alpha = (\theta - E_0)(E_0 - V_r)\log\frac{E_0-\theta}{E_0-V_r},$$

where $g_\mathrm{tot} = ag_\mathrm{L} + g_\mathrm{e}^0 + g_\mathrm{i}^0$ (for validity of the approximation see Fig. 7). Therefore, $\sigma_\mathrm{ISI}/\mu_\mathrm{ISI} = O\left(\left(g_\mathrm{e}^0\right)^{-1/2}\right)$. We conclude that with growing input intensity, the firing rate diverges and $\mathrm{C_V} \to 0$.

High conductance limit of the AHP-LIF model

Effective reversal potential

We follow the assumption that the fluctuations in $V_\mathrm{ef}(g_\mathrm{e}, g_\mathrm{i})$ are very small and therefore $V_\mathrm{ef}^\mathrm{AHP}$ (Eq. (7)) is permanently above the threshold θ. With the ISI $\mu_\mathrm{ISI}^\mathrm{AHP} \ll \tau_\mathrm{AHP}$, $g_\mathrm{AHP}(t) \approx \langle g_\mathrm{AHP}(t)\rangle = \frac{\Delta g \tau_\mathrm{AHP}}{\mu_\mathrm{ISI}^\mathrm{AHP}}$. Analogously to the Eq. (54)), we can use the following implicit equation to approximate the mean ISI:

$$\mu_\mathrm{ISI}^\mathrm{AHP} = -\frac{aC}{g_\mathrm{tot}^\mathrm{AHP}} \log\frac{\theta - E_0^\mathrm{AHP}}{V_r - E_0^\mathrm{AHP}},, \tag{56}$$

where

$$g_\mathrm{tot}^\mathrm{AHP} = ag_\mathrm{L} + g_\mathrm{e}^0 + g_\mathrm{i}^0 + \frac{\Delta g \tau_\mathrm{AHP}}{\mu_\mathrm{ISI}^\mathrm{AHP}}, \tag{57}$$

$$E_0^\mathrm{AHP} = \frac{ag_\mathrm{L}E_\mathrm{L} + g_\mathrm{e}^0 E_\mathrm{e} + g_\mathrm{i}^0 E_\mathrm{i} + \frac{\Delta g \tau_\mathrm{AHP}}{\mu_\mathrm{ISI}^\mathrm{AHP}} E_\mathrm{K}}{g_\mathrm{tot}^\mathrm{AHP}}. \tag{58}$$

We continue to evaluate the high-conductance limit of E_0^AHP:

$$\begin{aligned}&\lim_{g_\mathrm{e}^0\to+\infty} E_0^\mathrm{AHP} = V_\infty^\mathrm{AHP}(c) \equiv \\ &\equiv \lim_{g_\mathrm{e}^0\to+\infty} \frac{\frac{ag_\mathrm{L}}{g_\mathrm{e}^0}E_\mathrm{L} + E_\mathrm{e} + cE_\mathrm{i} + \frac{\tau_\mathrm{AHP}}{g_\mathrm{e}^0\mu_\mathrm{ISI}^\mathrm{AHP}}\Delta g E_\mathrm{K}}{\frac{ag_\mathrm{L}}{g_\mathrm{e}^0} + 1 + c + \frac{\tau_\mathrm{AHP}}{g_\mathrm{e}^0\mu_\mathrm{ISI}^\mathrm{AHP}}\Delta g}.\end{aligned} \tag{59}$$

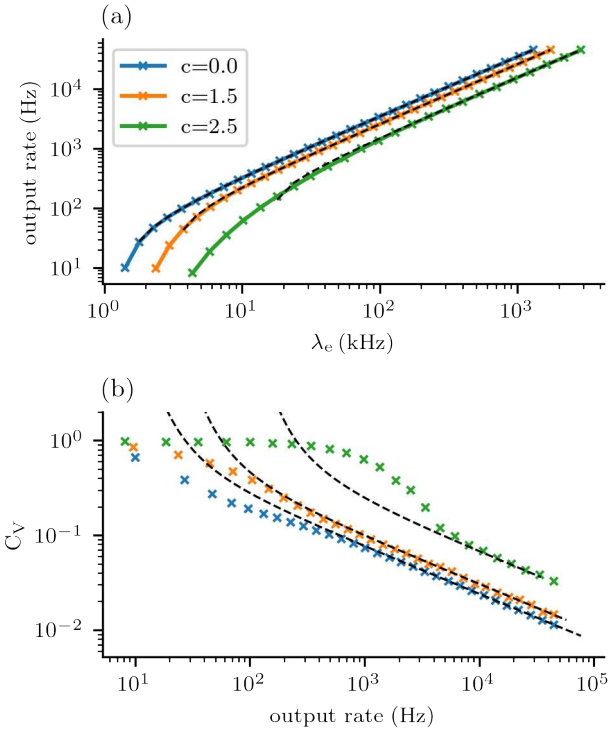

Fig 7. Approximation of the PSFR and C_V of LIF. Simulation results are color-coded. The dashed lines represent the approximations from the Eqs (54,55). The firing rate is approximated very well (A). C_V is approximated well for very high PSFRs ($> 1\,\text{kHz}$) (B). This is due to the short input time constants (3 ms for excitatory, 10 ms for inhibitory). For the simulation, we used the timestep $\Delta t = 0.1\,\text{ms}$ if the expected PSFR was $< 100\,\text{Hz}$ and $\Delta t \frac{\mu_{\text{ISI}}}{10\,\text{ms}}$ otherwise.

Clearly, $\frac{ag_L}{g_e^0} \to 0$. Therefore, it is important to evaluate the limit $A = \lim_{g_e^0 \to +\infty} g_e^0 \mu_{\text{ISI}}^{\text{AHP}}$. Then:

$$V_\infty^{\text{AHP}}(c) = \frac{E_e + cE_i + \frac{\tau_{\text{AHP}}}{A}\Delta g E_K}{1 + c + \frac{\tau_{\text{AHP}}}{A}\Delta g}. \tag{60}$$

By multiplying both sides of Eq. ((56)) with $g_{\text{tot}}^{\text{AHP}}$ and then taking the limit of both sides of the equation, we obtain:

$$ag_L\mu_{\text{ISI}} + g_e^0(1+c)\mu_{\text{ISI}} + \tau_{\text{AHP}}\Delta g = -aC\log\frac{\theta - V_\infty^{\text{AHP}}}{V_r - V_\infty^{\text{AHP}}}, \tag{61}$$

$$A(1+c) + \tau_{\text{AHP}}\Delta g = -aC\log\frac{\theta - V_\infty^{\text{AHP}}}{V_r - V_\infty^{\text{AHP}}}. \tag{62}$$

Numerical solution of Eq. ((62)) allows us to compare $V_\infty^{\text{AHP}}(c)$ with $V_\infty(c)$ and thus provides a comparison between the LIF model with and without the M-current adaptation (Fig. 8). For approximately $c > 5$ (with the used parameters), $V_\infty(c)^{\text{AHP}} \approx \theta$. Therefore, the neuron requires a very high input intensity for the fluctuations to be so small that $V_{\text{ef}}^{\text{AHP}}$ permanently exceeds the threshold, and in the range of biologically feasible inputs, the fluctuations in $V_{\text{ef}}^{\text{AHP}}$ lead to bursting when $V_{\text{ef}}^{\text{AHP}} > \theta$ and are silent when $V_{\text{ef}}^{\text{AHP}} \leq \theta$ (Fig. 8).

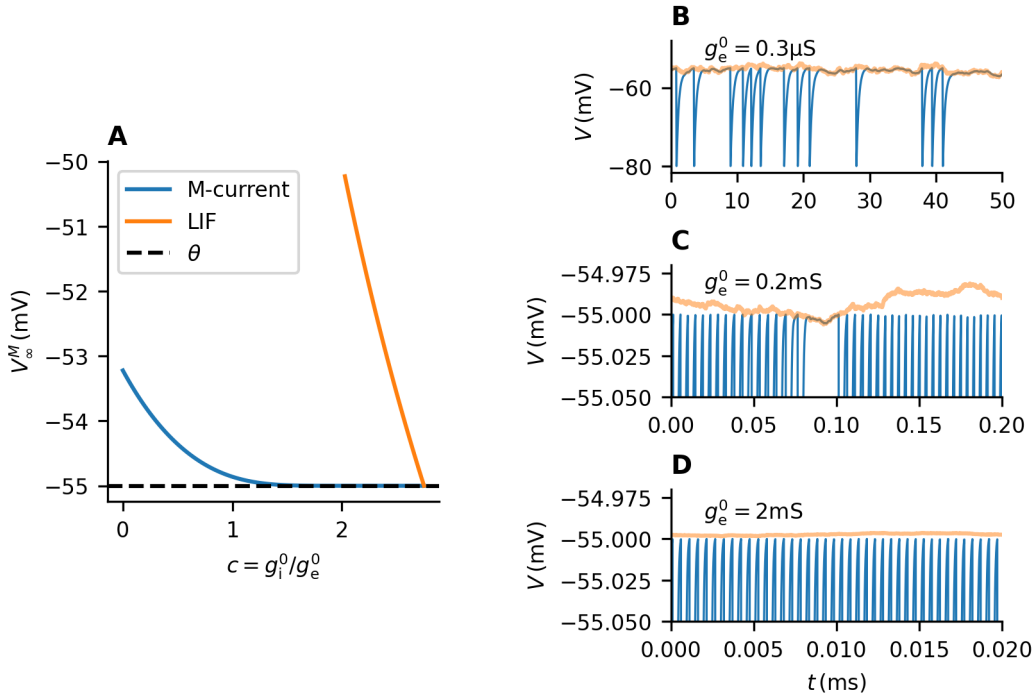

Fig 8. High conductance limit of the AHP-LIF model A: Equilibrium potential (in mV) in the infinite conductance limit (Eq. (60)) for different values of c (shown in blue). For high c, the value $V_\infty^{\mathrm{AHP}}(c)$ is very close to the threshold (dashed black line). The value of $V_\infty(c)$ (33), corresponding to the LIF model, is shown in orange for comparison. The M-current adaptation clearly pushes the equilibrium potential closer to the threshold, leading to bursting behavior. B-D: Time-course of the membrane potential of LIF with M-current adaptation with $c = 1.7$ for different values of input intensities. The membrane potential (shown in blue) follows closely $V_{\mathrm{ef}}^{\mathrm{AHP}}$ (shown in orange). When $V_{\mathrm{ef}}^{\mathrm{AHP}} > \theta$, the neuron is bursting; otherwise, the neuron is silent. With higher input intensities, the probability of $V_{\mathrm{ef}}^{\mathrm{AHP}} \leq \theta$ drops, and the firing rate becomes increasingly more regular.

The limit of $\mathrm{C_V}$

Neglecting the variance of $g_{\mathrm{AHP}}(t)$, the variance of ISIs can then be approximated analogously to Eq. ((55)) as:

$$\sigma_{\mathrm{ISI}}^2 = \left(\frac{\partial \mu_{\mathrm{ISI}}}{\partial g_{\mathrm{e}}}\right)^2 \sigma_{\mathrm{e}}^2 + \left(\frac{\partial \mu_{\mathrm{ISI}}}{\partial g_{\mathrm{i}}}\right)^2 \sigma_{\mathrm{i}}^2, \tag{63}$$

Our goal is to demonstrate that the coefficient of variation ($\mathrm{C_V}$) approaches zero. Using the definition of $\mathrm{C_V}$ (Eq. (26)) and Eq. (56), we have

$$\lim_{g_{\mathrm{e}}^0 \to +\infty} \mathrm{C_V} = \lim_{g_{\mathrm{e}}^0 \to +\infty} \frac{\sigma_{\mathrm{ISI}}}{\mu_{\mathrm{ISI}}} \tag{64}$$

$$= -\lim_{g_{\mathrm{e}}^0 \to +\infty} \frac{g_{\mathrm{tot}}^{\mathrm{AHP}}}{aC} \frac{\sigma_{\mathrm{ISI}}}{\log \frac{\theta - E_0^{\mathrm{AHP}}}{V_r - E_0^{\mathrm{AHP}}}} \tag{65}$$

$$= -\lim_{g_{\mathrm{e}}^0 \to +\infty} g_{\mathrm{tot}}^{\mathrm{AHP}} \sigma_{\mathrm{ISI}} \lim_{g_{\mathrm{e}}^0 \to +\infty} \left(\log \frac{\theta - E_0^{\mathrm{AHP}}}{V_r - E_0^{\mathrm{AHP}}}\right)^{-1}. \tag{66}$$

Since $-\infty < \lim_{g_e^0 \to +\infty} \left(\log \frac{\theta - E_0^{\mathrm{AHP}}}{V_r - E_0^{\mathrm{AHP}}} \right)^{-1} < 0$, it remains to be shown that $\lim_{g_e^0 \to +\infty} g_{\mathrm{tot}}^{\mathrm{AHP}} \sigma_{\mathrm{ISI}} = 0$, which can be shown by using the implicit differentiation formula.

References

D. Amit and N. Brunel. Model of global spontaneous activity and local structured activity during delay periods in the cerebral cortex. *Cereb. Cortex*, 7(3):237–252, 4 1997. ISSN 14602199. doi: 10.1093/cercor/7.3.237.

D. J. Amit and M. V. Tsodyks. Effective neurons and attractor neural networks in cortical environment. *Network*, 3(2):121–137, 1 1992. ISSN 0954-898X. doi: 10.1088/0954-898X{_}3{_}2{_}003.

M. Augustin, J. Ladenbauer, and K. Obermayer. How adaptation shapes spike rate oscillations in recurrent neuronal networks. *Front. Comput. Neurosci.*, 7, 2013. ISSN 1662-5188. doi: 10.3389/fncom.2013.00009.

T. Barta and L. Kostal. The effect of inhibition on rate code efficiency indicators. *PLoS Comput Biol.*, 15(12):e1007545, 12 2019. doi: 10.1371/journal.pcbi.1007545.

J. Benda and A. V. M. Herz. A Universal Model for Spike-Frequency Adaptation. *Neural Comput.*, 15(11):2523–2564, 11 2003. ISSN 0899-7667. doi: 10.1162/089976603322385063.

J. Benda, L. Maler, and A. Longtin. Linear Versus Nonlinear Signal Transmission in Neuron Models With Adaptation Currents or Dynamic Thresholds. *J. Neurophysiol*, 104(5):2806–2820, 11 2010. doi: 10.1152/jn.00240.2010.

O. Bernander, R. J. Douglas, K. A. Martin, and C. Koch. Synaptic background activity influences spatiotemporal integration in single pyramidal cells. *Proc. Natl. Acad. Sci. U.S.A.*, 88(24):11569–11573, 12 1991. doi: 10.1073/pnas.88.24.11569.

R. Betkiewicz, B. Lindner, and M. P. Nawrot. Circuit and Cellular Mechanisms Facilitate the Transformation from Dense to Sparse Coding in the Insect Olfactory System. *eNeuro*, 7(2):0305–18, 3 2020. ISSN 2373-2822. doi: 10.1523/ENEURO.0305-18.2020.

N. Brunel. Dynamics of Sparsely Connected Networks of Excitatory and Inhibitory Spiking Neurons. *J. Comput. Neurosci.*, 8:183–208, 2000. doi: https://doi.org/10.1023/A:1008925309027.

N. Brunel, F. S. Chance, N. Fourcaud, and L. F. Abbott. Effects of Synaptic Noise and Filtering on the Frequency Response of Spiking Neurons. *Phys. Rev. Lett.*, 86(10): 2186–2189, 3 2001. doi: 10.1103/physrevlett.86.2186.

M. J. Chacron, A. Longtin, M. St-Hilaire, and L. Maler. Suprathreshold Stochastic Firing Dynamics with Memory in P-Type Electroreceptors. *Phys. Rev. Lett.*, 85(7): 1576–1579, 8 2000. doi: 10.1103/physrevlett.85.1576.

M. J. Chacron, B. Lindner, and A. Longtin. Noise Shaping by Interval Correlations Increases Information Transfer. *Phys. Rev. Lett.*, 92(8):080601, 2 2004. ISSN 0031-9007. doi: 10.1103/PhysRevLett.92.080601.

M. M. Churchland, B. M. Yu, J. P. Cunningham, L. P. Sugrue, M. R. Cohen, G. S. Corrado, W. T. Newsome, A. M. Clark, P. Hosseini, B. B. Scott, D. C. Bradley, M. A. Smith, A. Kohn, J. A. Movshon, K. M. Armstrong, T. Moore, S. W. Chang, L. H. Snyder, S. G. Lisberger, N. J. Priebe, I. M. Finn, D. Ferster, S. I. Ryu, G. Santhanam, M. Sahani, and K. V. Shenoy. Stimulus onset quenches neural variability: a widespread cortical phenomenon. *Nat. Neurosci*, 13(3):369–78, 3 2010. ISSN 1546-1726. doi: 10.1038/nn.2501.

P. Dayan and L. F. Abbott. *Theoretical Neuroscience: Computational and Mathematical Modeling of Neural Systems*. The MIT Press, 2005. ISBN 0262541858.

R. R. de Ruyter van Steveninck. Reproducibility and Variability in Neural Spike Trains. *Science*, 275(5307):1805–1808, 3 1997. doi: 10.1126/science.275.5307.1805.

M. Deger, M. Helias, C. Boucsein, and S. Rotter. Statistical properties of superimposed stationary spike trains. *J. Comput. Neurosci*, 32(3):443–463, 6 2012. ISSN 0929-5313. doi: 10.1007/s10827-011-0362-8.

S. Denève and C. K. Machens. Efficient codes and balanced networks. *Nat. Neurosci*, 19 (3):375–382, 3 2016. ISSN 1097-6256. doi: 10.1038/nn.4243.

A. Destexhe. Inhibitory "noise". *Front Cell Neurosci*, 2010. ISSN 16625102. doi: 10.3389/fncel.2010.00009.

A. Destexhe and D. Paré. Impact of Network Activity on the Integrative Properties of Neocortical Pyramidal Neurons In Vivo. *J. Neurophysiol*, 81(4):1531–1547, 4 1999. doi: 10.1152/jn.1999.81.4.1531.

A. Destexhe, M. Rudolph, J. M. Fellous, and T. J. Sejnowski. Fluctuating synaptic conductances recreate in vivo-like activity in neocortical neurons. *Neuroscience*, 107 (1):13–24, 2001. ISSN 0306-4522.

A. Destexhe, M. Rudolph, and D. Paré. The high-conductance state of neocortical neurons in vivo. *Nat. Rev. Neurosci.*, 4(9):739–751, 9 2003. doi: 10.1038/nrn1198.

F. Droste and B. Lindner. Exact analytical results for integrate-and-fire neurons driven by excitatory shot noise. *J. Comput. Neurosci*, 43(1):81–91, 2017. ISSN 1573-6873. doi: 10.1007/s10827-017-0649-5.

G. D'Onofrio, P. Lansky, and M. Tamborrino. Inhibition enhances the coherence in the Jacobi neuronal model. *Chaos Solitons Fractals*, 128:108–113, 11 2019. ISSN 09600779. doi: 10.1016/j.chaos.2019.07.040.

F. Farkhooi, E. Muller, and M. P. Nawrot. Adaptation reduces variability of the neuronal population code. *Phys Rev E*, 83(5):050905, 5 2011. ISSN 1539-3755. doi: 10.1103/PhysRevE.83.050905.

P. Fatt and B. Katz. The effect of inhibitory nerve impulses on a crustacean muscle fibre. *J. Physiol.*, 121(2):374–389, 8 1953. ISSN 00223751. doi: 10.1113/jphysiol.1953.sp004952.

N. Fourcaud and N. Brunel. Dynamics of the Firing Probability of Noisy Integrate-and-Fire Neurons. *Neural Comput.*, 14(9):2057–2110, 9 2002. doi: 10.1162/089976602320264015.

W. Gerstner and R. Naud. How Good Are Neuron Models? *Science*, 326(5951):379–380, 10 2009. doi: 10.1126/science.1181936.

W. Gerstner, W. M. Kistler, and R. Naud. *Neuronal Dynamics*. Cambridge University Press, 2019. ISBN 1107635195.

G. E. Ha and E. Cheong. Spike Frequency Adaptation in Neurons of the Central Nervous System. *Exp. Neurobiol*, 26(4):179–185, 8 2017. ISSN 1226-2560. doi: 10.5607/en.2017.26.4.179.

D. P. Heyman and M. J. Sobel. *Stochastic Models in Operations Research: Stochastic Processes and Operating Characteristics*. Dover Books on Computer Science Series. Dover Publications, 2004. ISBN 9780486432595.

J. F. C. Kingman. *Poisson Processes (Oxford Studies in Probability)*. Clarendon Press, 1993. ISBN 978-0-19-853693-2.

R. Kobayashi and K. Kitano. Impact of slow K+ currents on spike generation can be described by an adaptive threshold model. *J. Comput. Neurosci.*, 40(3):347–362, 4 2016. doi: 10.1007/s10827-016-0601-0.

R. Kobayashi, Y. Tsubo, and S. Shinomoto. Made-to-order spiking neuron model equipped with a multi-timescale adaptive threshold. *Front. Comput. Neurosci.*, 3:9, 2009. doi: 10.3389/neuro.10.009.2009.

R. Kobayashi, S. Kurita, A. Kurth, K. Kitano, K. Mizuseki, M. Diesmann, B. J. Richmond, and S. Shinomoto. Reconstructing neuronal circuitry from parallel spike trains. *Nat. Commun.*, 10(1):4468, 10 2019. doi: 10.1038/s41467-019-12225-2.

L. Kostal, P. Lansky, and J.-P. Rospars. Neuronal coding and spiking randomness. *Eur. J. Neurosci*, 26(10):2693–2701, 11 2007. ISSN 0953816X. doi: 10.1111/j.1460-9568.2007.05880.x.

V. Lánská, P. Lánský, and C. E. Smith. Synaptic Transmission in a Diffusion Model for Neural Activity. *J. Theor. Biol.*, 166(4):393–406, 2 1994. doi: 10.1006/jtbi.1994.1035.

M. Levakova, L. Kostal, C. Monsempès, P. Lucas, and R. Kobayashi. Adaptive integrate-and-fire model reproduces the dynamics of olfactory receptor neuron responses in a moth. *J R Soc Interface*, 16(157):20190246, 8 2019. doi: 10.1098/rsif.2019.0246.

B. Lindner. Superposition of many independent spike trains is generally not a Poisson process. *Phys Rev E*, 73(2):022901, 2 2006. ISSN 1539-3755. doi: 10.1103/PhysRevE.73.022901.

B. Lindner and A. Longtin. Comment on "Characterization of Subthreshold Voltage Fluctuations in Neuronal Membranes," by M. Rudolph and A. Destexhe. *Neural Comput.*, 18(8):1896–1931, 8 2006. ISSN 0899-7667. doi: 10.1162/neco.2006.18.8.1896.

B. Lindner and L. Schimansky-Geier. Transmission of Noise Coded versus Additive Signals through a Neuronal Ensemble. *Phys. Rev. Lett.*, 86(14):2934–2937, 4 2001. doi: 10.1103/physrevlett.86.2934.

B. Lindner, M. J. Chacron, and A. Longtin. Integrate-and-fire neurons with threshold noise: A tractable model of how interspike interval correlations affect neuronal signal transmission. *Phys Rev E*, 72(2):021911, 8 2005. ISSN 1539-3755. doi: 10.1103/PhysRevE.72.021911.

D. Martinez. Oscillatory Synchronization Requires Precise and Balanced Feedback Inhibition in a Model of the Insect Antennal Lobe. *Neural Comput.*, 17(12): 2548–2570, 12 2005. ISSN 0899-7667. doi: 10.1162/089976605774320566.

M. Matsumura, T. Cope, and E. Fetz. Sustained excitatory synaptic input to motor cortex neurons in awake animals revealed by intracellular recording of membrane potentials. *Exp. Brain Res.*, 70(3):463–469, 5 1988. ISSN 0014-4819. doi: 10.1007/BF00247594.

W. Mittmann, U. Koch, and M. Häusser. Feed-forward inhibition shapes the spike output of cerebellar Purkinje cells. *J. Physiol.*, 563(2):369–378, 2 2005. doi: 10.1113/jphysiol.2004.075028.

C. Monier, F. Chavane, P. Baudot, L. J. Graham, and Y. Frégnac. Orientation and Direction Selectivity of Synaptic Inputs in Visual Cortical Neurons. *Neuron*, 37(4): 663–680, 2 2003. doi: 10.1016/s0896-6273(03)00064-3.

R. Moreno-Bote and N. Parga. Role of Synaptic Filtering on the Firing Response of Simple Model Neurons. *Phys. Rev. Lett.*, 92(2):028102, 1 2004. doi: 10.1103/physrevlett.92.028102.

R. Moreno-Bote and N. Parga. Membrane Potential and Response Properties of Populations of Cortical Neurons in the High Conductance State. *Phys. Rev. Lett.*, 94 (8):088103, 3 2005. doi: 10.1103/physrevlett.94.088103.

R. Moreno-Bote and N. Parga. Auto- and Crosscorrelograms for the Spike Response of Leaky Integrate-and-Fire Neurons with Slow Synapses. *Phys. Rev. Lett.*, 96(2): 028101, 1 2006. ISSN 0031-9007. doi: 10.1103/PhysRevLett.96.028101.

R. Moreno-Bote and N. Parga. Response of Integrate-and-Fire Neurons to Noisy Inputs Filtered by Synapses with Arbitrary Timescales: Firing Rate and Correlations. *Neural Comput.*, 22(6):1528–1572, 6 2010. ISSN 0899-7667. doi: 10.1162/neco.2010.06-09-1036.

R. Moreno-Bote, A. Renart, and N. Parga. Theory of Input Spike Auto- and Cross-Correlations and Their Effect on the Response of Spiking Neurons. *Neural Comput.*, 20(7):1651–1705, 7 2008. ISSN 0899-7667. doi: 10.1162/neco.2008.03-07-497.

D. Paré, E. Shink, H. Gaudreau, A. Destexhe, and E. J. Lang. Impact of Spontaneous Synaptic Activity on the Resting Properties of Cat Neocortical Pyramidal Neurons In Vivo. *J. Neurophysiol.*, 79(3):1450–1460, 3 1998. doi: 10.1152/jn.1998.79.3.1450.

S. P. Peron and F. Gabbiani. Role of spike-frequency adaptation in shaping neuronal response to dynamic stimuli. *Biol. Cybern.*, 100(6):505–520, 6 2009. ISSN 0340-1200. doi: 10.1007/s00422-009-0304-y.

M. J. E. Richardson. Effects of synaptic conductance on the voltage distribution and firing rate of spiking neurons. *Phys Rev E*, 69(5):051918, 5 2004. doi: 10.1103/physreve.69.051918.

M. J. E. Richardson and W. Gerstner. Synaptic Shot Noise and Conductance Fluctuations Affect the Membrane Voltage with Equal Significance. *Neural Comput.*, 17(4):923–947, 4 2005. doi: 10.1162/0899766053429444.

M. J. E. Richardson and W. Gerstner. Statistics of subthreshold neuronal voltage fluctuations due to conductance-based synaptic shot noise. *Chaos*, 16(2):26106, 6 2006. doi: 10.1063/1.2203409.

M. Rudolph, M. Pospischil, I. Timofeev, and A. Destexhe. Inhibition Determines Membrane Potential Dynamics and Controls Action Potential Generation in Awake and Sleeping Cat Cortex. *J. Neurosci.*, 27(20):5280–5290, 5 2007. doi: 10.1523/jneurosci.4652-06.2007.

A. Sanzeni, M. H. Histed, and N. Brunel. Response nonlinearities in networks of spiking neurons. *PLoS Comput. Biol.*, 16(9):e1008165, 9 2020. ISSN 1553-7358. doi: 10.1371/journal.pcbi.1008165.

T. Schwalger and L. Schimansky-Geier. Interspike interval statistics of a leaky integrate-and-fire neuron driven by Gaussian noise with large correlation times. *Phys Rev E*, 77(3):031914, 3 2008. ISSN 1539-3755. doi: 10.1103/PhysRevE.77.031914.

B. Sengupta, S. B. Laughlin, and J. E. Niven. Balanced Excitatory and Inhibitory Synaptic Currents Promote Efficient Coding and Metabolic Efficiency. *PLoS Comput. Biol.*, 9(10):e1003263, 10 2013. doi: 10.1371/journal.pcbi.1003263.

M. N. Shadlen and W. T. Newsome. Noise, neural codes and cortical organization. *Curr. Opin. Neurobiol.*, 4(4):569–579, 8 1994. doi: 10.1016/0959-4388(94)90059-0.

M. N. Shadlen and W. T. Newsome. The Variable Discharge of Cortical Neurons: Implications for Connectivity, Computation, and Information Coding. *J. Neurosci.*, 18(10):3870–3896, 5 1998. doi: 10.1523/jneurosci.18-10-03870.1998.

W. R. Softky and C. Koch. The highly irregular firing of cortical cells is inconsistent with temporal integration of random EPSPs. *J. Neurosci*, 13(1):334–350, 1 1993. doi: 10.1523/jneurosci.13-01-00334.1993.

M. Steriade, I. Timofeev, and F. Grenier. Natural Waking and Sleep States: A View From Inside Neocortical Neurons. *J. Neurophysiol.*, 85(5):1969–1985, 5 2001. doi: 10.1152/jn.2001.85.5.1969.

D. Sterratt, B. Graham, A. Gillies, and D. Willshaw. *Principles of computational modelling in neuroscience*. Cambridge University Press, 2011. ISBN 9780511975899. doi: 10.1017/CBO9780511975899.

S. P. Strong, R. Koberle, R. R. de Ruyter van Steveninck, and W. Bialek. Entropy and Information in Neural Spike Trains. *Phys. Rev. Lett.*, 80(1):197–200, 1 1998. doi: 10.1103/physrevlett.80.197.

C. Teeter, R. Iyer, V. Menon, N. Gouwens, D. Feng, J. Berg, A. Szafer, N. Cain, H. Zeng, M. Hawrylycz, C. Koch, and S. Mihalas. Generalized leaky integrate-and-fire models classify multiple neuron types. *Nat. Commun*, 9(1):709, 2 2018. doi: 10.1038/s41467-017-02717-4.

P. H. E. Tiesinga, J. V. José, and T. J. Sejnowski. Comparison of current-driven and conductance-driven neocortical model neurons with Hodgkin-Huxley voltage-gated channels. *Phys Rev E*, 62(6):8413–8419, 12 2000. doi: 10.1103/physreve.62.8413.

T. Toyoizumi, K. Aihara, and S.-i. Amari. Fisher Information for Spike-Based Population Decoding. *Phys. Rev. Lett.*, 97(9):098102, 8 2006. ISSN 0031-9007. doi: 10.1103/PhysRevLett.97.098102.

H. C. Tuckwell. *Introduction to Theoretical Neurobiology*. Cambridge University Press, 4 1988. doi: 10.1017/cbo9780511623271.

C. v. Vreeswijk and H. Sompolinsky. Chaos in Neuronal Networks with Balanced Excitatory and Inhibitory Activity. *Science*, 274(5293):1724–1726, 12 1996. ISSN 0036-8075. doi: 10.1126/science.274.5293.1724.

J. Wolfart, D. Debay, G. L. Masson, A. Destexhe, and T. Bal. Synaptic background activity controls spike transfer from thalamus to cortex. *Nat. Neurosci.*, 8(12): 1760–1767, 10 2005. doi: 10.1038/nn1591.

L. Wolff and B. Lindner. Mean, Variance, and Autocorrelation of Subthreshold Potential Fluctuations Driven by Filtered Conductance Shot Noise. *Neural Comput.*, 22(1):94–120, 1 2010. ISSN 0899-7667. doi: 10.1162/neco.2009.02-09-958.

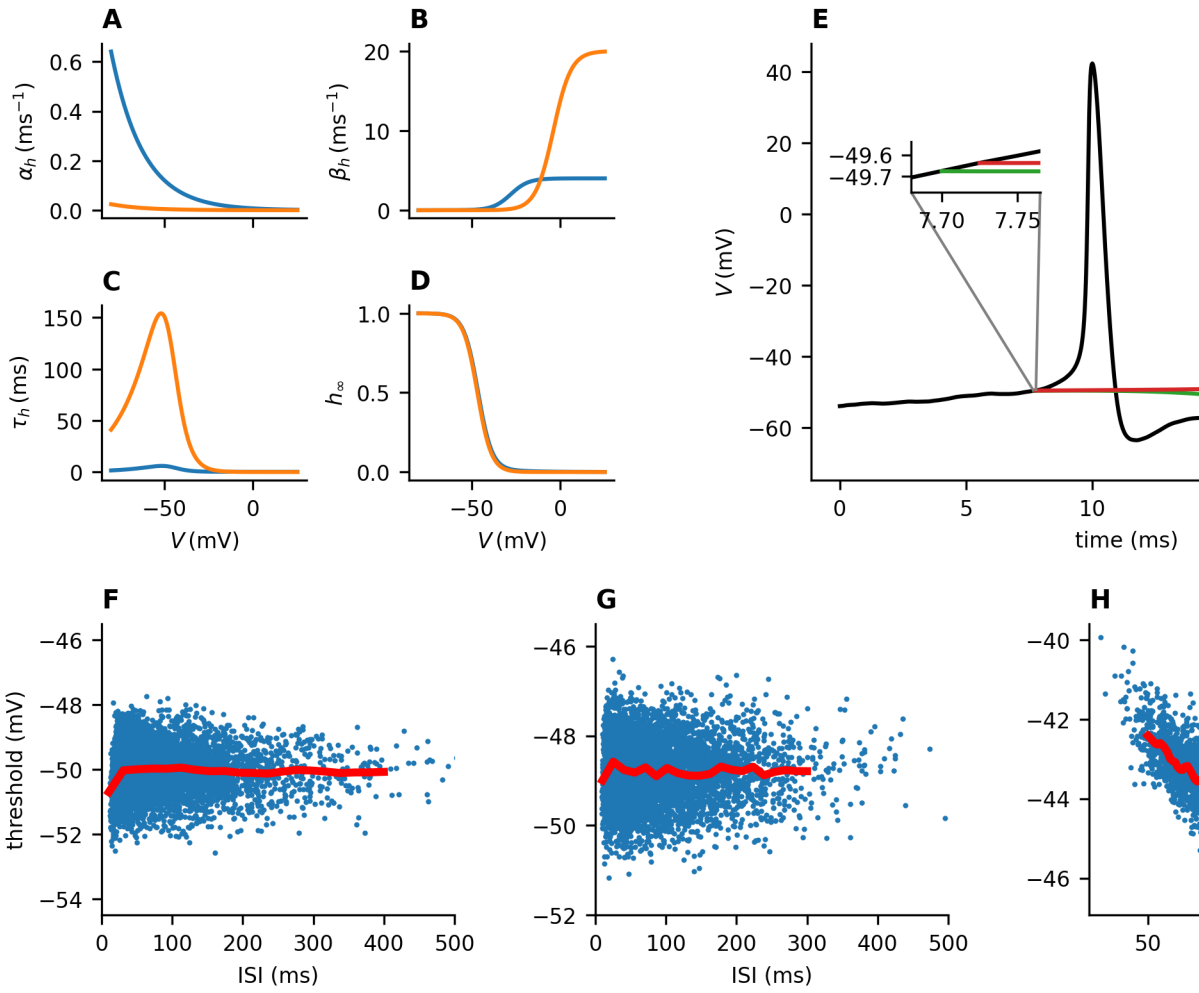

Supplementary Figure 1: Construction and validation of dynamic threshold HH model. A-D: The
(A) and inactivation (B) rate functions of the gating variable h of the non-adapting HH model (HH-0). The orang
functions for the HH-DT model. As an effect of this modification, the recovery time in the HH-DT model is prol
activation h_∞ remains relatively unchanged (D). E: Computation of the threshold. If no additional pre-synaptic
spike is observed (green trace). If the pre-synaptic spikes stop arriving $\Delta t = 0.025$ ms later, a spike is observed.
as being reached at $t = 7.725$ ms. F-H: Comparison of the calculated threshold with the preceding interspike int
threshold decreases with time after a spike is fired by estimating the firing threshold individually for each spike dur
input, resulting in a post-synaptic firing rate of approximately 10 Hz Neither the non-adapting model (HH-0, panel
adaptation (HH-M, panel G) displays signs of significant dependence between the threshold and ISI. For the dy
panel H) we observed a clear decrease in the threshold with increasing duration of the preceding ISI. The red line, a
by a KNN regression.

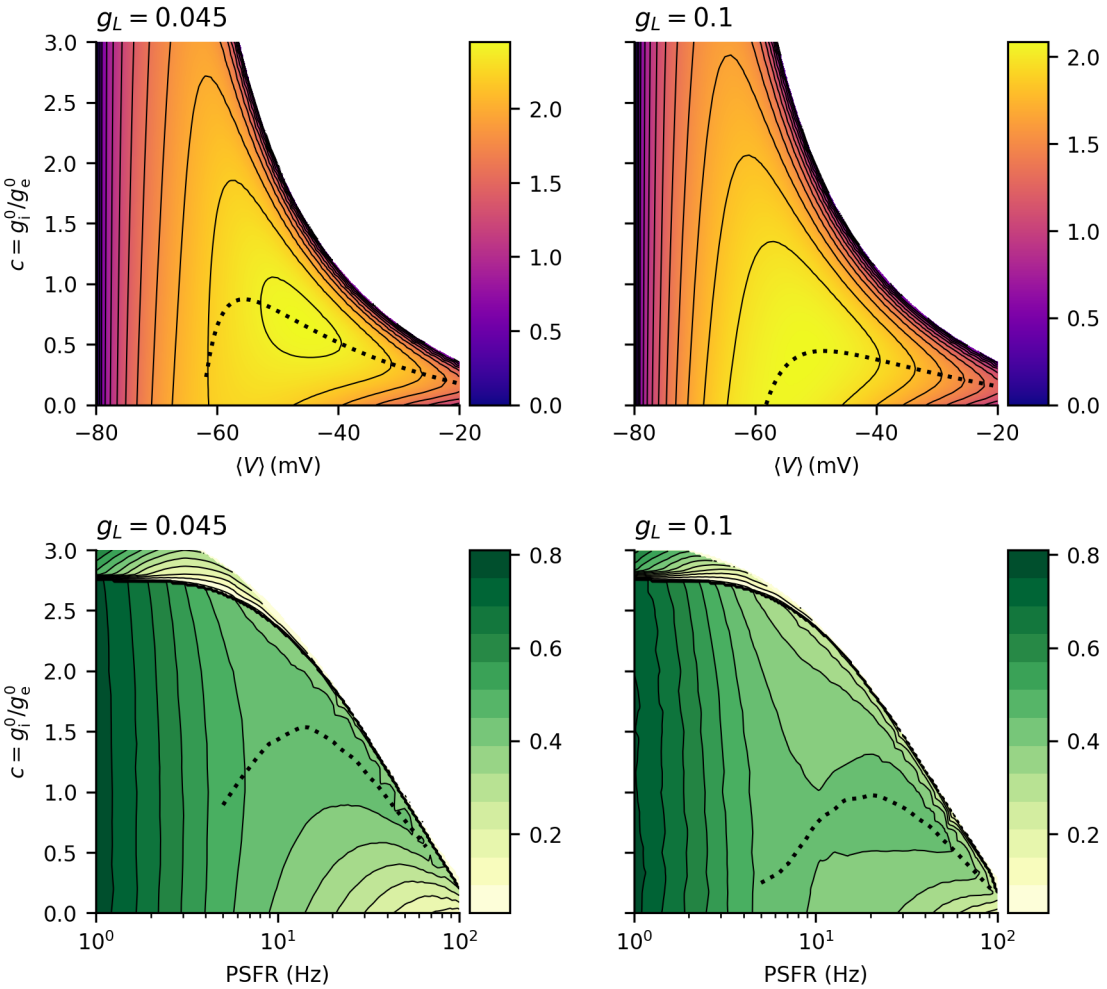

Supplementary Figure 2: Varying the membrane time constant. Top row: The membrane time constan
leak conductance g_L. With greater leak conductance, the membrane potential V follows V_{ef} more closely and t
membrane potential fluctuations more universally (approximation of σ_V, calculated from ETA, is colorcoded).
decreases / increases the membrane potential are separated by the dotted line. Bottom row: The structure of the c
firing regularity (C_V, colorcoded) changes with c and PSFR follows the structure of the membrane potential fluct
With higher g_L, higher c increases the firing regularity for a wider range of firing rates and a wider range of c. Th
the separation between the regions where higher c leads to higher / lower firing regularity.

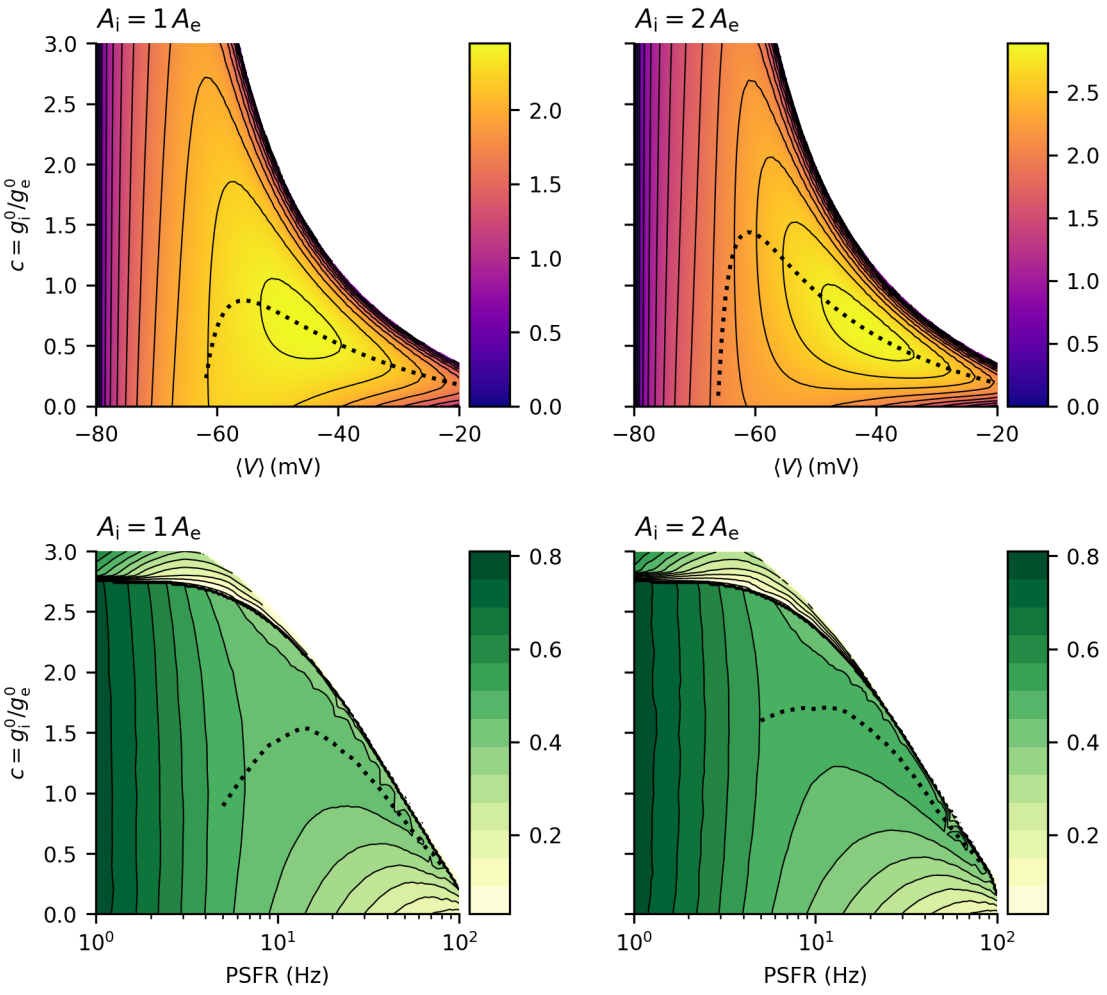

Supplementary Figure 3: Varying the aplitude of inhibitory synapses. With greater amplitude of the i (21)), the stabilisation of the membrane potential is observed only for higher values of c (top row). This is refle of the DT-LIF model (bottom row), analogously to the Supplementary Figure 2. The dotted line approximates regions where higher c leads to higher / lower membrane potential fluctuations (for the top row) or higher / low bottom row).

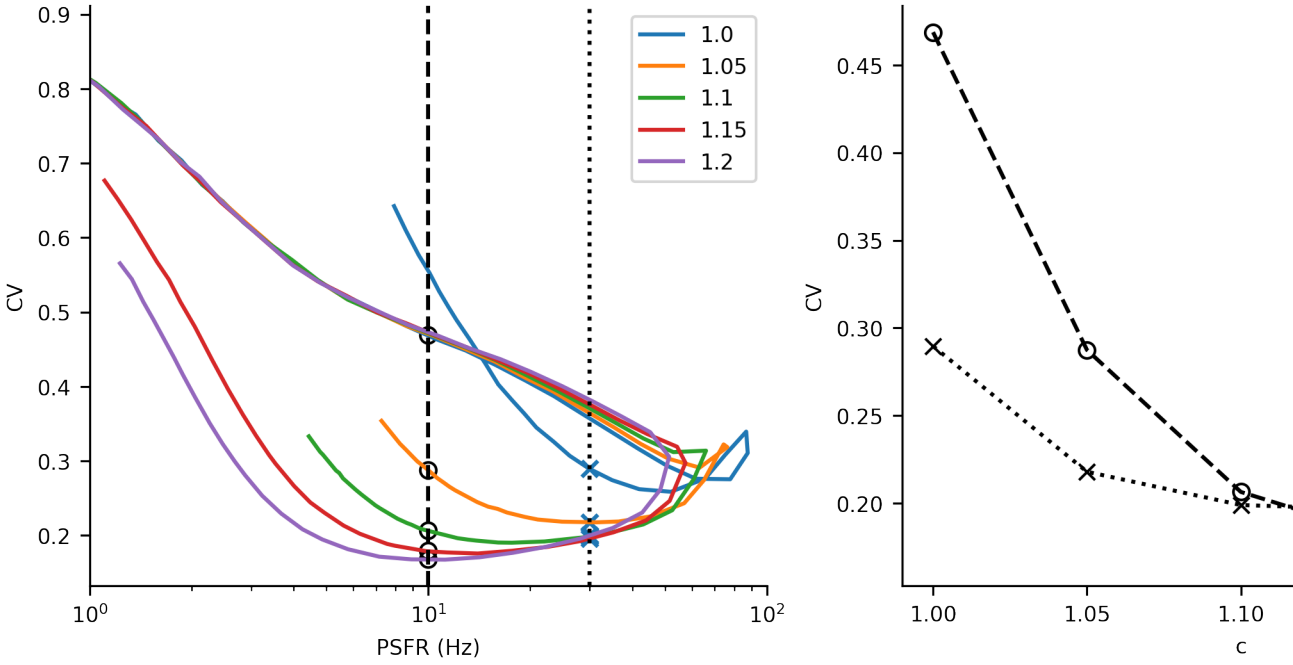

Supplementary Figure 4: Continuous change of C_V in the HH-DT model. Left: Same as Fig. 4C, but fo
Dashed and dotted vertical lines with points indicate the lowest value of C_V for each c. These are then shown in

Attachment II

Unpublished report

Dynamic threshold spike frequency adaptation leads to neural variability quenching with stimulus onset

Tomas Barta[1,2,3*], Lubomir Kostal[1**]

1 Institute of Physiology of the Czech Academy of Sciences, Prague, Czech Republic
2 Institute of Ecology and Environmental Sciences of Paris, INRAE, Sorbonne Université, CNRS, IRD, UPEC, Université de Paris, 78000 Versailles, France
3 Charles University, First Medical Faculty, Prague, Czech Republic

* tomas.barta@fgu.cas.cz ** kostal@biomed.cas.cz

Abstract

Neural variability quenching is a decrease of trial-to-trial variability of neural variability evoked by a stimulus. This phenomenon has been observed across scales in the brain including the membrane potential of individual cells (Monier et al., 2003) and firing activity (Churchland et al., 2010). Monier et al. (2003) suggested that the decrease of membrane potential variability is due to an increase in inhibitory activity associated with the stimulus onset. However, the origins of the decrease of firing activity variability (Fano factor) as well as its utility are still unclear.

Our theoretical study verified that increased inhibitory input to a neuron may decrease the membrane potential variability, despite increasing the variability of the input current (Barta and Kostal, 2021). Moreover, we showed that the spike frequency adaptation mechanism (SFA) of the neuron affects whether the neuron will fire spikes more or less regularly with higher inhibitory input.

In our continued effort, we show that our previous results are relevant in classical models of recurrent neural networks with excitatory and inhibitory subpopulations, where the feedforward input in the network is purely excitatory and the inhibitory input is determined by the network properties. We used a recurrent neural network of exponential integrate-and-fire neurons with SFA (Zerlaut et al., 2017). Each neuron responded to a stimulus with different intensity, mitigating the effect of preferred and non-preferred stimuli. When the SFA was implemented by after-hyperpolarization current the Fano factor increased after the stimulus onset, while in networks with SFA implemented by voltage-gated sodium channel inactivation (dynamic firing threshold), the Fano factor decreased, even for neurons whose firing rate did not change upon stimulus onset. Next, we analyze to which extent the differences between the SFA mechanisms affect information transmission properties.

Our work both provides one of the possible mechanisms that can lead to neural variability quenching as well as analyzes its possible utility by evaluating information transmission capabilities.

1 Methods

1.1 Single neuron dynamics

To model the single neuron dynamics, we used the adaptive exponential integrate-and-fire model (Brette and Gerstner, 2005), which we modified to incorporate

Table 1. Parameters of the LIF model

Membrane capacitance	C_m	150 pF
Leak conductance	g_L	10 nS
Resting potential	E_L	−80 mV
	V_{thr}	−50 mV
	k_a	2 mV for exc.
		0.5 mV for inh.
Exc. reversal potential	E_{e}	0 mV
Inh. reversal potential	E_{i}	−80 mV
Exc. synapse decay	τ_{exc}	5 ms
Inh. synapse decay	τ_{inh}	5 ms
Exc. synapse strength	w^0_{exc}	1 nS
Inh. synapse strength	w^0_{inh}	5 nS

dynamic threshold by adding slow gating variable s to the term with the exponential function:

$$C_m \frac{\mathrm{d}V^i}{\mathrm{d}t} = g_L(E_L - V^i) + I^i_{\text{syn}}(V^i, t) + (1 - s^i)k_a e^{\frac{V^i - V_{\text{thr}}}{k_a}} - I^i_w + I^i_{\text{bcg}} + I^i_{\text{stim}}, \quad (1)$$

$$\tau_w \frac{\mathrm{d}I^i_w}{\mathrm{d}t} = -I^i_w + a \cdot (V^i - E_L) + \sum_{t_s \in \{t_{\text{spike}}\}^i} b\delta(t - t_s), \quad (2)$$

$$\tau_w \frac{\mathrm{d}s^i}{\mathrm{d}t} = -s^i + \sum_{t_s \in \{t_{\text{spike}}\}^i} c(1 - s^i)\delta(t - t_s), \quad (3)$$

with an action potential recorded when V^i crosses the threshold 0 mV and reset at E_L. $\{t_{\text{spike}}\}^i$ is the set of all action potentials fired by the i-th neuron.

The exponential term represents the conductance of the voltage-gated Na^+ channels and the gating variable s represents the ratio of inactivated Na^+ channels. We used the model parameters as in (Zerlaut et al., 2017), with the exception of the adaptation parameters, in order to compare different adaptation mechanisms. The parameters are provided in the Table 1.

As in (Zerlaut et al., 2017), only excitatory neurons were adapting. In the case of dynamic threshold adaptation $b = 0$ and $c = 0.15$, meaning that 15% of all open channels become blocked with every fired action potential. In the case of after-hyperpolarization currents (AHP), we set $c = 0$ and $b = 20$ pA.

1.2 Network properties

The network consists of 10000 neurons, out of which 7500 are excitatory and 2500 are inhibitory. Regardless of the neuron type, the connection probability is 5% (Zerlaut et al., 2017).

The synaptic current I^i_{syn} is the current from conductance-based recurrent synapses:

$$I^i_{\text{syn}} = -g^i_{\text{exc}}(V - E_{\text{exc}}) - g^i_{\text{inh}}(V - E_{\text{inh}}), \quad (4)$$

$$\frac{\mathrm{d}g^i_{\text{exc}}}{\mathrm{d}t} = -\frac{g^i_{\text{exc}}}{\tau_{\text{exc}}} + \sum_{j=1}^{N} \sum_{t_s \in \{t_{\text{spike}}\}^j} w^{ji}_{\text{exc}}\delta(t - t_s), \quad (5)$$

$$\frac{\mathrm{d}g^i_{\text{inh}}}{\mathrm{d}t} = -\frac{g^i_{\text{inh}}}{\tau_{\text{inh}}} + \sum_{j=1}^{N} \sum_{t_s \in \{t_{\text{spike}}\}^j} w^{ji}_{\text{inh}}\delta(t - t_s), \quad (6)$$

where $\tau_e xc = \tau_{\text{inh}} = 5\,\text{ms}$ are synaptic decay time constants, w^{ji}_{exc} and w^{ji}_{inh} the synaptic weights. $w^{ji}_{\text{exc}} = 0$ if the j-th neuron is inhibitory, $w^{ji}_{\text{inh}} = 0$ if the j-th neuron is excitatory and otherwise for any connection the probability of the weight being non-zero is 5% and then $w^{ji}_{\text{exc}} = w^0_{\text{exc}} = 1\,\text{nS}$ and $w^{ji}_{\text{inh}} = w^0_{\text{inh}} = 5\,\text{nS}$.

1.3 External input

The external excitatory input is modeled as an Ornstein-Uhlenbeck process (Destexhe et al., 2001; Uhlenbeck and Ornstein, 1930):

$$I^i_{\text{ext}} = -g_{\text{ext}}(V^i - E_{\text{ext}})\frac{\mathrm{d}g^i_{\text{ext}}}{\mathrm{d}t} = -\frac{g^i_{\text{ext}} - \mu_{\text{ext}}(t)}{\tau_{\text{exc}}} + \sqrt{2\tau_{\text{exc}}}\sigma_{\text{exc}}(t)\eta^i(t), \tag{7}$$

where $\eta^i(t)$ is white noise, μ_{ext} and σ_{ext} are set so that the stationary mean and standard deviation of g_{ext} match those of a Poisson shot noise with an exponential kernel with a time constant τ_{exc}, amplitude w^0_{exc} and intensity λ^i_{ext}:

$$\mu_{\text{ext}}(t) = w^0_{\text{exc}}\lambda^i_{\text{ext}}(t)\tau_{\text{exc}}, \tag{8}$$

$$\sigma_{\text{ext}}(t) = \sqrt{\frac{\tau_{\text{exc}}\lambda^i_{\text{ext}}(t)}{2}}w^0_{\text{exc}}. \tag{9}$$

During the 12 s simulation, we modelled λ^i_{ext} as

$$\lambda^i_{\text{ext}} = \begin{cases} \lambda_{\text{bcg}} & \text{for } t < 6\,\text{s}, \\ \lambda_{\text{bcg}} + \lambda_{\text{stim}}\sin(\alpha_i - \alpha_{\text{stim}}) & \text{for } t \geq 6\,\text{s}, \end{cases} \tag{10}$$

where α_i is the preferred orientation of the i-th neuron and α_{stim} is the stimulus orientation, $\lambda_{\text{bcg}} = 1\,\text{kHz}$ and $\lambda_{\text{stim}} = 6\,\text{kHz}$.

We assume that neurons $1, \ldots, N_{\text{exc}}$, where $N_{\text{exc}} = 7500$ are excitatory and neurons $N_{\text{exc}}, \ldots, N$, where $N = 10000$ are inhibitory. We then set the preferred orientations as

$$\alpha_i = \begin{cases} \frac{\pi}{2}\frac{i}{N_{\text{exc}}} & \text{for } i \leq N_{\text{exc}}, \\ \frac{\pi}{2}\frac{i - N_{\text{exc}}}{N - N_{\text{exc}}} & \text{for } i > N_{\text{exc}}. \end{cases} \tag{11}$$

2 Results and discussion

We fixed the connectivity matrix and ran the simulation 3600 for each SFA mechanism - AHP and dynamic threshold. Raster plots from an example simulation are shown in Fig. 1A-C. The neurons show transient activity at the beginning of the simulation and after the stimulus onset. After the stimulus onset, the activity of neurons receiving strong input increases, while the activity of neurons receiving only weak external input is attenuated. For some neurons, the steady state activity remains approximately the same as before the stimulus onset.

We calculated the spiking statistics - the mean number of spikes and variance of the number of spikes before and after the stimulus onset. We left out the transient periods 1 s after the simulation start and 1 s after the stimulus onset. We plotted the spike count variance against the mean spike count (Fig. 1D-E). In each situation (AHP / dynamic threshold + before/after stimulus onset) the mean count - count variance formed a continuous curve with very little variance and the trial-to-trial variability of a neuron is essentially determined by its firing rate. Comparing this curve before and after stimulus onset shows us whether trial-to-trial variability increased or decreased after the stimulus onset. For AHP SFA, the trial-to-trial variability increased after the stimulus onset, while with dynamic threshold the trial-to-trial variability decreased after the stimulus onset.

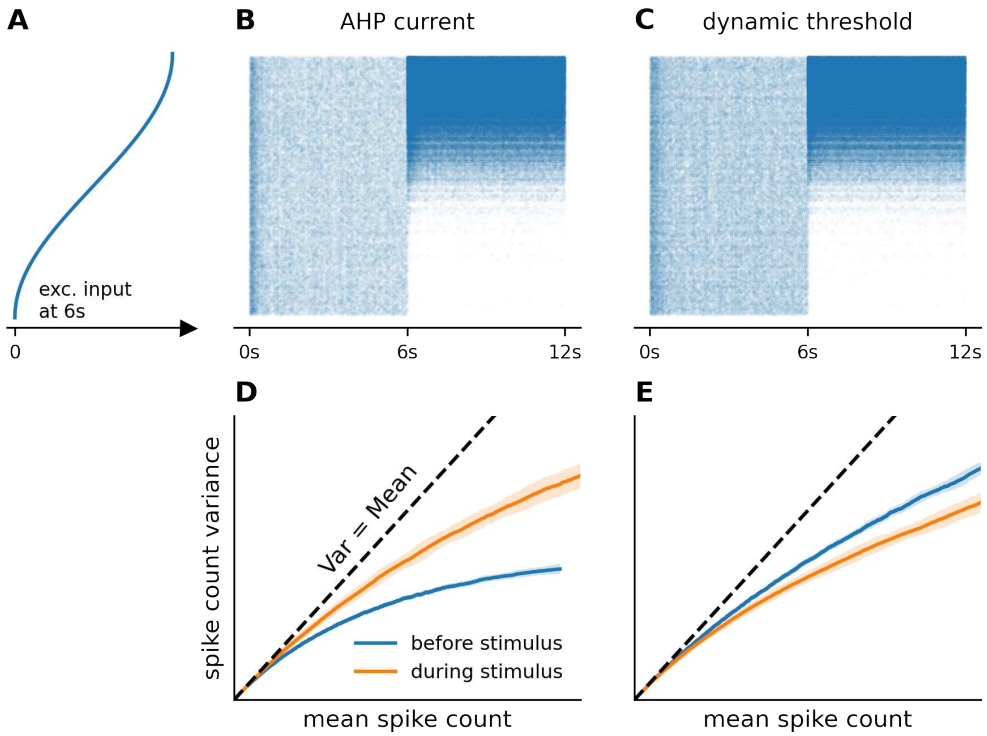

Fig 1. Trial-to-trial variability after stimulus onset depends on spike frequency adaptation mechanism. A: The curve illustrates the strength of the external input on top of the background input that each neuron starts receiving after 6 s. Each neuron receives a different input due to a different preferred stimulus. **B-C:** Raster plots of the 8000 excitatory neurons from one trial of the simulation with AHP (**B**) and dynamic threshold (**C**). **D-E:** With each spike frequency adaptation (SFA) mechanism we ran the simulation 3600 times. For each neuron, we calculated the mean number of spikes and their variance before the stimulus onset (in the interval between 1 s and 5 s after the simulation start) and after the stimulus onset (interval between 7 s and 12 s after the simulation start). With the AHP SFA, the trial-to-trial variability of the neurons increased after the stimulus onset, while with the dynamic threshold SFA the trial-to-trial variability decreased after the stimulus onset.

References

T. Barta and L. Kostal. Regular spiking in high-conductance states: The essential role of inhibition. *Phys Rev E*, 103(2):022408, 2 2021. ISSN 2470-0045. doi: 10.1103/PhysRevE.103.022408.

R. Brette and W. Gerstner. Adaptive Exponential Integrate-and-Fire Model as an Effective Description of Neuronal Activity. *J. Neurophysiol*, 94(5):3637–3642, 11 2005. ISSN 0022-3077. doi: 10.1152/jn.00686.2005.

M. M. Churchland, B. M. Yu, J. P. Cunningham, L. P. Sugrue, M. R. Cohen, G. S. Corrado, W. T. Newsome, A. M. Clark, P. Hosseini, B. B. Scott, D. C. Bradley, M. A. Smith, A. Kohn, J. A. Movshon, K. M. Armstrong, T. Moore, S. W. Chang, L. H. Snyder, S. G. Lisberger, N. J. Priebe, I. M. Finn, D. Ferster, S. I. Ryu, G. Santhanam, M. Sahani, and K. V. Shenoy. Stimulus onset quenches neural variability: a widespread cortical phenomenon. *Nat. Neurosci*, 13(3):369–78, 3 2010. ISSN 1546-1726. doi: 10.1038/nn.2501.

A. Destexhe, M. Rudolph, J. M. Fellous, and T. J. Sejnowski. Fluctuating synaptic conductances recreate in vivo-like activity in neocortical neurons. *Neuroscience*, 107 (1):13–24, 2001. ISSN 0306-4522.

C. Monier, F. Chavane, P. Baudot, L. J. Graham, and Y. Frégnac. Orientation and Direction Selectivity of Synaptic Inputs in Visual Cortical Neurons. *Neuron*, 37(4): 663–680, 2 2003. doi: 10.1016/s0896-6273(03)00064-3.

G. E. Uhlenbeck and L. S. Ornstein. On the Theory of the Brownian Motion. *Phys. Rev.*, 36(5):823–841, 9 1930. doi: 10.1103/physrev.36.823.

Y. Zerlaut, S. Chemla, F. Chavane, and A. Destexhe. Modeling mesoscopic cortical dynamics using a mean-field model of conductance-based networks of adaptive exponential integrate-and-fire neurons. *J. Comput. Neurosci*, 44(1):45–61, 2 2017. ISSN 0929-5313. doi: 10.1007/s10827-017-0668-2.

Attachment III

Manuscript published in *PLoS Computational Biology* **103**, 022408. Published on 2nd December 2019, IF 4.779
doi: https://doi.org/10.1371/journal.pcbi.1007545

The effect of inhibition on rate code efficiency indicators

Tomas Barta[1,2,3*], Lubomir Kostal[1]

1 Institute of Physiology of the Czech Academy of Sciences, Prague, Czech Republic
2 Charles University, First Medical Faculty, Prague, Czech Republic
3 Institute of Ecology and Environmental Sciences, INRA, Versailles, France

* tomas.barta@fgu.cas.cz

Abstract

In this paper we investigate the rate coding capabilities of neurons whose input signal are alterations of the base state of balanced inhibitory and excitatory synaptic currents. We consider different regimes of excitation-inhibition relationship and an established conductance-based leaky integrator model with adaptive threshold and parameter sets recreating biologically relevant spiking regimes. We find that given mean post-synaptic firing rate, counter-intuitively, increased ratio of inhibition to excitation generally leads to higher signal to noise ratio (SNR). On the other hand, the inhibitory input significantly reduces the dynamic coding range of the neuron. We quantify the joint effect of SNR and dynamic coding range by computing the metabolic efficiency - the maximal amount of information per one ATP molecule expended (in bits/ATP). Moreover, by calculating the metabolic efficiency we are able to predict the shapes of the post-synaptic firing rate histograms that may be tested on experimental data. Likewise, optimal stimulus input distributions are predicted, however, we show that the optimum can essentially be reached with a broad range of input distributions. Finally, we examine which parameters of the used neuronal model are the most important for the metabolically efficient information transfer.

Author summary

Neurons communicate by firing action potentials, which can be considered as all-or-none events. The classical rate coding hypothesis states that neurons communicate the information about stimulus intensity by altering their firing frequency. Cortical neurons typically receive a signal from many different neurons, which, depending on the synapse type, either depolarize (excitatory input) or hyperpolarize (inhibitory input) the neural membrane. We use a neural model with excitatory and inhibitory synaptic conductances to reproduce in-vivo like activity and investigate how the intensity of presynaptic inhibitory activity affects the neuron's ability to transmit information through rate code. We reach a counter-intuitive result that increase in inhibition improves the signal-to-noise ratio of the neural response, despite introducing additional noise to the input signal. On the other hand, inhibition also limits the neuronal output range. However, in the end, the actual amount of information transmitted (in bits per energy expended) is remarkably robust to the inhibition level present in the system. Our approach also yields predictions in the form of post-synaptic firing rate histograms, which can be compared with in-vivo recordings.

Introduction

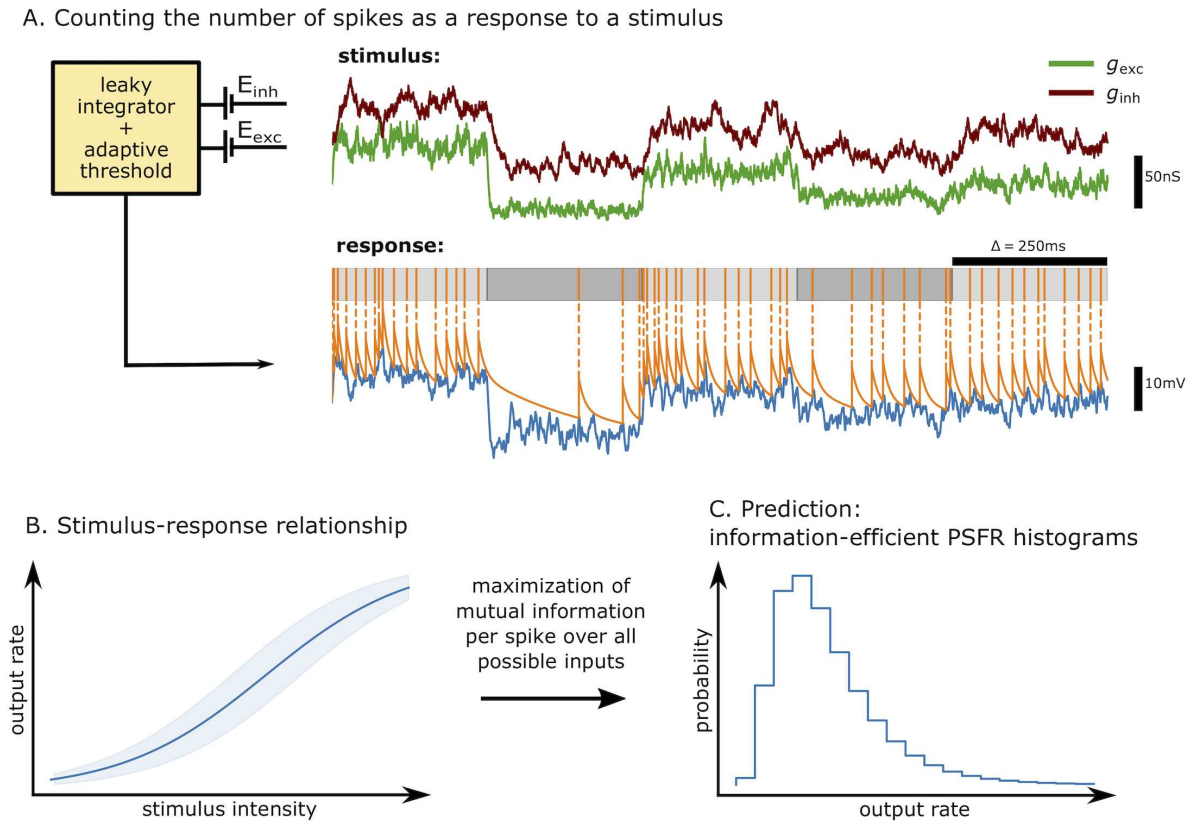

Fig 1. Graphical abstract. (A) Stimulus consisting of excitatory and inhibitory synaptic conductances, generated as shot noise with an exponential envelope, is delivered to the neuronal model, a passive leaky membrane with a dynamic threshold. The measured response is the number of spikes in a specified time window (e.g., 250 ms). (B) For each stimulus intensity the full response distribution is obtained. The mean response (solid) and its standard deviation (shaded) are shown for illustration. (C) We find the probability distribution of inputs that maximizes the mutual information between the stimulus and the response per single spike. The predicted histogram of post-synaptic firing rates (PSFR) can be compared with experimental data.

Cortical neurons receive input in the form of bombardment by action potentials (spikes) from other neurons and process and communicate the received information further by transmitting their own action potentials to other neurons. Individual action potentials do not differ in their time course and therefore, from the information processing point of view, they can be seen as all-or-none events. The response to a particular stimulus is therefore represented by a spike train - a sequence of times when an action potential was produced [1].

According to the efficient-coding hypothesis [2], neurons are adapted to process the information from their natural surrounding efficiently. This inspired a number of studies based on optimality arguments (e.g., [3–9]), with the information efficiency usually being interpreted by the means of Shannon's information theory [10].

Given that the cortex has only a limited energy budget and information transfer is costly [11–13], we expect that neurons balance information rates and energetic expenses. The idea of energy efficient neural coding was popularized by Levy and Baxter [14]. In

their work they focus on the representational capacity of a noiseless population of neurons and show that optimizing the representational capacity *per spike* leads to low firing rates, typically observed in vivo. The introduction of realistic noise [15] and further biophysical details limits the analytical tractability and studies of noisy neurons are generally limited to numerical analyses of single cells and simplified populations.

Typical approaches to information-theoretical analyses of single cells are either the use of the direct method [16,17] to evaluate the reproducibility of a response to a given stimulus or the computation of the mutual information between the stimulus and the response [18] and eventually evaluating the information capacity of the neuron as an information channel [19–21]. The attractiveness of information capacity stems from Shannon's channel coding theorem which guarantees the existence of a code that is asymptotically able to transmit information at the rate given by the capacity [22]. See [23–26] for reviews of the use of information theory in computational neurosciences.

Both the direct method and capacity analysis can be extended to account for the metabolic expenses. One of the earliest efforts to relate the information capacity to the metabolic expenses is that of Laughlin et at. [27], where the Gaussian distribution of response variability is assumed for a cell encoding the stimulus in the graded potential. Balasubramanian [28] discussed the possibilities of applying the formalism of capacity of constrained channels [29] to neural systems and Polavieja [30,31] showed that rate coding neurons [32] with additive response noise that the predicted shapes of post-synaptic firing rate (PSFR) distributions obtained from such formalism qualitatively match the experimentally measured distributions [33]. These inspiring results provided ground for investigating the information-energy balance for more realistic neuronal models, such as the Hodgkin-Huxley model [34] or a formal model based on an empirical stimulus-response relationship [35]. Studies concerning the efficiency of neurons employing different methods of information encoding have also been conducted (e.g., Leaky integrate and Fire with descending threshold [36], generalized inverse Gaussian neuron model [37–39]).

In the presented work we utilize the MAT (Multi-timescale Adaptive Threshold) model [40] which has been shown to be very good at predicting in-vivo recorded spike trains [40–47], while maintaining only a modest number of free parameters. Therefore information-theoretical analysis of this model allows us to make predictions for a wide variety of neurons (Fig 1).

The main contributions and the structure of this work can be summarized as follows:

(i) By applying the results of Witsenhausen [48] in the context of neural systems, we conclude that the maximal mutual information between input and output of a neuron using rate code must be generally reachable with only a finite number of inputs.

(ii) We qualitatively discuss the stimulus-response relationships and the capacity-cost functions and show the stabilizing effect of inhibition on the membrane potential fluctuations and discuss the implications for the given neuronal model.

(iii) We analyze the effect of inhibition on information-metabolic efficiency and more intuitive indicators of information transmission efficiency. We find that for a given mean post-synaptic firing rate, counter-intuitively, increased ratio of inhibition to excitation generally leads to higher signal to noise ratio (SNR). On the other hand, the inhibitory input significantly reduces the dynamic coding range of the neuron.

(iv) We present the predicted PSFR histograms and discuss the comparability with experimental data. In combination with the relative simplicity of fitting the parameters of the MAT model to real neurons, the presented framework allows us to predict the PSFR histograms for a wide variety of neurons. Furthermore, we

observe that the shapes of the histograms depend only marginally the rate coding time scale.

(v) We show the predicted optimal input distributions and point out to the robustness of metabolic efficiency and the PSFR histogram towards changes in the input distribution.

(vi) We explain the effect of model parameters on the obtained results and the significance of the spontaneous firing rate. We use parameter values fitted by Kobayashi et. al. [40] on experimental data for further biological relevance and to provide insight into what influences the information-metabolic efficiency on a large scale.

Materials and Methods

Neuronal model

The membrane potential of the MAT model is governed by the equation:

$$\tau_{\mathrm{m}} \frac{\mathrm{d}V}{\mathrm{d}t} = -(V - E_{\mathrm{L}}) + RI_{\mathrm{syn}}, \tag{1}$$

where τ_{m} is the membrane time constant, V is the membrane potential, $E_{\mathrm{L}} = -80\,\mathrm{mV}$ the leakage potential, I_{syn} is the synaptic current. Spikes are fired when the membrane potential reaches (or is above) the value of a dynamic threshold $\theta(t)$. The dynamics of θ is described by

$$\theta(t) = \sum_{k} D(t - t_k) + \omega, \tag{2}$$

$$D(t) = \sum_{j=1}^{L} H(t)\alpha_j \exp(-t/\tau_j) \tag{3}$$

where k iterates through all the previous spikes, t_k is the k-th spike's time and H is the Heaviside function. Therefore the threshold is composed of L exponentially decaying components and an asymptotic threshold value ω. The j-th component increases by α_j every time a spike occurs and then decays with the time constant τ_j. Absolute refractory period of 2 ms is introduced, during which the dynamics of the membrane potential and the threshold remain unchanged, but a spike cannot be fired. The parameters used to replicate the behavior of neurons from different classes (regular spiking - RS, intrisic bursting - IB, fast spiking - FS, chattering - CH) were identified by Kobayashi et al. [40]. All relevant model parameters are specified in S1 Appendix.

The synaptic current is given by

$$I_{\mathrm{syn}}(t) = g_{\mathrm{exc}}(t)(V - E_{\mathrm{exc}}) + g_{\mathrm{inh}}(t)(V - E_{\mathrm{inh}}), \tag{4}$$

where g_{exc}, g_{inh} are the total conductances of the excitatory and inhibitory synapses and $E_{\mathrm{exc}} = 0\,\mathrm{mV}$, $E_{\mathrm{inh}} = -75\,\mathrm{mV}$ are the respective synaptic reversal potentials. We consider the excitatory and inhibitory conductances to be

$$g_{\mathrm{exc}}(t) = \sum_{t_j < t} \bar{g}_{\mathrm{exc}} H(t_j - t) \exp\left((t_j - t)/\tau_{\mathrm{exc}}\right), \tag{5}$$

$$g_{\mathrm{inh}}(t) = \sum_{t_k < t} \bar{g}_{\mathrm{inh}} H(t_k - t) \exp\left((t_k - t)/\tau_{\mathrm{inh}}\right), \tag{6}$$

where the times $\{t_j\}$, $\{t_k\}$ are generated by independent Poisson point processes with intensities λ_{exc}, λ_{inh} (to mimic the arrival of excitatory and inhibitory synapses), $\bar{g}_{\text{exc}}$ and $\bar{g}_{\text{inh}}$ correspond to peak conducatances of individual synapses and τ_{exc}, τ_{inh} are time constants of those synapses, which were chosen as 3 ms for the excitatory and 10 ms for the inhibitory synapses [49]. We denote the excitatory part λ_{exc} as the *stimulus intensity* [34].

To recreate biologically plausible conditions, we calculate the peak conductances and minimal intensities of Poisson processes $\lambda_{\text{exc}}^{(\text{bcg})}$, $\lambda_{\text{inh}}^{(\text{bcg})}$ (where "bcg" stands for the background network activity), so that the mean and standard deviation of g_{exc} and g_{inh} correspond to values reported in [49], which were obtained from a detailed biophysical simulation. The values of the peak conductances are $\bar{g}_{\text{exc}} = 1.50\,\text{nS}$ and $\bar{g}_{\text{inh}} = 1.53\,\text{nS}$ and the rates of arrival of action potentials corresponding to the background activity are $\lambda_{\text{exc}}^{(\text{bcg})} = 2.67\,\text{kHz}$, $\lambda_{\text{inh}}^{(\text{bcg})} = 3.73\,\text{kHz}$ (S3 Appendix).

The *response* of the neuron y is the number of observed spikes in a time window Δ, the corresponding firing rate is then y/Δ. Since the differential equation describing the membrane potential (Eq (1)) is stochastic due to the randomness introduced by the input current, the response is described by a random variable Y for each input λ_{exc}. In our work we compare the results for five different lengths of coding time windows: 100 ms, 200 ms, 300 ms, 400 ms and 500 ms.

The numerical integration procedure is described in S2 Appendix.

Metabolic cost of neuronal activity

The metabolic cost of neuronal activity is determined mainly by the activity of the Na^+/K^+ ionic pump in the neuronal membrane, pumping the excess Na^+ out of the neuron. The main contributors to the overall cost are then: 1. reversal of Na^+ entry at resting potential, 2. reversal of ion fluxes through post-synaptic receptors, 3. reversal of Na^+ entry for action potentials and 4. additional costs associated with the action potential [12, 50, 51].

We follow the estimates from [11], i.e., we set the cost of maintaining the resting potential at $w_{\text{rest}} = 0.342 \cdot 10^9$ ATP molecules per second, the cost of reversal of Na^+ entry for action potentials at $0.384 \cdot 10^9$ ATP molecules per single action potential and the costs associated with vesicle release due to action potential at $0.328 \cdot 10^9$ ATP molecules, adding up to $w_{\text{spike}} \approx 0.71 \cdot 10^9$ ATPs/spike

To calculate the cost needed to reverse the ion fluxes through post-synaptic receptors, we follow the approach used in [13]. We calculated the conductance of Na^+ channels:

$$g_{\text{Na}} = \frac{g_{\text{exc}}}{1 - \frac{E_{\text{Na}}}{E_{\text{K}}}}, \tag{7}$$

where $E_{\text{Na}} = 90\,\text{mV}$, $E_{\text{K}} = -105\,\text{mV}$ are the reversal potentials of Na^+ and K^+ channels. The current due to influx of Na^+ ions is then

$$I_{\text{Na}}(t) = g_{\text{Na}}(t)(V(t) - E_{\text{Na}}). \tag{8}$$

Integrating the current over Δ and dividing by the charge of an electron e gives us the total number of Na^+ that have to be extruded. The ion pump uses one ATP molecule for 3 Na^+ extruded.

Substituting $g_{\text{Na}}(t)$ and $V(t)$ by their mean values ($\bar{g}_{\text{Na}}(t)$, $\bar{V}(t)$) for excitation and inhibition intensities λ_{exc}, λ_{inh}, we obtain the approximate formula for the cost of reversal of the synaptic currents:

$$w_{\text{syn}}(\lambda_{\text{exc}}, \lambda_{\text{inh}}) = \frac{1}{3e}\bar{g}_{\text{Na}}(\lambda_{\text{exc}}, \lambda_{\text{inh}})(\bar{V}(\lambda_{\text{exc}}, \lambda_{\text{inh}}) - E_{\text{Na}})\Delta. \tag{9}$$

The total cost of the signaling, given the input $(\lambda_{\text{exc}}, \lambda_{\text{inh}})$, is then:

$$w(\lambda_{\text{exc}}, \lambda_{\text{inh}}) = (w_{\text{rest}} + w_{\text{syn}})\Delta + w_{\text{spike}} n(\lambda_{\text{exc}}, \lambda_{\text{inh}}), \tag{10}$$

where $n(\lambda_{\text{exc}}, \lambda_{\text{inh}})$ is the average number of spikes observed for the given input.

Information capacity and capacity-cost function

In the framework of information theory, the input is a random variable X with probability density function $p(x)$. In our case, x is the stimulus intensity, λ_{exc}, which is a real number from an interval $[a, b]$. We can than define the corresponding marginal output probability distribution q_p:

$$q_p(y) = \int_a^b p(x) f(y|x) \, \mathrm{d}x. \tag{11}$$

The conditional probability distribution $f(y|x)$ describing the probability of observing an output y given an input (stimulus) x has to be obtained first [22]. Due to the non-linear character of Eqs (1-6) the closed-form solution for $f(y|x)$ is not available, therefore we used extensive Monte Carlo simulation to obtain the numerical approximation. The amount of information about the stimulus $X = x$ from observing the response $Y = y$ is defined as [22, p. 16]

$$i(x; y) = \log_2 \frac{f(y|x)}{q_p(y)}. \tag{12}$$

By averaging the value of information over all possible outputs, we get the specific information (since Y is discrete) [52–54]

$$i(x; Y) = \sum_{y=0}^{+\infty} i(x; y) q_p(y). \tag{13}$$

By averaging the specific information over all possible inputs, we get the mutual information

$$I(X; Y) = \int_a^b i(x; Y) p(x) \, \mathrm{d}x. \tag{14}$$

The *information capacity* expresses the maximal amount of information that can be reliably transmitted per single channel use and is defined as

$$C = \sup_{p(x)} I(X; Y), \tag{15}$$

where the supremum is taken over all possible input probability distributions. Since the duration of one channel use is Δ, $\frac{C}{\Delta}$ is the capacity in bits per second.

Given the input probability distribution $p(x)$ the average metabolic cost W_p is then

$$W_p = \int_a^b p(x) w(x) \, \mathrm{d}x, \tag{16}$$

where $w(x)$ is given by Eq (10) We maximize mutual information over all possible input probability distributions p that satisfy the condition $W_p < W$ for some selected W, and thus obtain the *capacity-cost function* [29]:

$$C(W) = \sup_{p(x): W_p < W} I(X; Y). \tag{17}$$

It follows from the Lagrangian theorem [55, 56], that $C(W)$ is attained either at the cost corresponding to the unrestrained capacity $W_{\max}$ for $W > W_{\max}$ or at W. The quantity $\frac{C(W)}{W}$ for $W \leq W_{\max}$ then expresses the amount of information per unit cost, which motivates the definition of *information-metabolic efficiency* E [28, 35, 57], i.e. the maximal amount of information per unit cost

$$E = \frac{C(W^*)}{W^*}, \tag{18}$$

$$W^* = \underset{W \in [0,+\infty)}{\arg\max} \frac{C(W)}{W}. \tag{19}$$

where W^* is the optimal average cost.

We will refer to a regime in which the neuron encodes the maximal possible amount of information per energy as to an *information-metabolically efficient regime*. In such regime, the inputs x are assigned probabilities $p^*(x)$ and the probability of observing an output $Y = y$ is

$$P(Y = y) = \int_a^b p^*(x) f(y|x). \tag{20}$$

Since the response y is the number of spikes in a time window Δ, we can use Eq (20) to calculte the mean PSFR:

$$\text{PSFR} = \frac{1}{\Delta} y \tag{21}$$

$$\langle \text{PSFR} \rangle = \frac{1}{\Delta} \sum_{y=0}^{+\infty} y P(Y = y). \tag{22}$$

Properties of information-theoretic optima and numerical optimization

Theoretical results show that the support of the optimal input distribution $p^*(x)$ for certain channels (neuron with gamma distributed inter-spike interval [21], energy constrained Gaussian channel [56], Rayleigh-fading channel [58]) contains only a finite number of points. Moreover, as a consequence of Dubin's theorem [48], it is guaranteed that for any channel with a finite number of possible output states the optimal input distribution has to be discrete. The number of support points is at most equal to the number of possible outputs. Since the number of action potentials in a finite time window is limited, it generally follows that the optimal input distribution in the rate-coding scheme must contain only finitely many stimulus values of non-zero probability.

The theory presented above holds for memoryless information channels without feedback, i.e., the response to the stimulus depends only on the current stimulus and not on any past stimuli or responses of the channel. However, real neurons exhibit adaptation to the stimulus, therefore the stimulus-response relationship $f(y|x)$ is also affected by the probability distribution of stimuli $p(x)$. In order to mitigate the effect of history, we developed a fixed-point based method to ensure that the distribution of stimuli $p(x)$ used to obtain $f(y|x)$ is the same as the predicted optimal distribution (S5 Appendix).

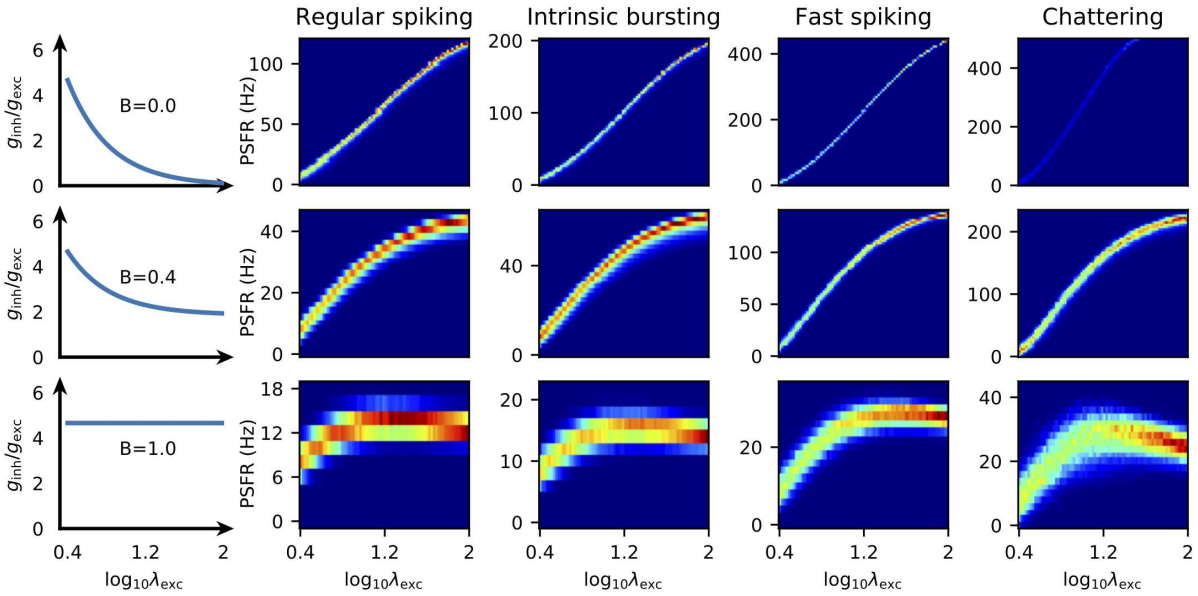

Fig 2. Stimulus-response relationships Stimulus-response relationships for the MAT neurons specified by the parameters in Table A in S1 Appendix. Each row corresponds to a different inhibition regime. The ratio of inhibitory to excitatory conductance as a function of stimulus intensity is displayed in the leftmost column. The time window Δ was in this case chosen as 500 ms. The x-axis is logarithm of the rate of bombardment by excitatory synapses (Eq 23). The y-axis shows the post-synaptic firing rate (Eq 21). The rate of inhibitory synapses is specified by B (Eq 24). This Figure is also available with equally scaled y-axes for all neurons and regimes (S1 Figure).

Results

The capacity-cost functions

We evaluated the information transmission capabilities for different stimulation scenarios distinguished by the amount of inhibition associated with the stimulus. In each scenario, the frequency of excitatory synapses ranged from $\lambda_{\text{exc}}^{(\text{bcg})}$ to approximately $40 \cdot \lambda_{\text{exc}}^{(\text{bcg})}$, therefore the intensity of the stimulus can be represented by $A \in [1, 40]$:

$$\lambda_{\text{exc}} = A \cdot \lambda_{\text{exc}}^{(\text{bcg})}. \tag{23}$$

The frequency of inhibitory synapses added on top of $\lambda_{\text{inh}}^{(\text{bcg})}$ generally scales linearly with the intensity added on top of $\lambda_{\text{exc}}^{(\text{bcg})}$, i.e. with $A - 1$. The frequency of inhibitory synapses can be than expressed with an *inhibition scaling factor* B as

$$\lambda_{\text{inh}} = \lambda_{\text{inh}}^{(\text{bcg})} \left(1 + B(A - 1)\right). \tag{24}$$

From the stimulus-response relationships (Fig 2) it is obvious that the fast spiking (FS) and chattering (CH) neurons have an advantage of a wide range of possible outputs. Also the excitation-only stimulation scenario ($B = 0$) allows for higher firing rates (i.e., offers wider coding range). However, when the metabolic expenses are taken into account the range of possible outputs becomes less important (because of the high associated expenses). This can be seen in Fig 3 where the capacity cost function for four different parameter sets of the MAT model (Table A in S1 Appendix) is shown and it is illustrated how the capacity cost function translates to bits per spike. The RS neuron is

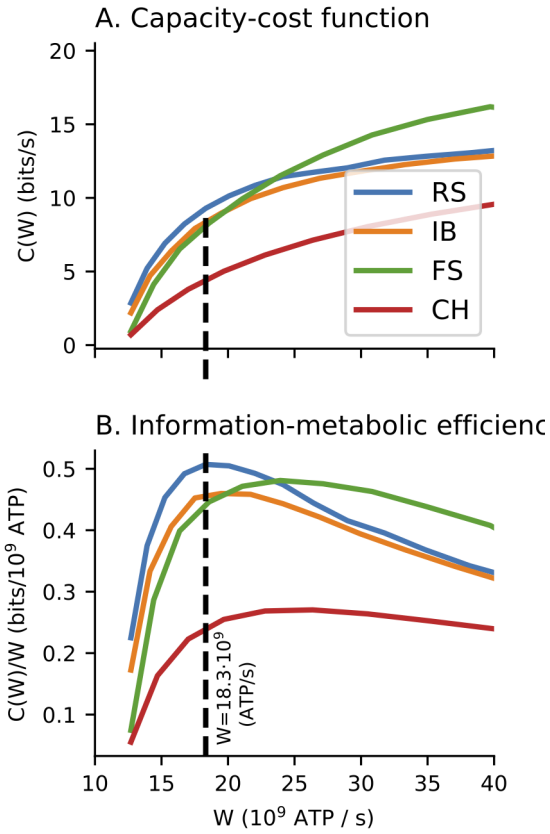

Fig 3. Capacity-cost function Capacity-cost function (panel A) and capacity per spike (panel B) for the case of coding time window $\Delta = 100\,\text{ms}$ and inhibition scaling factor $B = 0.4$. The dashed vertical line indicates the cost at which the optimal capacity per spike for the RS neuron is reached.

generally the most efficient independently either of the inhibition scaling factor B or the coding time window. Moreover, since at any allowed cost either the RS of the FS neuron offer the highest amount of transmitted information, we conclude that the bursting behavior is not beneficial for rate coding. This was also observed experimentally for temporal code [59].

Inhibition stabilizes the membrane potential

We observed that higher inhibition to excitation ratios leads to lower membrane potential fluctuations. This arises as an effect of synaptic filtering and reversal potentials, which are both biologically important parts of neural communication and essential for observation of this phenomenon (see S4 Appendix for details). In [60], similar effect was reported for a membrane potential model without synaptic filtering, however, only for a strongly hyperpolarized membrane. The suppression of membrane potential fluctuations has also been observed in vivo [61].

The decrease in the membrane potential's standard deviation leads to a more reliable firing rate (response) and subsequently higher signat-to-noise ratio (SNR) in regimes with stronger inhibition (Fig 4). For given time window Δ and inhibition

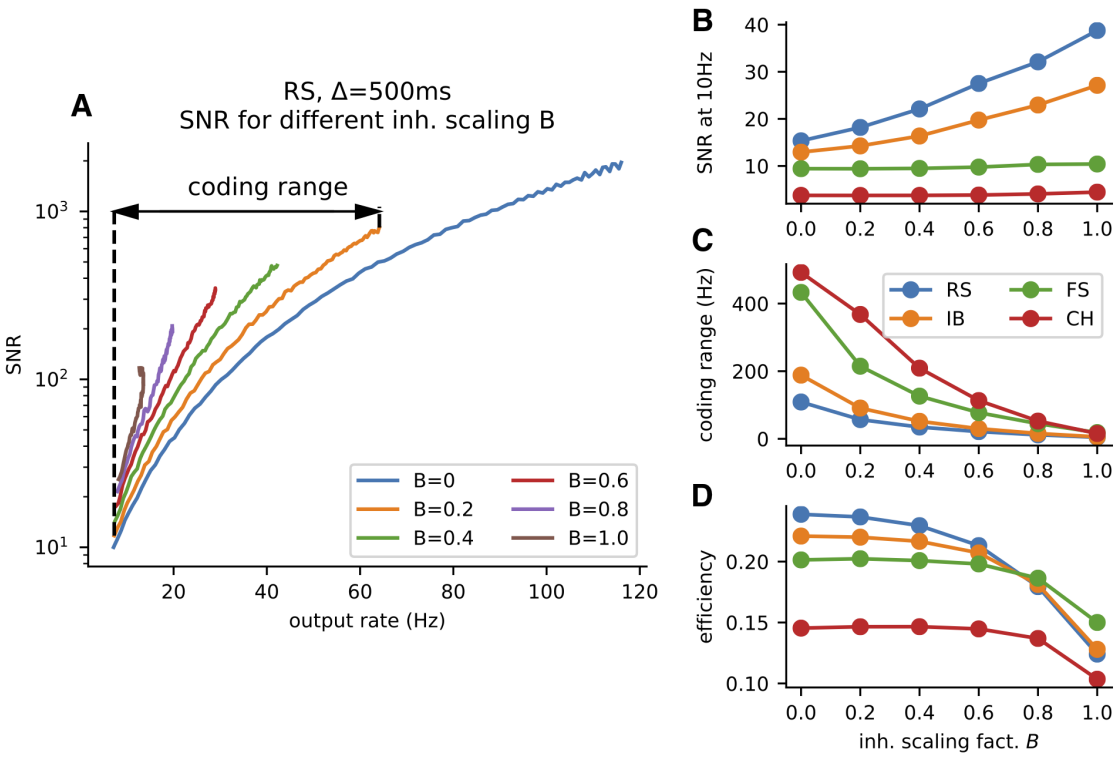

Fig 4. The effect of inhibition on metabolically efficient information transfer. (A) Signal-to-noise ratio (SNR, Eq (25)) of the RS neuron's response as a function of the mean post-synaptic firing rate $r(x)$ (Eq 26). Higher inhibition leads to a higher SNR, however, also to a lower coding range. The coding range for $B = 0.2$ is visualized in the plot. (B) The SNR at 10 Hz at different inhibition levels for all four neurons. The effect of the decreased membrane potential fluctuations on the FS and CH neurons is negligible, as opposed to the RS and IB neurons. (C) Decrease of the coding range with inhibition. (D) The metabolic efficiency in bits per spike (Eq (18)). The initial increase in the efficiency is almost negligible, however, the drop for $B = 1$ caused by the narrow coding range is apparent. The time window used for this figure is $\Delta = 500$ ms.

scaling factor B, SNR is defined as

$$\mathrm{SNR}(x;\Delta,B) = \left(\frac{r(x;\Delta,B)}{s(x;\Delta,B)}\right)^2, \tag{25}$$

where $r(x;\Delta,B)$ is the mean response to the stimulus x, given the time window Δ and the inhibition scaling factor B, $s(x;\Delta,B)$ is the standard deviation of the response:

$$r(x) = \frac{1}{\Delta}\sum_{y=0}^{+\infty} y f(y|x), \tag{26}$$

$$s(x) = \frac{1}{\Delta}\sqrt{\sum_{y=0}^{+\infty} y^2 f(y|x) - r(x)^2}. \tag{27}$$

The effect of inhibition on metabolic efficiency

The higher ratio of inhibition to excitation also has some negative consequences:

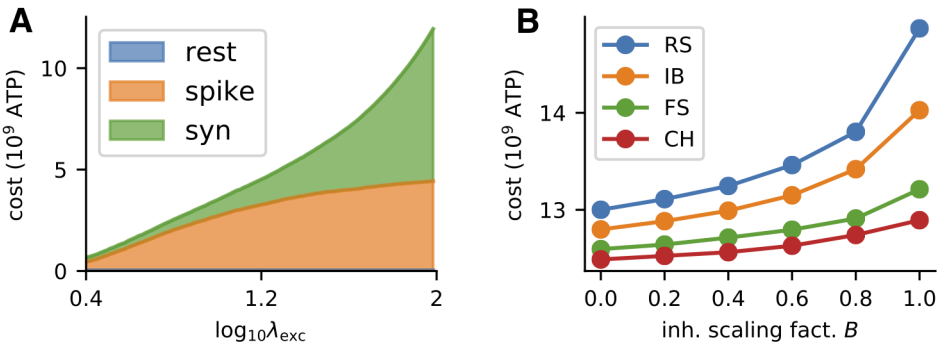

Fig 5. Metabolic cost of neural activity (A) Cost of response for a given input $x = \lambda_{\text{exc}}$, RS neuron (Tab A in S1 Appendix), $\Delta = 100\,\text{ms}$, $B = 0.4$. (B) Cost of maintaining a firing rate of 12 Hz for 100 ms for different values of inhibition to excitation ratio.

1. The inhibition limits the possible depolarization of the membrane and the neuron is unable to attain high firing rates. We quantify this by defining the coding range:
$$\text{CR}(\Delta, B) = \max_{x_1, x_2} \left(r(x_2; \Delta, B) - r(x_1; \Delta, B) \right). \tag{28}$$
We observe that the coding range is generally decreased with increased amount of inhibition (Fig 2, Fig 4A).

2. To attain identical mean firing rate with higher excitation to inhibition ratio, the excitatory synaptic current has to be larger and therefore such stimulation is associated with higher metabolic costs (Fig 5).

Surprisingly, the information theoretical efficiency is generally unaffected by the level of inhibition, meaning that the increase in signal to noise ratio and decrease of coding range effectively even out. This holds up to a certain point, when the coding range becomes too narrow and the efficiency of information transfer starts dropping dramatically (Fig 4D).

The optimal PSFR histograms

By evaluating the information-metabolic efficiency we also obtain the optimal input-output statistics. The resulting optimal post-synaptic firing rate (PSFR) histograms (Eq (11)) provide a potentially testable prediction (Fig 6). Our predictions need to be tested against long in-vivo recordings, such as in [33, 62, 63]. Qualitatively, our predictions agree with the observations in [33], that the probabilities of large firing rates are suppressed, moreover, the tail is approximately exponential with respect to the metabolic cost (Eq 10), as observed by Polavieja [30, 31]. Polavieja assumes that the overall cost grows linearly with the output rate. For the case of metabolic cost considered in this paper, the nonlinearity is important mostly for high firing rates.

Optimal input distributions

As we showed in the Methods section, the optimal input distribution has non-zero probability only for a finite number of points. However, the optimal conditions can be nearly reached by many different input distributions (Fig 7). Generally, we see a trend

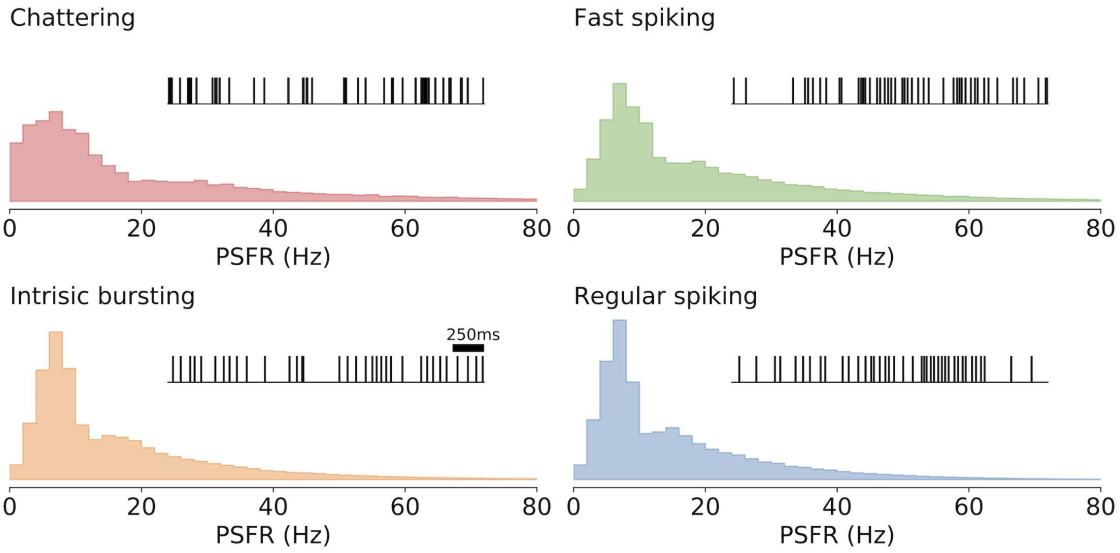

Fig 6. Predicted PSFR histograms. Post-synaptic firing rate histograms corresponding to the metabolically efficient regime with the coding time window $\Delta = 500\,\text{ms}$ and inhibition scaling factor $B = 0.4$ for the four different neurons. Unlike the statistics of the input, the output statistics can be measured in vivo and can therefore be used to verify whether a neuron employs metabolically efficient coding. A typical spike train in the efficient regime is shown for each neuron.

towards more pronounced discreteness if we desire to be closer to the true optimum. However, the increases in efficiency and effect on the PSFR distribution are only marginal. Therefore, unlike in the case of PSFR distribution which is robust, the optimal input distribution is difficult to relate to real data.

Yet we can observe that in the metabolically efficient regime, significant portion of the probability is given to the weakest input, i.e., purely spontaneous activity. For a population of independently encoding neurons this would mean that at any moment, most of them would be exhibiting only spontaneous activity.

Rate coding time-scale

Naturally, longer time windows will lead to a higher signal to noise ratio (Eq (25)) - we will be better able to identify a stimulus if we "listen" longer (Fig 8A). For a truly memoryless channel, however, the use of a shorter time window must always result in higher information capacity (measured in bits per second). Mutual information from two subsequent uses of a memoryless channel (with inputs $\mathbf{x} = \{x_1, x_2\}$ and outputs $\mathbf{y} = \{y_1, y_2\}$) is always lower or equal than double of the mutual information resulting from a single use [64]:

$$I(\mathbf{x};\mathbf{y}) = 2I(x_1;y_1) - I(y_1;y_2), \tag{29}$$

$I(y_1;y_2)$ being maximal for extreme correlation between the inputs, i.e. $x_1 = x_2$. Moreover, $I(\{x_1,x_2\};y_1+y_2) < I(\{x_1,x_1\};\{y_1,y_2\})$, since we are losing information about the temporal structure of the response. Therefore, given any probability distribution of the inputs, the mutual information for channel with a half-sized coding time window will always be higher (in bits per second):

$$I(\{x_1,x_1\};y_1+y_2) < I(\{x_1,x_1\};\{y_1,y_2\}) < 2I(x_1;y_1). \tag{30}$$

In our case, the neurons are not truly memoryless channels. They exhibit adaptation, which we took into consideration in the optimization process by using an

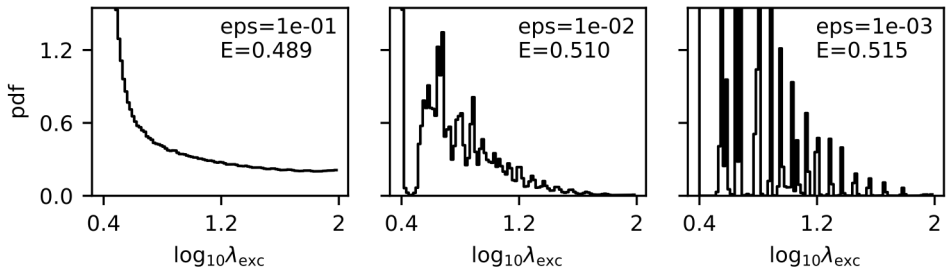

Fig 7. Approximately optimal input probability distributions The plots show different input probability distributions obtained from different steps of the Jimbo-Kunisawa algorithm. For each input distribution the estimated efficiency E (in bits / 10^9 ATP) is given in the plot together with the relative error `eps` (to the true value of the efficiency). The true value of the efficiency (Eq (18)) can be nearly reached with very different input probability distributions.

algorithm we developed specifically for this purpose (S5 Appendix). Due to adaptation, the number of spikes is influenced by the previous stimulus, thus additional noise to the stimulus-response relationship is introduced. We illustrate this by comparing the PSFR histogram for a given stimulus intensity and a coding time window $\Delta = 500\,\text{ms}$ with the PSFR histogram for a coding time window $\Delta = 100\,\text{ms}$, five times convoluted with itself, corresponding to and equal mean PSFR (Fig 8B). For a memoryless channel, the distributions would be identical. However, the distribution obtained by using a shorter time window is more spread.

We observe that while the length of time window doesn't significantly influence the mean PSFR, the information capacity with the optimal mean PSFR drops and so does the associated efficiency in bits per spike (Fig 8C-E). Therefore we can conclude the adaptation effects aren't significant enough to make coding on longer time scales more beneficial. Interestingly, however, not only the mean PSFR do not seem to be much affected by the length of the coding time window (Fig 8C), but also the shape of the PSFR histogram (computed from the optimal input distribution by Eq (11)) seems to be rather unaffected by the length of the coding time window (Fig 8F-I).

The effect of model parameters and spontaneous firing rate

In order to provide a meaningful comparison of different firing patterns, we have so far considered such parameters of the MAT model that lead to an approximately equal spontaneous firing rate (by spontaneous firing rate we mean the average response to the background noise, specified in S3 Appendix). However, it is known that neurons across different layers of the cortex exhibit different spontaneous firing rates (e.g., [65–67]).

To calculate the spontaneous activity we take advantage of the approximate formula describing the stationary firing rate f of MAT model if stimulated with a constant current I [68]:

$$f \doteq \frac{1}{\tau_2 \log\left(\frac{\alpha_2}{IR-\omega}+1\right)}. \tag{31}$$

In order to gain a general insight into the dependence of the predictions on the model parameters, we calculated the predicted mean PSFR (Eq (22)) and efficiency (Eq (18)) for 34 parameter sets corresponding to 34 neurons from the layers 2/3 and 5 of the rat motor cortex (used in [40]), kindly provided by Prof. Kobayashi. As expected, both

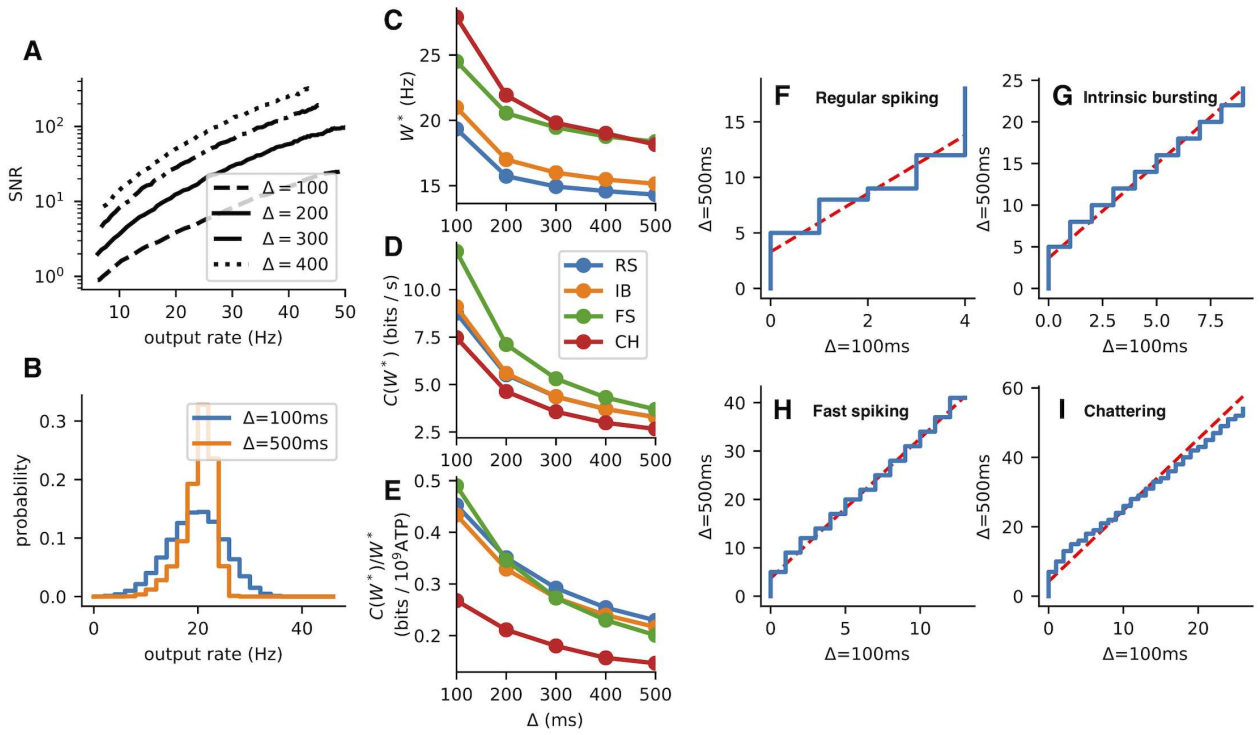

Fig 8. The effect of coding time window on metabolically efficient information transmission. (A) Signal to noise ratio for different coding time windows as a function of the mean response $r(x)$ (Eq 26). (B) Comparison of response to a given stimulus (producing a response rate of approx 20 Hz) for different coding time windows. In order to get comparable results, the distribution on number of spikes in 100 ms was five times convoluted with itself. The distribution for 100 ms is more spread due to the adaptation effects. (C) Optimal mean PSFR (Eq 22). (D) Information capacity with the optimal metabolic expenses. (E) Metabolic efficiency in bits per spikes. The decrease with the length of the coding time window shows us, that the adaptation effects visible in B don't play a significant role in this case. (F-I): Quantile-quantile plots comparing the PSFR distributions for different coding time windows. The red dashed line is a linear fit, acting as a visual guide. In the case of metabolically-efficient coding invariant on time scale, the q-q plots shouldn't deviate significantly from the line. This holds for the RS and FS neurons, for the most part also for the IB neuron. For all plots in the figure the inhibition scaling factor $B = 0.4$ was used.

efficiency and the optimal mean PSFR are strongly related to the spontaneous firing rate (Fig 9).

We confirmed that Eq (31) can be utilized to predict the spontaneous firing rate (see S6 Appendix for details) and therefore we conclude that the spontaneous firing rate and consequently also the information-metabolic efficiency are governed predominantly by α_2 and ω. Moreover, increase in any of the two parameters leads to an increase in the spontaneous firing rate and therefore increase in the mean optimal PSFR and decrease in the information-metabolic efficiency.

Discussion

The information capacity tells us what is the maximal amount of information a neuron could potentially reliably transfer. It is, however, beyond the scope of this work to investigate whether neurons utilize their full capacity and if so, how [34, 69]. The

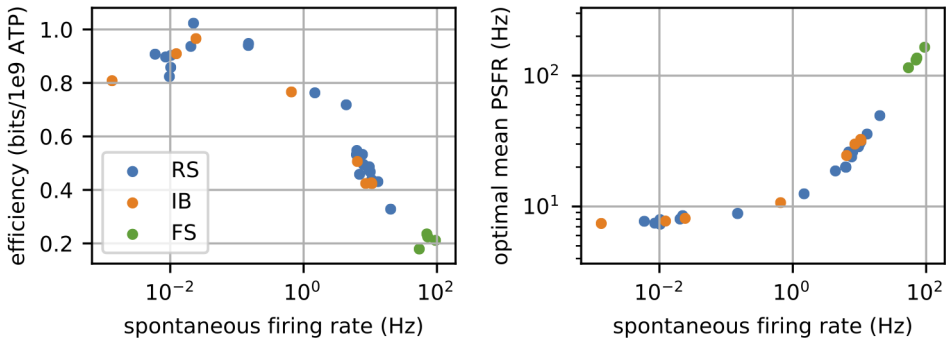

Fig 9. Cortical neurons The x-axis in both graphs is the spontaneous firing rate of the 34 neuronal models corresponding to the cortical neurons, i.e., their response to the simulated background noise. The information-metabolic efficiency (Eq (18)) and optimal mean PSFR (Eq (22)) was calculated for the case of constant inhibition ($B = 0$, $\Delta = 100\,\text{ms}$).

efficient coding hypothesis [2] leads us to believe that neurons are in some sense optimal. They need to transfer information fast and reliably and minimize the metabolic costs at the same time. This paper uses the value of information capacity per spike to take into account both information transmission and metabolic costs. Maximization of the information capacity per metabolic expenses leads to suppression of high post-synaptic firing rates observed in in-vivo recordings [33].

Analyses of this type generally have to rely on number of assumptions, including the nature of the input and the coding time scale. To mimic the nature of real neuronal synapses, we consider excitatory and inhibitory input with reversal potentials. The typical approach is to model the excitatory and inhibitory conductances as an Ornstein-Uhlenbeck process [34, 40, 49, 70], however, it has been shown that for consistency reasons, modeling the input as a shot noise with an exponential envelope is more appropriate [71]. We recreate the effect of the background network activity, during which the excitatory and inhibitory synaptic currents seem to be approximately balanced [72–77]. We then systematically explore several different input regimes differing in the amount of inhibition accompanying excitation during stimulation. This allows us to compare the different regimes by their information-energetic efficiency. Such systematic exploration also allows us to make less assumptions about the actual nature of the neuronal input and the results can also provide insight into what kind of dependency between excitation and inhibition is optimal.

The MAT model is remotely related to the model analyzed by Suksompong et. al. [36], where the threshold function can be generalized to behave similarly to MAT model. However, the key differences are in the assumptions on encoding (in [36] the information is assumed to be encoded in a sequence of inter-spike intervals, whereas we consider the rate coding) and in the input.

If the investigated neuronal model exhibits adaptation to the stimulus (as e.g. the MAT model does), the coding time scale is typically significantly limited from below, so that the influence of previous stimuli on the current response is negligible. We try to overcome this issue by proposing an algorithm which partially takes into account the effect of the previous stimulus. This is an important part of the optimization process, because otherwise we could overestimate the benefits of inhibition on the information-metabolic efficiency (Fig A in S5 Appendix).

The comparison of different noise levels was inspired by the work [70], where it was

suggested that balanced excitatory and inhibitory currents lead to more efficient information transfer. Our results can't be compared straightforwardly with [70] for several reasons. In our work, the state with balanced excitatory and inhibitory currents was considered to be the base state and we were investigating different regimes of stimulation of such neuron, whereas the work of Sengupta et. al. [70] focuses on the benefits of the balanced state. Moreover, in [70] the direct method [17] was used for evaluating information, which measures the entropy of spike trains without any reference to the stimuli, whereas we were investigating the information-transmission properties with the assumption that the neurons use rate code and computed the information capacity [10, 22] to evaluate the limits of information transmission. We observed a positive effect of higher inhibition, however, in the investigated stimulation scenarios the overall information efficiencies in bits per spike were largely unaffected by the inhibitory presynaptic activity. Robustness of the information-metabolically optimal properties with respect to the change of amount of inhibition in the system has also been recently reported by Harris et al. [78].

Numerically, our results are consistent with, e.g., [34], with the information efficiency being in the order of 0.1 bits per 10^9 ATP molecules expended. Despite the differences in spiking patterns among the neuronal classes (RS, IB, FS, CH), as quantified by local variability [79], we find that the information metabolic efficiency of the rate code is mainly governed by neuronal spontaneous activity.

We considered both the excitatory and inhibitory rates (added on top of the modulatory background network activity) to scale linearly with the stimulus intensity, since this is the simplest scenario that can be considered. For most of the stimulation scenarios, we did not observe a significant change in the information-metabolic efficiency, however, if the inhibitory rates scaled slower than linearly, we could achieve both high signal to noise ratio and a wide coding range. Such regime is likely to employ very high rates of synaptic bombardment, therefore in such case one should also consider the cost of the pre-synaptic activity.

Our results deal with a single neuron, in accord with most of the previously published work [25]. Nevertheless, Eqs (15) or (17) are easily extendable to the case of a simple homogeneous population [80]. One may also investigate the multidimensional stimulus-response relationship in a group of coupled neurons, however, the corresponding optimization is performed over joint probability distributions which becomes quickly untractable as the population size grows. It is also worth noting that the problem of optimal information transmission through nodes in general networks is still open and Eq (15) might not be directly useful [81].

To summarize the results of our work as follows:

- By employing a novel method for calculating the information transmission capabilities of channels displaying adaptation to the stimulus (S5 Appendix) we calculated numerically the information transmission capabilities of the MAT model [40] for biologically relevant parameters under metabolic constraints on different time scales and with different levels of inhibition.

- We used the results of Richardson [71] to show that inhibition can stabilize the membrane potential, leading to a more reliable response of the MAT model. To the best of our knowledge, this counter-intuitive effect of inhibition, for which we provide a theoretical justification, has not yet been reported.

- We found that the regular spiking (RS) neuron offers best information transmission per single spike, but when more energy is available, more information can be transmitted by the behavior common to fast spiking (FS) neurons. Neurons exhibiting the bursting behavior (IB, CH) were shown not to be very effective for rate coding in the investigated regimes.

- Due to adaptation effects shorter rate coding time windows led to lower signal to noise ratios. Despite the increase in noise, information can be transferred more efficiently with shorter time windows. However, we observed that the length of the time window does not significantly affect the shape of the PSFR histograms, which have the potential to be compared to experimental data.
- We found that the metabolic efficiency is surprisingly robust towards the changes in the amount of inhibition accompanying the excitation. Moreover, we observed that increased inhibition leads to higher signal to noise ratio, but also to a drop in the coding range. This does not affect the metabolic efficiency significantly until a certain point, when the coding range is so narrow that information cannot be transferred efficiently by rate code.
- We pointed out that the optimal input for a neuron using rate code has non-zero probability only for a finite number of inputs. However, by showing different input distribution, which nearly achieve the information-metabolic efficiency, we illustrated that the discreteness of the input is not a necessary condition for an effective communication.

The core of the simulation code was written in C++ and packaged as a Python module using Cython. This module is available on GitHub (`https://github.com/Tom83B/matsim`). The analysis of the data was done in Python using the NumPy and SciPy libraries. All necessary code was also uploaded to a GitHub repository (`https://github.com/Tom83B/rate-code-eff-2019`).

Acknowledgements

We would like to thank Prof. Ryota Kobayashi for helpful discussion and for providing additional data.

References

1. Dayan P, Abbott LF. Theoretical Neuroscience: Computational and Mathematical Modeling of Neural Systems. The MIT Press; 2005.
2. Barlow HB. Possible principles underlying the transformation of sensory messages. In: Rosenblith W, editor. Sensory Communication. Cambridge: MIT Press; 1961. p. 217–234.
3. Laughlin S. A simple coding procedure enhances a neuron's information capacity. Z Naturforsch [C]. 1981;36:910–912.
4. Atick JJ. Could information theory provide an ecological theory of sensory processing? Netw Comput Neural Syst. 1992;3(2):213–251.
5. Lewicki MS. Efficient coding of natural sounds. Nat Neurosci. 2002;5(4):356–363.
6. Machens CK, Gollisch T, Kolesnikova O, Herz AVM. Testing the efficiency of sensory coding with optimal stimulus ensembles. Neuron. 2005;47(3):447–456.
7. Smith EC, Lewicki MS. Efficient auditory coding. Nature. 2006;439(7079):978–982.
8. Hermundstad AM, Briguglio JJ, Conte MM, Victor JD, Balasubramanian V, Tkačik G. Variance predicts salience in central sensory processing. eLife. 2015;3:e03722.

9. Levakova M, Kostal L, Monsempès C, Jacob V, Lucas P. Moth olfactory receptor neurons adjust their encoding efficiency to temporal statistics of pheromone fluctuations. PLoS Comput Biol. 2018;14(11):e1006586. doi:10.1371/journal.pcbi.1006586.

10. Shannon C. A mathematical theory of communication. Bell system technical journal. 1948;27.

11. Attwell D, Laughlin SB. An Energy Budget for Signaling in the Grey Matter of the Brain. J Cereb Blood Flow Metab. 2001;21(10):1133–1145. doi:10.1097/00004647-200110000-00001.

12. Harris JJ, Jolivet R, Attwell D. Synaptic energy use and supply. Neuron. 2012;75(5):762–777.

13. Harris JJ, Jolivet R, Engl E, Attwell D. Energy-Efficient Information Transfer by Visual Pathway Synapses. Curr Biol. 2015;25(24):3151–3160.

14. Levy WB, Baxter RA. Energy Efficient Neural Codes. Neural Comput. 1996;8(3):531–543. doi:10.1162/neco.1996.8.3.531.

15. Stein RB, Gossen ER, Jones KE. Neuronal variability: noise or part of the signal? Nat Rev Neurosci. 2005;6(5):389–397.

16. de Ruyter van Steveninck RR. Reproducibility and Variability in Neural Spike Trains. Science. 1997;275(5307):1805–1808. doi:10.1126/science.275.5307.1805.

17. Strong SP, Koberle R, de Ruyter van Steveninck RR, Bialek W. Entropy and Information in Neural Spike Trains. Phys Rev Lett. 1998;80(1):197–200. doi:10.1103/physrevlett.80.197.

18. Borst A, Theunissen FE. Information theory and neural coding. Nat Neurosci. 1999;2(11):947–957.

19. Stein RB. The Information Capacity of Nerve Cells Using a Frequency Code. Biophys J. 1967;7(6):797–826. doi:10.1016/s0006-3495(67)86623-2.

20. de Ruyter van Steveninck RR, Laughlin SB. The rate of information transfer at graded-potential synapses. Nature. 1996;379(6566):642–645. doi:10.1038/379642a0.

21. Ikeda S, Manton JH. Capacity of a single spiking neuron channel. Neural Comput. 2009;21(6):1714–1748.

22. Gallager RG. Information Theory and Reliable Communication. New York, NY, USA: John Wiley & Sons, Inc.; 1968.

23. Dimitrov AG, Miller JP. Neural coding and decoding: communication channels and quantization. Netw Comput Neural Syst. 2001;12(4):441–472.

24. Dimitrov AG, Lazar AL, Victor JD. Information theory in neuroscience. J Comput Neurosci. 2011;30:1–5.

25. McDonnell MD, Ikeda S, Manton JH. An introductory review of information theory in the context of computational neuroscience. Biol Cybern. 2011;105:55–70.

26. Wibral M, Lizier JT, Priesemann V. Bits from brains for biologically inspired computing. Front Robot AI. 2015;2:5.

27. Laughlin SB, de Ruyter van Steveninck RR, Anderson JC. The metabolic cost of neural information. Nat Neurosci. 1998;1(1):36–41. doi:10.1038/236.

28. Balasubramanian V, Kimber D, Berry II MJ. Metabolically Efficient Information Processing. Neural Comput. 2001;13(4):799–815. doi:10.1162/089976601300014358.

29. McEliece RJ. The Theory of Information and Coding. Cambdridge, UK: Cambridge University Press; 2002.

30. de Polavieja GG. Errors Drive the Evolution of Biological Signalling to Costly Codes. J Theor Biol. 2002;214(4):657–664. doi:10.1006/jtbi.2001.2498.

31. de Polavieja GG. Reliable biological communication with realistic constraints. Phys Rev E. 2004;70(6). doi:10.1103/physreve.70.061910.

32. Adrian ED. The basis of sensation. W W Norton and Co, New York. 1928;.

33. Treves A, Panzeri S, Rolls ET, Booth M, Wakeman EA. Firing rate distributions and efficiency of information transmission of inferior temporal cortex neurons to natural visual stimuli. Neural Comput. 1999;11:601–632.

34. Kostal L, Kobayashi R. Optimal decoding and information transmission in Hodgkin–Huxley neurons under metabolic cost constraints. Biosystems. 2015;136:3–10. doi:10.1016/j.biosystems.2015.06.008.

35. Kostal L, Lansky P, McDonnell MD. Metabolic cost of neuronal information in an empirical stimulus-response model. Biol Cybern. 2013;107(3):355–365. doi:10.1007/s00422-013-0554-6.

36. Suksompong P, Berger T. Capacity Analysis for Integrate-and-Fire Neurons With Descending Action Potential Thresholds. IEEE Trans Inf Theory. 2010;56(2):838–851. doi:10.1109/tit.2009.2037042.

37. Xing J, Berger T, Sungkar M, Levy WB. Energy Efficient Neurons With Generalized Inverse Gaussian Conditional and Marginal Hitting Times. IEEE Trans Inf Theory. 2015;61(8):4390–4398. doi:10.1109/tit.2015.2444401.

38. Sungkar M, Berger T, Levy WB. Mutual Information and Parameter Estimation in the Generalized Inverse Gaussian Diffusion Model of Cortical Neurons. IEEE Trans Mol Biol Multiscale Commun. 2016;2(2):166–182. doi:10.1109/tmbmc.2017.2656861.

39. Sungkar M, Berger T, Levy WB. Capacity achieving input distribution to the generalized inverse Gaussian neuron model. In: 2017 55th Annual Allerton Conference on Communication, Control, and Computing (Allerton). IEEE; 2017.

40. Kobayashi R, Tsubo Y, Shinomoto S. Made-to-order spiking neuron model equipped with a multi-timescale adaptive threshold. Front Comput Neurosci. 2009;3:9.

41. Jolivet R, Kobayashi R, Rauch A, Naud R, Shinomoto S, Gerstner W. A benchmark test for a quantitative assessment of simple neuron models. J Neurosci Methods. 2008;169(2):417–424. doi:10.1016/j.jneumeth.2007.11.006.

42. Jolivet R, Schürmann F, Berger TK, Naud R, Gerstner W, Roth A. The quantitative single-neuron modeling competition. Biol Cybern. 2008;99(4-5):417–426. doi:10.1007/s00422-008-0261-x.

43. Gerstner W, Naud R. How Good Are Neuron Models? Science. 2009;326(5951):379–380. doi:10.1126/science.1181936.

44. Jahangiri AF, Gerling GJ. A multi-timescale adaptive threshold model for the SAI tactile afferent to predict response to mechanical vibration. Int IEEE EMBS Conf Neural Eng. 2011; p. 152–155.

45. Kobayashi R, Kitano K. Impact of slow K+ currents on spike generation can be described by an adaptive threshold model. J Comput Neurosci. 2016;40(3):347–362. doi:10.1007/s10827-016-0601-0.

46. Gerstner W, Kistler WM, Naud R. Neuronal Dynamics. Cambridge University Press; 2019. Available from: https://www.ebook.de/de/product/22190732/wulfram_gerstner_werner_m_kistler_richard_naud_neuronal_dynamics.html.

47. Levakova M, Kostal L, Monsempès C, Lucas P, Kobayashi R. Adaptive integrate-and-fire model reproduces the dynamics of olfactory receptor neuron responses in a moth. J R Soc Interface. 2019;16(157):20190246. doi:10.1098/rsif.2019.0246.

48. Witsenhausen H. Some aspects of convexity useful in information theory. IEEE Trans Inf Theory. 1980;26(3):265–271. doi:10.1109/TIT.1980.1056173.

49. Destexhe A, Rudolph M, Fellous JM, Sejnowski TJ. Fluctuating synaptic conductances recreate in vivo-like activity in neocortical neurons. Neuroscience. 2001;107:13–24.

50. Sengupta B, Stemmler M, Laughlin SB, Niven JE. Action Potential Energy Efficiency Varies Among Neuron Types in Vertebrates and Invertebrates. PLoS Comput Biol. 2010;6(7):e1000840. doi:10.1371/journal.pcbi.1000840.

51. Harris JJ, Attwell D. The Energetics of CNS White Matter. J Neurosci. 2012;32(1):356–371. doi:10.1523/jneurosci.3430-11.2012.

52. Butts DA, Goldman MS. Tuning Curves, Neuronal Variability, and Sensory Coding. PLoS Biol. 2006;4(4):e92.

53. Bezzi M. Quantifying the information transmitted in a single stimulus. Biosystems. 2007;89:4–9.

54. Kostal L, D'Onofrio G. Coordinate invariance as a fundamental constraint on the form of stimulus-specific information measures. Biol Cybern. 2018;112(1–2):13–23.

55. Luenberger DG. Optimization by Vector Space Methods. 1st ed. New York, NY, USA: John Wiley & Sons, Inc.; 1997.

56. Smith JG. The Information Capacity of Amplitude- and Variance-Constrained Scalar Gaussian Channels. Information and Control. 1971;18(3):203–219.

57. Verdu S. On channel capacity per unit cost. IEEE Trans Inf Theory. 1990;36(5):1019–1030. doi:10.1109/18.57201.

58. Abou-Faycal IC, Trott MD, Shamai S. The capacity of discrete-time memoryless Rayleigh-fading channels. IEEE Trans Inf Theory. 2001;47(4):1290–1301. doi:10.1109/18.923716.

59. Reinagel P, Reid RC. Temporal Coding of Visual Information in the Thalamus. J Neurosci. 2000;20(14):5392–5400. doi:10.1523/jneurosci.20-14-05392.2000.

60. Richardson MJE. Effects of synaptic conductance on the voltage distribution and firing rate of spiking neurons. Phys Rev E. 2004;69(5). doi:10.1103/physreve.69.051918.

61. Monier C, Chavane F, Baudot P, Graham LJ, Frégnac Y. Orientation and Direction Selectivity of Synaptic Inputs in Visual Cortical Neurons. Neuron. 2003;37(4):663–680. doi:10.1016/s0896-6273(03)00064-3.

62. Isomura Y, Harukuni R, Takekawa T, Aizawa H, Fukai T. Microcircuitry coordination of cortical motor information in self-initiation of voluntary movements. Nat Neurosci. 2009;12(12):1586–1593. doi:10.1038/nn.2431.

63. Tsubo Y, Isomura Y, Fukai T. Power-Law Inter-Spike Interval Distributions Infer a Conditional Maximization of Entropy in Cortical Neurons. PLoS Comput Biol. 2012;8(4):e1002461. doi:10.1371/journal.pcbi.1002461.

64. Kostal L. Information capacity in the weak-signal approximation. Phys Rev E. 2010;82(2). doi:10.1103/physreve.82.026115.

65. Shafi M, Zhou Y, Quintana J, Chow C, Fuster J, Bodner M. Variability in neuronal activity in primate cortex during working memory tasks. Neuroscience. 2007;146(3):1082–1108. doi:10.1016/j.neuroscience.2006.12.072.

66. O'Connor DH, Peron SP, Huber D, Svoboda K. Neural Activity in Barrel Cortex Underlying Vibrissa-Based Object Localization in Mice. Neuron. 2010;67(6):1048–1061. doi:10.1016/j.neuron.2010.08.026.

67. Buzsáki G, Mizuseki K. The log-dynamic brain: how skewed distributions affect network operations. Nat Rev Neurosci. 2014;15:264–278. doi:10.1038/nrn3687.

68. Yamauchi S, Kim H, Shinomoto S. Elemental Spiking Neuron Model for Reproducing Diverse Firing Patterns and Predicting Precise Firing Times. Front Comput Neurosci. 2011;5. doi:10.3389/fncom.2011.00042.

69. Kostal L, Kobayashi R. Critical size of neural population for reliable information transmission. Phys Rev E (Rapid Commun). 2019;100(1):050401(R).

70. Sengupta B, Laughlin SB, Niven JE. Balanced Excitatory and Inhibitory Synaptic Currents Promote Efficient Coding and Metabolic Efficiency. PLoS Comput Biol. 2013;9(10):e1003263. doi:10.1371/journal.pcbi.1003263.

71. Richardson MJE, Gerstner W. Synaptic Shot Noise and Conductance Fluctuations Affect the Membrane Voltage with Equal Significance. Neural Comput. 2005;17(4):923–947. doi:10.1162/0899766053429444.

72. Bernander O, Douglas RJ, Martin KA, Koch C. Synaptic background activity influences spatiotemporal integration in single pyramidal cells. Proc Natl Acad Sci USA. 1991;88(24):11569–11573. doi:10.1073/pnas.88.24.11569.

73. Paré D, Shink E, Gaudreau H, Destexhe A, Lang EJ. Impact of Spontaneous Synaptic Activity on the Resting Properties of Cat Neocortical Pyramidal Neurons In Vivo. J Neurophysiol. 1998;79(3):1450–1460. doi:10.1152/jn.1998.79.3.1450.

74. Destexhe A, Rudolph M, Paré D. The high-conductance state of neocortical neurons in vivo. Nat Rev Neurosci. 2003;4(9):739–751. doi:10.1038/nrn1198.

75. Mittmann W, Koch U, Häusser M. Feed-forward inhibition shapes the spike output of cerebellar Purkinje cells. J Physiol (Lond). 2005;563(2):369–378. doi:10.1113/jphysiol.2004.075028.

76. Wolfart J, Debay D, Masson GL, Destexhe A, Bal T. Synaptic background activity controls spike transfer from thalamus to cortex. Nat Neurosci. 2005;8(12):1760–1767. doi:10.1038/nn1591.

77. Rudolph M, Pospischil M, Timofeev I, Destexhe A. Inhibition Determines Membrane Potential Dynamics and Controls Action Potential Generation in Awake and Sleeping Cat Cortex. J Neurosci. 2007;27(20):5280–5290. doi:10.1523/jneurosci.4652-06.2007.

78. Harris JJ, Engl E, Attwell D, Jolivet RB. Energy-efficient information transfer at thalamocortical synapses. PLoS Comput Biol. 2019;15(8):e1007226. doi:10.1371/journal.pcbi.1007226.

79. Kobayashi R, Kurita S, Kurth A, Kitano K, Mizuseki K, Diesmann M, et al. Reconstructing neuronal circuitry from parallel spike trains. Nat Commun. 2019;10(1). doi:10.1038/s41467-019-12225-2.

80. Kostal L, Lansky P. Information capacity and its approximations under metabolic cost in a simple homogeneous population of neurons. Biosystems. 2013;112(3):265–275. doi:10.1016/j.biosystems.2013.03.019.

81. El Gamal A, Kim YH. Network Information Theory. New York: Cambridge University Press; 2011.

Supporting information

S1 Appendix. Parameters of the MAT model.

S2 Appendix. Numerical simulation of the leaky integrator.

S3 Appendix. Spontaneous activity.

S4 Appendix. Variability of the steady-state membrane potential.

S5 Appendix. Information capacity of channels exhibiting adaptation.

S6 Appendix. Approximation of spontaneous firing rate.

S1 Figure. Stimulus-response relationships with identical scales. Same as Fig 2, but the scales are same for all the neurons and inhibition scaling factors B. Each row corresponds to a different inhibition regime. The ratio of inhibitory to excitatory conductance as a function of stimulus intensity is displayed in the leftmost column. The time window Δ was in this case chosen as 500 ms. The x-axis is logarithm of the rate of bombardment by excitatory synapses (Eq 23). The y-axis shows the post-synaptic firing rate (Eq 21).

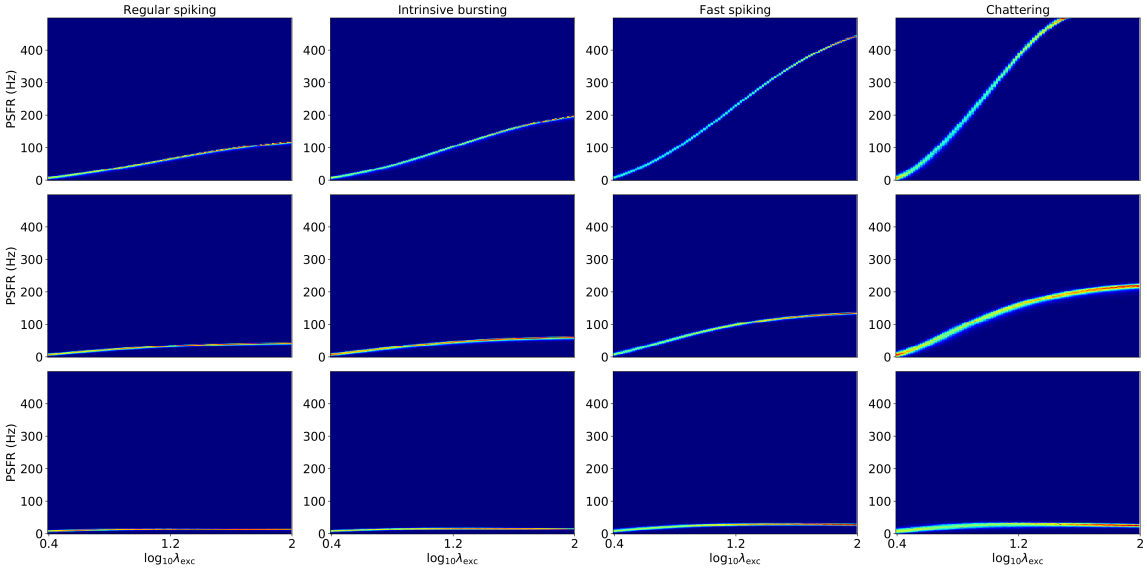

S1 Fig. – Stimulus-response relationships with identical scales. Same as Fig 2, but the scales are same for all the neurons and inhibition scaling factors B. Each row corresponds to a different inhibition regime. The ratio of inhibitory to excitatory conductance as a function of stimulus intensity is displayed in the leftmost column. The time window Δ was in this case chosen as 500 ms. The x-axis is logarithm of the rate of bombardment by excitatory synapses (Eq 23). The y-axis shows the post-synaptic firing rate (Eq 21).

Table S1.1: Parameters of studied neurons

	α_1	α_2	ω
Regular spiking (RS)	30 mV	2.0 mV	−65 mV
Intrinsive bursting (IB)	7.5 mV	1.5 mV	−64.3 mV
Fast spiking (FS)	10 mV	0.2 mV	−62.4 mV
Chattering (CH)	−0.5 mV	0.4 mV	−61.8 mV

S1 Appendix

Parameters of the MAT model.

Kobayashi et al. (2009) identified sets of parameters of the MAT model that correspond to real cortical neurons belonging to different classes, based on their spiking pattern (FS, IB, RS) or are capable of reproducing the same general behavior (CH). The following parameters were common for all four neurons: $\tau_\mathrm{m} = 5\,\mathrm{ms}$, $R = 50\,\mathrm{M}\Omega$ and $\tau_1 = 10\,\mathrm{ms}$, $\tau_2 = 200\,\mathrm{ms}$, $L = 2$. We used the values of α_1 and α_2 as suggested in Kobayashi et al. (2009) and chose the value of ω so that the mean firing rate in the presence of spontaneous background activity (i.e. $\lambda_\mathrm{exc} = \lambda_\mathrm{exc}^{(\mathrm{bcg})}$, $\lambda_\mathrm{inh} = \lambda_\mathrm{inh}^{(\mathrm{bcg})}$) was approximately 8 Hz in the steady state. This is roughly in accordance with spontaneous firing rates observed in awake animals (e.g., Steriade et al. (2001); O'Connor et al. (2010)). The exact value of spontaneous firing rate is not crucial, since it does not affect the qualitative character of the results. The used values of the free parameters α_1, α_2 and ω are given in Table S1.1.

References

R. Kobayashi, Y. Tsubo, and S. Shinomoto. Made-to-order spiking neuron model equipped with a multi-timescale adaptive threshold. *Front Comput Neurosci*, 3:9, 2009.

D. H. O'Connor, S. P. Peron, D. Huber, and K. Svoboda. Neural activity in barrel cortex underlying vibrissa-based object localization in mice. *Neuron*, 67(6):1048–1061, sep 2010. doi: 10.1016/j.neuron.2010.08.026.

M. Steriade, I. Timofeev, and F. Grenier. Natural waking and sleep states: A view from inside neocortical neurons. *Journal of Neurophysiology*, 85(5): 1969–1985, may 2001. doi: 10.1152/jn.2001.85.5.1969.

S2 Appendix.

Numerical simulation of the leaky integrator.

Eq (1) may be rewritten as:

$$\frac{\mathrm{d}V}{\mathrm{d}t} = -\frac{1}{\tau(g_\mathrm{e}, g_\mathrm{i})}\left(V - \hat{V}(g_\mathrm{e}, g_\mathrm{i})\right), \tag{S2.1}$$

where

$$\tau(g_\mathrm{e}, g_\mathrm{i}) = \frac{\tau_m}{1 + R(g_\mathrm{e} + g_\mathrm{i})}, \tag{S2.2}$$

$$\hat{V} = \frac{E_\mathrm{L} + R(g_\mathrm{e}E_\mathrm{e} + g_\mathrm{i}E_\mathrm{i})}{1 + R(g_\mathrm{e} + g_\mathrm{i})}. \tag{S2.3}$$

Considering the conductances to be constant during the integration time step $\Delta t = 0.1\,\mathrm{ms}$, we can integrate the equation as follows:

$$V_{n+1} = \hat{V} + (V_n - \hat{V})\exp(-\Delta t/\tau). \tag{S2.4}$$

S3 Appendix.

Spontaneous activity.

In (Destexhe et al., 2003) the values of average and standard deviation of the conductances during spontaneous background activity were reported as 0.012 and 0.0030 µS for g_{exc} and 0.057 and 0.0066 µS for g_{inh}. The goal was to reproduce these values using shot noise with exponential decay described by Eqs (5,6).

When the spike arrival times are Poissonian, the following holds (e.g., Rajdl and Lansky (2015)):

$$\mathrm{E}(g_{\mathrm{exc}}(t)) = \tau_{\mathrm{exc}}\bar{g}_{\mathrm{exc}}\lambda_{\mathrm{exc}}, \tag{S3.1}$$

$$\mathrm{Var}(g_{\mathrm{exc}}(t)) = \frac{1}{2}\tau_{\mathrm{exc}}\lambda_{\mathrm{exc}}\bar{g}^2_{\mathrm{exc}}. \tag{S3.2}$$

Then it follows, that for fixed τ_{exc} and mean and variance given, the intensity and peak conductance have to be chosen as

$$\bar{g}_{\mathrm{exc}} = 2\frac{\mathrm{Var}(\mathrm{g_{exc}(t)})}{\mathrm{E}(\mathrm{g_{exc}(t)})} \tag{S3.3}$$

$$\lambda_{\mathrm{exc}} = \frac{\mathrm{E}(\mathrm{g_{exc}(t)})}{\bar{g}_{\mathrm{exc}}\tau_{\mathrm{exc}}}. \tag{S3.4}$$

Computation of $\bar{g}_{\mathrm{exc}}$ and λ_{exc} is then identical.

References

A. Destexhe, M. Rudolph, and D. Paré. The high-conductance state of neocortical neurons in vivo. *Nature Reviews Neuroscience*, 4(9):739–751, sep 2003. doi: 10.1038/nrn1198.

K. Rajdl and P. Lansky. Stein's neuronal model with pooled renewal input. *Biological Cybernetics*, 109(3):389–399, apr 2015. doi: 10.1007/s00422-015-0650-x.

S4 Appendix.

Variability of the steady-state membrane potential.

Mean and variance of the membrane potential (given by Eq (1)), driven by Poissonian shot noise conductances, can be approximated as (Richardson and Gerstner, 2005):

$$\langle V \rangle = \mu_V + E_0 \tag{S4.1}$$

$$\langle V^2 \rangle - \langle V \rangle^2 = \left(\frac{\sigma_{\text{exc}}}{g_0}\right)^2 \mathcal{E}_{\text{exc}}^2 \frac{\tau_{\text{exc}}}{\tau_{\text{exc}} + \tau_0} + \left(\frac{\sigma_{\text{inh}}}{g_0}\right)^2 \mathcal{E}_{\text{inh}}^2 \frac{\tau_{\text{inh}}}{\tau_{\text{inh}} + \tau_0}, \tag{S4.2}$$

where σ_{exc}^2, σ_{inh}^2 are the variances of the shot noise (Eq (S3.2)) and

$$g_0 = \frac{1}{R} + g_{\text{exc0}} + g_{\text{inh0}}, \tag{S4.3}$$

$$E_0 = \frac{1}{g_0}\left(\frac{1}{R}E_L + g_{\text{exc0}}E_{\text{exc}} + g_{\text{inh0}}E_{\text{inh}}\right), \tag{S4.4}$$

$$\mathcal{E}_{\text{exc}} = E_{\text{exc}} - E_0, \tag{S4.5}$$

$$\mathcal{E}_{\text{inh}} = E_{\text{inh}} - E_0, \tag{S4.6}$$

$$\tau_0 = \frac{\tau_m}{R g_0}, \tag{S4.7}$$

$$\mu_V = \left(\frac{\sigma_{\text{exc}}}{g_0}\right)^2 \mathcal{E}_{\text{exc}} \frac{\tau_{\text{exc}}}{\tau_{\text{exc}} + \tau_0} + \left(\frac{\sigma_{\text{inh}}}{g_0}\right)^2 \mathcal{E}_{\text{inh}} \frac{\tau_{\text{inh}}}{\tau_{\text{inh}} + \tau_0} \tag{S4.8}$$

g_{exc0}, g_{inh0} denote the shot noise means (S3 Appendix):

$$g_{\text{exc0}} = \tau_{\text{exc}} \bar{g}_{\text{exc}} \lambda_{\text{exc}}, \tag{S4.9}$$

$$g_{\text{inh0}} = \tau_{\text{inh}} \bar{g}_{\text{inh}} \lambda_{\text{inh}}. \tag{S4.10}$$

These approximations provide a very good estimate of the mean and standard deviation of the membrane potential (Fig S4.1). Both in the theoretical approximations and in the simulated values we see that given the same mean value of the membrane potential, with higher inhibition to excitation ratio, the standard deviation of the membrane potential drops. Some insight can be gained by analyzing the limit case, i.e., λ_{exc} and λ_{inh} both tending to infinity while the inhibition scaling factor B is held constant. Then:

$$\langle V \rangle \to \frac{\tau_{\text{exc}} \bar{g}_{\text{exc}} E_{\text{exc}} + B \tau_{\text{inh}} \bar{g}_{\text{inh}} E_{\text{inh}}}{\tau_{\text{exc}} \bar{g}_{\text{exc}} + B \tau_{\text{inh}} \bar{g}_{\text{inh}}}, \tag{S4.11}$$

$$\sigma_V = \sqrt{\langle V^2 \rangle - \langle V \rangle^2} \to 0. \tag{S4.12}$$

With increasing B, $\langle V \rangle$ drops and therefore, hypothetically, we can reach zero variance of the membrane potential and the lower the desired mean value, the higher B is needed.

Although we used the Poisson shot noise with an exponential filtering as an input, the results apply also for the Ohrstein-Uhlenbeck input approximation. The only difference will be in Eq (S4.1), because for the Ohrstein-Uhlenbeck approximation $\langle V \rangle = E_0$ (Richardson, 2004; Richardson and Gerstner, 2005).

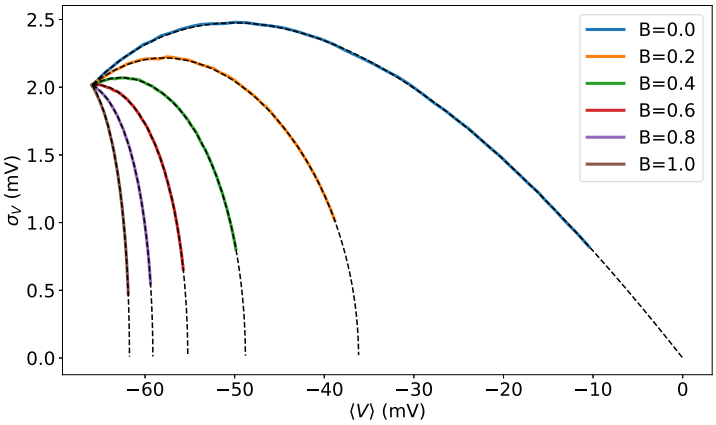

Figure S4.1: Standard deviation of the membrane potential as a function of its mean. Color-coded are different inhibition to inhibition scaling factor B. Dashed lines indicate the theoretical approximations (Eqs (S4.1, S4.2))

References

M. J. E. Richardson. Effects of synaptic conductance on the voltage distribution and firing rate of spiking neurons. *Physical Review E*, 69(5), may 2004. doi: 10.1103/physreve.69.051918.

M. J. E. Richardson and W. Gerstner. Synaptic shot noise and conductance fluctuations affect the membrane voltage with equal significance. *Neural Computation*, 17(4):923–947, apr 2005. doi: 10.1162/0899766053429444.

S5 Appendix.

Information capacity of channels exhibiting adaptation.

Classical algorithm for computation of the information capacity C (Eq (15)) of a memoryless channel withou feedback and the optimal input distribution is the Blahut-Arimoto algorithm (Blahut, 1972). Blahut (1972) also offers an extension of the algorithm for computation of the constrained capacity $C(W)$ (Eq (17)), however, the cost restriction is not straightforward and we used the cutting plane algorithm (Huang and Meyn, 2005; Kelley, 1960) for computation of the capacity-cost function instead (for condensed summary of the algorithm in the context of neuroscience see (Kostal and Lansky, 2013, Appendix A)).

For evaluating the capacity-cost functions, is is necessary to evaluate $C(W)$ for many different values of the cost W. When only the optimal state (maximal amount of transferred information per unit of cost) is of interest, it is possible to use the Jimbo-Kunisawa algorithm Jimbo and Kunisawa (1979); Suksompong and Berger (2010), for which the input distribution converges towards the state of maximal $C(W)/W$.

For neurons, it takes some time for the neuron to reach its steady state. A transition between an intense stimulus to a less intense one is usually followed by a period of silence when no spike is fired, because the dynamic threshold takes some time to reach the new level of the membrane potential. On the other hand, transitions from a less intense stimulus to a more intense one causes an immediate increase in the firing rate which then slowly decreases until it reaches its steady state value. Thus the statistics of transitions between stimuli can have a significant effect on the observed response statistics to individual stimuli.

To mitigate the effect of past stimuli, ideally, we want the stimulus response relationship to be generated with the same input statistics as the S-R relationship predicts to be the optimum. However, the optimal input statistics depend on the S-R relationship. We solved the problem in the following manner:

1. For each possible stimulus s, we evaluate the stimulus response relationship $P_s(y|x)$ - i.e. the S-R relationship if the previous stimulus is always s
2. We select an arbitrary starting input probability assignment p^0
3. We compute the n-th S-R relationship as $P^n(y|x) = \sum_{s\in\mathcal{S}} p^n(s)P_s(y|x)$
4. The input probability assignment that is optimal given the S-R relationship (found using e.g. the cutting plane or Jimbo-Kunisawa algorithm) is then the $(n+1)$-th input probability assignment p_{n+1}.

Steps 3. and 4. are repeated until a self-consistent solution is found.

By comparing the efficiency after the first iteration with the efficiency after 5 iterations for different levels of inhibition (Fig S5.1), we see the necessity of the described algorithm. Simply calculating the efficiency by the Jimbo-Kunisawa algorithm (i.e., stopping after the first iteration) could lead us to the incorrect conclusion that higher levels of inhibition lead to substantially higher efficiency.

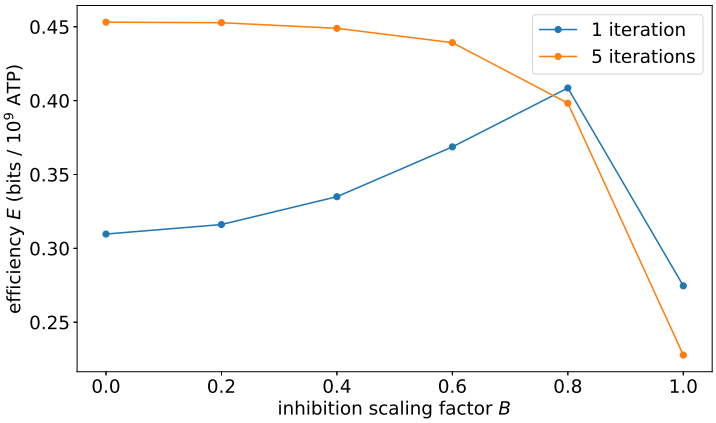

Figure S5.1: Comparison of efficiencies calculated after 1 iteration of our algorithm and after 5 iterations. IB neuron (Table S1.1), $\Delta = 100\,\text{ms}$.

References

R. Blahut. Computation of channel capacity and rate-distortion functions. *IEEE Transactions on Information Theory*, 18(4):460–473, jul 1972. doi: 10.1109/tit.1972.1054855.

J. Huang and S. Meyn. Characterization and computation of optimal distributions for channel coding. *IEEE Transactions on Information Theory*, 51(7):2336–2351, jul 2005. doi: 10.1109/tit.2005.850108.

M. Jimbo and K. Kunisawa. An iteration method for calculating the relative capacity. *Information and Control*, 43(2):216–223, nov 1979. doi: 10.1016/s0019-9958(79)90719-8.

J. E. J. Kelley. The cutting-plane method for solving convex programs. *Journal of the Society for Industrial and Applied Mathematics*, 8(4):703–712, dec 1960. doi: 10.1137/0108053.

L. Kostal and P. Lansky. Information capacity and its approximations under metabolic cost in a simple homogeneous population of neurons. *Biosystems*, 112(3):265–275, jun 2013. doi: 10.1016/j.biosystems.2013.03.019.

P. Suksompong and T. Berger. Capacity analysis for integrate-and-fire neurons with descending action potential thresholds. *IEEE Transactions on Information Theory*, 56(2):838–851, feb 2010. doi: 10.1109/tit.2009.2037042.

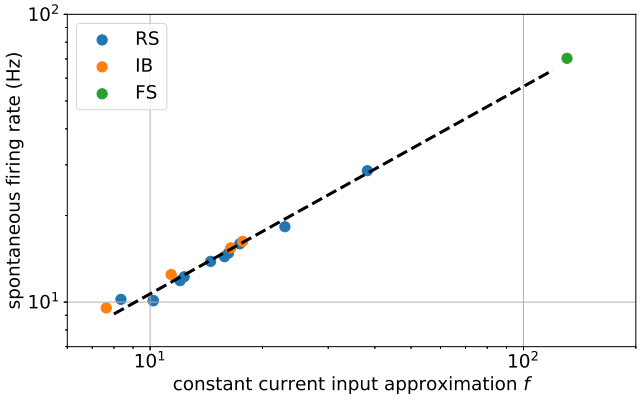

Figure S6.1: The scatter plot compares the analytical calculation obtained from Eq (31). The dashed line represents a linear fit on the log-log plot providing the functional dependence between the prediction and the spontaneous firing rate.

S6 Appendix.

Approximation of spontaneous firing rate.

Yamauchi et al. (2011) provide an approximate formula for the firing rate of the MAT model stimulated by a constant current I (Eq (31)). In our case, the neurons are not stimulated by a constant current, but by a shot noise resulting in a fluctuating membrane potential. However, we found that by substituting IR with $V_0 \doteq -63\,\mathrm{mV}$ this formula can be utilized to predict well the spontaneous firing rate for a large portion of the neurons (Fig S6.1). The value $-63\,\mathrm{mV}$ roughly represents the usual value of the membrane potential when a spike is fired during the spontaneous activity. The formula in Eq (31) can provide predictions only for those parameter sets, for which $\omega > V_0$, thus excluding 15 neurons, generally with a negligible spontaneous activity. Moreover, the approximation does not apply for high firing rates, therefore also 3 FS neurons were excluded.

Linear fit in the Fig S6.1 provides us with a formula for the spontaneous firing rate $y_{\mathrm{spont}} \approx 10^{0.31} f^{0.72}$. Although the formula does not give a strict approximation of the spontaneous firing rate, it clearly explains almost all of the variance for the neurons with $\omega > V_0$, moreover, the dependence is monotonic. Therefore increase in f will lead to an increase in the spontaneous firing rate y_{spont}.

References

S. Yamauchi, H. Kim, and S. Shinomoto. Elemental spiking neuron model for reproducing diverse firing patterns and predicting precise firing times. *Frontiers in Computational Neuroscience*, 5, 2011. doi: 10.3389/fncom.2011.00042.

Attachment IV

Manuscript published on *bioRxiv*. Published on 15th March 2023
doi: https://doi.org/10.1101/2023.03.13.532471

Shared input and recurrency in neural networks for metabolically efficient information transmission

Tomas Barta[1,2,3*], Lubomir Kostal[1**]

1 Institute of Physiology of the Czech Academy of Sciences, Prague, Czech Republic
2 Institute of Ecology and Environmental Sciences of Paris, INRAE, Sorbonne Université, CNRS, IRD, UPEC, Université de Paris, 78000 Versailles, France
3 Charles University, First Medical Faculty, Prague, Czech Republic

* tomas.barta@fgu.cas.cz
** kostal@biomed.cas.cz

Abstract

Shared input to a population of neurons induces noise correlations, which decreases the information carried by a population activity. The inhibitory feedback in recurrent neural networks can reduce the noise correlations and thus increase the information carried by the averaged population activity. However, the activity of inhibitory neurons is costly. The inhibitory feedback decreases the gain of the population, and depolarization of its neurons thus requires stronger excitatory synaptic input, which is associated with higher ATP molecules consumption. Assuming that the goal of neural populations is to transmit as much information as possible at minimal metabolic costs, it is unclear whether the increased information transmission reliability provided by the inhibitory feedback compensates for the additional costs. We analyze this problem in a network of leaky integrate-and-fire neurons receiving correlated input. By maximizing mutual information with metabolic cost constraints, we show that there is an optimal strength of recurrent connections in the network, which maximizes the value of mutual information-per-cost. For higher values of input correlation, the mutual information-per-cost is higher for recurrent networks with inhibitory feedback compared to feedforward networks without any inhibitory neurons. Our results, therefore, show that an optimal synaptic strength of a recurrent network can be inferred from metabolically efficient coding arguments and that the decorrelation of the input by inhibitory feedback compensates for the associated increased metabolic costs.

Author summary

Information processing in neurons is mediated by electrical activity through ionic currents. To reach homeostasis, neurons have to actively work to reverse these ionic currents. This process consumes energy in the form of ATP molecules. Typically the more energy the neuron can use, the more information it can transmit. It is generally assumed that due to evolutionary pressures, neurons evolved to process and transmit information efficiently at high rates but also at low costs. Many studies addressed this balance between transmitted information and metabolic costs for the activity of single neurons. However, information is often carried by the activity of a population of neurons instead of single neurons, and few studies investigated this balance in the context of recurrent neural networks, which can be found in the cortex. In such

networks, the external input from thalamocortical synapses introduces pairwise correlations between the neurons, complicating the information transmission. These correlations can be reduced by inhibitory feedback through recurrent connections between inhibitory and excitatory neurons in the network. However, such activity increases the metabolic cost of the activity of the network. By analyzing the balance between decorrelation through inhibitory feedback and correlation through shared input from the thalamus, we find that both the shared input and inhibitory feedback can help increase the information-metabolic efficiency of the system.

1 Introduction

The efficient coding hypothesis poses that neurons evolved due to evolutionary pressure to transmit information as efficiently as possible (Barlow, 1961). Moreover, the brain has only a limited energy budget, and neural activity is costly (Attwell and Laughlin, 2001; Harris et al., 2012). The metabolic expenses associated with the neural activity should, therefore, be considered, and neural systems likely work in an information-metabolically efficient manner, balancing the trade-off between transmitted information and cost of the neural activity (Levy and Baxter, 1996; Balasubramanian et al., 2001; Laughlin, 2001; Niven and Laughlin, 2008; Yu and Yu, 2017).

The principles of information-metabolically efficient coding have been successfully applied to study the importance of inhibition-excitation balance in neural systems. It has been shown that the mutual information between input and output per unit of cost for a single neuron is higher if the excitatory and inhibitory synaptic currents to the neuron are approximately equal if the source of noise lies in the stochastic nature of the voltage-gated $Na^+$and K^+channels (Sengupta et al., 2013). In a rate coding scheme, where the source of noise lies in the random arrival of pre-synaptic action potentials, the mutual information per unit of cost has been shown to be rather unaffected by an increase of pre-synaptic inhibition associated with an excitatory input (Barta and Kostal, 2019).

However, the balance of excitation and inhibition is likely more important in the context of recurrent neural networks than in the context of single neurons. In recurrent neural networks, the inhibitory input to neurons associated with the stimulus (Monier et al., 2003) arises as inhibitory feedback from a population of inhibitory neurons. The inhibitory feedback prevents a self-induced synchronization of the neural activity (Brunel, 2000) and reduces noise correlations induced by shared input to neurons in the population (Renart et al., 2010; Tetzlaff et al., 2012; Bernacchia and Wang, 2013). Noise correlations are detrimental to information transmission by neural populations (Abbott and Dayan, 1999; Averbeck et al., 2006) and information is likely transmitted by an activity of a population of neurons instead of a single neuron (Shadlen and Newsome, 1998). Therefore, when studying the effect of excitation-inhibition balance on information transmission, it is essential to consider the context of neural populations.

A number of studies analyzed the effect of noise correlations on the information transmission properties (Abbott and Dayan, 1999; Averbeck et al., 2006; Moreno-Bote et al., 2014). However, these studies did not analyze the relationship between the noise correlations and the metabolic cost of neural activity. In our work, we consider a computational model of a small part of a sensory cortex and noise correlations caused by shared connections from an external thalamic population. The noise correlations then may be reduced by inhibitory feedback, which, however, increases the cost of the neural activity (Barta and Kostal, 2019). Our point of interest is the trade-off between improved information transmission due to lower noise correlations and the increase in metabolic costs due to the stronger inhibitory feedback.

2 Methods

2.1 Network model

We modeled a network consisting of three subpopulations: external (ext), excitatory (exc), and inhibitory (inh). The external subpopulation consisted of Poisson neurons, defined by their firing intensity λ^0_{ext} (same for all the neurons in the subpopulation). Neurons in the excitatory and inhibitory subpopulations were modeled as leaky integrate-and-fire (LIF) neurons:

$$C_m \frac{\mathrm{d}V^i}{\mathrm{d}t} = g_L(E_L - V^i) + I^i_{\text{rec}}(V^i, t) + I^i_{\text{ext}}(V^i, t) + I_{\text{bcg}^{\text{i}}}(V^i, t), \tag{1}$$

$$I^i_{\text{rec}}(V^i, t) = g^i_{\text{exc}}(E_{\text{e}} - V^i) + g^i_{\text{inh}}(E_{\text{i}} - V^i), \tag{2}$$

$$I^i_{\text{ext}}(V^i, t) = g^i_{\text{ext}}(E_{\text{e}} - V^i) \tag{3}$$

$$I^i_{\text{bcg}}(V^i, t) = g^i_{\text{bcg,exc}}(E_{\text{e}} - V^i) + g^i_{\text{bcg,inh}}(E_{\text{i}} - V^i), \tag{4}$$

$$\tau_{\text{exc}} \frac{\mathrm{d}g^i_{\text{ext}}}{\mathrm{d}t} = -g^i_{\text{ext}} + \sum_{j=1}^{n_{\text{ext}}} \sum_{t_s \in \mathcal{T}^j_{\text{ext}}} W^{ij}_{\text{ext}} \delta(t - t_s), \tag{5}$$

$$\tau_{\text{exc}} \frac{\mathrm{d}g^i_{\text{exc}}}{\mathrm{d}t} = -g^i_{\text{exc}} + \sum_{j=1}^{n_{\text{exc}}} \sum_{t_s \in \mathcal{T}^j_{\text{exc}}} W^{ij}_{\text{exc}} \delta(t - t_s), \tag{6}$$

$$\tau_{\text{inh}} \frac{\mathrm{d}g^i_{\text{ext}}}{\mathrm{d}t} = -g^i_{\text{inh}} + \sum_{j=1}^{n_{\text{inh}}} \sum_{t_s \in \mathcal{T}^j_{\text{inh}}} W^{ij}_{\text{inh}} \delta(t - t_s), \tag{7}$$

$$\tau_{\text{exc}} \frac{\mathrm{d}g^i_{\text{bcg,exc}}}{\mathrm{d}t} = (\mu_{\text{bcg,exc}} - g^i_{\text{bcg,exc}}) + \tau_{\text{exc}} \sigma_{\text{bcg,exc}} \sqrt{\frac{2}{\tau_{\text{exc}}}} \eta^i_{\text{exc}}(t), \tag{8}$$

$$\tau_{\text{inh}} \frac{\mathrm{d}g^i_{\text{bcg,inh}}}{\mathrm{d}t} = (\mu_{\text{bcg,inh}} - g^i_{\text{bcg,inh}}) + \tau_{\text{inh}} \sigma_{\text{bcg,inh}} \sqrt{\frac{2}{\tau_{\text{inh}}}} \eta^i_{\text{inh}}(t). \tag{9}$$

I_{rec} is the synaptic current arising from the recurrent connections (exc-exc, exc-inh, inh-exc, inh-inh), I_{ext} is the excitatory current from external neurons, and I_{bcg} is the current from synapses from neighboring cortex areas. $\mathcal{T}^j_{\text{ext}}$, $\mathcal{T}^j_{\text{exc}}$, $\mathcal{T}^j_{\text{inh}}$ represent the spike times of the j-th external, excitatory, and inhibitory neuron respectively. The matrices $\mathbf{W}_{\text{ext}}$, $\mathbf{W}_{\text{exc}}$, $\mathbf{W}_{\text{inh}}$ contain the synaptic connection strengths, $W^{ij}_X = a_X$ ($X \in \{\text{ext}, \text{exc}, \text{inh}\}$) if the j-th neuron connects to the i-th neuron and 0 otherwise. The input from neighboring cortical areas is modeled as the Ornstein-Uhlenbeck process with means $\mu_{\text{bcg,exc}}$ and $\mu_{\text{bcg,inh}}$ and standard deviations of the limiting distributions $\sigma_{\text{bcg,exc}}$ and $\sigma_{\text{bcg,inh}}$ (Uhlenbeck and Ornstein, 1930; Destexhe et al., 2001). We set the values of the background activity to match the moments of an exponential Poisson shot noise with rates $\lambda_{\text{bcg,exc}} = 0.5\,\text{kHz}$ and $\lambda_{\text{bcg,inh}} = 0.125\,\text{kHz}$ (Rajdl and Lansky, 2015):

$$\mu_X = a_X \tau_X \lambda_X, \tag{10}$$

$$\sigma_X = a_X \sqrt{\frac{\lambda_X \tau_X}{2}}, \tag{11}$$

where X represents the excitatory or inhibitory background activity.

When the membrane potential V crosses the firing threshold (θ_{exc}, θ_{inh}) a spike is fired and the membrane potential is reset to E_L.

The network consisted of $n_{\text{ext}} = 1000$ neurons in the external population, $n_{\text{exc}} = 800$ neurons in the excitatory population, and $n_{\text{inh}} = 200$ neurons in the inhibitory population. The connections were set randomly with connection probability for the recurrent connections (exc. to exc., exc. to inh., inh. to inh., inh. to exc.) set to

Table 1. Parameters of the LIF model

Membrane capacitance	C_m	150 pF
Leak conductance	g_L	10 nS
Resting potential	E_L	−80 mV
Exc. reversal potential	E_e	0 mV
Inh. reversal potential	E_i	−80 mV
Exc. synapse decay	τ_exc	5 ms
Inh. synapse decay	τ_inh	5 ms
Exc. threshold	θ_exc	−55 mV
Inh. threshold	θ_inh	−60 mV
Ext. synapse amplitude	a_ext	1 nS
Exc. synapse amplitude	a_exc	0.01–1 nS
Inh. synapse amplitude	a_inh	$g \cdot a_\mathrm{exc}$
Exc. inh. synapse amplitude	$a_\mathrm{bcg,exc}$	a_ext
Bcg. inh. synapse amplitude	$a_\mathrm{bcg,inh}$	$g \cdot a_\mathrm{ext}$
Inh. scaling factor	g	20

$P_\mathrm{rec} = 20\%$ and connection probability from the external population (ext. to exc. and ext. to inh., P_ext) was varied from to 1% to 100% (Fig. 1A). We created the connection matrices $\mathbf{W}_X$ by generating a matrix of random uniformly distributed numbers $\mathbf{R}_X$ from the interval $[0, 1)$ and set $W_X^{ij} = a_X$ if $R_\mathrm{ext}^{ij} < P_\mathrm{ext}$ or $R_X^{ij} < P_X$ for $X \in \{\mathrm{exc}, \mathrm{inh}\}$. The random matrix $\mathbf{R}_\mathrm{ext}$ was the same for all values of P_ext. In simulations where we controlled for the effects caused by the random number of connections from the external population, we fixed the number of connections by setting only the $k = n_\mathrm{ext} P_\mathrm{ext}$ elements in each row of W_ext non-zero, in the location of k largest elements of the i-th row of $\mathbf{R}_\mathrm{ext}$.

The simulations were carried out with the Brian 2 package (Stimberg et al., 2019) in Python with a 0.1 ms time step.

2.2 Obtaining the input-output relationship of the network

We considered the total number of action potentials n from the excitatory and inhibitory subpopulations in a time window $\Delta T = 1\,\mathrm{s}$ as an output of the network. We modeled the stimulus as an input from the thalamic neurons, parametrized by the mean input rate to a single neuron:

$$\lambda_\mathrm{ext} = n_\mathrm{ext} \lambda_\mathrm{ext}^0 \frac{100\%}{P_\mathrm{ext}}, \tag{12}$$

where λ_ext^0 is the firing rate of a single neuron in the external population and $n_\mathrm{ext} \frac{100\%}{P_\mathrm{ext}}$ is the mean number of pre-synaptic external neuron for each neuron in the excitatory and inhibitory populations. For each set of parameters (a_rec and P_ext pair) we determined the input $\lambda_\mathrm{ext}^\mathrm{max}(a_\mathrm{rec}, P_\mathrm{ext})$ for which the output reached 30 kHz. In order to obtain the input-output relationship, we discretized the input space to 30 equidistant stimulus intensities: $\lambda_\mathrm{ext}^i(a_\mathrm{rec}, P_\mathrm{ext}) = \frac{i}{30} \lambda_\mathrm{ext}^\mathrm{max}(a_\mathrm{rec}, P_\mathrm{ext})$, where $i = 0, \ldots, 30$. With a fixed network connectivity, we simulated the network 1080 times for each $\lambda_\mathrm{ext}^i(a_\mathrm{rec}, P_\mathrm{ext})$.

We then fit 7th-degree polynomial functions to the mean output of the network as a function of the stimulus λ_ext and to the Fano factor as a function of the mean output, where Fano factor is defined as:

$$\mathrm{FF} = \frac{\mathrm{Var}[N]}{\mathrm{E}[N]}, \tag{13}$$

where N is a random variable representing the number of output action potentials n. Weights of the polynomial fit were set as $\frac{1}{y^2}$, where y is the independent variable. We

then discretized the input space to 1000 equidistant stimulus intensities and estimated the mean output μ and Fano factor FF for each intensity from the polynomial functions. We then estimated the input-output relationship, defined by a conditional probability distribution $f(n|\lambda_{\text{ext}})$ as a lognormal distribution for each λ_{ext}, with corresponding parameters to match the estimated mean and Fano factor:

$$f(n|\lambda_{\text{ext}}) = \frac{1}{Z}\frac{1}{n\sigma_{\log}\sqrt{2\pi}}\exp\left(-\frac{(\ln n - \mu_{\log}^2)}{2\sigma_{\log}^2}\right), \tag{14}$$

$$\sigma_{\log} = \sqrt{\ln\left(\frac{\text{FF}}{\mu}+1\right)}, \tag{15}$$

$$\mu_{\log} = \ln\mu - \frac{\sigma_{\log}^2}{2}, \tag{16}$$

$$Z = \sum_{n=0}^{+\infty}\frac{1}{n\sigma_{\log}\sqrt{2\pi}}\exp\left(-\frac{(\ln n - \mu_{\log}^2)}{2\sigma_{\log}^2}\right). \tag{17}$$

This way we avoided the sampling bias when calculating information measures from the data (Treves and Panzeri, 1995).

2.3 Metabolic cost of neural activity

In our calculations, we focus on the energy in the form of ATP molecules required to pump out Na^+ ions. We take into account the Na^+ influx due to excitatory post-synaptic currents, Na^+ influx during action potentials, and Na^+ influx to maintain the resting potential. To this end, we follow the calculations in (Attwell and Laughlin, 2001) and (Harris et al., 2012), which we modify for our neuronal model.

We assume the standard membrane capacitance per area as $c_m = 1\,\mu\text{F/cm}^2$ and the cell diameter as $D = 69\,\mu\text{m}$, giving the total capacitance $C_m = \pi D^2 c_m = 150\,\text{pF}$. Therefore, to depolarize the neuron by $\Delta V = 100\,\text{mV}$ the minimum charge influx is $\Delta V C_m = 1.5\times10^{-11}\,\text{C}$ and the minimum number of Na^+ ions $\frac{\Delta V C_m}{e} \doteq 9.375\times10^7$, where $e \doteq 1.6\times10^{-19}\,\text{C}$ is the elementary charge. The minimal number of Na^+ ions is then quadrupled to get a more realistic estimate of the Na^+ influx due to the simultaneous opening of the K^+ channels (Attwell and Laughlin, 2001). The Na^+ influx must be then pumped out by the Na^+/K^+-ATPase, which requires one ATP molecule per 3 Na^+ ions. The cost of a single action potential can be then estimated as $\frac{4}{3}\times9.375\times10^7\,\text{ATP} = 1.25\times10^8\,\text{ATP}$. However, about 80% of the metabolic costs associated with an action potential are expected to come from the propagation of the action potential through the neuron's axons. Therefore, we estimate the total cost as $6.25\times10^8\,\text{ATP}$.

Next, we assume that the excitatory synaptic current is mediated by the opening of Na^+ and K^+ channels with reversal potentials $E_{\text{Na}} = 90\,\text{mV}$ and $E_{\text{K}} = -105\,\text{mV}$. For the excitatory synaptic current, it then has to hold

$$(g_{\text{exc}} + g_{\text{ext}})(V - E_{\text{e}}) = g_{\text{Na}}(V - E_{\text{Na}}) + g_{\text{K}}(V - E_{\text{K}}), \tag{18}$$

$$g_{\text{Na}} + g_{\text{K}} = g_{\text{ext}} + g_{\text{exc}}. \tag{19}$$

Therefore:

$$I_{\text{Na}} = \frac{g_{\text{K}}(V - E_{\text{K}})}{(g_{\text{exc}} + g_{\text{ext}})(V - E_{\text{e}})}. \tag{20}$$

The sodium entering with the sodium current I_{Na} again has to be pumped out by the Na^+/K^+-ATPase and therefore we calculate the cost of the synaptic current as $\frac{1}{3e}I_{\text{Na}}\Delta T\,\text{ATP}$, where ΔT is the time interval over which we are measuring the cost.

Each input to the network (parametrized by λ_{ext}) is then associated with a cost, which we express as

$$w(\lambda_{\text{ext}}) = \Bigg((N_{\text{exc}}\mu_{\text{exc}} + N_{\text{inh}}\mu_{\text{inh}} + N_{\text{ext}}\lambda_{\text{ext}}\frac{100\%}{P_{\text{ext}}})W_{\text{AP}} + \\ + \frac{N_{\text{exc}}\langle I_{\text{Na}}^{\text{exc}}\rangle + N_{\text{inh}}\langle I_{\text{Na}}^{\text{inh}}\rangle}{3e} \Bigg) \Delta T, \tag{21}$$

where $\mu_{\text{exc}} = \mu_{\text{exc}}(\lambda_{\text{ext}})$, $\mu_{\text{inh}} = \mu_{\text{inh}}(\lambda_{\text{ext}})$ are the mean firing rates of a single excitatory and inhibitory neuron (given the input λ_{ext}), $\langle I_{\text{Na}}^{\text{exc}}\rangle = \langle I_{\text{Na}}^{\text{exc}}\rangle(\lambda_{\text{ext}})$ and $\langle I_{\text{Na}}^{\text{inh}}\rangle = \langle I_{\text{Na}}^{\text{inh}}\rangle(\lambda_{\text{ext}})$ are the average excitatory synaptic currents in a single excitatory and inhibitory neuron.

2.4 Measuring the information content

We treat the neural network as a memoryless information channel (Shannon, 1948; Thomas M. Cover, 2006). The firing rates of the external population λ_{ext} are the input to the channel, and the number of action potentials n the excitatory population fires in the time window $\Delta T = 1\,\text{s}$ is the output of the channel. The input is then described by a random variable Λ and the output by a random variable N. The mutual information between the input and the output $I(\Lambda; N)$ is calculated as

$$I(\Lambda; N) = \int_{\lambda_{\text{ext}}^{\min}}^{\lambda_{\text{ext}}^{\max}} p(\lambda_{\text{ext}}) i(\lambda_{\text{ext}}; N)\, \mathrm{d}\lambda_{\text{ext}}, \tag{22}$$

$$i(\lambda_{\text{ext}}; N) = \sum_{n=0}^{+\infty} i(\lambda_{\text{ext}}; n) q_p(n), \tag{23}$$

$$i(\lambda_{\text{ext}}; n) = \log_2 \frac{f(n|\lambda_{\text{ext}})}{q_p(n)}, \tag{24}$$

$$q_p(n) = \int_{\lambda_{\text{ext}}^{\min}}^{\lambda_{\text{ext}}^{\max}} p(\lambda_{\text{ext}}) f(n|\lambda_{\text{ext}})\, \mathrm{d}\lambda_{\text{ext}}, \tag{25}$$

where $f(n|\lambda_{\text{ext}})$ is the probability distribution of N given that $\Lambda = \lambda_{\text{ext}}$, $p(\lambda_{\text{ext}})$ is the input probability distribution, $i(\lambda_{\text{ext}}; n)$ is the amount of information that observing n spikes gives us about the stimulus λ_{ext}, $i(\lambda_{\text{ext}}; N)$ is than the average amount of information we get from the input λ_{ext}, $q_p(n)$ is the marginal output probability distribution.

Given the input probability distribution $p(\lambda_{\text{ext}})$, we can calculate the average metabolic cost as

$$W_p = \int_{\lambda_{\text{ext}}^{\min}}^{\lambda_{\text{ext}}^{\max}} p(\lambda_{\text{ext}}) w(\lambda_{\text{ext}})\, \mathrm{d}\lambda_{\text{ext}}. \tag{26}$$

The capacity-cost function $C(W)$ is then the lowest upper bound on the amount of mutual information (in bits) achievable given the constraint that $W_p < W$:

$$C(W) = \sup_{p(\lambda_{\text{ext}}): W_p < W} I(\Lambda; N). \tag{27}$$

The information-metabolic efficiency E is then the maximal amount of mutual information per molecule of ATP between the input and the output:

$$E = \frac{C(W^*)}{W^*}, \tag{28}$$

$$W^* = \operatorname*{arg\,max}_{W \in [0, +\infty)} \frac{C(W)}{W}. \tag{29}$$

The capacity-cost function can be obtained numerically with the Blahut-Arimoto algorithm (Blahut, 1972), or the information-metabolic efficiency can be conveniently obtained directly with the Jimbo-Kunisawa algorithm Jimbo and Kunisawa (1979); Suksompong and Berger (2010).

2.4.1 Low noise approximation of constrained information capacity

If the trial-to-trial variability is very low, a lower bound on the capacity-cost function can be found (Kostal and Lansky, 2013; Kostal et al., 2013). We used this low-noise approximation to gain analytical insight into the importance of different properties of the neural system for information-metabolically efficient information transmission. In the low noise approximation, the optimal input distribution maximizing the mutual information constrained by metabolic expenses W is given by:

$$p(\lambda_{\text{ext}}) = \sqrt{\frac{J(\lambda_{\text{ext}})}{2\pi e}} \exp\left[\lambda_1 - 1 - \lambda_W w(\lambda_{\text{ext}})\right]. \tag{30}$$

where $J(\lambda_{\text{ext}})$ is the Fisher information and λ_1 and λ_W are Lagrange multipliers which can be obtained from the normalization condition:

$$\int_{\lambda_{\text{ext}}^{\min}}^{\lambda_{\text{ext}}^{\max}} p(\lambda_{\text{ext}}) w(\lambda_{\text{ext}})\, \mathrm{d}\lambda_{\text{ext}} \tag{31}$$

and the average metabolic cost constraint (Eq. 26). In the Gaussian approximation, the Fisher information is given by

$$J(\lambda_{\text{ext}}) = \frac{\mu'_{\text{ext}}(\lambda_{\text{ext}})^2}{\sigma_{\text{exc}}(\lambda_{\text{ext}})^2}, \tag{32}$$

where $\sigma_{\text{exc}}(\lambda_{\text{ext}})$ is the standard deviation of the spike counts at input intensity λ_{ext}. The low noise estimate on the capacity-cost function is then

$$C_{\text{low}}(W) = 1 - \lambda_1 + \lambda_W W. \tag{33}$$

3 Results

3.1 Constrained information maximization in a simple linear model

In order to gain an insight into what affects the information-metabolic efficiency of a neural population, we first solve the problem for a simple linear system. The mean response of the system is given by $\gamma(\lambda_{\text{ext}}) = g\lambda_{\text{ext}}$, where λ_{ext} is the stimulus and g is the gain of the system. The Fano factor (Eq. 13) is constant, and we assume that the output is continuous and normally distributed. The input-output relationship is therefore described by

$$f(n|\lambda_{\text{ext}}) = \frac{1}{\sqrt{2g\lambda_{\text{ext}}\text{FF}}} \exp\left[-\frac{1}{2}\left(\frac{n - g\lambda_{\text{ext}}}{g\lambda_{\text{ext}}\text{FF}}\right)^2\right]. \tag{34}$$

and the Fisher information (Eq. 32) is

$$J(\lambda_{\text{ext}}) = \frac{g}{\lambda_{\text{ext}}\text{FF}} \tag{35}$$

Next, we assume that the cost of the activity $w(\lambda_{\text{ext}})$ depends linearly on the input:

$$w(\lambda_{\text{ext}}) = w_0\lambda_{\text{ext}} + W_0 = \frac{w_0}{g}\gamma(\lambda_{\text{ext}}) + W_0, \tag{36}$$

where W_0 is the cost of the resting state.

The probability distribution derived from the low-noise approximation (Eq. 30) is then

$$p(\lambda_{\text{ext}}) = \sqrt{\frac{1}{2\pi}\frac{g}{\lambda_{\text{ext}}\text{FF}}}\exp(\lambda_1 - 1 - \lambda_W w_0\lambda_{\text{ext}}). \tag{37}$$

After applying the normalization conditions (Eqs. 26 and 31) and using Eq. (33) we obtain the lower bound on the capacity-cost function:

$$C_{\text{low}}(W) = \frac{1}{2}\log\left[(W - W_0)\frac{1}{w_{\text{AP}}}\frac{1}{\text{FF}}\right], \tag{38}$$

$$w_{\text{AP}} = \frac{w_0}{g}, \tag{39}$$

where w_{AP} is the cost of increasing the output intensity by one action potential.

The gain g, cost scaling w_0, and Fano factor FF cannot be considered constant for the real neural populations. However, the Eq. (38) provides an insight into the importance of these properties, which we will study numerically for a more realistic neural system.

In the following, we use:

$$g = \mu'_{\text{ext}}(\lambda_{\text{ext}}), \tag{40}$$

$$w_0 = w'(\lambda_{\text{ext}}). \tag{41}$$

3.2 Inhibitory feedback decorrelates the neural activity

With the increasing probability of shared input (P_{ext}), the mean pairwise correlation between the firing output of neurons increases (feedforward network, Fig. 1B). We showed that these correlations can be removed by recurrent connections, as long as the synaptic currents from the recurrent connections are inhibition dominated. We set the excitatory recurrent synaptic amplitude as $a_{\text{exc}} = 0.01\,\text{nS}$ to create a small perturbation from the feedforward network and varied the scaling g determining the amplitude of inhibitory synapses ($a_{\text{inh}} = g a_{\text{exc}}$) from 15 to 25. Correlations between neurons were decreased for $g \geq 20$ (Fig. 1C), which was also associated with stronger negative net current from the recurrent synapses (Fig. 1D). For the network considered further in our work we set $g = 20$. Simultaneously increasing the strength of the recurrent synapses with fixed g led to a further decrease of the correlations among the neurons (Fig. 1E) while further decreasing the net current from the recurrent synapses (Fig. 1F).

3.3 Trial-to-trial variability of single neurons vs. a population

In the inhibition-dominated network, the input needed from the external population in order to evoke a given average firing rate has to be higher than in the case of the feedforward network. The resulting increase in the synaptic noise leads to higher trial-to-trial variability in the LIF model (Fig. 2 A-C; see also (Barta and Kostal, 2021)).

In the case of the total population activity, however, the pairwise correlations between the neurons have a significant effect on the trial-to-trial variability. Denoting

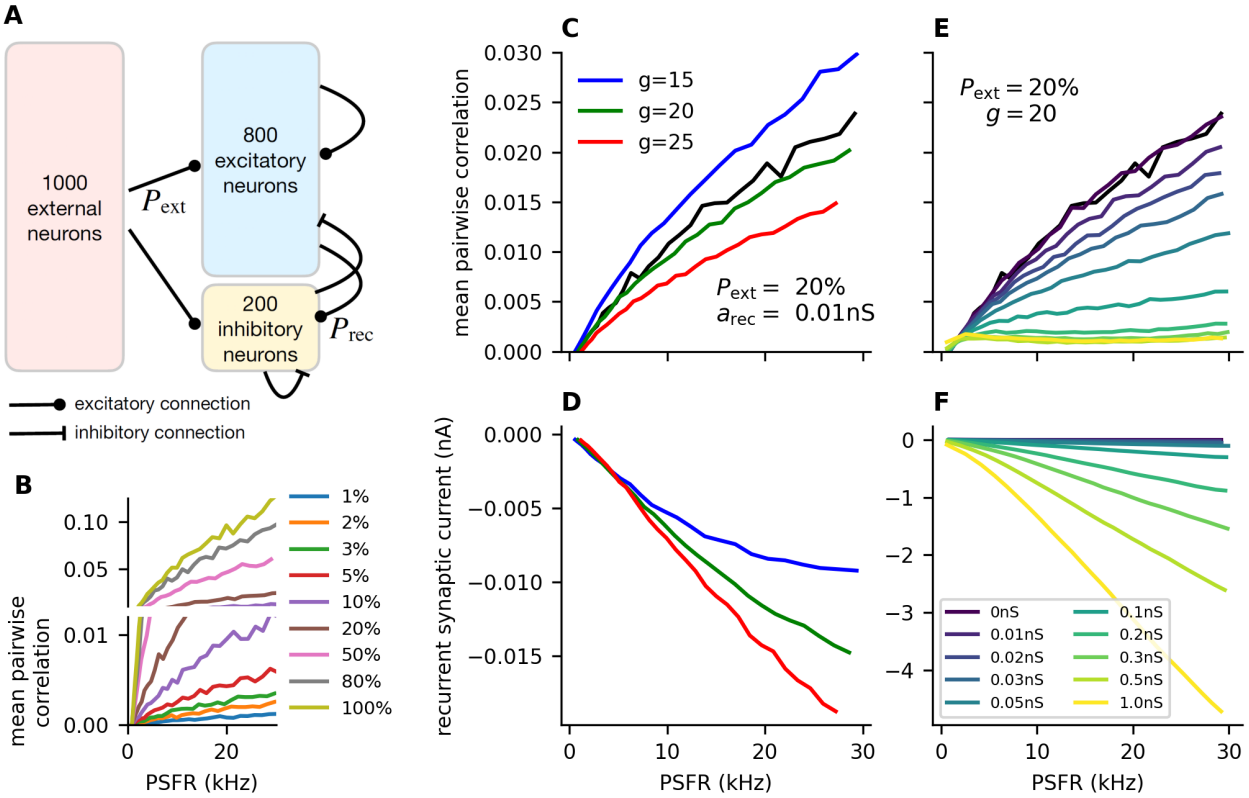

Fig 1. Inhibitory feedback decreases noise correlations. A: Schematic illustration of the simulated neural network. Poisson neurons in the external population make random connections to the neurons in the excitatory and inhibitory subpopulations. The connection probability $P_{\text{ext}} \in [0.01, 1]$ is varied to achieve different levels of shared external input to the neurons. The neurons in the inhibitory (inh.) and excitatory (exc.) subpopulations make recurrent connections (exc. to exc., exc. to inh., inh. to inh., inh. to exc.) with probability $P_{\text{rec}} = 20\%$. The strength of those connections is parametrized by a_{rec} (Tab. 1). **B:** Mean pairwise correlation between any two neurons in the exc. and inh. subpopulations plotted against the mean output of the network for different values of P_{ext} in a feedforward network ($a_{\text{rec}} = 0\,\text{nS}$). **C:** Mean pairwise correlations as in **B**, for different values of g (ratio of inhibitory-to-excitatory synaptic strength), $a_{\text{rec}} = 0.01\,\text{nS}$. **D:** The total current from recurrent synapses for different values of g, as in C. **E-F:** Same as **C-D**, but with fixed $g = 20$ and different values of a_{rec}.

the random variable representing the number of spikes of the i-th neuron observed during a time window ΔT as N_i, we get for the Fano factor of the population activity:

$$\text{FF} = \frac{\text{Var}(\sum_i N_i)}{\text{E}\left[\sum_i N_i\right]} \tag{42}$$

$$= \frac{\sum_i \text{Var}(N_i)}{\sum_i \text{E}\left[N_i\right]} + \frac{2\sum_{i<j} \text{Cov}(N_i, N_j)}{\sum_i \text{E}\left[N_i\right]} \tag{43}$$

$$= \frac{\sum_i \text{Var}(N_i)}{\sum_i \text{E}\left[N_i\right]} \left(1 + \frac{2\sum_{i<j} \text{Cov}(N_i, N_j)}{\sum_i \text{Var}\left(N_i\right)}\right) \tag{44}$$

$$= \frac{v}{\mu}\left(1 + (k-1)\frac{c}{v}\right) \tag{45}$$

$$\approx \text{FF}_0\left(1 + kr\right) \tag{46}$$

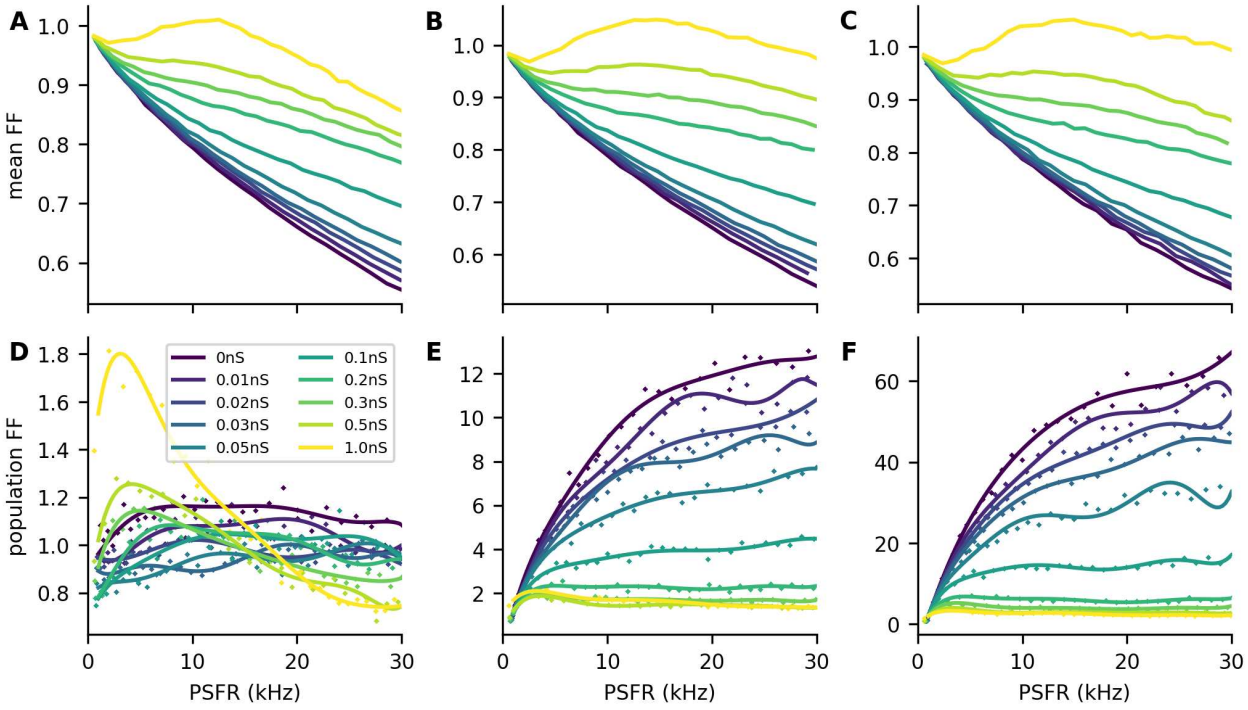

Fig 2. Fano factor of single neurons and of populations. A-C: Mean Fano factor of individual neurons for different values of P_{ext}: 0.01 (**A**), 0.2 (**B**), 1 (**C**) and the strength of the recurrent synapses (a_{rec}) colorcoded. The mean Fano factor increases with the strength of the recurrent synapses. **D-F:** Same as **A-C**, but for Fano factor of the population activity. The points represent the population Fano factor obtained from the simulation and the lines represent the fit with a 7th degree polynomial. For $P_{\text{ext}} = 0.01$ the increase in trial-to-trial variability of individual neurons (**A**) can have a stronger effect on the population Fano factor than decreasing the pairwise correlations, resulting in an increase of the population Fano factor with high values of a_{rec} (**D**). For higher values of P_{ext} the pairwise correlations greatly increase the population Fano factor, which is then decreased with increasing a_{rec}.

where c is the mean pairwise covariance, v the mean variance of a neuron, μ is the mean number of spikes in ΔT, k the number of neurons and r the Pearson correlation coefficient. The last approximation holds for neurons with identical variances and pairwise covariances (Abbott and Dayan, 1999). It provides an insight into how the pairwise correlations and Fano factor of individual neurons affect the Fano factor of the total activity. If the correlations or number of neurons are small ($r \cdot k \ll 1$), the decorrelation by strengthening the recurrent synapses does not significantly decrease the population Fano factor. Instead, the population Fano factor may increase due to the increase of the Fano factor of individual neurons (Fig. 2D, $P_{\text{ext}} = 1\%$). If greater correlations are induced due to the shared input to the network, the correlations have a dominating effect on the population Fano factor, which can then be greatly decreased by strengthening the recurrent synapses and in turn decreasing the pairwise correlations (Fig. 2E-F).

3.4 Inhibitory feedback is metabolically costly

3.4.1 Stronger recurrence strength increases the cost of the resting state

The cost of the resting state is an important factor for information-metabolic efficiency (Barta and Kostal, 2019). In our network, increasing the recurrence strength decreased the spontaneous activity of the neurons, due to inhibition dominating the recurrent currents. However, the simultaneous increase in the strength of the recurrent excitatory synapses increases the cost of the excitatory synaptic currents (Fig. 3A-C).

3.4.2 Inhibitory feedback decreases gain

Due to the net current from the recurrent synapses being hyperpolarizing, with stronger recurrent synapses, a stronger excitatory current is necessary to bring the neuron to a given post-synaptic firing rate and higher pre-synaptic firing rates are necessary. Therefore, the gain g of the network decreases and with increasing a_{rec} the cost of synaptic currents and the cost of external activity increase (Fig. 3D-E).

3.5 Shared input decreases gain

The number of synapses from the external population for each neuron in the excitatory and inhibitory subpopulations follows the binomial distribution:

$$p(k) = \binom{N_{\text{ext}}}{k} P_{\text{ext}}^k (1 - P_{\text{ext}})^{N_{\text{ext}} - k}, \tag{47}$$

with a mean number of synapses given by $N_{\text{ext}} \cdot P_{\text{ext}}$ and variance $N_{\text{ext}} \cdot P_{\text{ext}}(1 - P_{\text{ext}})$. We scaled the firing rate of the individual neurons in the external population as $\lambda_{\text{exc}}^0 = \frac{\lambda_{\text{exc}}}{N_{\text{ext}} \cdot P_{\text{ext}}}$. Therefore the mean output to a single neuron was always λ_{ext}, independently of P_{ext} and the variance of the input across neurons was $\lambda_{\text{ext}} N_{\text{ext}} \frac{1 - P_{\text{ext}}}{P_{\text{ext}}}$.

It follows from the convexity of the single neuron tuning curve in the analyzed input range (S1 Fig) that out of two inputs with an identical mean λ_{ext}, but different variances across neurons, the input with the higher variance will lead to a higher average firing rate. If we assume that the input across neurons follows a normal distribution with mean λ_{ext} and variance σ^2 and the single neuron tuning curve can be approximated by an exponential function in the form of $c_1 \exp(c_2 x)$, where x is the input intensity to the single neuron, we obtain for the mean firing rate:

$$\int_{-\infty}^{+\infty} \frac{1}{\sigma\sqrt{2\pi}} \exp\left[-\frac{(x - \lambda_{\text{ext}})^2}{\sigma^2}\right] c_1 \exp(-c_2 x) = \frac{c_1}{\sqrt{2}} \exp\left(\frac{c_2}{4}(c_2\sigma^2 - 4\lambda_{\text{ext}})\right), \tag{48}$$

which grows with the standard deviation of the input.

Accordingly, we observed that networks with higher P_{ext} needed higher λ_{ext} in order to produce the same mean PSFR as networks with lower P_{ext} (Fig. 4A-C). Moreover, the mean Fano factor of individual neurons increased with increasing P_{ext} (Fig. 4D-F). This effect could be for the most part removed by fixing the number of connections from the external population to each neuron in the excitatory and inhibitory populations to $P_{\text{ext}} N_{\text{ext}}$ (S2 Fig).

3.6 Optimal regimes for metabolically efficient information transmission

We illustrated that the recurrence strength 1. increases the metabolic cost of the neural activity and 2. decreases the trial-to-trial variability of the population response by decreasing the correlations between the neurons. Similarly, the increased probability of

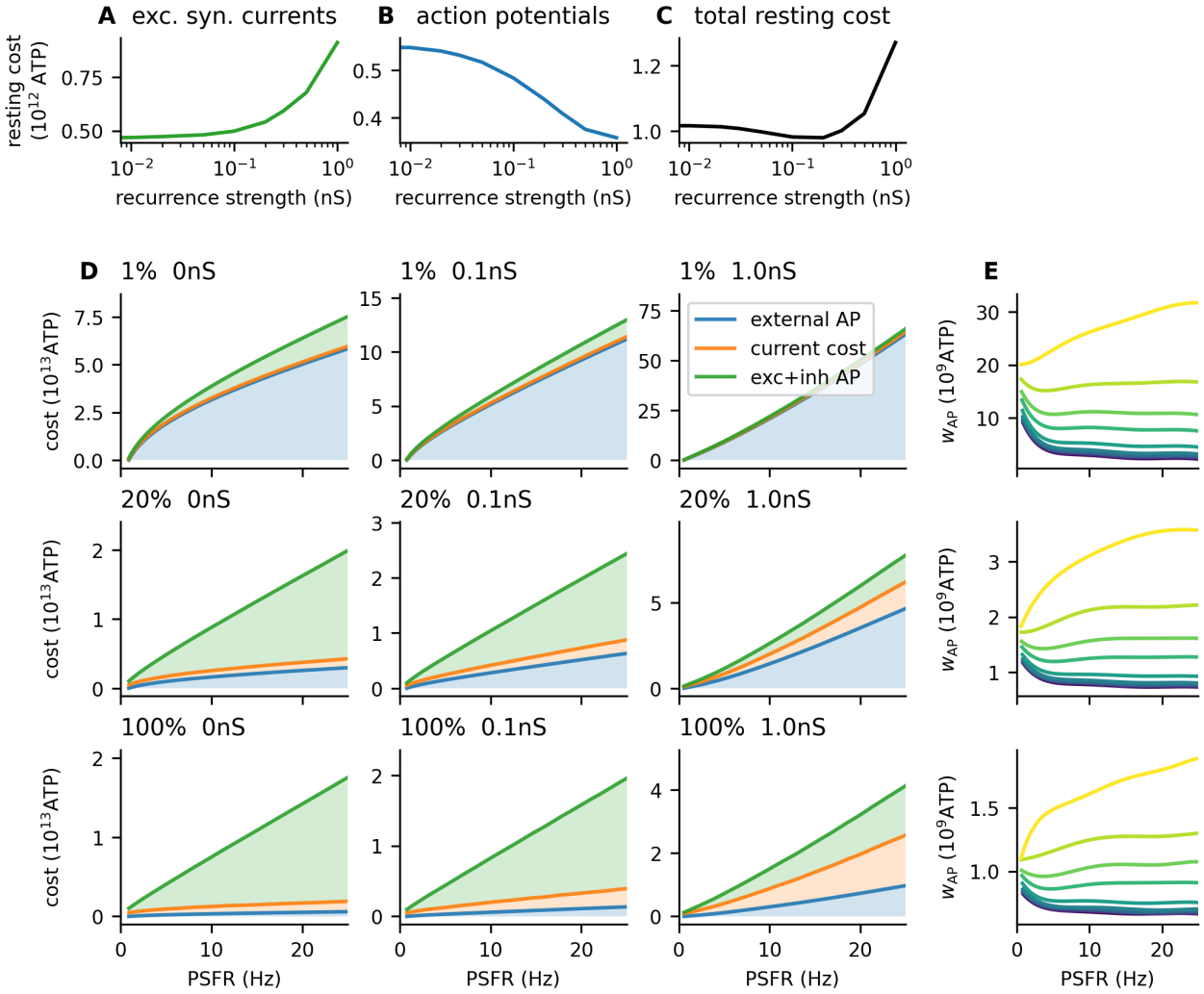

Fig 3. Metabolic cost of the network activity. A-C: Cost at the resting state ($\lambda_{\text{ext}} = 0$). **A:** Cost of the excitatory synaptic currents from the background activity and excitatory action potentials evoked by the background activity. **B:** Cost of the action potentials (both excitatory and inhibitory) evoked by the background activity. **C:** The total resting cost obtained summing **A** and **B**. **D:** The total cost of the network activity is plotted against the output of the network (the total post-synaptic firing rate). Filled areas represent individual contributions of each cost component: cost of action potential from the external population, cost of the excitatory synaptic currents, and cost of the post-synaptic (evoked) action potentials. As P_{ext} increases, the contribution of external action potentials to the overall cost decreases. With increasing a_{rec}, the contribution of excitatory synaptic currents increases. **E:** The cost of increasing the mean input by one action potential (w_{AP}, Eq. 39) is significantly lower for higher P_{ext}. However, while the difference between $P_{\text{ext}} = 1\%$ and $P_{\text{ext}} = 20\%$ is approximately 10-fold, the difference between $P_{\text{ext}} = 20\%$ and $P_{\text{ext}} = 100\%$ is only approximately 2-fold, as the cost of the external population starts to contribute less to the overall cost.

a synapse from an external neuron to a neuron in the excitatory or inhibitory population decreases the cost of the neural activity but increases the trial-to-trial variability of the population response by increasing the noise correlations. To find the balance between the cost of the network activity (Eq. 26) and the mutual information between the input and the output (Eq. 22) we calculated the information-metabolic

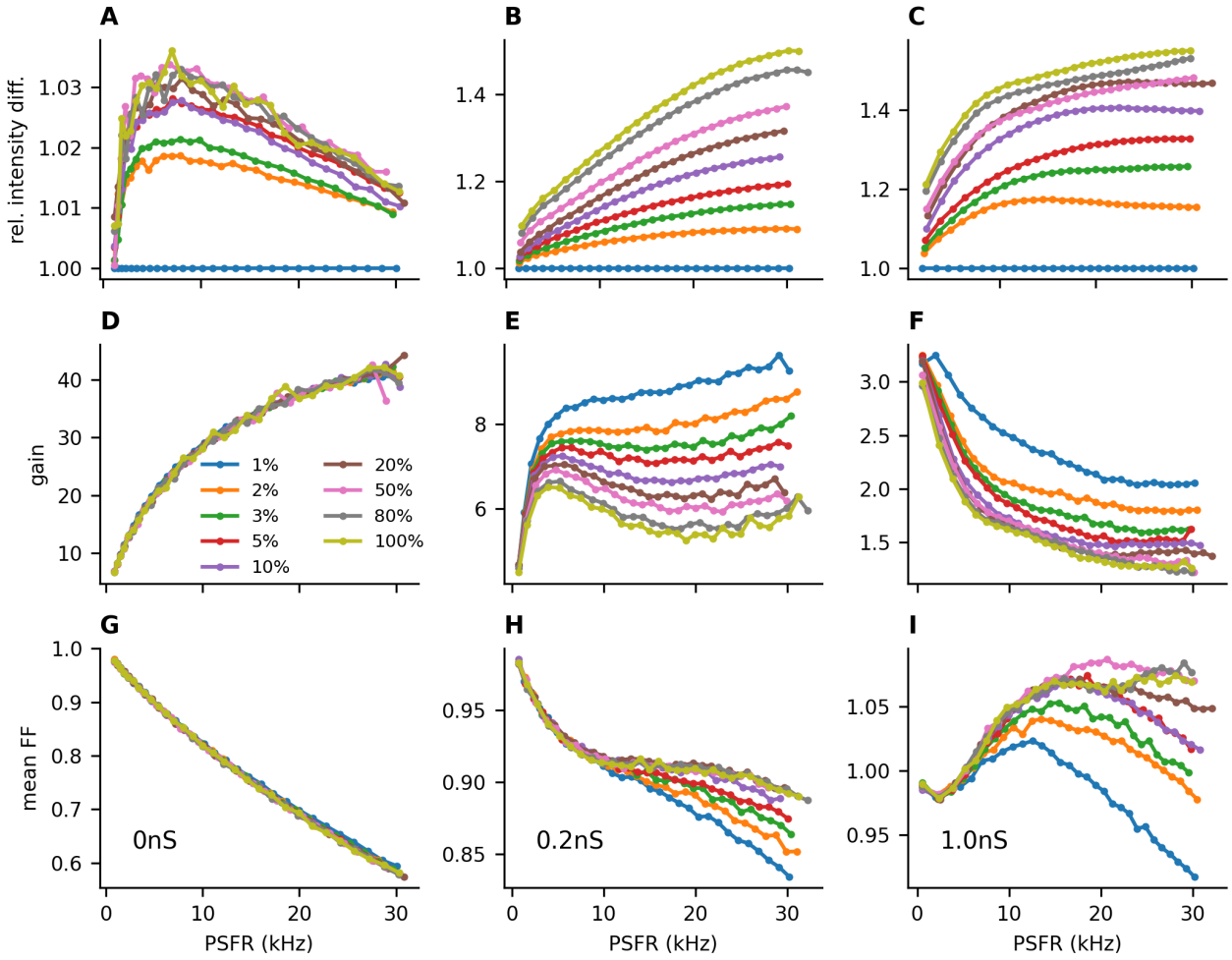

Fig 4. Shared input decreases gain and increases individual trial-to-trial variability. A-C: The input intensity λ_{ext} needed to evoke given firing rate (x-axis) with different connection probabilities P_{ext}, relative to the input intensity for $P_{\text{ext}} = 1\%$. **A:** $a_{\text{rec}} = 0\,\text{nS}$, **B:** $a_{\text{rec}} = 0.2\,\text{nS}$, **C:** $a_{\text{rec}} = 1\,\text{nS}$. With higher P_{ext}, higher values of λ_{ext} are needed for higher values of P_{ext} to achieve the same post-synaptic firing rates as with lower values of P_{ext}. This effect becomes more pronounced with stronger recurrent synapses (**E-F**). **D-F:** Gain of the network (Eq. 40). Higher P_{ext} leads to a lower gain of the population activity. **G-I:** Higher values of P_{ext} also increase the Fano factor of individual neurons.

efficiency, which maximizes the ratio of the mutual information to the cost of the network activity (Eq. 28).

For low values of P_{ext} ($\leq 10\%$), increasing the strength of the recurrent input did not lead to an increase in the information-metabolic efficiency. For higher values of P_{ext} the information-metabolic efficiency was maximized for a_{rec} between 0.1 nS and 0.5 nS (Fig. 5A-B), meaning that the strength of the recurrent excitatory synapses was 2× to 5× lower that the strength of the synapses from the external population.

Moreover, varying P_{ext} had a significant effect on the information-metabolic efficiency across all values of a_{rec}. Namely, low values of P_{ext} resulted in lower values of information-metabolic efficiency across all values of a_{rec}, showing that shared input from the external population is beneficial for metabolically efficient information transmission. Overall, the highest values of information-metabolic efficiency

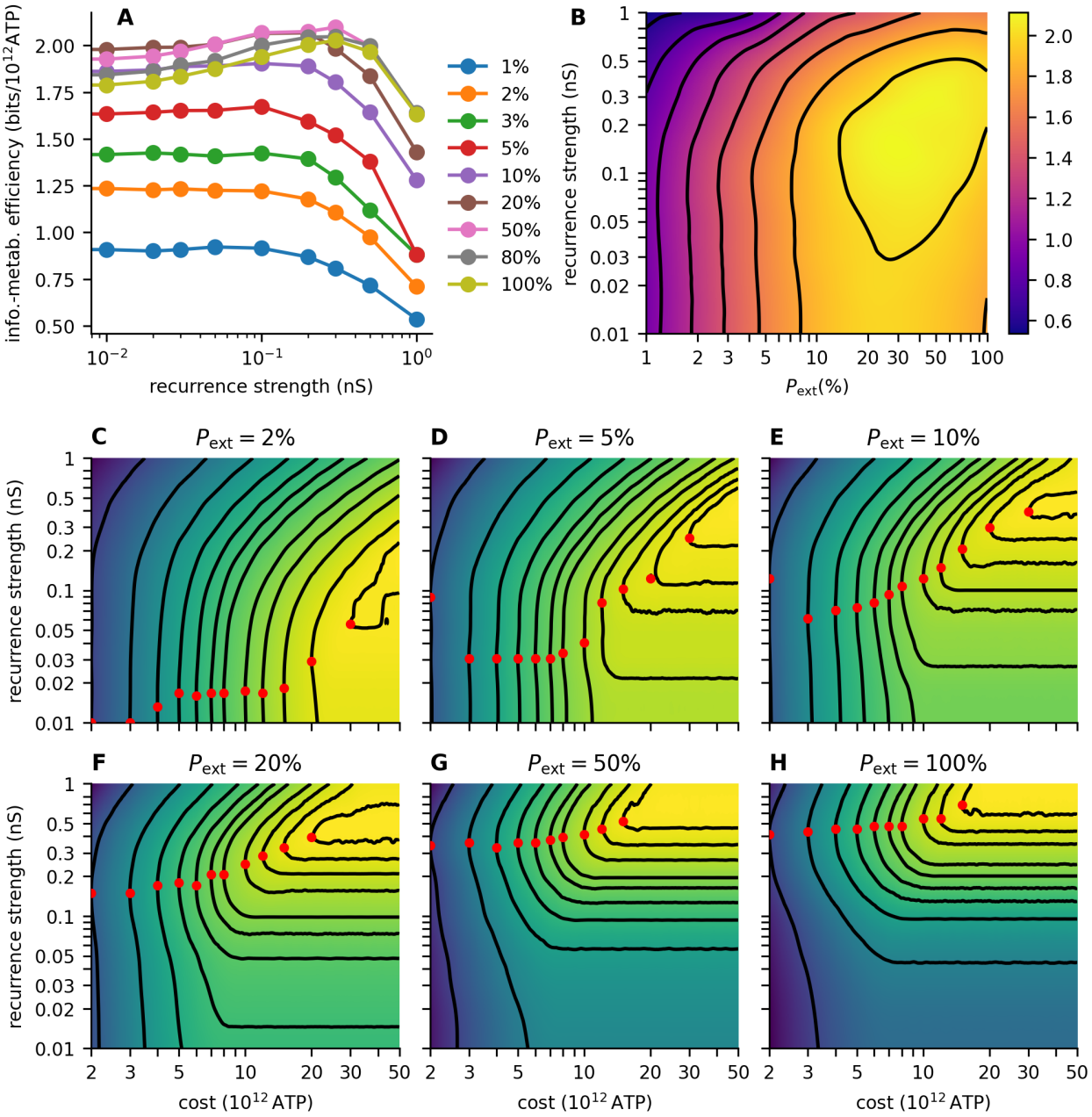

Fig 5. Information transmission with cost constraints. A: Information-metabolic efficiency E (Eq. 28) for different values of recurrence strength a_{rec}. P_{ext} is color-coded. **B:** Contour plot of the information-metabolic efficiency. Contours are at 0.6, 0.8, 1, 1.2, 1.4, 1.6, 1.8, and 2 bits/s. **C-H:** Contour plots showing the capacity-cost function $C(W)$ (Eq. 27) with dependence on the recurrence strength a_{rec} for different values of P_{ext}. The contours show the maximal capacities constraint at different values of W (see Tab. 2 for the costs and capacity values at the contours). The heatmaps in **B-H** were calculated with piece-wise cubic 2D interpolation (SciPy interpolator CloughTocher2DInterpolator (Virtanen et al., 2020)) from the grid calculated with P_{ext} values 1%, 2%, 3%, 5%, 10%, 20%, 50%, 80%, 100% and a_{rec} values 0, 0.01, 0.02, 0.03, 0.05, 0.1, 0.2, 0.3, 0.5, 1 nS.

Table 2. Capacity-cost function values (in bits)

$P_{\text{ext}} \setminus W$ (10^{12}ATP)	2	3	4	5	6	7	8	10	12	15	20	30
0.02	2.30	3.19	3.73	4.11	4.40	4.63	4.83	5.13	5.36	5.62	5.88	6.05
0.05	3.14	3.96	4.41	4.73	4.96	5.14	5.28	5.49	5.63	5.78	5.89	5.96
0.10	3.50	4.23	4.62	4.88	5.08	5.22	5.35	5.52	5.63	5.74	5.86	5.96
0.20	3.69	4.31	4.65	4.89	5.06	5.20	5.31	5.48	5.61	5.73	5.82	
0.50	3.67	4.24	4.56	4.78	4.95	5.10	5.20	5.36	5.48	5.57		
1.00	3.52	4.07	4.39	4.61	4.79	4.93	5.03	5.20	5.30	5.38		

($E \geq 2\,\text{bit}/10^{12}\text{ATP}$) were reached for a_{rec} between 0.05 nS and 0.5 nS and P_{ext} between 20% and 100% (Fig. 5B).

We analyzed the effect of the resting cost (Fig. 3A-C) by setting the resting cost equal in all cases to W_0, the resting cost of the feedforward network. This did not have a significant effect on the information-metabolic efficiencies (S3 Fig).

Neural circuits might not necessarily maximize the ratio of information to cost. Instead, neurons and neural circuits could modulate their properties to maximize information transmission with the available energy resources (Balasubramanian et al., 2001). For example, neurons in the mouse visual cortex have been shown to decrease the conductance of their synaptic channels after food restriction (Padamsey et al., 2022).

Accordingly, we studied how the optimal strength of recurrent synapses changes with the available resources. We calculated the optimal value of a_{rec} for different values of available resources (3, 4, 5, 6, 7, 8, 10, 12, 15, 20, 30, 40 $\times 10^{12}$ ATP). In Fig. 5C-H, we plotted $C(W; a_{\text{rec}})$, the capacity-cost function (Eq. 27) extended by one dimension with a_{rec}. For each cost W, the optimal a_{rec} is highlighted, and the corresponding contour of $C(W)$ is shown (see Tab. 2 for the values of $C(W)$). With decreasing W, the optimal value of a_{rec} typically decreases. This effect is more robust with high values of P_{ext}, as the contours are more curved at the optimum.

We calculated the extended capacity-cost functions with input distributions obtained from the low-noise approximation. To verify that the low noise approximation applies in the case of the studies system, we compared the information-metabolic efficiency obtained with the Jimbo-Kunisawa algorithm. The relative difference did not exceed 10% and did not have a significant impact on the information-metabolic efficiency heatmap structure (S4 Fig).

4 Discussion

Populations in the cortex transmitting information by their summed (or averaged) activity can be considered as a low noise information channel, due to the decrease in trial-to-trial variability (Kostal and Lansky, 2013). The decrease in the trial-to-trial variability of the response will be lower in the presence of positive noise correlations (Abbott and Dayan, 1999). Positive noise correlations can be reduced by inhibitory feedback, which, however, increases the cost of the neural activity (Barta and Kostal, 2019).

In our work, we studied the balance between increasing the transmitted information by decreasing the noise correlations and the associated increase in the cost of the activity. We showed that in a linear system, if the Fano factor of the population activity is constant, as long as the ratio $\frac{g}{w_0 \text{FF}}$ (g is the gain of the system, or slope of the stimulus-response curve, w_0 is the slope of the stimulus-cost curve) remains constant, the cost-constrained capacity will remain constant as well.

We proceeded to calculate the stimulus-response relationship and the metabolic cost for a more biologically realistic neural system. In the studied system, the population

Fano factor could not be considered constant. Instead, correlations between neurons increased with the mean output of the system, and the mean Fano factor of single neurons was also dependent on the mean output of the system, leading to complex dependence of the population Fano factor on the mean output of the system (Fig. 2D-F). We showed that reducing the noise correlations by strengthening the inhibitory feedback decreases the population Fano factor for large values of P_{ext} but may increase the population Fano factor for low values of P_{ext} due to an increase of the mean single neuron Fano factor FF_0.

We illustrated the effect of inhibition-dominated recurrence and shared input on the metabolic cost of neural activity. Increased strength of recurrence increased the cost of excitatory synaptic currents due to the stronger excitatory synapses and stronger input from the external population, as well as the cost of the activity of the external population. A higher connection probability from the external population (higher shared input probability) led to a decrease in the external population activity cost, as the overall activity of the external population could be lower to result in the same mean input to the post-synaptic neurons. On the other hand, due to less variable input to single neurons with high values of P_{ext}, the mean input across all neurons had to be higher with higher values of P_{ext} to evoke the same mean post-synaptic activity.

We found that high values of P_{ext} are beneficial for metabolically efficient information transmission, despite the increased noise correlations. For high values of P_{ext}, increasing the recurrence strength was also beneficial, suggesting that the two mechanisms - decreasing input cost by high connection probability from the external population P_{ext} and decreasing noise correlations by recurrent activity may act together to produce a metabolically efficient code.

Increasing the recurrence strength can lead to about a 10% to 15% increase in the information-metabolic efficiency. The magnitude of the increase is dependent on the cost of the action potentials. If the cost of synaptic currents could be neglected compared to the cost of the action potentials, there would be a higher benefit in increasing the inhibitory feedback since the increases in the cost of the synaptic current could also be neglected.

Although in the cortex, the neurons also connect to neighboring areas of the cortex and not only within the studied subpopulation, we did not consider the cost of synaptic currents evoked in neurons not involved in our simulation. We assume that such synaptic currents would take part in the background activity of a different area. Therefore, if we included these costs and considered multiple cortical areas, we would include the background activity cost multiple times.

In our model of the cortical area, we considered two neural subpopulations: excitatory and inhibitory, each subpopulation was homogeneous, but we set the threshold of the inhibitory neurons lower, in order to mimic the behavior of fast-spiking inhibitory neurons. The difference between excitatory, regular spiking neurons and inhibitory, fast-spiking neurons is often described not only by differences in the threshold but also in differences in the adaptation properties (Kobayashi et al., 2009; Zerlaut et al., 2017; Bernardi et al., 2021). In our case, we did not consider adaptation for simplicity, as estimating the information capacity of a neural system with adaptation is computationally considerably more difficult (Barta and Kostal, 2019).

In our work, we assumed that the neural circuit maximizes the mutual information between the input and the output while minimizing the cost of the neural activity. Such an approach does not provide any information about how the information is encoded. It only calculates the limit on the amount of information that can be reliably transmitted. Yet, the principles of mutual information maximization have proven very useful in explaining the properties of neural systems. The tuning curves of blowfly's contrast-sensitive neurons are adapted to the distribution of contrasts encountered in

the natural environment (Laughlin, 1981); the power spectrum of distribution of odor in pheromone plumes follows the power spectrum predicted for an optimal input to olfactory receptor neurons (Kostal et al., 2008); distributions of post-synaptic firing rates of single neurons during *in-vivo* recordings follow distributions predicted from cost-constrained mutual information maximization (Treves et al., 1999; de Polavieja, 2002, 2004).

By assuming a particular coding scheme, it is possible to place further constraints on the complexity of information encoding, with the assumption that complex codes are not an efficient way to transmit information (Kostal and Kobayashi, 2015, 2019). We did not attempt this in our study. It would be interesting to study whether the inhibitory feedback decreases or increases the encoding complexity.

We have shown that a cortical area can adapt to the amount of available energy resources. In the event of scarceness of resources, information transmission can be adapted by weakening the synaptic weights, thus expanding less resources to reduce the noise correlations. Such a mechanism is implemented in the mouse visual cortex (Padamsey et al., 2022). Padamsey et al. showed that in food-restricted mice, the orientation tuning curves of individual orientation-sensitive neurons in the visual cortex become broader due to weakened synaptic conductances. In our work, we studied the properties of a population instead of single neurons and we considered a population encoding the stimulus intensity instead of the stimulus identity, such as orientation. Extending this model to a situation in which stimulus identity is encoded and shared input is introduced due to the overlap of receptive fields would be interesting.

Neurons recorded *in-vivo* typically exhibit a Fano factor close to one, constant over a broad range of post-synaptic firing rates Gur et al. (1997); Geisler and Albrecht (1997); Shadlen and Newsome (1998). In the optimal regimes with stronger recurrent synapses, the Fano factor decreased only very slowly over the studied range of post-synaptic firing rates (up to 30 Hz in a single neuron). With weaker synaptic strengths, the Fano factor of a single neuron decreases rapidly with an increasing post-synaptic firing rate. Our model predicts that less available resources would lead to weaker recurrent synapses. This hypothesis is straightforward to test by calculating the Fano factors during stimulus presentation (both population and single neuron) in food-restricted animals and comparing them to controls. We expect that the population Fano factor will increase (alternatively, the noise correlations will increase) with food scarcity, and single neuron Fano factors will decrease.

Supporting information

S1 Fig. Input-output relationship of a single neurons. To leave out the network effects, we plotted the tuning curves for the feedforward network separately for the excitatory (blue) and inhibitory (yellow) neurons. The thick line represents the median response across the neurons, which shows that their tuning curves are convex in the studied range. The shaded area shows the spread of the tuning curves across neurons (2.5 to 97.5 percentile). With low values of P_{ext}, the tuning curves across neurons vary significantly and are skewed to the higher firing rates.

S2 Fig. Fixing number of external connections to remove gain dependency. Same as Fig. 4, but each excitatory and inhibitory neuron receives exactly $P_{\text{ext}}N_{\text{ext}}$ connections from the external population. The dependency on P_{ext} is removed.

S3 Fig. Effect of equalizing the resting cost on the information-metabolic efficiency. We observed that the cost of the resting state is different for different recurrence strengths a_{rec} (Fig. 3A-C). This could potentially explain the higher

information-metabolic efficiency E (Eq. 28) for intermediate values of a_{rec} and its decrease for high values of a_{rec}. To quantify the effect of the resting cost, we set the resting cost in each case to the resting cost of the feedforward network $W_0(a_{\mathrm{rec}} = 0)$. The differences in the cost of the resting state do not have a qualitative effect on the conclusions. **A:** The same contour plot as in Fig. 5B. **B:** Contour plot with equalized resting costs (contours as in Fig. 5B: 0.6, 0.8, 1, 1.2, 1.4, 1.6, 1.8 and 2 bits/s). **C:** Heatmap of the relative differences.

S4 Fig. Accuracy of information-metabolic efficiency approximation. To calculate the capacity-cost functions, we calculated the mutual information using Eq. (22) with input probability distribution calculated from the Eqs. (30) and (32). Here we compare the information-metabolic efficiencies calculated with the approximation and the Jimbo-Kunisawa algorithm. **A:** The same contour plot as in Fig. 5B, information-metabolic efficiencies calculated with the Jimbo-Kunisawa algorithm. **B:** Information-metabolic efficiencies calculated with the Fisher-information-based input distribution. **C:** Heatmap of the relative differences. Note that the approximation can only reach lower values than the actual information-metabolic efficiency.

Acknowledgments

This work was supported by Charles University, project GA UK No. 1042120. TB benefited from a fellowship from the Plant Health and Environment Division of INRAE.

References

L. F. Abbott and P. Dayan. The Effect of Correlated Variability on the Accuracy of a Population Code. *Neural Comput.*, 11(1):91–101, 1 1999. ISSN 0899-7667. doi: 10.1162/089976699300016827.

D. Attwell and S. B. Laughlin. An Energy Budget for Signaling in the Grey Matter of the Brain. *J. Cereb. Blood Flow Metab.*, 21(10):1133–1145, 2001. doi: 10.1097/00004647-200110000-00001.

B. B. Averbeck, P. E. Latham, and A. Pouget. Neural correlations, population coding and computation. *Nat. Rev. Neurosci.*, 7(5):358–366, 5 2006. ISSN 1471-003X. doi: 10.1038/nrn1888.

V. Balasubramanian, D. Kimber, and M. J. Berry II. Metabolically Efficient Information Processing. *Neural Comput.*, 13(4):799–815, 4 2001. doi: 10.1162/089976601300014358.

H. B. Barlow. Possible Principles Underlying the Transformations of Sensory Messages. In *Sensory Communication*, pages 217–234. The MIT Press, 9 1961. doi: 10.7551/mitpress/9780262518420.003.0013.

T. Barta and L. Kostal. The effect of inhibition on rate code efficiency indicators. *PLoS Comput Biol.*, 15(12):e1007545, 12 2019. doi: 10.1371/journal.pcbi.1007545.

T. Barta and L. Kostal. Regular spiking in high-conductance states: The essential role of inhibition. *Phys Rev E*, 103(2):022408, 2 2021. ISSN 2470-0045. doi: 10.1103/PhysRevE.103.022408.

A. Bernacchia and X.-J. Wang. Decorrelation by Recurrent Inhibition in Heterogeneous Neural Circuits. *Neural Comput.*, 25(7):1732–1767, 7 2013. ISSN 0899-7667. doi: 10.1162/NECO_a_00451.

D. Bernardi, G. Doron, M. Brecht, and B. Lindner. A network model of the barrel cortex combined with a differentiator detector reproduces features of the behavioral response to single-neuron stimulation. *PLOS Comput Biol*, 17(2), 2 2021. ISSN 1553-7358. doi: 10.1371/journal.pcbi.1007831.

R. Blahut. Computation of channel capacity and rate-distortion functions. *IEEE Trans Inf Theory*, 18(4):460–473, 7 1972. doi: 10.1109/tit.1972.1054855.

N. Brunel. Dynamics of Sparsely Connected Networks of Excitatory and Inhibitory Spiking Neurons. *J. Comput. Neurosci.*, 8:183–208, 2000. doi: https://doi.org/10.1023/A:1008925309027.

G. G. de Polavieja. Errors Drive the Evolution of Biological Signalling to Costly Codes. *J. Theor. Biol.*, 214(4):657–664, 2 2002. doi: 10.1006/jtbi.2001.2498.

G. G. de Polavieja. Reliable biological communication with realistic constraints. *Phys Rev E*, 70(6), 12 2004. doi: 10.1103/physreve.70.061910.

A. Destexhe, M. Rudolph, J. M. Fellous, and T. J. Sejnowski. Fluctuating synaptic conductances recreate in vivo-like activity in neocortical neurons. *Neuroscience*, 107 (1):13–24, 2001. ISSN 0306-4522.

W. S. Geisler and D. G. Albrecht. Visual cortex neurons in monkeys and cats: Detection, discrimination, and identification. *Vis Neurosci*, 14(5):897–919, 9 1997. ISSN 0952-5238. doi: 10.1017/S0952523800011627.

M. Gur, A. Beylin, and D. M. Snodderly. Response Variability of Neurons in Primary Visual Cortex (V1) of Alert Monkeys. *J. Neurosci*, 17(8):2914–2920, 4 1997. ISSN 0270-6474. doi: 10.1523/JNEUROSCI.17-08-02914.1997.

J. J. Harris, R. Jolivet, and D. Attwell. Synaptic energy use and supply. *Neuron*, 75(5): 762–777, 2012.

M. Jimbo and K. Kunisawa. An iteration method for calculating the relative capacity. *Information and Control*, 43(2):216–223, 11 1979. doi: 10.1016/s0019-9958(79)90719-8.

R. Kobayashi, Y. Tsubo, and S. Shinomoto. Made-to-order spiking neuron model equipped with a multi-timescale adaptive threshold. *Front. Comput. Neurosci.*, 3:9, 2009. doi: 10.3389/neuro.10.009.2009.

L. Kostal and R. Kobayashi. Optimal decoding and information transmission in Hodgkin-Huxley neurons under metabolic cost constraints. *Biosystems*, 136:3–10, 10 2015. doi: 10.1016/j.biosystems.2015.06.008.

L. Kostal and R. Kobayashi. Critical size of neural population for reliable information transmission. *Phys. Rev. E (Rapid Commun.)*, 100(1):050401(R), 2019.

L. Kostal and P. Lansky. Information capacity and its approximations under metabolic cost in a simple homogeneous population of neurons. *Biosystems*, 112(3):265–275, 6 2013. doi: 10.1016/j.biosystems.2013.03.019.

L. Kostal, P. Lansky, and J.-P. Rospars. Efficient olfactory coding in the pheromone receptor neuron of a moth. *PLoS Comput. Biol.*, 4:e1000053, 2008.

L. Kostal, P. Lansky, and M. D. McDonnell. Metabolic cost of neuronal information in an empirical stimulus-response model. *Biol. Cybern.*, 107(3):355–365, 6 2013. ISSN 1432-0770. doi: 10.1007/s00422-013-0554-6.

S. Laughlin. A simple coding procedure enhances a neuron's information capacity. *Z. Naturforsch. [C]*, 36(9-10):910–912, 1981. ISSN 0341-0382.

S. Laughlin. Energy as a constraint on the coding and processing of sensory information. *Curr. Opin. Neurobiol*, 11(4):475–480, 8 2001. ISSN 09594388. doi: 10.1016/S0959-4388(00)00237-3.

W. B. Levy and R. A. Baxter. Energy Efficient Neural Codes. *Neural Comput.*, 8(3): 531–543, 4 1996. doi: 10.1162/neco.1996.8.3.531.

C. Monier, F. Chavane, P. Baudot, L. J. Graham, and Y. Frégnac. Orientation and Direction Selectivity of Synaptic Inputs in Visual Cortical Neurons. *Neuron*, 37(4): 663–680, 2 2003. doi: 10.1016/s0896-6273(03)00064-3.

R. Moreno-Bote, J. Beck, I. Kanitscheider, X. Pitkow, P. Latham, and A. Pouget. Information-limiting correlations. *Nature Neuroscience*, 17(10):1410–1417, 10 2014. ISSN 1097-6256. doi: 10.1038/nn.3807.

J. E. Niven and S. B. Laughlin. Energy limitation as a selective pressure on the evolution of sensory systems. *J. Exp. Biol.*, 211(11):1792–1804, 6 2008. ISSN 1477-9145. doi: 10.1242/jeb.017574.

Z. Padamsey, D. Katsanevaki, N. Dupuy, and N. L. Rochefort. Neocortex saves energy by reducing coding precision during food scarcity. *Neuron*, 110(2):280–296, 1 2022. ISSN 08966273. doi: 10.1016/j.neuron.2021.10.024.

K. Rajdl and P. Lansky. Stein's neuronal model with pooled renewal input. *Biol. Cybern.*, 109(3):389–399, 4 2015. doi: 10.1007/s00422-015-0650-x.

A. Renart, J. de la Rocha, P. Bartho, L. Hollender, N. Parga, A. Reyes, and K. D. Harris. The Asynchronous State in Cortical Circuits. *Science*, 327(5965):587–590, 1 2010. ISSN 0036-8075. doi: 10.1126/science.1179850.

B. Sengupta, S. B. Laughlin, and J. E. Niven. Balanced Excitatory and Inhibitory Synaptic Currents Promote Efficient Coding and Metabolic Efficiency. *PLoS Comput. Biol.*, 9(10):e1003263, 10 2013. doi: 10.1371/journal.pcbi.1003263.

M. N. Shadlen and W. T. Newsome. The Variable Discharge of Cortical Neurons: Implications for Connectivity, Computation, and Information Coding. *J. Neurosci.*, 18(10):3870–3896, 5 1998. doi: 10.1523/jneurosci.18-10-03870.1998.

C. Shannon. A mathematical theory of communication. *Bell system technical journal*, 27, 1948.

M. Stimberg, R. Brette, and D. F. Goodman. Brian 2, an intuitive and efficient neural simulator. *eLife*, 8, 8 2019. ISSN 2050-084X. doi: 10.7554/eLife.47314.

P. Suksompong and T. Berger. Capacity Analysis for Integrate-and-Fire Neurons With Descending Action Potential Thresholds. *IEEE Trans Inf Theory*, 56(2):838–851, 2 2010. doi: 10.1109/tit.2009.2037042.

T. Tetzlaff, M. Helias, G. T. Einevoll, and M. Diesmann. Decorrelation of Neural-Network Activity by Inhibitory Feedback. *PLoS Comp. Biol.*, 8(8):e1002596, 8 2012. ISSN 1553-7358. doi: 10.1371/journal.pcbi.1002596.

J. A. T. Thomas M. Cover. *Elements of Information Theory*. Wiley Series in Telecommunications and Signal Processing. Wiley-Interscience, 2nd ed edition, 2006. ISBN 9780471241959,0471241954.

A. Treves and S. Panzeri. The Upward Bias in Measures of Information Derived from Limited Data Samples. *Neural Comput.*, 7(2):399–407, 3 1995. ISSN 0899-7667. doi: 10.1162/neco.1995.7.2.399.

A. Treves, S. Panzeri, E. T. Rolls, M. Booth, and E. A. Wakeman. Firing rate distributions and efficiency of information transmission of inferior temporal cortex neurons to natural visual stimuli. *Neural Comput.*, 11(3):601–632, 4 1999. ISSN 0899-7667.

G. E. Uhlenbeck and L. S. Ornstein. On the Theory of the Brownian Motion. *Phys. Rev.*, 36(5):823–841, 9 1930. doi: 10.1103/physrev.36.823.

P. Virtanen, R. Gommers, T. E. Oliphant, M. Haberland, T. Reddy, D. Cournapeau, E. Burovski, P. Peterson, W. Weckesser, J. Bright, S. J. van der Walt, M. Brett, J. Wilson, K. J. Millman, N. Mayorov, A. R. J. Nelson, E. Jones, R. Kern, E. Larson, and C. J. Carey. SciPy 1.0: fundamental algorithms for scientific computing in Python. *Nature Methods*, 17(3):261–272, 3 2020. ISSN 1548-7091. doi: 10.1038/s41592-019-0686-2.

L. Yu and Y. Yu. Energy-efficient neural information processing in individual neurons and neuronal networks. *J. Neurosci. Res.*, 95(11):2253–2266, 11 2017. ISSN 03604012. doi: 10.1002/jnr.24131.

Y. Zerlaut, S. Chemla, F. Chavane, and A. Destexhe. Modeling mesoscopic cortical dynamics using a mean-field model of conductance-based networks of adaptive exponential integrate-and-fire neurons. *J. Comput. Neurosci*, 44(1):45–61, 2 2017. ISSN 0929-5313. doi: 10.1007/s10827-017-0668-2.

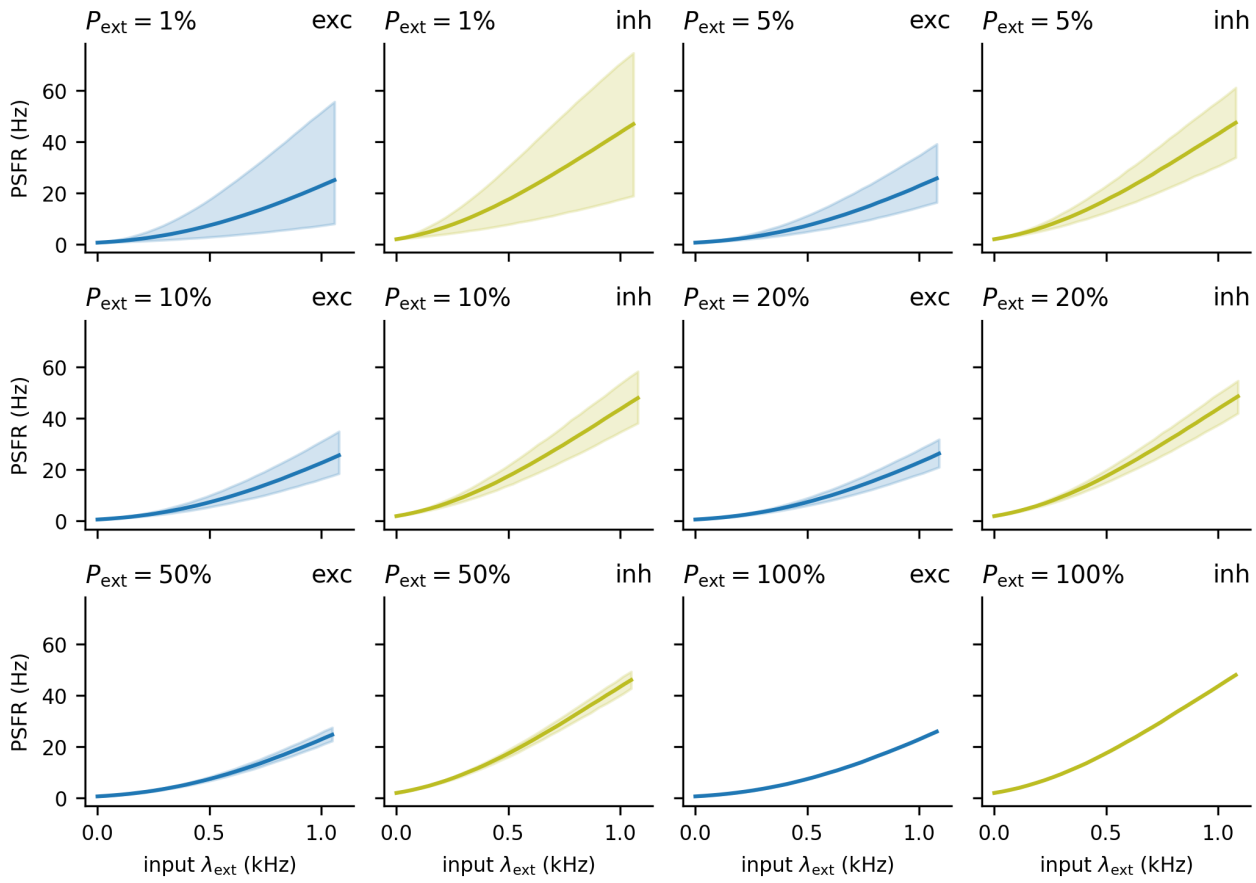

S1 Fig. Input-output relationship of single neurons. To leave out the network effects, we plotted the tuning curves for the feedforward network, separately for the excitatory (blue) and inhibitory (yellow) neurons. The thick line represents the median response across the neurons, which shows that their tuning curves are convex in the studied range. The shaded area shows the spread of the tuning curves across neurons (2.5 to 97.5 percentile). With low values of P_{ext}, the tuning curves across neurons vary significantly and are skewed to the higher firing rates.

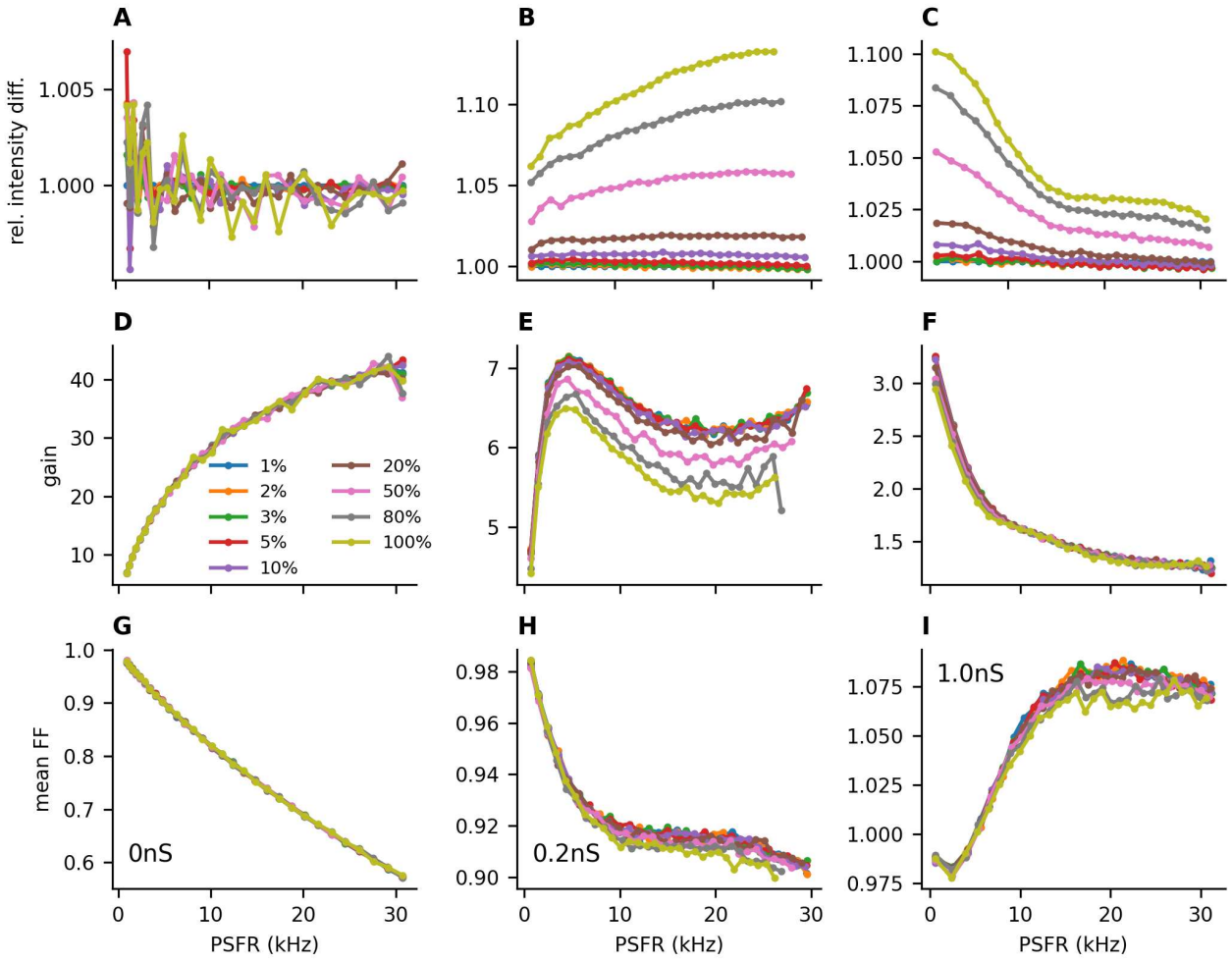

S2 Fig. Fixing the number of external connections to each neuron. Same as Fig. 4, but exactly $k_{\text{ext}} \frac{P_{\text{ext}}}{100\%}$ external neurons connected to each excitatory and inhibitory neuron. This removed a large part of the dependence on P_{ext} seen in Fig. 4.

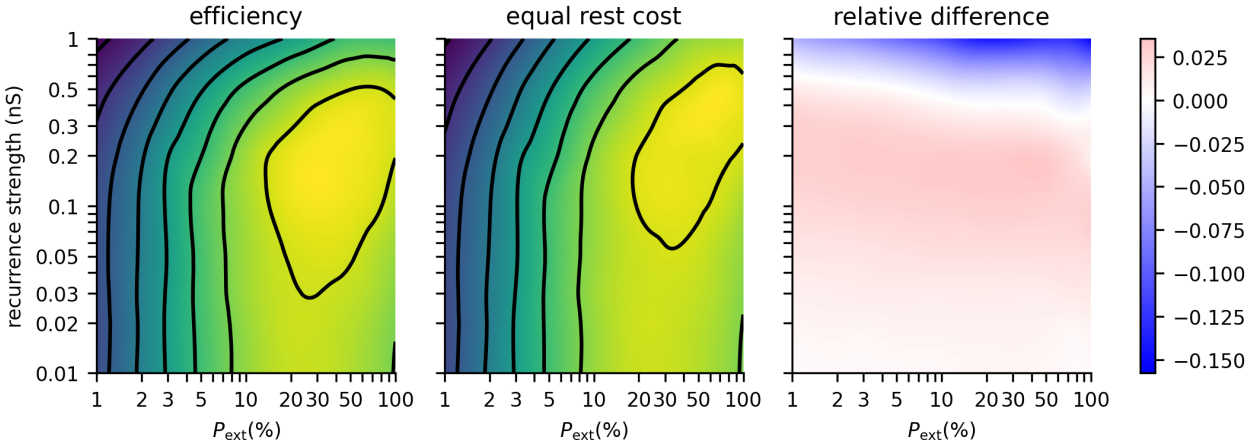

S3 Fig. Effect of equalizing the resting cost on the information-metabolic efficiency. We observed that the cost of the resting state is different for different recurrence strengths a_{rec} (Fig. 3A-C). This could potentially explain the higher information-metabolic efficiency E (Eq. 28) for intermediate values of a_{rec} and its decrease for high values of a_{rec}. To quantify the effect of the resting cost, we set the resting cost in each case to the resting cost of the feedforward network $W_0(a_{\text{rec}} = 0)$. The differences in the cost of the resting state do not have a qualitative effect on the conclusions. **A:** The same contour plot as in Fig. 5B. **B:** Contour plot with equalized resting costs (contours as in Fig. 5B: 0.6, 0.8, 1, 1.2, 1.4, 1.6, 1.8 and 2 bits/s). **C:** Heatmap of the relative differences.

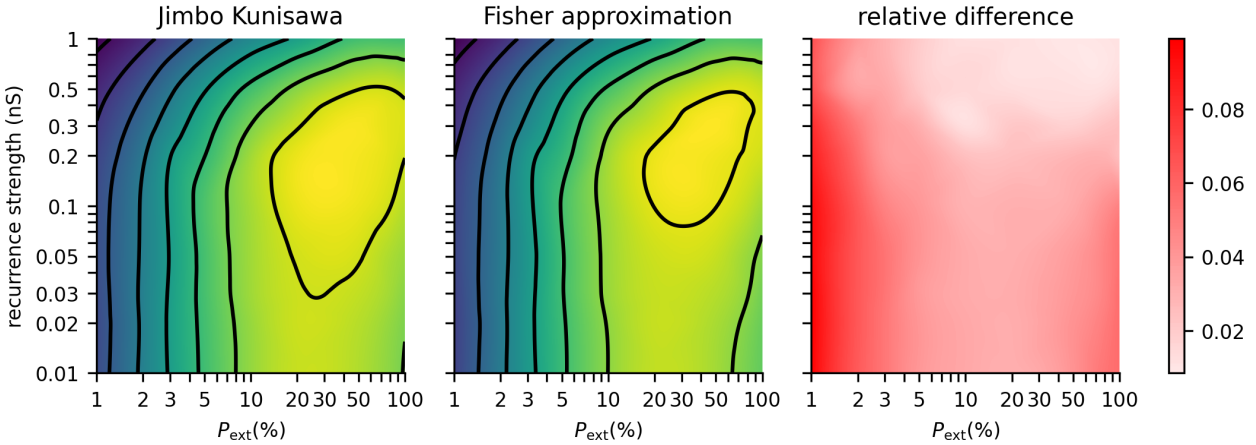

S4 Fig. Accuracy of information-metabolic efficiency approximation. To calculate the capacity-cost functions, we calculated the mutual information using Eq. (22) with input probability distribution calculated from the Eqs. (30) and (32). Here we compare the information-metabolic efficiencies calculated with the approximation and the Jimbo-Kunisawa algorithm. **A:** The same contour plot as in Fig. 5B, information-metabolic efficiencies calculated with the Jimbo-Kunisawa algorithm. **B:** Information-metabolic efficiencies calculated with the Fisher-information-based input distribution. **C:** Heatmap of the relative differences. Note that the approximation can only reach lower values than the actual information-metabolic efficiency.

Attachment V

Manuscript published on *bioRxiv*. Published on 22nd July 2022
doi: https://doi.org/10.1101/2022.07.21.501055

Stimulus duration encoding occurs early in the moth olfactory pathway

Tomas Barta[1,2,3*], Christelle Monsempès[1*], Elodie Demondion[1*], Abhishek Chatterjee[1*], Lubomir Kostal[2**], Philippe Lucas[1***]

1 Institute of Ecology and Environmental Sciences of Paris, INRAE, Sorbonne Université, CNRS, IRD, UPEC, Université de Paris, 78000 Versailles, France
2 Institute of Physiology of the Czech Academy of Sciences, Prague, Czech Republic
3 Charles University, First Medical Faculty, Prague, Czech Republic

* tomas.barta@fgu.cas.cz
** kostal@biomed.cas.cz
*** philippe.lucas@inrae.fr

Abstract

Flying insects encounter turbulent environments, where chemotaxis along a concentration gradient makes little sense. Detection of the onset and offset of discrete odor pulses is then expected to become crucial for navigation, but it is not well understood how the olfactory system encodes the offset of the odor pulse. Previous works indicated that the duration of a male moth olfactory receptor neuron's (ORN) spike firing response to pheromone stimuli greatly exceeds the pulse duration. However, these works were based on imprecise odor delivery systems. We built an odor delivery system capable of delivering much sharper pheromone stimuli. The stimuli evoked ORN firing responses that faithfully tracked the stimulus duration, provided the stimulus lasted at least 200 ms. A transient inhibition marked the termination of such stimuli. Shorter stimuli produced a firing response exceeding the stimulus duration. The response shapes could be explained by adaptation of the ORN on only two time scales. With simulations, we showed that the observed limits in stimulus offset detection propagate to the antennal lobe and are likely to be behaviorally significant. Our results increase the understanding of the mechanisms necessary for male moths to navigate through pheromone plumes.

Introduction

Flying insects heavily rely on olfactory cues to search for their mating partner, food and oviposition sites. The turbulent airflow breaks the odor signal, e.g., sex pheromone from a female, into pockets containing odor and pockets with clean air. A male moth searching for a mating partner can then encounter pockets with high concentration of pheromone even at large distances from the female (Jones, 1983; Murlis et al., 2000; Justus et al., 2002; Celani et al., 2014). The odor plume does not form a continuous gradient pointing to its source and obtaining a reliable concentration average would take too long for flying insects to efficiently track odor plumes. Instead, the insect has to implement different searching strategies, such as an upwind surge during an odor encounter and cast, crosswind flight without progressing upwind, when the odor signal is lost (Willis and Baker, 1984; Vickers and Baker, 1994; Kennedy, 1983; van Breugel

and Dickinson, 2014; Cardé, 2021). This searching strategy requires the insect to reliably detect the onset and offset of the odor pocket.

The olfactory receptor neurons (ORNs) typically respond to the odor onset by a fast and intense action potential firing activity. On the other hand, ORNs were not always observed to stop rapidly the firing activity after the odor offset. For example, pheromone sensitive ORNs in moths have been considered to terminate their response very slowly (Kaissling et al., 1989; Jarriault et al., 2010; Grémiaux et al., 2012; Rospars et al., 2014; Tuckman et al., 2021a,b). The apparent inability to detect the pheromone stimulus offset by moth ORNs is very surprising, given that male moths are extremely sensitive to the sex pheromone of their conspecific females (Kaissling and Priesner, 1970; Mayer and Mankin, 1990; Angioy et al., 2003; Kaissling, 2009), they exhibit a rich and complex repertoire of maneuvers when navigating pheromone plumes (Willis et al., 2013; Vickers, 2006; Cardé, 2021), can successfully track female pheromone plumes at large distances (Cardé and Charlton, 1984; Elkinton et al., 1987; Shorey, 1976; Wall and Perry, 1987) and their olfactory system has been shown to be very efficient (Kostal et al., 2008; Levakova et al., 2018). The most detailed studies that have attempted to link the odor plume structure with orientation behavior in terrestrial animals are from plume tracking behavior of male moths to female sex pheromone. A driving ambition of this long studied model was the use of insect sex pheromones in pest management (Witzgall et al., 2010). These studies are also a source for bioinspired navigation models and biohybrid odor-seeking robots (Ando et al., 2013; Martinez et al., 2014; Anderson et al., 2020).

It has been suggested that the slow termination of ORN response depends on the physiochemical properties of the odorant molecules and their interaction with the odor delivery device surfaces (Martelli et al., 2013). Moth pheromone molecules have a relatively low volatility, as indicated by their low vapor pressure (Olsson et al., 1983) and when used as olfactory stimuli they are likely to exhibit slower dynamics, compared to more volatile compounds. Therefore, we investigated if the slow response termination is a physiological property of ORNs and is important for encoding, or if it is an artefact caused by interactions of pheromone molecules with the odor delivery device.

The analysis of the dynamics of odor coding requires either monitoring or controlling the temporal resolution of odor stimuli. Monitoring the odor stimulus can be done with a photo-ionization detector (PID) with high temporal resolution (Justus et al., 2002). Unfortunately, common moth pheromones cannot be detected by a PID, because their ionization energies are too high for the PID lamp. Proton transfer reaction-mass spectrometers (PTR-MS) can monitor the dynamic of odor plumes (Riffell et al., 2014), including pheromone plumes. However, the sensitivity of PTR-MS remains too low to monitor pheromone stimuli at physiological concentrations. Therefore, we developed a new odor delivery device to better control the stimulus dynamics.

With our new odor delivery system we observed a tri-phasic pattern in the ORN responses from the moth species *Agrotis ipsilon* and *Spodoptera littoralis*, consisting of an excitatory response at the stimulus onset, inhibitory phase at the stimulus offset and a less intense excitatory activity (rebound activity) following the inhibitory phase. This is in contrast to the widely held belief that responses to pheromone in moth ORNs terminate very slowly and is in fact reminiscent of the projection neuron's (PN) response profile. Yet, when ORNs were subjected to short stimuli, the inhibitory phase disappeared and the response consisted of a single long-lasting burst that significantly exceeded the stimulus duration.

The observed qualitative differences in the response, i.e., mono-phasic response to short stimuli and tri-phasic response to long stimuli, point to slow adaptation of the ORNs. In order to asses the slow adaptation process, we had to isolate the ORN processing capabilities from the dynamics of the odor delivery. To this end, we measured

the local field potential (LFP) in the sensilla, which is tightly correlated with the depolarizing current entering the ORN. Recording both the LFP and the firing response allows to study independently the transduction processes leading to the generation of the receptor current and how the spike generating mechanism in the soma responds to this current (Nagel and Wilson, 2011). We performed an optimization procedure which allowed us to narrow down the adaptation processes to only two time-scales, providing novel insights into the possible mechanisms leading to the adaptation.

1 Results

1.1 New odor delivery device improves the speed of odor onset and offset

A common type of odor delivery device in insect olfactory studies consists of Pasteur pipettes containing a filter paper loaded with one of the odors/doses to test. An electrovalve (EV) redirects an airstream through the pipette, the small tip of which is introduced into a hole on the side of a glass tube that bathes the insect antenna with a constant humidified and filtered air-stream (Montagné et al., 2012). However, the time constants of rising and falling odor concentrations at the onset and offset of the stimulus can be very long, depending on the physicochemical properties of the odorant (Vetter et al., 2006; Martelli et al., 2013; Gorur-Shandilya et al., 2019). First, odors are sticky and adsorption / desorption on surfaces contributes to low-pass filtering of the stimulus dynamics as the odors travels along the tube. Next, the temporal structure of the odor stimuli disintegrates within 10–20 mm from the exit of the odor stimulus device when the airflow is no more restrained within a tubing.

We built an odor delivery device in which we ensured that the effects of odor molecules interacting with surfaces have minimal effect on the dynamics of the delivered stimulus. The insect was placed directly in front of an electrovalve controlling the odorant supply (Figure 1–Figure Supplement2). We tested with linalool (due to its low volatility) that the odor delivery device is capable of delivering sharp and short odor pulses (Figure 1A). Adding a glass tube between the PID and the electrovalve (15 cm length, 1 cm diameter) resulted in much slower PID responses and short stimuli evoked only very little response (Figure 1B).

Using more volatile compounds (acetone, α-pinene) resulted in sharper PID responses (Figure 1C). We suspected that the slowdown of the response dynamics with linalool is not a property of the odor delivery device, but of the PID. To verify this, we performed an experiment where we completely cut off the odor delivery device from the PID by inserting a plastic barrier between them during the stimulation. The time course of the PID response offset remained slow (Figure 1D). Although the observed PID response offset was slightly faster in the first 500 ms after the stimulus termination in the experiment with using the plastic barrier, after 500 ms the sustained response was identical (Figure 1E-J), indicating that the observed slow dynamics of the response and the long lasting response are mostly a property of the PID and not of the odor delivery device. Possibly the odorant molecules adhere to the surface of the PID and thus slow down their onset and offset detection by the PID. Therefore, we conclude that it is risky to use PID signal as a proxy for odor concentration and the physiochemical properties of the used odorant need to be considered.

1.2 Moth ORN response shape tracks odor pulse durations

We presented the pheromone sensitive ORNs of *A. ipsilon* with stimuli of different durations (3 ms, 5 ms, 10 ms, 20 ms, 50 ms, 100 ms, 200 ms, 500 ms, 1 s, 2 s, 5 s) of 100 pg

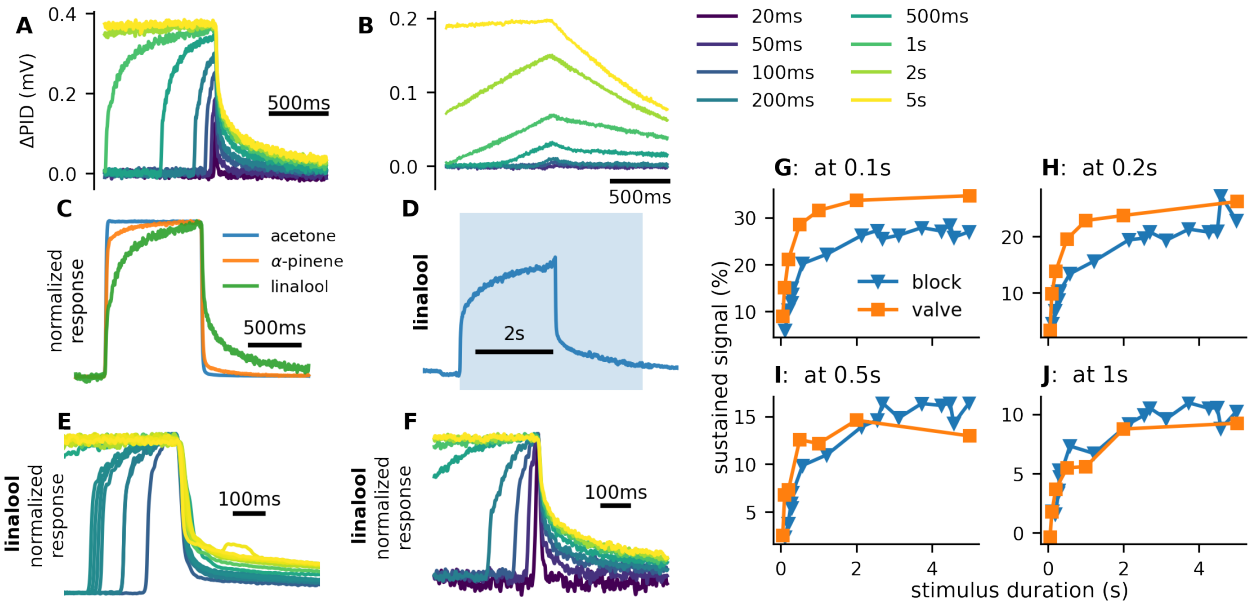

Fig 1. New odor delivery device can deliver square stimuli. A: We verified with PID response to linalool that the odor delivery device is capable of delivering sharp and short odor pulses. On the contrary, adding a 15 cm glass tube after the valve produces responses which are much less sharp and short stimuli (up to 200 ms) evoke very little PID response or no response at all (**B**, we used pure linalool instead of 10% dilution to compensate for airflow mixing in the glass tube). **C:** More volatile compounds produce sharper PID responses. **D:** Shaded area indicates linalool stimulation. Approximately 2.8 s after the stimulus onset a plastic barrier was dropped between the PID and the odor delivery device to prevent any odor molecules from the odor delivery device from reaching the PID. The offset of the PID signal remained slow. **E:** We dropped the barrier at different times after the stimulus onset. The longer the stimulus was, the slower was the PID response offset. We observed the same pattern when we used our odor delivery device to deliver stimuli of different durations (**F**). **G-J:** We compared the value (averaged in a 20 ms window) of the PID at different times after the stimulus offset to its peak value. 0.5 s after the stimulus termination the sustained signal is the same regardless of whether stimulus was terminated regularly (with the electrovalve) or mid-odor delivery with a plastic barrier. This shows that most of the slow dynamics observed with the PID are due to the properties of the PID and not the odor delivery device. All PID responses in the figure were filtered with 49 Hz 2-pole Butterworth lowpass filter to remove noise.

Figure 1–Figure supplement 1. Schematics of the developed odor delivery device.

Figure 1–Figure supplement 2. Testing of equilibration times and source stability.

dose. The neurons responded by intense firing activity, reaching its peak approximately 20 ms to 50 ms after the stimulus onset, regardless of the stimulus duration. The time course of the response changed qualitatively with the stimulus duration (Figure 2A-B). For a stimulus duration below 100 ms the neurons continued firing for around 100 ms after the stimulus offset, while slowly returning to their spontaneous activity (Figure 2C-D). For stimuli longer than 200 ms the firing response terminated sharply with the stimulus offset. The firing response was then followed by an inhibitory phase, lasting approximately 300 ms (Figure 2E). During the inhibitory phase (interval 100 ms to 400 ms after the firing response termination) the firing activity was significantly suppressed, compared to the activity that followed (rebound phase, measured as the activity in the period 1 s to 3 s after the firing response termination). The rebound activity increases with stimulus duration, making the inhibitory phase more pronounced and indicating that two opposing processes are at play (Figure 2F). A mono-phasic

response to short stimuli and inhibitory phase after long stimuli were also observed with higher (1 ng) and lower (10 pg) pheromone doses (Figure 3A-B). Moreover, in the dose range 10 pg to 1 ng the shape of the firing profile is mostly independent of pheromone concentration (Figure 3C), a property that has been illustrated on *Drosophila* ORNs only with highly volatile odors and may help intensity invariant odor identity coding (Martelli et al., 2013). We also saw the same response patterns with the ORNs of *S. littoralis* (Figure 2–Figure Supplement1). These results lead us to the conclusion that the previously reported sustained pheromone responses of the moth ORNs are an artefact caused by interactions of the odor molecules with the tubing of the odor delivery device and should not occur in the nature when the moth is flying sufficiently far away from any surfaces that could release previously adsorbed pheromone molecules.

Flying insects use both olfactory and mechanosensory input (from wind speed) to track odor plumes. Antennal lobe neurons integrate both sensory inputs (Tuckman et al., 2021a,b). The detection of mechanosensory information in insect antennae is attributed primarily to Johnston's organ and Böhm's bristles in the pedicel of the antenna (Budick et al., 2007; Sane et al., 2007; Dieudonné et al., 2014). However, it was recently proposed in the honeybee that mechanosensory signals can also be transduced by olfactory sensilla on the antenna, with changes of sensilla position potentially modulating ORN responses (Tiraboschi et al., 2021). To verify that the observed response pattern is not an artefact caused by change in the mechanical pressure at the stimulus offset, we performed recordings where we maintained constant mechanical pressure throughout odor stimuli by delivering odorless air with an electrovalve in opposing phase to the valve controlling the odor delivery. With this setting, we still observed the tri-phasic response pattern (Figure 2–Figure Supplement2).

We still observed some sustained activity long after the stimulus end, with onset after the inhibitory phase. The intensity of the activity increased both with duration and dose of the stimulus (Figure 3B) and could last more than 15 min (Figure 2–Figure Supplement3). Our new setup strongly reduces the surface where odor molecules can adsorb and then desorb and stimulate the antenna, therefore we conclude that the sustained response has a physiological origin, e.g., pheromone molecules adhering to the sensilla.

1.3 Rapid response termination stems from slow spike frequency adaptation

We recorded the LFP simultaneously with the firing activity in response to 20 ms, 200 ms and 2 s stimuli (dose 1 ng). The LFP shape reflects the depolarizing current flowing from the sensillar lymph into the neuron (with a multicompartmental model of the ORN we estimated that the LFP corresponds to the depolarizing current filtered with exponential kernel with 10 ms decay, Figure 4–Figure Supplement1). After the stimulus onset, the LFP decreases (downward deflection of the LFP signal) due to positive charge flowing from the sensillar lymph into the ORN (exciting the neuron; the amplitude of the LFP deflection is correlated with the peak firing rate; Figure 5–Figure Supplement1B). The LFP typically exhibits some level of adaptation (upward deflection) followed by an additional downward deflection (Figure 4A-D). Shortly after the stimulus offset (within 10 ms) the LFP starts increasing, signifying a decrease in the depolarizing current. After an initial rapid increase, the LFP continues to slowly increase towards the level before the stimulus. This can be either due to a different, slower, signalling pathway or some of the odor molecules can be slowed down by first adhering to the sensilla, before eventually reaching the odor receptors.

The transiency of the firing rate indicates that the firing rate responds to the slope of the depolarizing current, as previously observed in *Drosophila* (Nagel and Wilson,

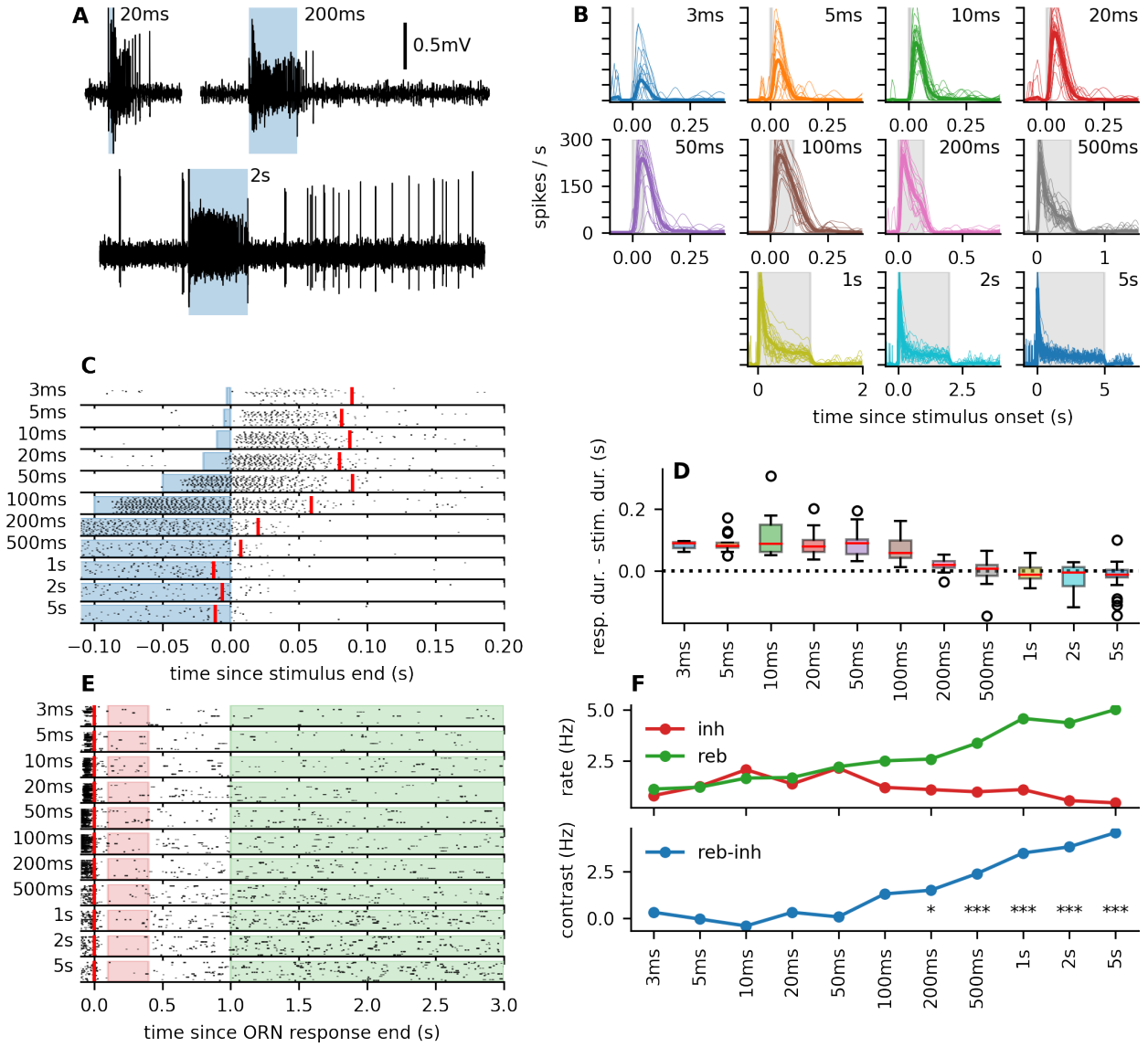

Fig 2. Different stimulus durations produce qualitatively different response terminations. A: Representative voltage traces in response to 20 ms, 200 ms and 2 s stimuli. **B:** Firing responses of the ORNs to stimuli of different durations. Thin lines represent responses of individual neurons, thick line is the average response across all measured neurons (blue area indicates the stimulus period, N=21-23 sensilla). **C:** Raster plots of the spike trains, aligned at the stimulus offset. Responses to stimuli 100 ms and shorter continue after the stimulus offset, while the ends of responses to longer stimuli coincide with the stimulus offset. The red vertical line represents the point in time where 50% of the ORNs' responses finished (see Materials and methods). **D:** Box-plot of how much the response ends exceed the stimulus duration. Color-coded is the stimulus duration, same as in **B**. **E:** Raster plots aligned to the median response end. We compared the firing rates in the red filled area (0.1 s to 0.4 s after the response end) with the firing rates in the green filled area (1 s to 3 s after the response end) to evaluate the contrast between the inhibitory phase and the rebound activity, as shown in **F** (top panel: firing rate during inhibitory / rebound phase, bottom panel: difference between the rebound and inhibitory activity; stars indicate Wilcoxon rank test significance levels).

Figure 2–Figure supplement 1. Response patterns of *Spodoptera littoralis*.

Figure 2–Figure supplement 2. Control experiment with compensating airflow.

Figure 2–Figure supplement 3. Sustained firing activity measured over long periods.

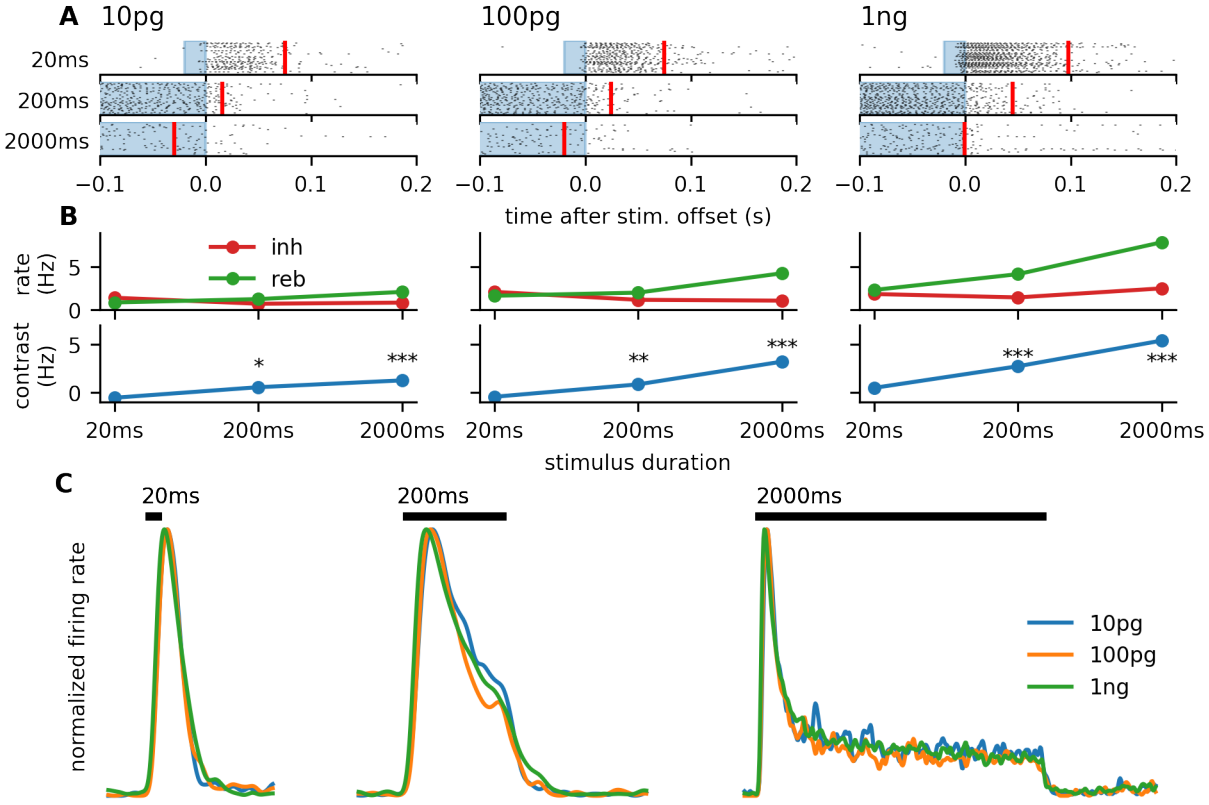

Fig 3. Response properties are maintained with different odor doses. A: Raster plots aligned to the stimulus termination, as in Figure 2C, but with different odorant doses (N=52-57 sensilla). For all doses the spiking response exceeds the short (20 ms) stimulus but terminates rapidly with the longer stimulus (2 s). **B:** The equivalent of Figure 2F for different odorant doses. With all tested doses the neurons exhibited the transient inhibition after the 200 ms and 2 s stimuli. **C:** Firing rate shapes normalized to the peak for different stimulus durations and doses. The general shape is independent of the odorant dose. The black bar indicates the stimulus presence.

2011). However, dependency purely on the LFP and its slope cannot fully explain the shape of the firing rate. Particularly, the average LFP response to 200 ms and 2 s is nearly identical in the period 50 ms before stimulus termination to 100 ms after stimulus termination, but the decreased firing rate indicates that the spike generating mechanism is clearly more adapted after 2 s stimulation (Figure 5E). The comparison of LFP to firing rate transformation between the response to 20 ms and the longer stimuli is not straightforward due to the weaker LFP response evoked by the 20 ms stimulus. To facilitate the comparison we shifted the responses by 50 ms, so that the LFP decay after 20 ms stimulation closely follows the LFP decay after 200 ms stimulation, while the firing rate is significantly higher (Figure 5A). These results illustrate a clear dependence of the firing activity on the ORN's history.

To formalize our claim we used a linear-nonlinear model to predict the firing rate from the LFP (Figure 5A):

$$f(t) = N((K_f * \mathrm{LFP})(t)). \tag{1}$$

The linear kernel K_f is composed of multiple gamma distribution-shaped kernels (Gorur-Shandilya et al., 2017; Jayaram et al., 2022) and a δ-function, therefore the

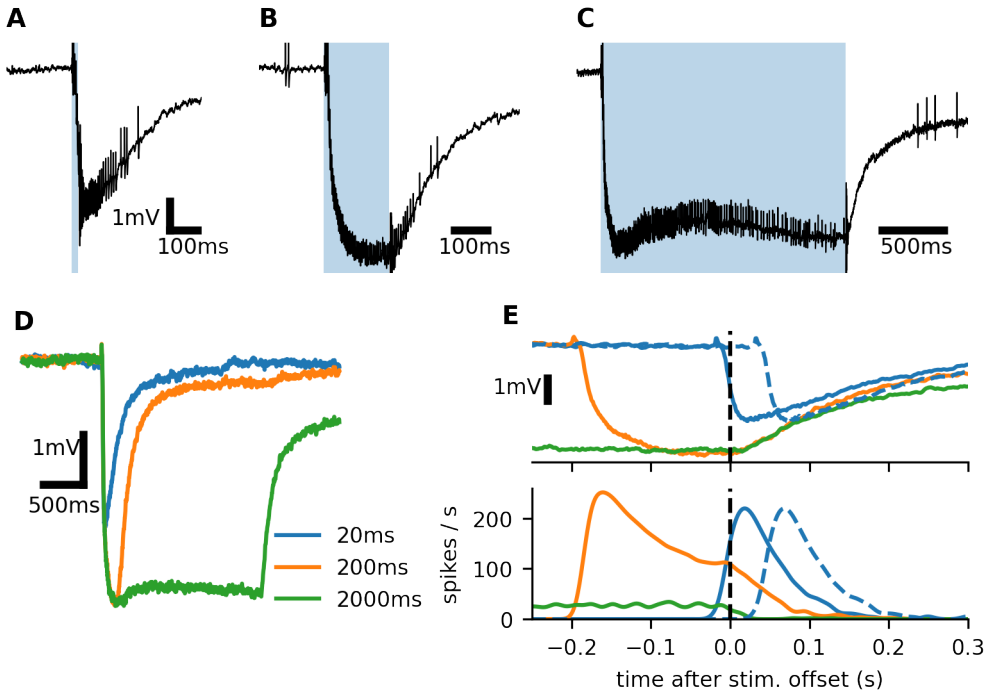

Fig 4. Firing rate depends on the history of the input. A-C: Raw recordings of a single ORN's response to three different stimulus durations. **D:** LFP responses averaged over 26 sensilla. Note that in response to the 2 s stimulus, LFP first increases after the initial decrease, indicating receptor adaptation and after continues to decrease again. This is apparent also in **C**. **E:** LFP (top) and average firing rate (bottom) aligned at the stimulus termination. The LFP after the stimulus offset is identical for the 200 ms and 2 s stimulus, yet their firing rates are dramatically different. The dashed blue lines indicate the response to the 20 ms stimulus, but shifted by 50 ms. Then the LFP time course after the stimulus offset is identical with the 200 ms stimulus, but the firing rates again greatly differ.

Figure 4–Figure supplement 1. Multicompartmental ORN model

Figure 4–Figure supplement 2. Heterogeneity of ORN responses

Figure 4–Figure supplement 3. LFP recordings with TTX

convolution can be equivalently expressed as

$$K_f * \mathrm{LFP}(t) = c_0 \cdot \mathrm{LFP}(t) + \sum_{k=1}^{n} c_k \cdot (g_k * \mathrm{LFP})(t) \tag{2}$$

$$g_k(t) = \begin{cases} \frac{1}{\Gamma(\alpha_k)\tau_k^{\alpha_k}} t^{\alpha_k - 1} e^{-\frac{t}{\tau_k}} & t \geq 0, \\ 0 & t < 0, \end{cases} \tag{3}$$

where c_k are the linear combination coefficients and τ_k are the time scales $\alpha_k \geq 1$ are the shapes of the gamma distributions. N is a rectifying nonlinearity ($N(x) = \max(0, x)$). Using lasso regression, we found that the firing rate can be reliably predicted from the LFP using only two time scales: 40 ms and 800 ms and the unfiltered LFP (see Materials and methods and Figure 5–Figure Supplement2 for details, note that the LFP provides a low-pass filtered representation of the depolarizing current).

We fitted the coefficients c_k to a 2 s stimulus (and the preceding 1 s of spontaneous activity) individually to each of 26 different neuron recordings by minimizing the square

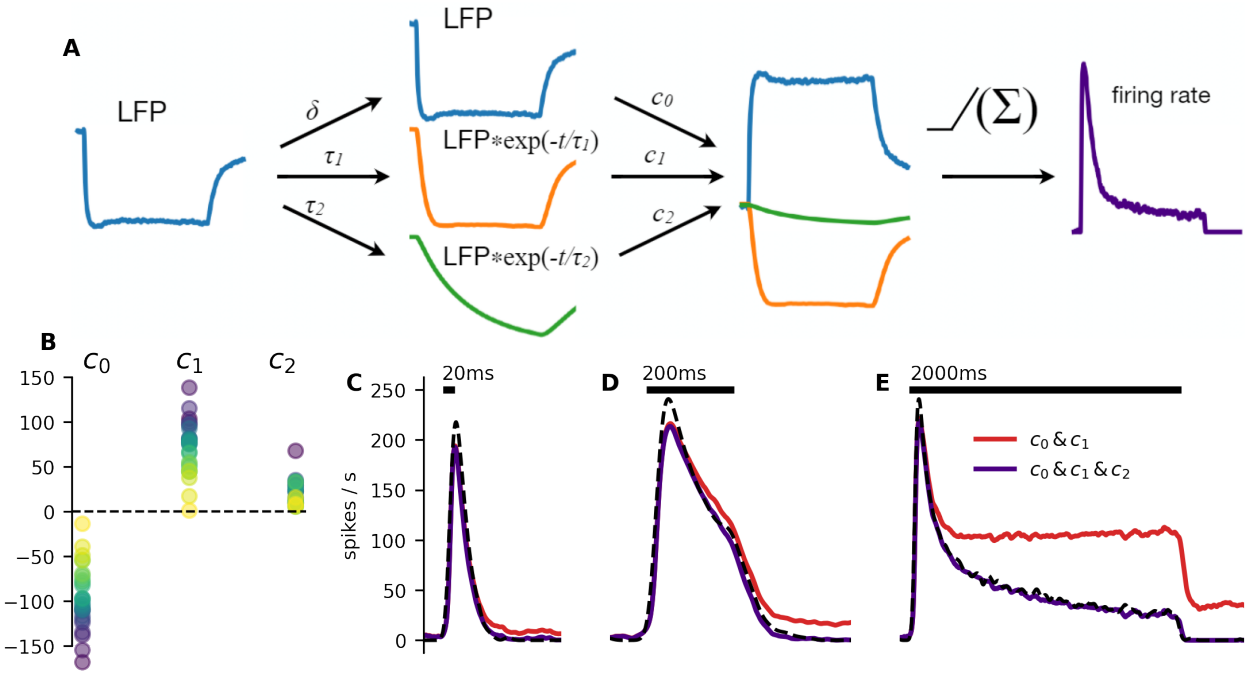

Fig 5. Slow spike-frequency adaptation is necessary to reproduce the ORNs' behavior. A: Illustration of the firing rate prediction process. The LFP was filtered with two different exponential kernels with time constants τ_1 and τ_2. Linear combination of the filtered values and the LFP, followed by a rectifying non-linearity, provides a prediction of the firing rate. This process is equivalent to directly convoluting the LFP with a linear filter composed of two exponential kernels and a δ-function. **B:** Values of the optimal coefficients for all the fitted neurons. Points are color coded by ORNs. **C-E:** Predictions of the firing rate with and without the slow (800 ms) component. Predictions with the full filter closely match the empirical firing rate (dashed black line). The reduced filter predicts well the responses to short stimuli, but fails to predict the response to the 2 s stimulus.

Figure 5–Figure supplement 1. Distributions of filter coefficients and their effect on spike firing properties

Figure 5–Figure supplement 2. Selection of filter time constants

Figure 5–Figure supplement 3. Firing rate prediction using odor transduction model

error between the prediction and the observed firing rate. The average values of the coefficients were $c_0 = -95.4$, $c_1 = 71.7$, $c_2 = 20.4$ (the coefficient distributions and their mutual dependence is shown in Figure 5B and Figure 5–Figure Supplement1A). The signs indicate that the neurons respond rapidly to LFP deflection by firing activity ($c_0 < 0$), which is then attenuated by adaptation on two different time scales ($c_k > 0$, $k \geq 1$). The ratio $\frac{c_1+c_2}{c_0}$ is negatively correlated with the steady state-to-peak ratio (Figure 5–Figure Supplement1D). Using only the LFP (indicating the depolarization of the neuron) and two adaptation time scales, we were able to predict very well the ORNs' firing responses (Figure 5C-E). Despite being fit only to the 2 s pulse, the predicted firing rate corresponds well even to the responses to the 20 ms and 200 ms pulses, including the firing profile after the stimulus offset, which is different for each pulse duration.

The presented model is the minimal model capable of capturing the shape of the firing response. With $c_2 = 0$ (set after the fitting procedure), the model still predicts well the response to short stimuli (during the short period, the neuron does not become adapted on the slow time scale), however, it does not predict the continued decrease of firing rate during the 2 s long stimulation. If the model is fitted without the slow

adaptation, aside from not predicting the time course of the firing rate well, the model does not predict the prolonged responses as well (Figure 5–Figure Supplement2D-F).

We fit the model to each neuron individually, because the pheromone sensitive ORNs of moth exhibit a significant cell-to-cell variability, as analyzed by Rospars et al. (2014). Apart from the variability in the firing responses, we also observed variability in the LFP shapes (in response to a 2 s stimulus). We verified that the response of a single neuron over multiple trials is stable (exhibits little variability) compared to the measured population Figure 4–Figure Supplement2.

It is also possible to obtain a full odor-to-firing-rate model. We used a simple transduction model to predict the LFP from the odor concentration (Nagel and Wilson, 2011):

$$\mathrm{R} \underset{s_b}{\overset{[\mathrm{O}]k_\mathrm{b}s_\mathrm{b}}{\rightleftharpoons}} \mathrm{OR} \underset{s_a}{\overset{k_a s_a}{\rightleftharpoons}} \mathrm{OR}^*, \tag{4}$$

$$\mathrm{LFP} = \mathrm{OR}^* * g_\mathrm{LFP}, \tag{5}$$

where R are the unbound receptors, OR are bound, but not activated receptors and OR^* are bound activated receptors, [O] is the odorant concentration, s_a and s_b are the unbinding and deactivation rates and k_a and k_b set the ratio between activation/deactivation and binding/unbinding rates and g_LFP is an exponential kernel with 10 ms decay (as estimated from our multicompartmental model; Figure 4–Figure Supplement1B-C). Because the spontaneous activity of moth ORNs is very low (0.34(3) Hz in *A. ipsilon* Jarriault et al., 2010; 0.5 Hz to 0.8 Hz in *S. littoralis* Pézier et al., 2007; see also Figure 2–Figure Supplement3), we neglected the activation of unbound receptors. The model predicts well the time course of the firing rate during stimulation and the firing rate offset (Figure 5–Figure Supplement3).

We hypothesized that the adaptation could be facilitated by hyperpolarizing Ca^{2+}-gated K^+ currents in the soma (Zufall et al., 1991; Lucas and Shimahara, 2002; Pézier et al., 2007). We illustrated on a multicompartmental model that such hyperpolarizing currents can affect the LFP by further decreasing it (Figure 4–Figure Supplement1D-G) and could thus account for the second downward deflection of LFP during 2 s stimulation. In such case, the second downward deflection could be removed by abolishing the spiking activity and thus also the Ca^{2+} influx due to action potentials. To test this hypothesis, we recorded the LFP after injecting the Na^+ channel antagonist tetrodotoxin (TTX, 50 µM) into the antenna. The TTX injections abolished the spiking activity, however the secondary deflection of the LFP remained (Figure 4–Figure Supplement3). Therefore we conclude that the secondary deflection is not caused by hyperpolarizing currents in the soma triggered by Ca^{2+} influx during action potentials.

1.4 Prolonged response to short stimuli is maintained by the antennal lobe

ORNs project their axons to the antennal lobe (AL) onto projection neurons (PNs) and local neurons (LNs). All ORNs expressing the same odorant receptor project their axons to the same glomerulus harboring the dendrites of PNs and LNs (Kay and Stopfer, 2006; Wilson, 2013). PNs create excitatory connections with other PNs and LNs provide an inhibitory feedback both to PNs and LNs. PNs then project their axons to higher brain centers. Therefore, understanding how the PNs reshape the firing response is essential for understanding the implications for behavior of the insect. Even though the observation of the inhibitory phase in moth ORNs is novel, previous studies observed the inhibitory phase in PNs, despite using the classical odor delivery device with Pasteur pipette (Jarriault et al., 2010; Martinez et al., 2013). Moreover, PNs are sensitive to the slope of ORN firing rate (Kim et al., 2015), which can explain their

transient responses. These results suggest that although ORNs are not obviously encoding the stimulus duration of short stimuli (Figure 2), the ORN responses could be processed by the AL to provide a more accurate representation of the stimulus duration.

We used the ORN firing rates as an input to an antennal lobe model (Tuckman et al., 2021a,b; see Materials and methods for details). We modelled a single glomerulus containing 10 PNs and 6 LNs. PNs create random excitatory connections to PNs and LNs withing the glomerulus and LNs create random inhibitory connection to PNs and other LNs (Figure 6A). The PNs are equipped with small conductance Ca^{2+}-activated K^+ channels (SK channels) which together with the inhibitory input facilitate spike frequency adaptation and make the PNs sensitive to the slope of the ORN input, as also observed with the *Drosophila* PNs (Kim et al., 2015). PNs then exhibit a transient inhibition at the end of the stimulus, even if no transient inhibition is observed in the ORN response, in agreement with Jarriault et al. (2010) (Figure 6B). Note that such feature cannot be reproduced with adaptation resulting purely from synaptic depression and LNs acting presynaptically, as suggested for *Drosophila* antennal lobe (Kazama and Wilson, 2008; Nagel et al., 2015). However, the response to short stimuli still significantly exceeds the stimulus duration (Figure 6C) and the firing profile shape with this model does not differ greatly from the firing profile shape of ORNs (Figure 6D). Therefore, we expect that the encoding of duration is not significantly altered by the antennal lobe and thus the longer responses to short stimuli likely propagate further and affect behavioral responses.

Although PNs can exhibit the inhibitory phase even when there is no inhibitory phase in the ORN response, their precision of stimulus duration encoding is improved by the observed dynamics in ORNs. To illustrate this, we made the ORN response less sharp by convolving it with an exponential kernel with 100 ms mean. The smoothed ORN firing profile then did not show any inhibitory phase, but the inhibitory phase was clear in the PN responses. However, the onset of the inhibitory phase did not mark the offset of the stimulus, unlike in the case of the unmodified ORN firing profile (Figure 6–Figure Supplement1).

2 Discussion

2.1 Tri-phasic response of moth ORNs

We found qualitative differences between the responses to short (¡200 ms) and long (¿200 ms) stimuli. While the spiking response to a short stimulus exceeds the stimulus duration, spiking response to a long stimulus ends with the stimulus. The response to long stimuli marks precisely the stimulus offset with an inhibitory phase. The inhibitory phase was followed by rebound activity. The intensity of the rebound activity increased both with stimulus duration and odor dose.

The observed firing pattern is reminiscent of the pattern observed previously in PNs. Our results therefore show that encoding of temporal structure of the plume happens already at the level of ORNs and not only at the level of PNs, as previously thought (Jarriault et al., 2010; Rospars et al., 2014; Tuckman et al., 2021b,a). Moreover, we showed with a simulation that the precise encoding of temporal structure by ORNs also improves the encoding by the PNs, compared to ORN responses with slow offset.

Inhibitory phase marking the end of stimulus has also been observed with various receptor-odor combinations in *Drosophila* (Nagel and Wilson, 2011; Martelli et al., 2013; Kim et al., 2011, 2015). Moreover, we observed independence of the firing response shape on the odor dose, also previously reported in *Drosophila* with volatile odors. The newly observed similarities between *Drosophila* and moth ORNs unite the research in these different species.

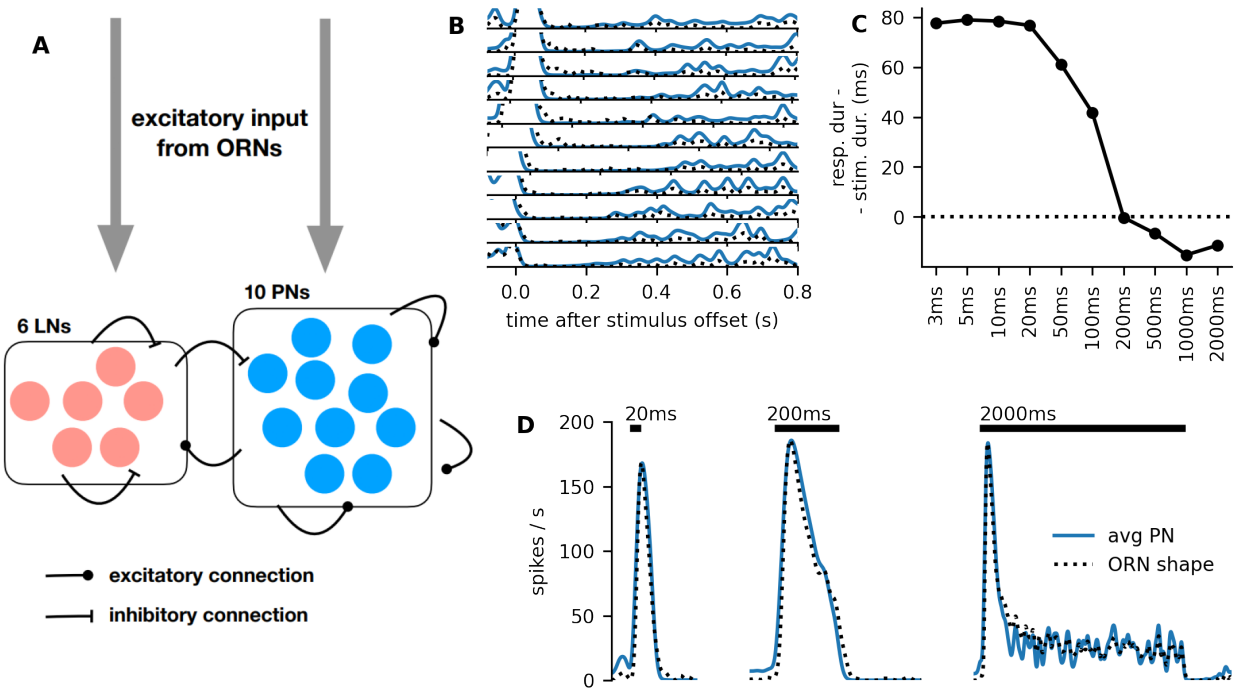

Fig 6. Modelling the antennal lobe. A: Illustration of the used model. **B:** The response end is clearly marked by an inhibitory phase, regardless of the stimulus duration (increasing from top to bottom, 3 ms to 5 s). The y-axis ranges from 0 Hz to 20 Hz. **C:** Although the inhibitory phase clearly marks the response end, the spiking response duration still exceeds significantly the stimulus duration for stimuli shorter than 200 ms. **D:** Average firing rates of the PNs in response to stimuli of different durations. Dotted ORN firing rates were used as an input. Note that the ORN input firing rate is not to scale and is normalized to the peak of the PN firing rate for shape comparison.

Figure 6–Figure supplement 1. PNs do not track odor pulse durations if ORN response is smooth

The inhibitory phase was followed by a sustained increase in the firing activity long after the stimulus termination and also a sustained LFP below the pre-stimulus level, indicating that the sustained firing activity is due to sustained activity of the receptors. With classical odor delivery devices with a Pasteur pipette, such sustained activity could be explained by a slow release of pheromone molecules after closing the valve that controls the stimulus. However, in our experiments, we strongly reduced the possibility of any pheromone molecules adhering to the odor delivery device. The sustained activity could be caused instead by odor molecules adhering to the sensilla and / or it could represent an elevated probability of spontaneous OR-Orco channel opening after prolonged ligand-receptor interaction.

Regardless of the exact mechanism leading to the sustained activity, ORNs seem to remain slightly depolarized long after the stimulus termination and the their detection threshold is thus decreased. It is possible that ORNs evolved to have a very low spontaneous activity prior to any stimulation and after sufficient pheromone exposure the activity is increased in order to decrease the detection threshold and ORNs should respond with higher intensity following a previous stimulus.

Sensitization of ORNs was observed in *Drosophila* ORNs (Getahun et al., 2013) and with heterologously expressed OR-Orco proteins (Mukunda et al., 2016). This OR sensitization process requires Orco activity and was proposed to depend on cAMP production that would activate two feedback loops involving protein kinase and

Ca^{2+}-calmodulin (Wicher, 2018).

2.2 Mechanism of the spike frequency adaptation

In *Drosophila melanogaster*, adaptation properties could be captured with a bi-lobed linear filter with a temporal width of approximately 200 ms (Nagel and Wilson, 2011; Martelli et al., 2013; see Brandão et al., 2021 for a recent review). Studies of ORN adaptation in moths suggest that their adaptation is slower (Jacob et al., 2017; Levakova et al., 2019). However, the moth studies related the firing activity to the binary state of the electrovalves controlling the odor delivery, it is therefore difficult to assess to what extent the observed signal processing timescales are a property of the odor delivery device or a property of the neuron.

We circumvented this issue by simultaneously measuring the local field potential (LFP) in the sensilla, where the ORN's outer dendrite resides. The LFP is tightly correlated with the depolarizing current entering the ORN. We built a model of transformation of the depolarizing current to the spiking activity and performed an optimization procedure which allowed us to narrow down the adaptation processes to only two time-scales, which are not directly inferable from the linear filters and importantly, provide novel insights into the possible mechanisms leading to the adaptation.

We showed that the shape of the ORN's firing response can be very well captured with only two adaptation time scales: 40 ms and 800 ms. This is the minimal model capable of explaining the transiency of the firing response and the observed temporal resolution limits of the ORN.

The slow adaptation time constant 800 ms approximately corresponds to Ca^{2+} extrusion time scales (0.4 s to 1 s in *Drosophila* ORNs; Si et al., 2019). This indicates that the adaptation of the spike generating mechanism could be Ca^{2+} dependent. Moth ORNs express Ca^{2+}-gated potassium channels (Lucas and Shimahara, 2002 in *Mamestra brassicae*; Zufall et al., 1991 in *Manduca sexta*; Pézier et al., 2007 in *S. littoralis*). Their expression in the soma would result in hyperpolarizing currents upon their activation.

Inactivation of voltage gated sodium channels (Na_V) could also be responsible for the phasicity of the spiking response (Lundstrom et al., 2008; Platkiewicz and Brette, 2010, 2011; Nagel and Wilson, 2011). However, the timescales typical for inactivation (and reactivation) of Na_V channels (4.8 ms measured in cultured honeybee ORNs (Kadala et al., 2011)) were not necessary to reproduce the firing rate profiles. Some Na_V channels also exhibit adaptation at slower time scales (Fleidervish et al., 1996; Kim and Rieke, 2003; Badel et al., 2008; Wang et al., 2013; Sarno et al., 2022). Patch clamp experiments on insect ORNs designed to measure slow adaptation of Na_V channels in insect ORNs would help to understand the physiological mechanisms behind their adaptation.

2.3 Modelling the ORN response

We proposed a minimal model that links the stimulus to the firing rate which captures well the firing profile of responses to isolated square pulses. This model can be easily used to model the input to the higher brain centers, which is otherwise often modelled as a piece-wise exponential function (Belmabrouk et al., 2011; Tuckman et al., 2021a,b). It can be extended to model the responses to more complex stimuli; however, the model captures all the features essential for our work. The following extensions could be considered:

1. Adaptation of the odor receptors
2. Persistent receptor activity

3. Nonlinearity of the slow adaptation process

Various receptor adaptation models were proposed for *Drosophila* ORNs (Nagel and Wilson, 2011; Cao et al., 2016; Gorur-Shandilya et al., 2017) and we believe that these models could be also successfully applied to the moth ORNs. However, in the case of moth, the long lasting pheromone transduction pathway (due to pheromone adherence to the sensilla and / or sustained increased probability of spontaneous receptor opening) needs to be included as well to balance the adaptation and maintain receptor activity after the stimulus offset and avoid transient LFP overshoot, as observed in some *Drosophila* ORNs (Nagel and Wilson, 2011). It is also possible that the physics of fluid (air) movement across morphologically distinct antennal types (globular in *Drosophila*, feather-like in *A. ipsilon*), and the wingbeat frequency of the insect (200 Hz in *Drosophila*, 5 Hz to 20 Hz in moths) that re-sculpt the odor plume could have both contributed to the evolution of the differentiated transduction process.

Our linear-nonlinear model predicts well the time course of the firing rate during stimulation and its offset after stimulus termination. However, the predicted duration of the inhibitory period is longer than what we generally observe. We believe that this can be explained by a voltage dependency of the slow adaptation process. Such non-linearity seems plausible, since either the Na_V channels can recover faster at low membrane potential values, or the voltage dependency of the Ca^{2+}-gated K^+ channels causes them to close rapidly at low membrane potential values (Lucas and Shimahara, 2002).

2.4 Implications for behavior and navigation efficiency

Behavioral experiments showed that male moths reach the pheromone source most reliably and with the least amount of counter-turning if the source is pulsating (Kennedy et al., 1980; Willis and Baker, 1984; Mafra-Neto and Cardé, 1994). Particularly, in (Mafra-Neto and Cardé, 1994), the pulse duration was 130 ms and the air-gap duration between pulses was 83 ms (experiments done with the almond moth *Cadra cautella*). These observations correlate well with our results showing that the ORNs exhibit prolonged firing response to short (¡200 ms) stimuli. Moreover, prolonged response to very short stimuli (e.g., 3 ms) can ensure that the brief encounter is registered by the brain and can be acted upon.

On the other hand, the slow (800 ms) adaptation allows the moth to respond rapidly to a loss of pheromone signal after a prolonged exposure, but possibly also to adapt to the background intensity within a pheromone plume. If the prolonged firing response to short stimuli causes prolonged upwind flight after stimulus offset, we expect faster switching from upwind flight to zig-zag casting after the stimulus offset with longer stimuli. Such behavioral experiments could show a clear connection between the temporal structure of the ORN and PN response and behavior.

3 Materials and methods

3.1 Insects

A. ipsilon and *S. littoralis* adult males were fed on an artificial diet. Pupae were sexed and males and females were kept separately in an inversed light–dark cycle (16 h:8 h light:dark photoperiod) at 22 °C. Experiments were carried out on 5-day-old males.

3.2 Chemicals

The main components of the pheromones of *A. ipsilon* (Z7-12:Ac, CAS 14959-86-5) and *S. littoralis* (Z9,E11-14:Ac, CAS 50767-79-8) were bought from Pherobank (purity ¿

99%). Linalool (CAS 78-70-6, purity ¿ 97%,) α-pinene (CAS 80-56-8, purity ¿98%) and acetone (CAS 67-64-1) were bought from Sigma-Aldrich. They were diluted at 10% in mineral oil (CAS 8012-95-1).

3.3 Odor delivery

Our odor delivery device is based on 2 serially connected electrovalves. The first electrovalve (any of EV1 - EV8, further referred to as upstream valve) odorizes the passing airflow. The second electrovalve (EV9, downstream valve) controls the timing of the stimulus (Figure 1–Figure Supplement1).

A charcoal-filtered and humidified air stream (2.5 bar) is divided into 8 flows (200 mL/min each) with an airflow divider (LFMX0510528B, The Lee Company, Westbrook, CT, USA). Each of the 8 flows is connected to a 3-way electrovalve (EV1 to EV8; LHDA1223111H, The Lee Company). Normally opened (NO, non-odorized) and normally closed (NC, odorized) exits of the eight valves are connected to a low dead-volume manifold (MPP-8, Warner Instruments, Holliston, MA, USA) or to odor sources, respectively. The non-odorized airflow permanently bathes the insect preparation. All outlets of odor sources are connected to a second MPP-8 manifold that is connected to an electrovalve (EV9; LHDA1233215H, The Lee Company). The NO exit of EV9 is introduced within a vacuum system. A small glass tube (10 mm total length, 1.16 mm internal diameter) bent at 90° facilitated focusing the stimuli on the insect antenna. EV9 and the small bent tube are thus the sole surface on which odor puffs controlled by EV9 can adsorb and thus alter the stimulus dynamics. The outlet of the small tube is positioned under the dissecting microscope at 1 mm from the recorded sensilla. An aluminium shield connected to the ground around EV9 minimizes artifacts during opening and closing of the valve. The downstream part of the stimulator (from manifold to EV9 and the attached small bent tube) was decontaminated after each experiment for 60 min at 80 °C with an airflow injected from the small bent tube and EV9 activated. All tubing but the exit of the permanent airflow was made of Teflon (internal diameter 1.32 mm). The shape of stimuli delivered to the antenna was measured with a mini PID (Aurora Scientific Inc, Aurora, Canada).

3.3.1 Equilibration and stability of the odor source

After opening the upstream electrovalve two processes are at play when an airflow passes through the odor source, with opposite effects on the concentration of odor reaching the downstream electrovalve, EV9.

1. Dilution of the head-space, which reduces the concentration of odor delivered to EV9 with an effect that increases with time until an asymptote is reached corresponding to an equilibrium of odor molecules passing from the liquid phase to the gas phase and those carried out of the vial by the airflow.

2. Reversible binding of odor molecules to the surfaces of the odor delivery device, which reduces the concentration of odor delivered to EV9 with an effect that gradually decreases over time until it becomes null when the adsorption/desorption equilibrium is reached.

We verified with linalool (diluted at 10%) and the PID how long the upstream valve must be open before the odor concentration delivered to the downstream valve is constant (further referred to as equilibration time). With no or short equilibration times ($\leq$2 s), PID responses were not square but had a decreasing amplitude indicating that the dilution of head-space was dominant. When the equilibrium time was at least 10 s, the PID response to a 0.5 s stimulus was square. Increasing the equilibration time to

Table 1. Number of sensilla recorded for each pulse duration. Number of neurons that responded by firing at least 5 spikes in the first 100 ms after stimulus onset is in the brackets.

pulse duration:	3 ms	5 ms	10 ms	20 ms	50 ms	100 ms
	22 (7)	22 (13)	23 (21)	22 (20)	21 (20)	23 (22)

pulse duration:	200 ms	500 ms	1 s	2 s	5 s
	23 (22)	23 (23)	23 (22)	23 (22)	23 (22)

more than 10 s had very little effect on the amplitude of the PID response (Figure 1–Figure Supplement2A-B). When using α-pinene and acetone, more volatile molecules than linalool, we kept the same 10 s equilibration time.

Since the PID cannot monitor pheromone stimuli, the equilibration time with pheromone was adjusted by measuring the amplitude of SSR responses to a 0.5 s stimulus with 100 pg of Z7-12:Ac. Equilibration times of 1 s, 3 s, 10 s, 30 s, 78 s were tested both in ascending and descending order. Stimuli were applied every 2 min. Equilibrations were stopped at each stimulus offset. The amplitude of responses increased for equilibration times of 1 s to 30 s and then remained stable, indicating that the odor binding to surfaces was the dominant effect (Figure 1–Figure Supplement2C). We thus kept an equilibration time of 30 s for further experiments.

We then measured the stability of the pheromone source first by applying 9 stimuli with 100 pg of Z7-12:Ac. Each stimulus was preceded by an equilibration time of 30 s. The inter stimulus interval was 2 min. The amplitude of responses remained constant over the 9 stimuli (Figure 1–Figure Supplement2D).

3.4 Single sensillum recordings

For single sensillum recordings, male moths were briefly anesthetized with CO_2 and restrained in a Styrofoam holder. One antenna was immobilized with adhesive tape.

Single sensillum recordings were carried out either with tungsten electrodes or with glass electrodes, the later allowing to record the local field potential (LFP) in addition to the firing response of ORNs. In both cases, one electrode was inserted into the antenna to serve as a reference. We targeted the ORNs tuned to the pheromone constituent Z7-12:Ac. The recording electrode was inserted at the base of one of the long trichoid sensilla located along antennal branches, the vast majority of which house an ORN tuned to the major pheromone component Z7-12:Ac. The reference electrode was inserted in an antennal segment next to the one bearing the recorded sensillum. Recordings were done using a CyberAmp 320 controlled by pCLAMP10 (Molecular Devices, San Jose, CA, USA). The signal was amplified ($\times$100), band-pass filtered (10 Hz to 3000 Hz) with tungsten electrodes or low-pass filtered (3000 Hz) with glass electrodes and sampled at 10 kHz with a Digidata 1440A acquisition board (Molecular Devices). Spikes were sorted using Spike 2 software (CED, Oxford, Great Britain).

3.4.1 Experimental protocols

To record the firing responses to pulses of different durations (Figure 2), we performed recordings with tungsten electrode from 23 sensilla and presented them with stimuli of durations 3 ms, 5 ms, 10 ms, 20 ms, 50 ms, 100 ms, 200 ms, 500 ms, 1 s, 2 s and 5 s (pheromone dose 100 pg) in a randomized order. There was a 2 min gap between stimuli. The number of recorded responses varies for each duration and is provided in Table 1.

Table 2. Number of sensilla recorded for each duration-dose pair. Number of neurons that responded by firing at least 5 spikes in the first 100 ms after stimulus onset is in the brackets.

	20 ms	200 ms	2 s
10 pg	57 (28)	57 (32)	57 (32)
100 pg	55 (33)	56 (44)	54 (38)
1 ng	53 (40)	52 (39)	52 (41)

To test the responses to different pheromone doses (Figure 3), we performed recordings with tungsten electrodes from 57 sensilla, presenting them with pulses of durations 20 ms, 200 ms and 2 s in a randomized order, but with an increasing pheromone dose. The number of responses recorded for each duration-dose pair is provided in Table 2.

We recorded the LFP simultaneously with the spiking activity for the pulse durations 20 ms, 200 ms and 2 s, presented in randomized order with 3 min inter-stimulus intervals (dose 1 ng). In some recordings with the glass electrode we observed a significant change in the shape of the firing response; particularly, the neurons started responding more tonically with time and did not exhibit the inhibitory period after 2 s pulse anymore. We assume that this is due to the glass electrode being more invasive than the sharper tungsten electrode, modifying the composition of the sensillar lymph and/or damaging the ORN. Therefore, in order to exclude neurons whose functioning was altered, we presented one more 2 s pulse after the the initial three pulses and included the recording in the analysis only if the second response to the 2 s pulse exhibited the inhibitory phase (here defined as zero spikes during the interval 50 ms to 500 ms). In total, we used 26 out of 37 recordings, therefore 26 responses for each duration. To filter out the LFP without action potentials we used a 15 Hz 2-pole Butterworth low-pass filter.

For the experiments using TTX, the drug was dissolved (50 µM) in saline (in mM: NaCl 154, KCl 3, glucose 24) and injected into the body of the antenna using a syringe-driven glass micropipette. Controls were saline injections. Recordings started 5 min after injection. The firing activity was completely abolished after all TTX injections and remained intact after saline injections.

3.5 Data analysis

3.5.1 Firing frequency

We estimated the firing rates by the kernel density estimation method. Each spike was substituted with a normal distribution probability distribution function with mean at the spike time and standard deviation $\sigma = \frac{\mathrm{bw}}{2}$, where bw is the kernel width.

In Figure 2 we used a time dependent kernel width in order to depict the responses to short stimuli with sufficient detail, but avoid high noise when the firing rate drops during longer stimulation. The time dependence was given by:

$$\mathrm{bw}(t) = \begin{cases} \mathrm{bw}_{\min} & t < 0, \\ \mathrm{bw}_{\max} - \mathrm{bw}_{\min} \exp\left(-t/\tau_{\mathrm{KDE}}\right) + \mathrm{bw}_{\min} & t > 0, \end{cases} \tag{6}$$

where $\mathrm{bw}_{\min} = 10\,\mathrm{ms}$, $\mathrm{bw}_{\max} = 100\,\mathrm{ms}$, $\tau_{\mathrm{KDE}} = 500\,\mathrm{ms}$ and we assume that the stimulus onset is at 0.

3.5.2 Response end of individual ORNs

The first inter-spike interval (ISI) that finishes after the stimulus offset and exceeds 100 ms is considered as the terminating ISI and the initiating AP as the time of the

response end. We calculated the response end only if the neuron fired at least 5 action potentials during the first 100 ms after the stimulus onset (numbers of responding neurons provided in brackets in Table 1 and Table 2). We then calculated the time of the response end for a group of neurons as the median of individual response ends (red vertical lines in Figure 2 and Figure 3). Note that if the ISI after the last spike during stimulation is longer than 100 ms, the calculated response end for the ORN is before the stimulus end.

3.6 Linear-nonlinear model for firing rate prediction

We used linear regression to predict the firing rate. As independent variables, we used values of the past LFP convolved with a gamma distribution-shaped function with different time constants and shape parameters (Gorur-Shandilya et al., 2017; Jayaram et al., 2022):

$$x(t;\tau,\alpha) = \int_0^{+\infty} V(t-s)\frac{1}{\Gamma(\alpha)\tau^\alpha}t^{\alpha-1}e^{-\frac{t}{\tau}}\,\mathrm{d}s, \tag{7}$$

where V is the LFP. The model is then specified by the time constants τ_1, ..., τ_n and the corresponding shape parameters α_1, ..., α_n. The estimated firing rate before the non-linearity is specified by the coefficients c_1, ..., c_n:

$$f(t) = \sum_{k=1}^{n} c_k x(t;\tau_k). \tag{8}$$

We estimated the coefficients with the least square method to provide the estimate of firing rate (estimated from the spike train with kernel width 30 ms) during the 2 s stimulus and 1 s of the preceding spontaneous activity.

In order to choose the time constants and shapes specifying the model, we initially used a model with 20 time constant, ranging from 1 ms to 3 s, equidistantly spaced on the logarithmic scale. Moreover, we used 17 different gamma distribution shapes α ranging from 1 to 5, equidistantly spaced. The model then contained 20×17 independent variables. We fit the model to the average LFP and average firing rate response during 2 s stimulus with lasso regression (optimal L1 penalty parameter was selected with cross-validation using the LassoCV regressor in Scikit-learn (Pedregosa et al., 2011)). The non-zero coefficients then concentrated around several (α, τ) pairs, but mostly at the $\alpha = 1$ edge, from which we selected the three time constants with $\alpha = 1$, i.e., exponential kernels (1 ms, 40 ms, 800 ms, Figure 5–Figure Supplement2A). For simplicity, we substituted the kernel with $\tau = 1$ ms with a δ-function.

Although the filter obtained from the full lasso regression looks different from the filters obtained with only three exponential kernels (Figure 5–Figure Supplement2B-C), the predicted firing rates are nearly identical (Figure 5–Figure Supplement2D-F).

3.7 Modelling odor transduction

We modelled the transduction described by ***Eq. 4*** by a set of differential equations:

$$\frac{\mathrm{d}}{\mathrm{d}t}\mathrm{R} = s_b \cdot \mathrm{OR} - [\mathrm{O}]k_b s_b \cdot \mathrm{R}, \tag{9}$$

$$\frac{\mathrm{d}}{\mathrm{d}t}\mathrm{OR} = [\mathrm{O}]k_b s_b \cdot \mathrm{R} + s_a \cdot \mathrm{OR}^* - k_a s_a \cdot \mathrm{OR} - s_b \cdot \mathrm{OR}, \tag{10}$$

$$\frac{\mathrm{d}}{\mathrm{d}t}\mathrm{OR}^* = -s_a \cdot \mathrm{OR}^* + k_a s_a \cdot \mathrm{OR}, \tag{11}$$

$$\frac{\mathrm{d}}{\mathrm{d}t}\mathrm{LFP} = -\frac{1}{\tau_{\mathrm{LFP}}}(\mathrm{LFP} - \beta \cdot \mathrm{OR}^*). \tag{12}$$

Table 3. Synaptic connection amplitudes.

	S_{exc}	S_{inh}	S_{slow}	S_{stim}
PN	0.01	0.0169	0.0338	0.004
LN	0.006	0.015	0.04	0.0031

R, OR and OR* indicate the ratios of unbound, bound and activated bound receptors, $\tau_{\text{LFP}} = 10\,\text{ms}$. The initial conditions are $\text{R} = 1$ and $\text{OR} = \text{OR}^* = \text{LFP} = 0$. We modelled the odor concentration as a square odor pulse: $[\text{O}] = 10^{-11}\,\text{M}$ during stimulation and 0 otherwise. Because we did not attempt to model the adaptation and the sustained activity (more important with long stimuli), we fitted the parameters s_b, k_b, s_a, k_a and β to the first 400 ms after stimulus onset of the average LFP from 20 ms and 200 ms stimulations. We fitted the parameters by minimizing the square error of the prediction with the L-BFGS-B algorithm implemented in SciPy (Virtanen et al., 2020). The fitted model parameters are $k_a = 6.57 \cdot 10^{11}\,\text{s}^{-1}\text{M}^{-1}$, $s_a = 7.36\,\text{s}^{-1}$, $k_b = 37.3$, $s_b = 131\,\text{s}^{-1}$, $\beta = -5.67\,\text{mV}$.

3.8 Antennal lobe model

We used a model of a single glomerulus from the AL model proposed by Tuckman et al. (2021a). In the following, we explicitely state when we deviate from the established model.

The glomerulus contained 10 PNs and 6 LN. The membrane potential dynamics of i-th PN and j-th LN were governed by the following dynamics:

$$\begin{aligned}\frac{\text{d}}{\text{d}t}V^i_{\text{PN}} = &-\frac{1}{\tau_V}(V^i_{\text{PN}} - E_L) - g^i_{\text{SK}}(t)(V^i_{\text{PN}} - E_{\text{SK}}) - g^i_{\text{stim}}(t)(V^i_{\text{PN}} - E_{\text{stim}}) - \\ &- g^i_{\text{exc}}(t)(V^i_{\text{PN}} - E_{\text{exc}}) - g^i_{\text{inh}}(t)(V^i_{\text{PN}} - E_{\text{inh}}) - g^i_{\text{slow}}(t)(V^i_{\text{PN}} - E_{\text{inh}}),\end{aligned} \quad (13)$$

$$\begin{aligned}\frac{\text{d}}{\text{d}t}V^j_{\text{LN}} = &-\frac{1}{\tau_V}(V^j_{\text{LN}} - E_L) - g^j_{\text{stim}}(t)(V^j_{\text{LN}} - E_{\text{stim}}) - \\ &- g^j_{\text{exc}}(t)(V^j_{\text{LN}} - E_{\text{exc}}) - g^j_{\text{inh}}(t)(V^j_{\text{LN}} - E_{\text{inh}}) - g^j_{\text{slow}}(t)(V^i_{\text{LN}} - E_{\text{inh}}),\end{aligned} \quad (14)$$

where τ_V is the membrane time constant, g_{SK} is the conductance of SK channels, g_{stim} is the excitatory conductance associated with the ORN input, g_{exc} is the excitatory synaptic conductance from PNs, g_{inh} is the fast inhibitory GABA_A conductance, g_{slow} is the slow GABA_B conductance. E_{SK}, E_{stim}, E_{exc}, E_{inh} are the reversal potentials associated with these conductances, E_L is the leak reversal potential. The reversal potentials are expressed in nondimensional units: $E_L = 0$, $E_{\text{exc}} = E_{\text{stim}} = \frac{14}{3}$, $E_{\text{SK}} = E_{\text{inh}} = -\frac{2}{3}$. The neuron fires a spike then the membrane potential V reaches the threshold $V_{\text{thr}} = 1$ and is then reset to E_L and held at E_L for τ_{ref}. The synaptic conductances g_X, $X \in \{\text{exc}, \text{inh}, \text{slow}, \text{stim}\}$ follow the equation

$$\tau_X \frac{\text{d}}{\text{d}t} g^i_X = -g^i_X + S_X \sum_{t_{\text{spike}} \in \{t^i_X\}} \delta(t - t_{\text{spike}}), \quad (15)$$

where $\{t^i_X\}$ represents the corresponding presynaptic spikes to the i-th, τ_X is the synaptic time constant for the given synapse type and the conductance increases by $\tau_X S_X$ with each presynaptic spike arrival. S_X differ for PNs and LNs and are specified in Table 3.

Table 4. Neuron connection probabilities.

PN→PN	PN→LN	LN→PN	LN→LN
0.75	0.75	0.38	0.25

The SK conductance g_{SK} was modelled only for the PNs and did not rise instantaneously, instead followed the equations:

$$\tau_{\mathrm{rise}}\frac{\mathrm{d}}{\mathrm{d}t}g^i_{\mathrm{SK}} = -(g^i_{\mathrm{SK}} - z), \tag{16}$$

$$\tau_{\mathrm{SK}}\frac{\mathrm{d}}{\mathrm{d}t}z = -z + S_{\mathrm{SK}}\sum_{t_{\mathrm{spike}}\in\{t^i\}}\delta(t - t_{\mathrm{spike}}), \tag{17}$$

where τ_{rise} characterizes the rise time, τ_{SK} is the decay time constant of the SK conductance and $\{t^i\}$ is the set of spikes fired by the i-th PN. Note that here, for simulation purposes, we deviate from the original model (Tuckman et al., 2021a) by modelling g^i_{SK} with a set of two equations instead of modelling the time course of g^i_{SK} following a single spike as a piece-wise function. S^i_{SK} was drawn from a normal distribution with mean $\mu = 0.5$ and $\sigma = 0.2$ (negative values were set to 0).

The connection between the neurons within the glomerulus were random with probabilities specified in Table 4.

To model the ORN input, we generated the spike trains of 10^4 ORNs from an inhomogeneous Poisson process, each ORN connects to any AL neuron with a 1% probability. The time course of each ORN was given by the average ORN firing rate (Figure 2, note that the input therefore differs from (Tuckman et al., 2021a)). We also added a constant ORN input of 30 Hz as a means to increase the spontaneous activity, as observed in experiments (Jarriault et al., 2010).

We simulated the network using the Brian 2 Python package (Stimberg et al., 2019).

3.9 Multicompartmental ORN model

The model is a simplified version of the moth pheromone transduction model by Gu et al. (2009). From this model we kept the morphology and the passive conductances (Figure 4–Figure Supplement1). The following set of equations describes the evolution of the potentials in the individual compartments:

$$\begin{aligned}\frac{\mathrm{d}V_{\mathrm{id}}}{\mathrm{d}t} =& \frac{G_e}{C_{md}(G_e+G_i)}(I_R + I_{ld} - I_e)\\ &+ \frac{G_e}{C_{ma}(G_e+G_i)}(I_a - I_e) + \frac{G_i}{C_{ms}(G_e+G_i)}(I_i - I_{ls} - I_{\mathrm{ad}}),\end{aligned} \tag{18}$$

$$\begin{aligned}\frac{\mathrm{d}V_{\mathrm{ed}}}{\mathrm{d}t} =& \frac{G_i}{C_{md}(G_e+G_i)}(I_e - I_R - I_{ld})\\ &+ \frac{G_e}{C_{ma}(G_e+G_i)}(I_a - I_e) + \frac{G_i}{C_{ms}(G_e+G_i)}(I_i - I_{ls} - I_{\mathrm{ad}}),\end{aligned} \tag{19}$$

$$\frac{\mathrm{d}V_{\mathrm{is}}}{\mathrm{d}t} = \frac{I_i - I_{ls} - I_{\mathrm{ad}}}{C_{ms}}, \tag{20}$$

$$\frac{\mathrm{d}V_{\mathrm{ea}}}{\mathrm{d}t} = \frac{I_a - I_e}{C_{ma}}. \tag{21}$$

Where the currents are described by:

$$I_{ls} = G_{ls}(V_{\mathrm{is}} - E_{ls}), \tag{22}$$
$$I_{ld} = G_{ld}(V_{\mathrm{ed}} - V_{\mathrm{id}} + E_{ld}), \tag{23}$$
$$I_i = G_i(V_{\mathrm{id}} - V_{\mathrm{is}}), \tag{24}$$
$$I_a = -G_a(V_{\mathrm{ea}} + E_a), \tag{25}$$
$$I_e = G_e(V_{\mathrm{ea}} - V_{\mathrm{ed}}). \tag{26}$$

I_R is the receptor current, which we either calculated by fixing the LFP (V_{ed}) and calculating what receptor current I_R is necessary to produce given LFP time course, or we fixed the I_R time course. To estimate I_R from given LFP, we substituted Eq. 19 by the numerical derivative of the LFP and expressed I_R using the numerical derivative to use in Eq. 18.

I_{ad} is the adaptation current. We considered $I_{\mathrm{ad}} \neq 0$ only to illustrate the effect of adaptation currents in the soma on the LFP. In such case, we fixed the input I_R to the model and fixed the time course of the somatic membrane potential V_{is} to correspond to the shape of the firing rate (again, by calculating its numerical derivative and eliminating Eq. 20). Then we calculated the necessary I_{ad} to balance the depolarizing effect of I_R.

We simulated the multicompartmental model with the explicit Runge-Kutta method of order 5(4) with upper limit on integration step 0.1 ms implemented in SciPy (Virtanen et al., 2020). We used the initial conditions $V_{\mathrm{ed}} = V_{\mathrm{ea}} = -35\,\mathrm{mV}$, $V_{\mathrm{id}} = V_{\mathrm{is}} = -62\,\mathrm{mV}$. This condition corresponds to $I_e = I_{ld} = I_i = I_{ls} = I_a = 0$, given that $I_R = I_{\mathrm{ad}} = 0$.

4 Acknowledgments

We are grateful to Claude Collet for a helpful discussion on sodium channels in the insect olfactory system and to Vincent Jacob for critical reading of the manuscript. This work was supported by the Charles University, project GA UK No. 1042120 and the Czech Science Foundation project 20-10251S. TB benefited from a fellowship from the Plant Health and Environment Division of INRAE.

5 Data availability

Associated data, computer code and Jupyter notebooks are available in a GitHub repository:

`https://github.com/Tom83B/moth-duration-encoding`.

References

M. J. Anderson, J. G. Sullivan, T. K. Horiuchi, S. B. Fuller, and T. L. Daniel. A bio-hybrid odor-guided autonomous palm-sized air vehicle. *Bioinspir. Biomim.*, 16(2): 026002, 3 2020. ISSN 1748-3182. doi: 10.1088/1748-3190/abbd81.

N. Ando, S. Emoto, and R. Kanzaki. Odour-tracking capability of a silkmoth driving a mobile robot with turning bias and time delay. *Bioinspir. Biomim.*, 8(1):016008, 2 2013. ISSN 1748-3182. doi: 10.1088/1748-3182/8/1/016008.

A. M. Angioy, A. Desogus, I. T. Barbarossa, P. Anderson, and B. S. Hansson. Extreme Sensitivity in an Olfactory System. *Chem. Senses*, 28(4):279–284, 5 2003. ISSN 14643553. doi: 10.1093/chemse/28.4.279.

L. Badel, S. Lefort, R. Brette, C. C. H. Petersen, W. Gerstner, and M. J. E. Richardson. Dynamic I-V Curves Are Reliable Predictors of Naturalistic Pyramidal-Neuron Voltage Traces. *J. Neurophysiol.*, 99(2), 2 2008. ISSN 0022-3077. doi: 10.1152/jn.01107.2007.

H. Belmabrouk, T. Nowotny, J.-P. Rospars, and D. Martinez. Interaction of cellular and network mechanisms for efficient pheromone coding in moths. *Proc. Natl. Acad. Sci. U.S.A.*, 108(49), 12 2011. ISSN 0027-8424. doi: 10.1073/pnas.1112367108.

S. C. Brandão, M. Silies, and C. Martelli. Adaptive temporal processing of odor stimuli. *Cell Tissue Res.*, 383(1):125–141, 1 2021. ISSN 0302-766X. doi: 10.1007/s00441-020-03400-9.

S. A. Budick, M. B. Reiser, and M. H. Dickinson. The role of visual and mechanosensory cues in structuring forward flight in ¡i¿Drosophila melanogaster¡/i¿. *J. Exp. Biol.*, 210(23):4092–4103, 12 2007. ISSN 1477-9145. doi: 10.1242/jeb.006502.

L.-H. Cao, B.-Y. Jing, D. Yang, X. Zeng, Y. Shen, Y. Tu, and D.-G. Luo. Distinct signaling of Drosophila chemoreceptors in olfactory sensory neurons. *Proc Natl Acad Sci USA*, 113(7), 2 2016. ISSN 0027-8424. doi: 10.1073/pnas.1518329113.

R. T. Cardé. Navigation Along Windborne Plumes of Pheromone and Resource-Linked Odors. *Annu. Rev. Entomol.*, 66(1):317–336, 1 2021. ISSN 0066-4170. doi: 10.1146/annurev-ento-011019-024932.

R. T. Cardé and R. E. Charlton. Olfactory sexual communication in Lepidoptera: strategy, sensitivity and selectivity. In T. Lewis, editor, *Insect communication*, pages 241–265. Academic press, London, 1984.

A. Celani, E. Villermaux, and M. Vergassola. Odor Landscapes in Turbulent Environments. *Phys Rev X*, 4(4):041015, 10 2014. ISSN 2160-3308. doi: 10.1103/PhysRevX.4.041015.

A. Dieudonné, T. L. Daniel, and S. P. Sane. Encoding properties of the mechanosensory neurons in the Johnston's organ of the hawk moth, ¡i¿Manduca sexta¡/i¿. *J. Exp. Biol.*, 1 2014. ISSN 1477-9145. doi: 10.1242/jeb.101568.

J. S. Elkinton, C. Schal, T. Onot, and R. T. Cardé. Pheromone puff trajectory and upwind flight of male gypsy moths in a forest. *Physiol. Entomol.*, 12(4):399–406, 12 1987. ISSN 0307-6962. doi: 10.1111/j.1365-3032.1987.tb00766.x.

I. A. Fleidervish, A. Friedman, and M. J. Gutnick. Slow inactivation of Na+ current and slow cumulative spike adaptation in mouse and guinea-pig neocortical neurones in slices. *J. Physiol. (Lond.)*, 493(1), 5 1996. ISSN 00223751. doi: 10.1113/jphysiol.1996.sp021366.

M. N. Getahun, S. B. Olsson, S. Lavista-Llanos, B. S. Hansson, and D. Wicher. Insect Odorant Response Sensitivity Is Tuned by Metabotropically Autoregulated Olfactory Receptors. *PLoS ONE*, 8(3):e58889, 3 2013. ISSN 1932-6203. doi: 10.1371/journal.pone.0058889.

S. Gorur-Shandilya, M. Demir, J. Long, D. A. Clark, and T. Emonet. Olfactory receptor neurons use gain control and complementary kinetics to encode intermittent odorant stimuli. *eLife*, 6:e27670, 2017. doi: https://doi.org/10.7554/eLife.27670.001.

S. Gorur-Shandilya, C. Martelli, M. Demir, and T. Emonet. Controlling and measuring dynamic odorant stimuli in the laboratory. *J. Exp. Biol.*, 222(23):jeb207787, 12 2019. ISSN 0022-0949. doi: 10.1242/jeb.207787.

A. Grémiaux, T. Nowotny, D. Martinez, P. Lucas, and J.-P. Rospars. Modelling the signal delivered by a population of first-order neurons in a moth olfactory system. *Brain Res.*, 1434, 1 2012. ISSN 00068993. doi: 10.1016/j.brainres.2011.09.035.

Y. Gu, P. Lucas, and J.-P. Rospars. Computational Model of the Insect Pheromone Transduction Cascade. *PLoS Comput. Biol.*, 5(3):e1000321, 3 2009. ISSN 1553-7358. doi: 10.1371/journal.pcbi.1000321.

V. Jacob, C. Monsempès, J.-P. Rospars, J.-B. Masson, and P. Lucas. Olfactory coding in the turbulent realm. *PLoS Comput. Biol.*, 13(12):e1005870, 12 2017. ISSN 1553-7358. doi: 10.1371/journal.pcbi.1005870.

D. Jarriault, C. Gadenne, P. Lucas, J.-P. Rospars, and S. Anton. Transformation of the Sex Pheromone Signal in the Noctuid Moth Agrotis ipsilon: From Peripheral Input to Antennal Lobe Output. *Chem. Senses*, 35(8):705–715, 10 2010. ISSN 0379-864X. doi: 10.1093/chemse/bjq069.

V. Jayaram, N. Kadakia, and T. Emonet. Sensing complementary temporal features of odor signals enhances navigation of diverse turbulent plumes. *eLife*, 11, 1 2022. ISSN 2050-084X. doi: 10.7554/eLife.72415.

C. Jones. On the structure of instantaneous plumes in the atmosphere. *J. Hazard. Mat.*, 7(2):87–112, 1 1983. ISSN 03043894. doi: 10.1016/0304-3894(83)80001-6.

K. A. Justus, J. Murlis, C. Jones, and R. T. Cardé. Measurement of odor-plume structure in a wind tunnel using a photoionization detector and a tracer gas. *Environ. Fluid Mech.*, 2(1/2), 2002. ISSN 15677419. doi: 10.1023/A:1016227601019.

A. Kadala, M. Charreton, I. Jakob, Y. Le Conte, and C. Collet. A use-dependent sodium current modification induced by type I pyrethroid insecticides in honeybee antennal olfactory receptor neurons. *Neurotoxicology*, 32(3):320–330, 6 2011. ISSN 0161813X. doi: 10.1016/j.neuro.2011.02.007.

K.-E. Kaissling. The Sensitivity of the Insect Nose: The Example of Bombyx Mori. In *Biologically inspired signal processing*, pages 45–52. Springer Verlag, 2009. doi: 10.1007/978-3-642-00176-5{_}3.

K.-E. Kaissling and E. Priesner. Die Riechschwelle des Seidenspinners. *Sci. Nat.*, 57(1): 23–28, 1 1970. ISSN 0028-1042. doi: 10.1007/BF00593550.

K. E. Kaissling, L. Z. Meng, and H. J. Bestmann. Responses of bombykol receptor cells to (Z,E)-4,6-hexadecadiene and linalool. *J. Comp. Physiol. A*, 165(2):147–154, 3 1989. ISSN 0340-7594. doi: 10.1007/BF00619189.

L. M. Kay and M. Stopfer. Information processing in the olfactory systems of insects and vertebrates. *Semin Cell Dev Biol.*, 17(4):433–442, 8 2006. ISSN 10849521. doi: 10.1016/j.semcdb.2006.04.012.

H. Kazama and R. I. Wilson. Homeostatic Matching and Nonlinear Amplification at Identified Central Synapses. *Neuron*, 58(3):401–413, 5 2008. ISSN 08966273. doi: 10.1016/j.neuron.2008.02.030.

J. S. Kennedy. Zigzagging and casting as a programmed response to wind-borne odour: a review. *Physiol Entomol*, 8(2):109–120, 6 1983. ISSN 0307-6962. doi: 10.1111/j.1365-3032.1983.tb00340.x.

J. S. Kennedy, A. R. Ludlow, and C. J. Sanders. Guidance system used in moth sex attraction. *Nature*, 288(5790):475–477, 12 1980. ISSN 0028-0836. doi: 10.1038/288475a0.

A. J. Kim, A. A. Lazar, and Y. B. Slutskiy. System identification of Drosophila olfactory sensory neurons. *J. Comput. Neurosci.*, 30(1), 2 2011. ISSN 0929-5313. doi: 10.1007/s10827-010-0265-0.

A. J. Kim, A. A. Lazar, and Y. B. Slutskiy. Projection neurons in Drosophila antennal lobes signal the acceleration of odor concentrations. *eLife*, 4, 5 2015. ISSN 2050-084X. doi: 10.7554/eLife.06651.

K. J. Kim and F. Rieke. Slow Na+ Inactivation and Variance Adaptation in Salamander Retinal Ganglion Cells. *J. Neurosci*, 23(4):1506–1516, 2 2003. ISSN 0270-6474. doi: 10.1523/JNEUROSCI.23-04-01506.2003.

L. Kostal, P. Lansky, and J.-P. Rospars. Efficient olfactory coding in the pheromone receptor neuron of a moth. *PLoS Comput. Biol.*, 4:e1000053, 2008.

M. Levakova, L. Kostal, C. Monsempès, V. Jacob, and P. Lucas. Moth olfactory receptor neurons adjust their encoding efficiency to temporal statistics of pheromone fluctuations. *PLoS Comput. Biol.*, 14(11):e1006586, 11 2018. doi: 10.1371/journal.pcbi.1006586.

M. Levakova, L. Kostal, C. Monsempès, P. Lucas, and R. Kobayashi. Adaptive integrate-and-fire model reproduces the dynamics of olfactory receptor neuron responses in a moth. *J R Soc Interface*, 16(157):20190246, 8 2019. doi: 10.1098/rsif.2019.0246.

P. Lucas and T. Shimahara. Voltage- and Calcium-activated Currents in Cultured Olfactory Receptor Neurons of Male Mamestra brassicae (Lepidoptera). *Chem. Senses*, 27(7):599–610, 9 2002. ISSN 14643553. doi: 10.1093/chemse/27.7.599.

B. N. Lundstrom, S. Hong, M. H. Higgs, and A. L. Fairhall. Two Computational Regimes of a Single-Compartment Neuron Separated by a Planar Boundary in Conductance Space. *Neural Comput.*, 20(5):1239–1260, 5 2008. ISSN 0899-7667. doi: 10.1162/neco.2007.05-07-536.

A. Mafra-Neto and R. T. Cardé. Fine-scale structure of pheromone plumes modulates upwind orientation of flying moths. *Nature*, 369(6476):142–144, 5 1994. ISSN 0028-0836. doi: 10.1038/369142a0.

C. Martelli, J. R. Carlson, and T. Emonet. Intensity Invariant Dynamics and Odor-Specific Latencies in Olfactory Receptor Neuron Response. *J. Neurosci*, 33(15), 4 2013. ISSN 0270-6474. doi: 10.1523/JNEUROSCI.0426-12.2013.

D. Martinez, A. Chaffiol, N. Voges, Y. Gu, S. Anton, J.-P. Rospars, and P. Lucas. Multiphasic On/Off Pheromone Signalling in Moths as Neural Correlates of a Search Strategy. *PLoS ONE*, 8(4):e61220, 4 2013. ISSN 1932-6203. doi: 10.1371/journal.pone.0061220.

D. Martinez, L. Arhidi, E. Demondion, J.-B. Masson, and P. Lucas. Using Insect Electroantennogram Sensors on Autonomous Robots for Olfactory Searches. *J. Vis. Exp.*, (90), 8 2014. ISSN 1940-087X. doi: 10.3791/51704.

M. S. Mayer and R. W. Mankin. A new Trichoplusia ni antennal receptor neuron that responds to attomolar concentrations of a minor pheromone component. *Experientia*, 46(3):257–259, 3 1990. ISSN 0014-4754. doi: 10.1007/BF01951757.

N. Montagné, T. Chertemps, I. Brigaud, A. François, M.-C. François, A. de Fouchier, P. Lucas, M. C. Larsson, and E. Jacquin-Joly. Functional characterization of a sex pheromone receptor in the pest moth Spodoptera littoralis by heterologous expression in Drosophila. *Eur. J. Neurosci.*, 36(5), 9 2012. ISSN 0953816X. doi: 10.1111/j.1460-9568.2012.08183.x.

L. Mukunda, F. Miazzi, V. Sargsyan, B. S. Hansson, and D. Wicher. Calmodulin Affects Sensitization of Drosophila melanogaster Odorant Receptors. *Front. Cell. Neurosci.*, 10, 2 2016. ISSN 1662-5102. doi: 10.3389/fncel.2016.00028.

J. Murlis, M. A. Willis, and R. T. Cardé. Spatial and temporal structures of pheromone plumes in fields and forests. *Physiol Entomol*, 25(3):211–222, 9 2000. ISSN 0307-6962. doi: 10.1046/j.1365-3032.2000.00176.x.

K. I. Nagel and R. I. Wilson. Biophysical mechanisms underlying olfactory receptor neuron dynamics. *Nat. Neurosci*, 14(2):208–216, 2 2011. ISSN 1097-6256. doi: 10.1038/nn.2725.

K. I. Nagel, E. J. Hong, and R. I. Wilson. Synaptic and circuit mechanisms promoting broadband transmission of olfactory stimulus dynamics. *Nat Neurosci*, 18(1):56–65, 1 2015. ISSN 1097-6256. doi: 10.1038/nn.3895.

A.-M. Olsson, J. A. Jönsson, B. Thelin, and T. Liljefors. Determination of the vapor pressures of moth sex pheromone components by a gas chromatographic method. *J. Chem. Ecol.*, 9(3), 3 1983. ISSN 0098-0331. doi: 10.1007/BF00988456.

F. Pedregosa, G. Varoquaux, A. Gramfort, V. Michel, B. Thirion, O. Grisel, M. Blondel, P. Prettenhofer, R. Weiss, V. Dubourg, J. Vanderplas, A. Passos, D. Cournapeau, M. Brucher, M. Perrot, and E. Duchesnay. Scikit-learn: Machine Learning in Python. *J Mach Learn Res*, 12:2825–2830, 2011.

A. Pézier, A. Acquistapace, M. Renou, J.-P. Rospars, and P. Lucas. Ca2+ Stabilizes the Membrane Potential of Moth Olfactory Receptor Neurons at Rest and Is Essential for Their Fast Repolarization. *Chem. Senses*, 32(4), 5 2007. ISSN 0379-864X. doi: 10.1093/chemse/bjl059.

J. Platkiewicz and R. Brette. A Threshold Equation for Action Potential Initiation. *PLoS Comput. Biol.*, 6(7):e1000850, 7 2010. ISSN 1553-7358. doi: 10.1371/journal.pcbi.1000850.

J. Platkiewicz and R. Brette. Impact of Fast Sodium Channel Inactivation on Spike Threshold Dynamics and Synaptic Integration. *PLoS Comput. Biol.*, 7(5):e1001129, 5 2011. ISSN 1553-7358. doi: 10.1371/journal.pcbi.1001129.

J. A. Riffell, E. Shlizerman, E. Sanders, L. Abrell, B. Medina, A. J. Hinterwirth, and J. N. Kutz. Flower discrimination by pollinators in a dynamic chemical environment. *Science*, 344(6191):1515–1518, 6 2014. ISSN 0036-8075. doi: 10.1126/science.1251041.

J.-P. Rospars, A. Grémiaux, D. Jarriault, A. Chaffiol, C. Monsempès, N. Deisig, S. Anton, P. Lucas, and D. Martinez. Heterogeneity and Convergence of Olfactory First-Order Neurons Account for the High Speed and Sensitivity of Second-Order Neurons. *PLoS Comput. Biol.*, 10(12):e1003975, 12 2014. ISSN 1553-7358. doi: 10.1371/journal.pcbi.1003975.

S. P. Sane, A. Dieudonné, M. A. Willis, and T. L. Daniel. Antennal Mechanosensors Mediate Flight Control in Moths. *Science*, 315(5813):863–866, 2 2007. ISSN 0036-8075. doi: 10.1126/science.1133598.

N. Sarno, A. Hernandez-Clavijo, A. Boccaccio, A. Menini, and S. Pifferi. Slow Inactivation of Sodium Channels Contributes to Short-Term Adaptation in Vomeronasal Sensory Neurons. *eNeuro*, 9(3):0471–21, 5 2022. ISSN 2373-2822. doi: 10.1523/ENEURO.0471-21.2022.

H. H. Shorey. *Animal communication by pheromones*. Academic press, 1976.

G. Si, J. K. Kanwal, Y. Hu, C. J. Tabone, J. Baron, M. Berck, G. Vignoud, and A. D. Samuel. Structured Odorant Response Patterns across a Complete Olfactory Receptor Neuron Population. *Neuron*, 101(5):950–962, 3 2019. ISSN 08966273. doi: 10.1016/j.neuron.2018.12.030.

M. Stimberg, R. Brette, and D. F. Goodman. Brian 2, an intuitive and efficient neural simulator. *eLife*, 8, 8 2019. ISSN 2050-084X. doi: 10.7554/eLife.47314.

E. Tiraboschi, L. Leonardelli, G. Segata, and A. Haase. Parallel Processing of Olfactory and Mechanosensory Information in the Honey Bee Antennal Lobe. *Front. Physiol*, 12, 12 2021. ISSN 1664-042X. doi: 10.3389/fphys.2021.790453.

H. Tuckman, J. Kim, A. Rangan, H. Lei, and M. Patel. Dynamics of sensory integration of olfactory and mechanical stimuli within the response patterns of moth antennal lobe neurons. *J. Theor. Biol.*, 509, 1 2021a. ISSN 00225193. doi: 10.1016/j.jtbi.2020.110510.

H. Tuckman, M. Patel, and H. Lei. Effects of Mechanosensory Input on the Tracking of Pulsatile Odor Stimuli by Moth Antennal Lobe Neurons. *Front. Neurosci.*, 15, 10 2021b. ISSN 1662-453X. doi: 10.3389/fnins.2021.739730.

F. van Breugel and M. H. Dickinson. Plume-Tracking Behavior of Flying Drosophila Emerges from a Set of Distinct Sensory-Motor Reflexes. *Curr. Biol.*, 24(3):274–286, 2 2014. ISSN 09609822. doi: 10.1016/j.cub.2013.12.023.

R. S. Vetter, A. E. Sage, K. A. Justus, R. T. Cardé, and C. G. Galizia. Temporal Integrity of an Airborne Odor Stimulus is Greatly Affected by Physical Aspects of the Odor Delivery System. *Chem. Sens.*, 31(4), 5 2006. ISSN 1464-3553. doi: 10.1093/chemse/bjj040.

N. J. Vickers. Winging It: Moth Flight Behavior and Responses of Olfactory Neurons Are Shaped by Pheromone Plume Dynamics. *Chem. Senses*, 31(2):155–166, 2 2006. ISSN 1464-3553. doi: 10.1093/chemse/bjj011.

N. J. Vickers and T. C. Baker. Reiterative responses to single strands of odor promote sustained upwind flight and odor source location by moths. *Proc Natl Acad Sci USA*, 91(13):5756–5760, 6 1994. ISSN 0027-8424. doi: 10.1073/pnas.91.13.5756.

P. Virtanen, R. Gommers, T. E. Oliphant, M. Haberland, T. Reddy, D. Cournapeau, E. Burovski, P. Peterson, W. Weckesser, J. Bright, S. J. van der Walt, M. Brett, J. Wilson, K. J. Millman, N. Mayorov, A. R. J. Nelson, E. Jones, R. Kern, E. Larson, and C. J. Carey. SciPy 1.0: fundamental algorithms for scientific computing in Python. *Nature Methods*, 17(3):261–272, 3 2020. ISSN 1548-7091. doi: 10.1038/s41592-019-0686-2.

C. Wall and J. N. Perry. Range of action of moth sex-attractant sources. *Entomol. Exp. Appl.*, 44(1):5–14, 6 1987. ISSN 00138703. doi: 10.1111/j.1570-7458.1987.tb02232.x.

L. Wang, Y. Nomura, Y. Du, and K. Dong. Differential Effects of TipE and a TipE-Homologous Protein on Modulation of Gating Properties of Sodium Channels from Drosophila melanogaster. *PLoS One*, 8(7), 7 2013. ISSN 1932-6203. doi: 10.1371/journal.pone.0067551.

D. Wicher. Tuning insect odorant receptors. *Frontiers in Cellular Neuroscience*, 12:94, 4 2018. ISSN 16625102. doi: 10.3389/FNCEL.2018.00094/BIBTEX.

M. A. Willis and T. C. Baker. Effects of intermittent and continuous pheromone stimulation on the flight behaviour of the oriental fruit moth, Grapholita molesta. *Physiol. Entomol.*, 9(3):341–358, 9 1984. ISSN 0307-6962. doi: 10.1111/j.1365-3032.1984.tb00715.x.

M. A. Willis, E. A. Ford, and J. L. Avondet. Odor tracking flight of male Manduca sexta moths along plumes of different cross-sectional area. *J. Comp. Physiol. A*, 199 (11):1015–1036, 11 2013. ISSN 0340-7594. doi: 10.1007/s00359-013-0856-0.

R. I. Wilson. Early Olfactory Processing in Drosophila : Mechanisms and Principles. *Annu. Rev. Neurosci*, 36(1):217–241, 7 2013. ISSN 0147-006X. doi: 10.1146/annurev-neuro-062111-150533.

P. Witzgall, P. Kirsch, and A. Cork. Sex Pheromones and Their Impact on Pest Management. *J. Chem. Ecol.*, 36(1):80–100, 1 2010. ISSN 0098-0331. doi: 10.1007/s10886-009-9737-y.

F. Zufall, M. Stengl, C. Franke, J. Hildebrand, and H. Hatt. Ionic currents of cultured olfactory receptor neurons from antennae of male Manduca sexta. *J. Neurosci*, 11(4): 956–965, 4 1991. ISSN 0270-6474. doi: 10.1523/JNEUROSCI.11-04-00956.1991.

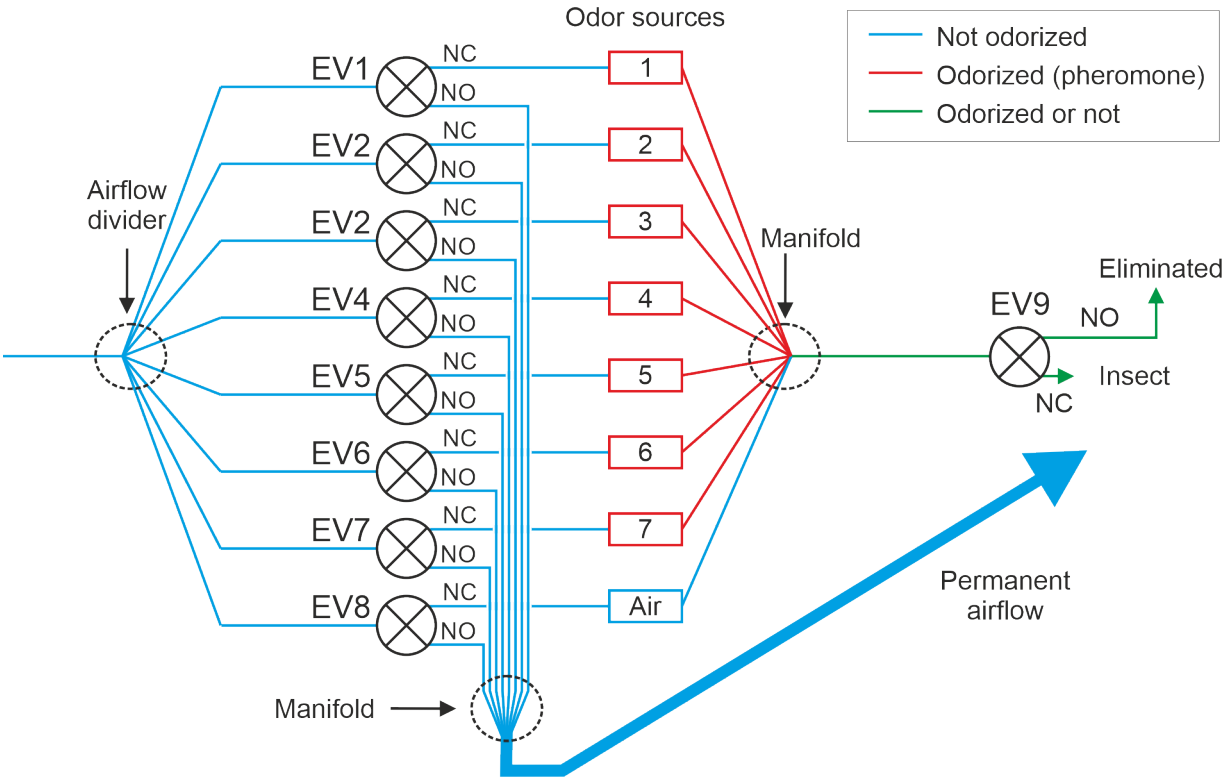

Figure 1–Figure supplement 1. Schematics of the developed odor delivery device.NO: normally open (no stimulus) and NC normally closed (during stimulus). The insect is placed 1 mm after EV9.

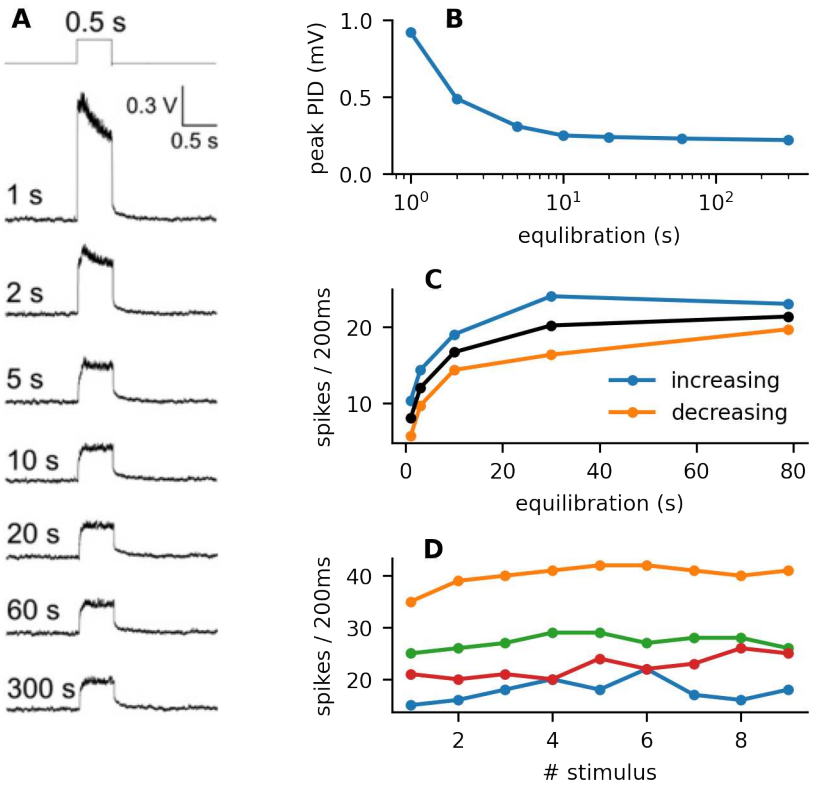

Figure 1–Figure supplement 2. Testing of equilibration times and source stability. A: Traces of PID recordings of linalool with different equilibration times. When the equilibration is too short, the PID response exhibits a transient peak. **B:** With an equilibration of approximately 10 s the peak is no longer present and the amplitude of the response does not change significantly with longer equilibration times. **C:** Number of spikes recorded in 200 ms in response to 100 pg of Z7-12:Ac for different equilibration times. Each ORN was presented with 5 stimuli with different equilibration times (1 s, 3 s, 10 s, 30 s, 79 s) either in increasing or decreasing order. For each order, the line is an average of 3 ORNs. The black line is an average of all 6 ORNs. **D:** We measured the stability of the pheromone source first by applying 9 stimuli with 0.1 ng of Z7-12:Ac. Each stimulus was preceded by an equilibration time of 30 s. The inter stimulus interval was 2 min. Each line represents the response of a single ORN.

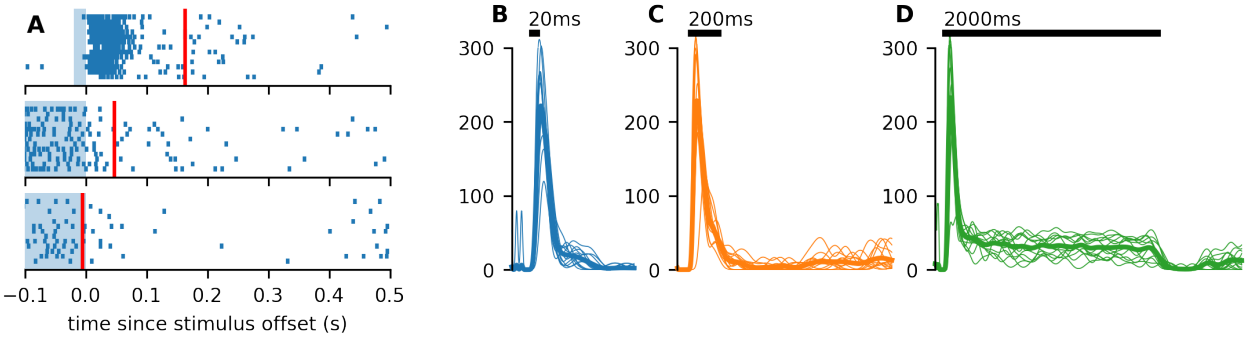

Figure 2–Figure supplement 1. Response patterns of *Spodoptera littoralis*. A: Raster plots of *Spodoptera littoralis* ORN responses to different stimulus durations, aligned to the stimulus offset, show that the response pattern to stimuli of different durations remains unchanged. ORNs exhibit a prolonged response to short stimuli and transient inhibition shortly after offset of long stimuli. **B-D:** Full firing profiles of responses to different stimulus durations.

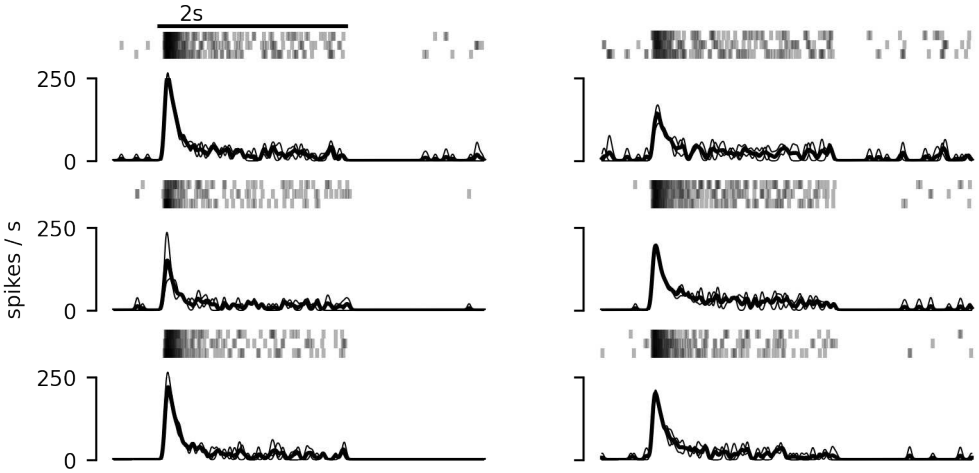

Figure 2–Figure supplement 2. Control experiment with compensating airflow. To avoid mechanical artefacts during odor stimuli, we added a second electrovalve to deliver non-odorized air. This valve was in opposing phase with the valve that delivers odor stimuli so that the airflow sent to the antenna was constant before, during and after stimuli. We still observed the inhibitory phase after the stimulus offset, indicating that it is not a mechanical artefact.

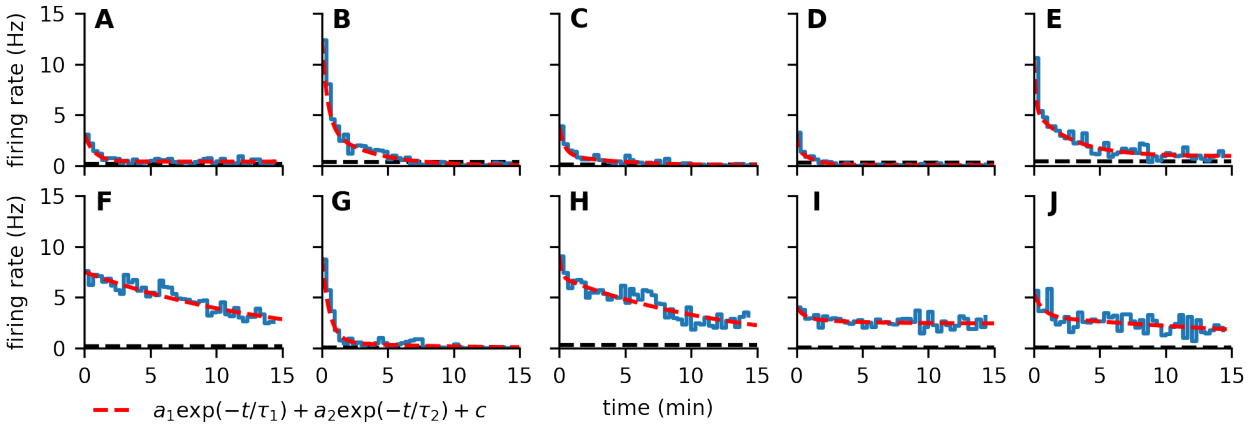

dose 10 pg

	a_1	τ_1	a_2	τ_2	c	spont.
A	2.69	43.66	0.00	43.3	0.39	0.18
B	8.66	25.96	3.83	202.0	0.00	0.36
C	2.76	23.24	1.12	266.6	0.00	0.13
D	1.51	5.52	1.70	67.5	0.04	0.27
E	5.16	8.53	4.52	169.1	0.93	0.44

dose 1 ng

	a_1	τ_1	a_2	τ_2	c	spont.
F	0.09	0.83	7.51	927.1	0.00	0.16
G	8.36	34.58	0.63	462.4	0.00	0.03
H	2.02	10.45	7.04	789.6	0.00	0.31
I	1.12	32.05	0.52	233.8	2.43	0.09
J	2.27	39.85	3.14	1672.8	0.00	0.09

Figure 2–Figure supplement 3. Sustained firing activity measured over long periods. We first measured the spontaneous activity during a 15 min period (black dashed lines) and then stimulated the ORN with either 10 pg (**A-E**) or 1 ng (**F-J**) dose of pheromone. Blue lines indicate the firing rate as measured by counting spikes in 20 s bins, starting 3 s after the pulse offset. Red dashed lines show a double exponential fit. The ORNs stimulated with a 1 ng did not return close to their spontaneous activity within the 15 min period (except for **G**). The fitter parameters are provided in the tables.

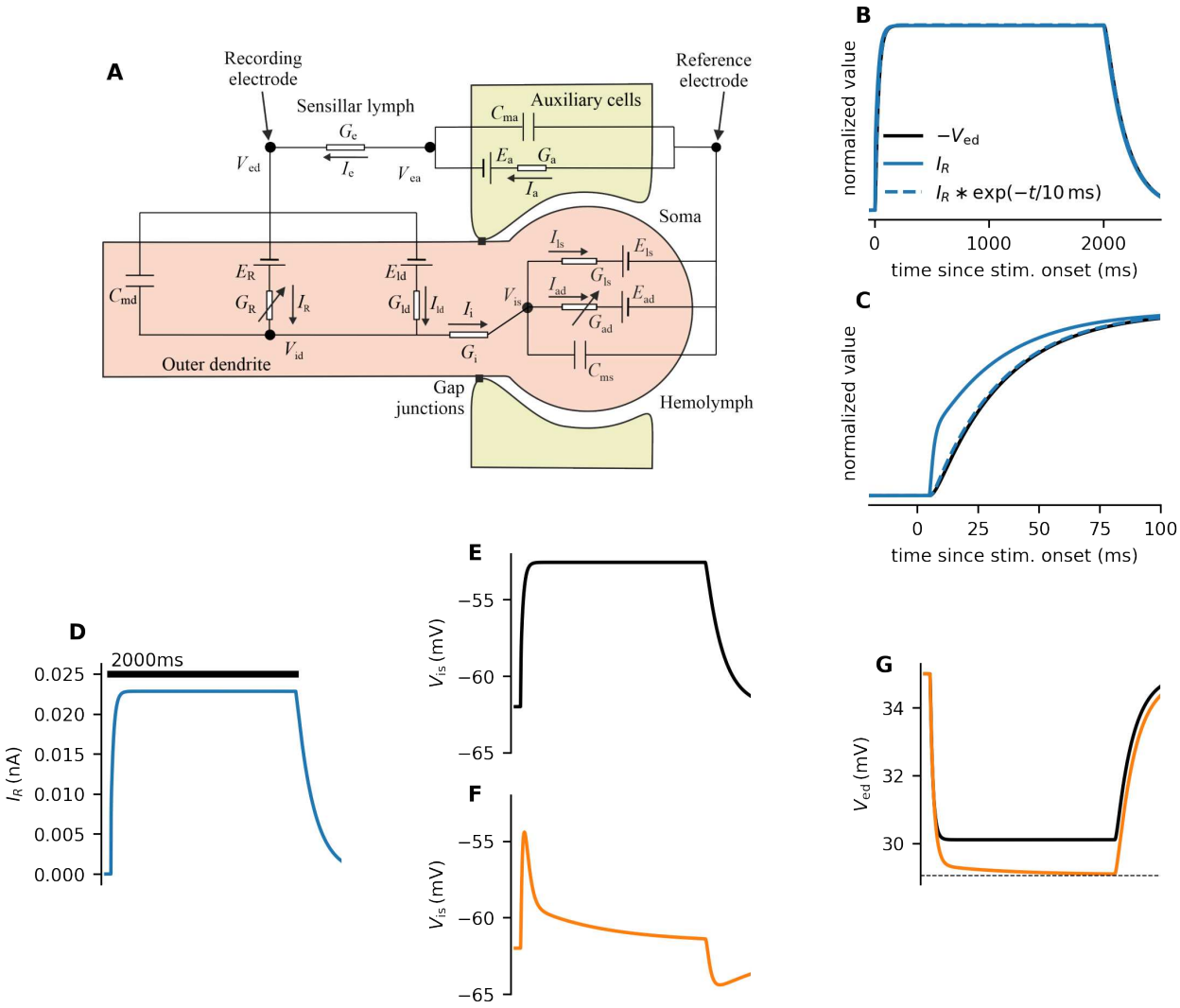

Figure 4–Figure supplement 1. Multicompartmental ORN model. A: Schematic illustration of the model. See Materials and methods for details. **B-C:** LFP (V_{ed}) and the corresponding estimated receptor current I_R (normalized, LFP changed from negative to positive). Dashed is the receptor current smoothed with an exponential filter: $I_R * \exp(-t/10\,\text{ms})$. **D:** The input current from **C**, used as an input the model can lead to different time course of the somatic membrane potential (V_{is}), depending on the adaptation currents in the soma (**E-F**). In **E**, no adaptation current is involved ($I_{ad} = 0$). In **F**, the adaptation current is calculated so that the somatic membrane potential resembles the firing rate of the ORN. The adaptation current then changes the time course of the LFP (**G**).

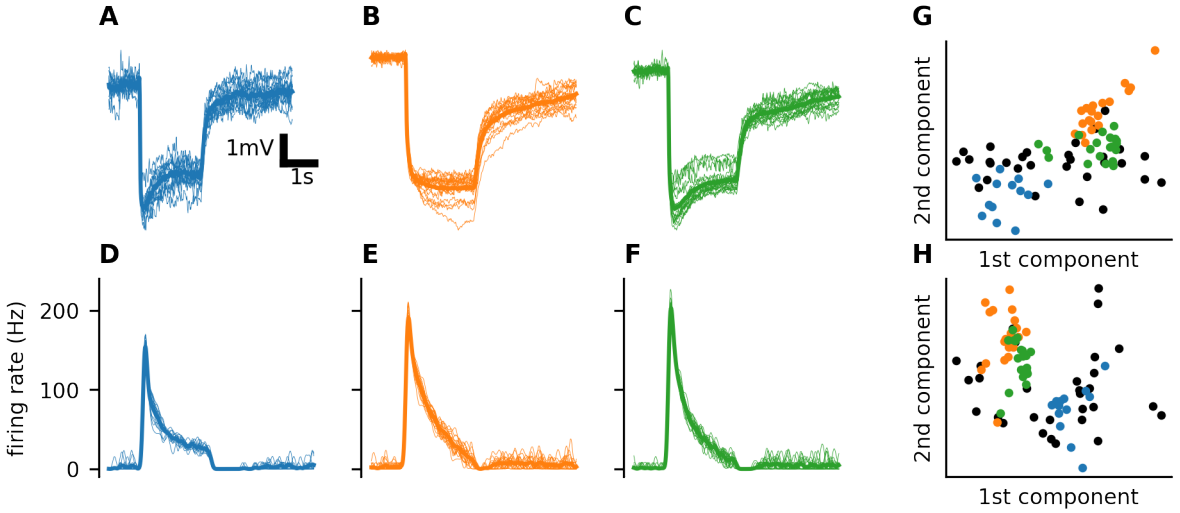

Figure 4–Figure supplement 2. Heterogeneity of ORN responses. A-C: LFP in response to a 2 s stimulus. Each panel (color) corresponds to a single neuron presented several times with the same stimulus. Thin lines are the individual trials, the thick line represents their average. **D-F:** Firing profiles of the three different neurons. Colors represent the neuron, as in **A-C**. Thin lines are the individual trials, the thick line represents their average. **G:** Scatter plot of the first two PCA components of the LFP. Each black point corresponds to a different neuron, while each of the colored points represents a single trial of one of the three neurons from **A-C**. The colored points are always concentrating around one spot, indicating that the responses of each neurons are stable in time and do not capture the heterogeneity of the whole population. **H:** Same as **G**, but for the firing rate profiles.

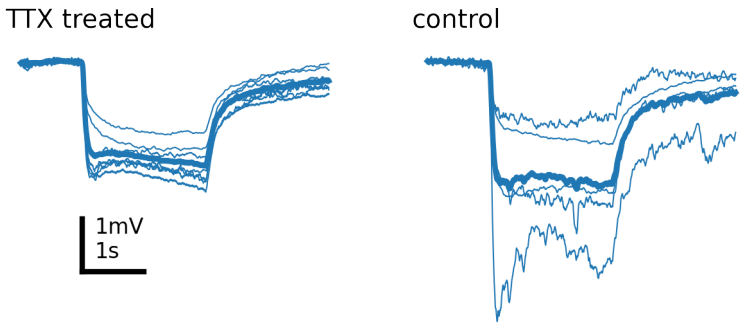

Figure 4–Figure supplement 3. LFP recordings with TTX. The TTX treated ORNs ($N = 7$) exhibited similar LFP response shape as the control ORNs ($N = 5$), including a peak in deflection towards the end of the stimulus, indicating that this slow deflection is not caused by the spiking activity.

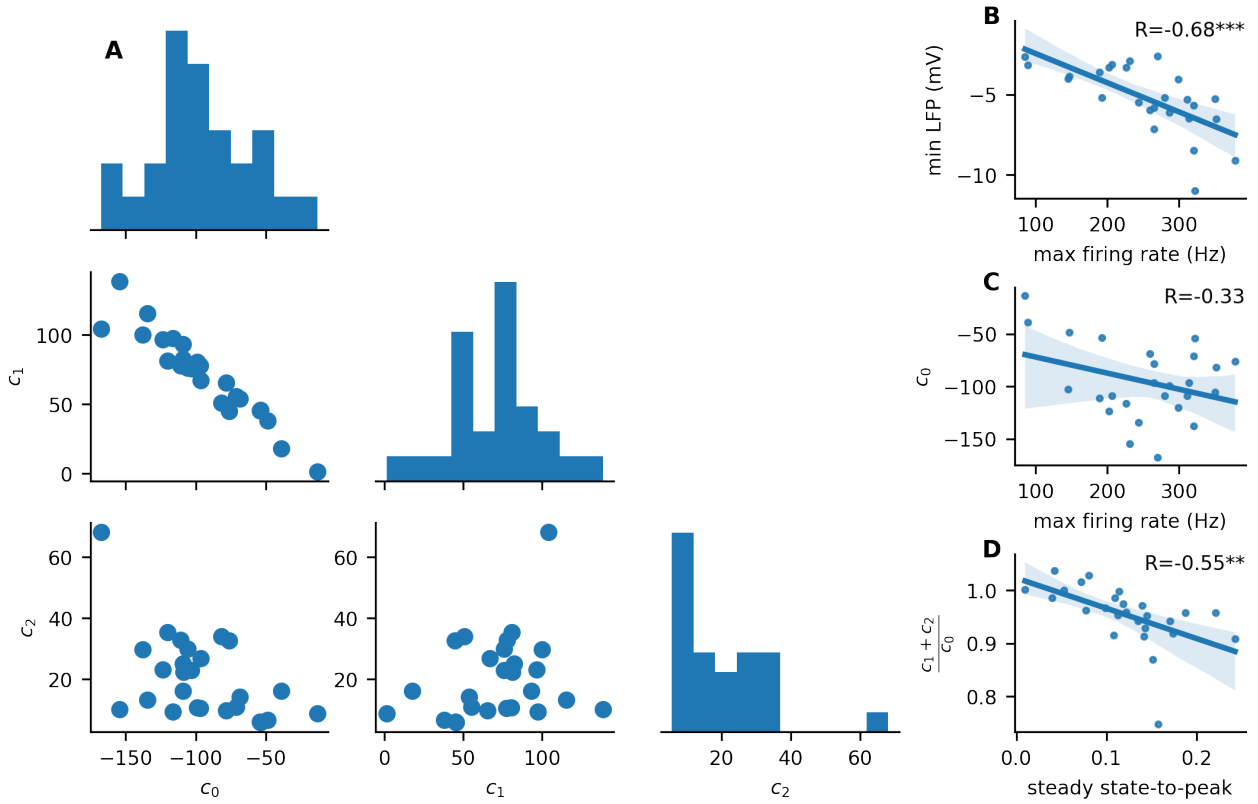

Figure 5–Figure supplement 1. Distributions of filter coefficients and their effect on spike firing properties. A: Distributions of filter coefficients c_0, c_1 and c_2 and their mutual dependence. While c_0 and c_1 are tightly correlated, c_2, responsible for the slow adaptation is rather independent. **B:** Higher amplitudes of initial LFP deflection (min. LFP during 200 ms stimulus) is correlated (Pearson correlation, $p = 1.5 \cdot 10^{-4}$) with the peak firing rate of the neuron (calculated with bw = 30 ms). **C:** We did not see a significant correlation between the peak firing rate and c_0 (Pearson correlation, $p = 0.097$). **D:** We saw a significant correlation (Pearson correlation, $p = 3.9 \cdot 10^{-3}$) between the steady state-to-peak ratio (ratio of the mean firing rate in the last 0.5 s of 2 s stimulus to the peak firing rate).

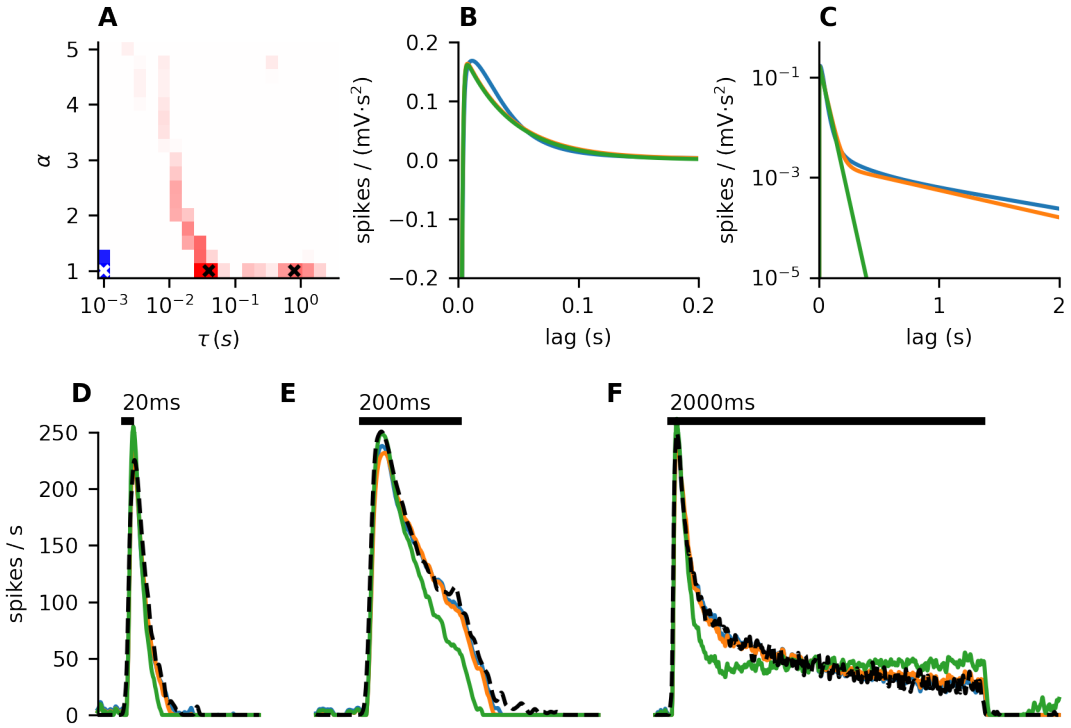

Figure 5–Figure supplement 2. Selection of filter time constants. A: heatmap of lasso regression coefficient values for different time constants τ and gamma distribution shapes α. Blue indicates a negative value, red positive value and white is zero. The non-zero values concentrate around several spots. Based on this analysis, we selected the time constants 1 ms, 40 ms and 800 ms, which are marked by crosses in the heatmap. **B:** Three different linear filters: filter corresponding to the lasso regression, filter obtained from linear regression with the three exponential kernels with the time constants 1 ms, 40 ms, 800 ms and filter obtained from linear regression with only two exponential kernels (1 ms and 40 ms). Note the difference with Figure 5E, where the filter with two kernels is obtained by fitting a filter with three kernels and only then removing the slow component. **C:** The same filters as in **B**, but on logarithmic scale to accent the differences between individual filters. **D-F:** Predictions of firing responses with the linear filters from **B**, color-coded accordingly. Note that even though the filters with three exponential kernels and the filter obtained from the lasso regression are obviously different, their predictions are almost identical.

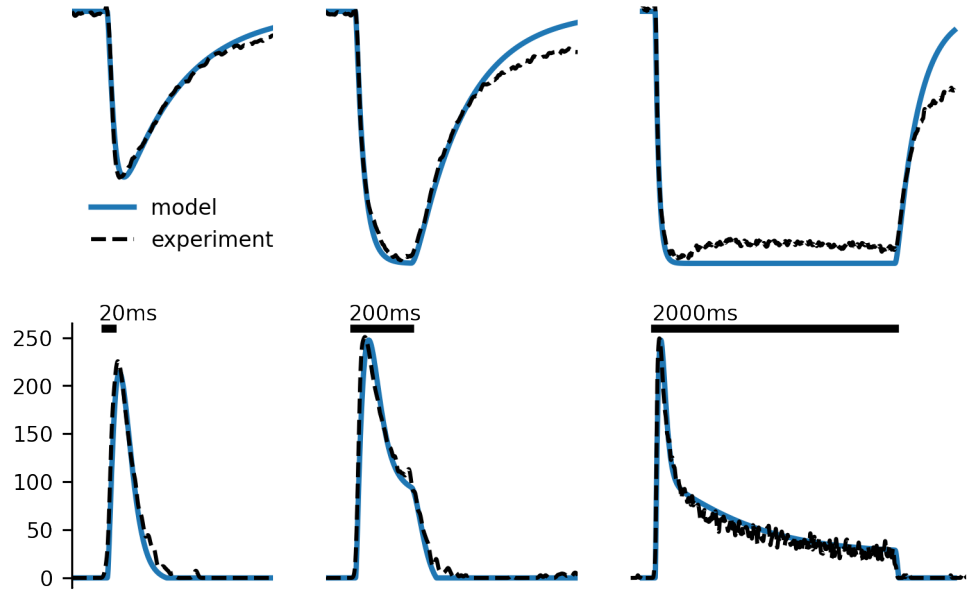

Figure 5–Figure supplement 3. Firing rate prediction using odor transduction model. Prediction of LFP (top row) and firing rate (bottom row) using an odor transduction model (***Eq. 4-Eq. 5***) combined with the linear-nonlinear model (***Eq. 1-Eq. 2***). The transduction model was fit to the average LFP (first 400 ms of the 20 ms and 200 ms stimuli) and the LN model was fit to transform the average LFP to the average firing rate (2 s stimulus) (indicated by the dashed lines). Note that the model neglects receptor adaptation and the sustained activity.

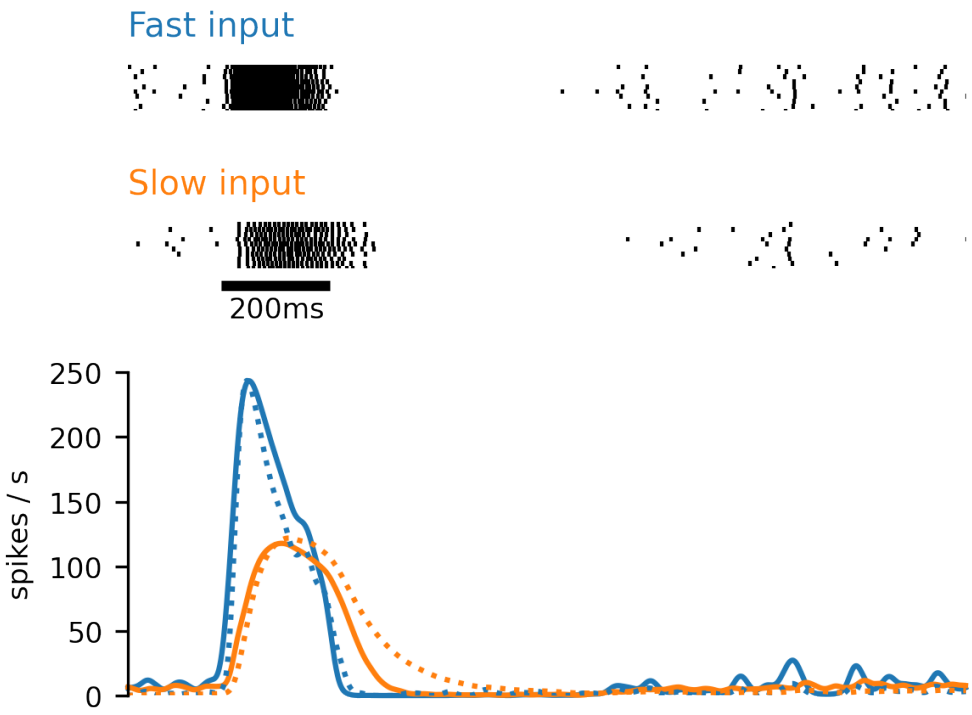

Figure 6–Figure supplement 1. PNs do not track odor pulse durations if ORN response is smooth. The raster plots at the top show the spike trains of the 10 PNs in response to the unmodified ORN firing profile (Fast input) and ORN firing profile smoothed with exponential kernel with 100 ms mean (Slow input). The PNs with the slow input also exhibit the inhibitory phase, but do not track the stimulus duration. The full lines in the bottom panel show the PN firing rate averaged over 36 simulations. The dotted lines show the ORN input.

Attachment VI

Unpublished report

Mathematical modeling of the spontaneous activity and triphasic response of the moth olfactory receptor neurons

Tomas Barta[1,2,3], Lubomir Kostal[2], Christelle Monsempès[1], Philippe Lucas[1]

1 Institute of Ecology and Environmental Sciences of Paris, INRAE, Sorbonne Université, CNRS, IRD, UPEC, Université de Paris, 78000 Versailles, France
2 Institute of Physiology of the Czech Academy of Sciences, Prague, Czech Republic
3 Charles University, First Medical Faculty, Prague, Czech Republic

1 Methods

1.1 Point process modeling

1.1.1 Spontaneous activity

To model the ISI distributions, we considered the exponential, gamma, and inverse Gaussian distributions and their mixtures. The probability density of a spike at the time t, considering that the previous spike happened at the time 0 is for the different distributions:

- Exponential
$$f_E(t) = \lambda \exp(-\lambda t) \tag{1}$$
- Gamma
$$f_G(t;\alpha) = \frac{\lambda^\alpha}{\Gamma(\alpha)} t^{\gamma-1} \exp(-\lambda t) \tag{2}$$
- Inverse Gaussian
$$f_{IG}(t;\mu) = \frac{\lambda}{2\pi x^3} \exp\left[\frac{\lambda(x-\mu)}{2\mu^2 x}\right] \tag{3}$$

where λ stands for the intensity of the process, α and μ are distribution parameters. We describe the mixture of two distributions as

$$f_{XY}(t;\theta_X,\theta_Y) = q f_X(t;\theta_X) + (1-q) f_Y(t;\theta_Y), \tag{4}$$

where q describes the fraction of the two distributions and θ_X and θ_Y are the distribution parameters.

The parameters of the ISI distribution (θ_1, θ_2, q) were fitted by maximizing the joint probability density function of the spike train $\{t_1, \ldots, t_n\}$ happening in the experimental time window T:

$$p(\theta_1,\theta_2,q|\{t\}) = \prod_{t\in\{t_i\}} f(t_k - t_{k-1};\theta_X,\theta_Y) \left(1 - \int_0^{T-t_n} f(u;\theta_X,\theta_Y)\,\mathrm{d}u\right), \tag{5}$$

the last term here represents the probability, that $t_{n+1} > T$ and we assume that $t_0 = 0$. To obtain the result, we maximized the value of $\log(p(\theta_X,\theta_Y,q|\{t\}))$ using the L-BFGS-B method implemented in SciPy (Virtanen et al., 2020).

1.1.2 Fitting inhomogeneous point processes

The inhomogeneous probability density function for the considered ISI distributions are (Barbieri et al., 2001b):

- Exponential

$$f_E^t(t_k;\tau|t_{k-1}) = \lambda(t_k)\exp\left[-\int_{t_{k-1}}^{t_k}\lambda(u)\,\mathrm{d}u\right] \tag{6}$$

- Gamma

$$f_G^t(t_k;\alpha|t_{k-1}) = \frac{\alpha\lambda(t_k)}{\Gamma(\alpha)}\left[\alpha\int_{t_{k-1}}^{t_k}\lambda(u)\,\mathrm{d}u\right]^{\alpha-1}\exp\left[\alpha\int_{t_{k-1}}^{t_k}\lambda(u)\,\mathrm{d}u\right] \tag{7}$$

- Inverse Gaussian

$$\begin{aligned} f_{IG}^t(t_k;\mu|t_{k-1}) = {} & \frac{\lambda(t_k)}{\left\{2\pi\left[\int_{t_{k-1}}^{t_k}\lambda(u)\,\mathrm{d}u\right]^3\right\}^{1/2}}\times \\ & \times\exp\left\{-\frac{1}{2}\frac{\left[\int_{t_{k-1}}^{t_k}\lambda(u)\,\mathrm{d}u-\mu\right]^2}{\mu^2\int_{t_{k-1}}^{t_k}\lambda(u)\,\mathrm{d}u}\right\}, \end{aligned} \tag{8}$$

where λ stands for the time-dependent intensity of the process, the superscript t indicates that the probability density function is inhomogeneous. The joint probability density of a spike train $\{t_1,\ldots,t_n\}$ can then be expressed as (Barbieri et al., 2001b; Brown et al., 2002):

$$\begin{aligned} f(t_1,t_2,\ldots,t_n\cap N(T)=n) = {} & \prod_{k=1}^{n} r(t_k|t_{k-1})\exp\left[-\int_{t_{k-1}}^{t_k} r(t|t_{k-1})\,\mathrm{d}t\right]\times \\ & \times\exp\left[-\int_{t_k}^{T} r(t|t_{k-1})\,\mathrm{d}t\right], \end{aligned} \tag{9}$$

where $r(t|t')$ is the hazard function:

$$r(t|t_{k-1}) = \frac{f_t(t|t_{k-1})}{1-\int_{t_{k-1}}^{t} f_t(u|t_{k-1})\,\mathrm{d}u}, \tag{10}$$

with f_t being the inhomogeneous probability density function.

In the case of a mixture process of two inhomogeneous probability density functions f_X^t and f_Y^t (each representing the inhomogeneous version of a homogeneous probability density function f_X and f_Y respectively), we expressed the inhomogeneous probability density function as

$$f_{XY}^t(t_k|t_{k-1}) = qf_X^t(t_k|t_{k-1}) + (1-q)f_Y^t(t_k|t_{k-1}), \tag{11}$$

where q specifies the ratio of the two probability density functions. The optimal parameters of f_X and f_Y can then be found by maximizing the joint probability density of the spike train (Eq. 9). We performed this maximization numerically on the logarithm of the joint probability density with the L-BFGS-B algorithm implemented in SciPy (Virtanen et al., 2020).

1.1.3 Quantile-quantile plots

In order to visually evaluate the goodness of fit of the inhomogeneous point processes, we used the quantile-quantile plots (Q-Q plots) of a time-rescaled spike train against an exponential distribution (Barbieri et al., 2001b,a; Brown et al., 2002). The rate-rescaling function is defined as

$$R(t) = \int_0^t r(t|H_t)\,\mathrm{d}t, \tag{12}$$

where H_t stands for the history of the process, in this case, the most recent action potential. The rescaled interspike intervals

$$\tau_k = R(t_k) - R(t_{k-1}) \tag{13}$$

should be distributed independently with an exponential distribution with a mean of 1.

1.2 ORN model

1.2.1 Spiking model.

Our model is based on the model of moth ORN in (Barta et al., 2022), which is a simplified version of the model by Gu et al. (2009). From this model we kept the morphology and the passive conductances (Fig. 1):

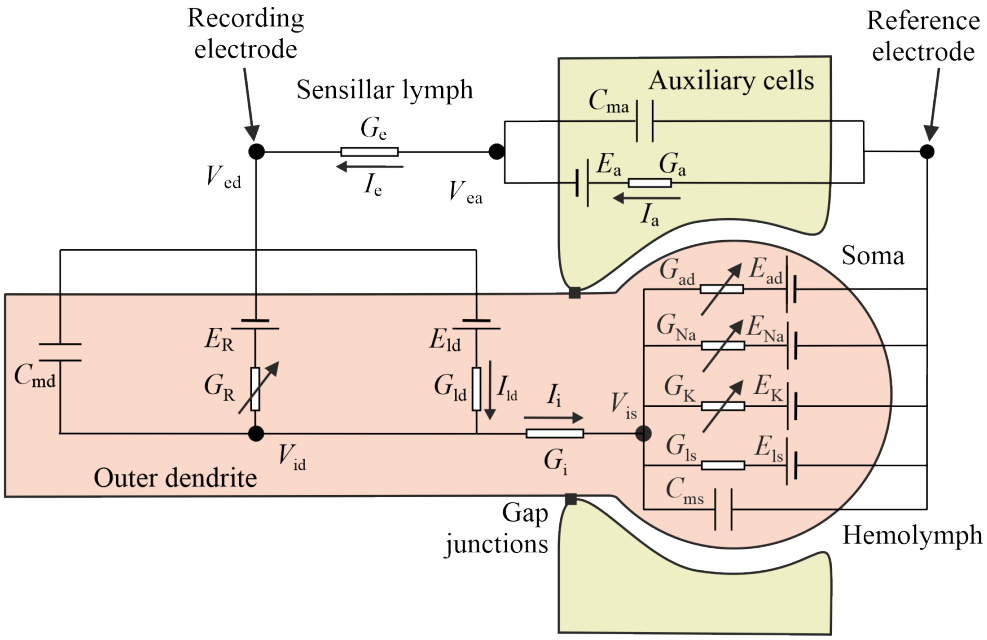

Fig 1. Schematics of the moth ORN model. The model is composed of three compartments: The outer dendrite, where the receptor channels are located, soma, where action potentials are initiated, hemolymph, where the reference electrode is placed and the sensillar lymph where is placed the recording electrode.

$$\begin{aligned}\frac{\mathrm{d}V_{\mathrm{id}}}{\mathrm{d}t} =& \frac{G_{\mathrm{e}}}{C_{\mathrm{md}}(G_{\mathrm{e}}+G_{\mathrm{i}})}(I_R + I_{\mathrm{ld}} - I_{\mathrm{e}}) \\ &+ \frac{G_{\mathrm{e}}}{C_{\mathrm{ma}}(G_{\mathrm{e}}+G_{\mathrm{i}})}(I_{\mathrm{a}} - I_{\mathrm{e}}) + \frac{G_{\mathrm{i}}}{C_{\mathrm{ms}}(G_{\mathrm{e}}+G_{\mathrm{i}})}(I_{\mathrm{i}} - I_{\mathrm{ls}} - I_{HH}),\end{aligned} \tag{14}$$

$$\begin{aligned}\frac{\mathrm{d}V_{\mathrm{ed}}}{\mathrm{d}t} =& \frac{G_{\mathrm{i}}}{C_{\mathrm{md}}(G_{\mathrm{e}}+G_{\mathrm{i}})}(I_{\mathrm{e}} - I_R - I_{\mathrm{ld}}) \\ &+ \frac{G_{\mathrm{e}}}{C_{\mathrm{ma}}(G_{\mathrm{e}}+G_{\mathrm{i}})}(I_{\mathrm{a}} - I_{\mathrm{e}}) + \frac{G_{\mathrm{i}}}{C_{\mathrm{ms}}(G_{\mathrm{e}}+G_{\mathrm{i}})}(I_{\mathrm{i}} - I_{\mathrm{ls}} - I_{HH}),\end{aligned} \tag{15}$$

$$\frac{\mathrm{d}V_{\mathrm{is}}}{\mathrm{d}t} = \frac{I_{\mathrm{i}} - I_{\mathrm{ls}} - I_{HH}}{C_{\mathrm{ms}}}, \tag{16}$$

$$\frac{\mathrm{d}V_{\mathrm{ea}}}{\mathrm{d}t} = \frac{I_{\mathrm{a}} - I_{\mathrm{e}}}{C_{\mathrm{ma}}}. \tag{17}$$

Where the currents are described by:

$$I_{\mathrm{ls}} = G_{\mathrm{ls}}(V_{\mathrm{is}} - E_{ls}), \tag{18}$$

$$I_{\mathrm{ld}} = G_{\mathrm{ld}}(V_{\mathrm{ed}} - V_{\mathrm{id}} + E_{ld}), \tag{19}$$

$$I_{\mathrm{i}} = G_{\mathrm{i}}(V_{\mathrm{id}} - V_{\mathrm{is}}), \tag{20}$$

$$I_{\mathrm{a}} = -G_{\mathrm{a}}(V_{\mathrm{ea}} + E_a), \tag{21}$$

$$I_{\mathrm{e}} = G_{\mathrm{e}}(V_{\mathrm{ea}} - V_{\mathrm{ed}}). \tag{22}$$

The current I_{HH} describes the spike generating mechanism:

$$I_{HH} = g_{\mathrm{Na}} m^3 h(V_{\mathrm{is}} - E_{\mathrm{Na}}) + g_{\mathrm{K}} n^4 (V_{\mathrm{is}} - E_{\mathrm{K}}) \tag{23}$$

where E_{Na} and E_{K} are the sodium and potassium reversal potentials, respectively; g_{Na}, g_{K} are peak conductances; and m, h and n are gating variables obeying the equation:

$$\frac{\mathrm{d}x}{\mathrm{d}t} = \alpha_x(V_{\mathrm{is}})(1-x) - \beta_x(V_{\mathrm{is}})x, \tag{24}$$

or equivalently:

$$\tau_x(V_{\mathrm{is}})\frac{\mathrm{d}x}{\mathrm{d}t} = -(x - x_\infty(V_{\mathrm{is}})), \tag{25}$$

where x is the respective gating variable, α_x and β_x are the activation and inactivation functions, respectively, and

$$\tau_x(V_{\mathrm{is}}) = \frac{1}{\alpha_x(V_{\mathrm{is}}) + \beta_x(V_{\mathrm{is}})}, \tag{26}$$

$$x_\infty(V_{\mathrm{is}}) = \frac{\alpha_x(V_{\mathrm{is}})}{\alpha_x(V_{\mathrm{is}}) + \beta_x(V_{\mathrm{is}})}. \tag{27}$$

The activation and inactivation functions are defined as follows:

$$\alpha_m = -0.32\frac{V_{\mathrm{is}} - V_T - 13}{\exp(-(V_{\mathrm{is}} - V_T - 13)/4) - 1}, \tag{28}$$

$$\beta_m = 0.28\frac{V_{\mathrm{is}} - V_T - 40}{\exp((V_{\mathrm{is}} - V_T - 40)/5) - 1}, \tag{29}$$

$$\alpha_h = A_h \exp(-(V_{\mathrm{is}} - V_T - V_S - 17)/18), \tag{30}$$

$$\beta_h = \frac{4}{1 + \exp(-(V_{\mathrm{is}} - V_T - V_S - 40)/5)}, \tag{31}$$

$$\alpha_n = -0.032\frac{V_{\mathrm{is}} - V_T - 15}{\exp(-(V_{\mathrm{is}} - V_T - 15)/5) - 1}, \tag{32}$$

$$\beta_n = 0.5\exp(-(V_{\mathrm{is}} - V_T - 10)/40). \tag{33}$$

Neuron properties		Hodgkin-Huxley		Input	
C_{md}	$3.28 \times 10^{-3}\,\mathrm{nF}$	g_{Na}	$500\,\mathrm{nS}$	μ_R	$7.2 \times 10^{-2}\,\mathrm{nS}$
G_{ld}	$0.4373\,\mathrm{nS}$	E_{Na}	$50\,\mathrm{mV}$	σ_R	$4.6 \times 10^{-2}\,\mathrm{nS}$
E_{ld}	$-97\,\mathrm{mV}$	g_{K}	$50\,\mathrm{nS}$	τ_R	$20\,\mathrm{ms}$
E_{R}	$0\,\mathrm{mV}$	E_{K}	$-90\,\mathrm{mV}$		
G_{i}	$0.4373\,\mathrm{nS}$	V_T	$-10\,\mathrm{mV}$		
C_{ms}	$1.44 \times 10^{-3}\,\mathrm{nF}$	V_S	$-58\,\mathrm{mV}$		
G_{ls}	$1.44\,\mathrm{nS}$				
C_{ma}	$30 \times 10^{-3}\,\mathrm{nF}$				
G_{a}	$3.1\,\mathrm{nS}$				
E_{a}	$-35\,\mathrm{mV}$				

Table 1. Neuron parameters, including the Hodgkin-Huxley spike generator and input parameters.

Parameters of the model are given in Tab. 1.

1.2.2 Receptor current.

We consider that an individual channel, when opened, has a conductance of $\overline{g}_R$ and stays open for the duration of τ_R. If the receptors open randomly with rate λ_R the mean conductance and the variance are (Stoyan et al., 1987)

$$\mu_R = \lambda_R \tau_R \overline{g}_R, \tag{34}$$

$$\sigma_R = \overline{g}_R \sqrt{\tau_R \lambda_R}. \tag{35}$$

We use the diffusion approximation (small $\overline{g}_R$ and large λ_R) and model the total conductance of the receptor channels by the Ornstein-Uhlenbeck process (Destexhe et al., 2001; Uhlenbeck and Ornstein, 1930):

$$\tau_R \frac{\mathrm{d}g_R}{\mathrm{d}t} = -(g_R - \mu_R) + 2\sigma_R \frac{\mathrm{d}W}{\mathrm{d}t}, \tag{36}$$

where W is the Wiener process.

The used parameters of the input are given in Tab. 1.

2 Results

2.1 Spontaneous activity can be modeled as a mixture of inverse Gaussian and gamma distributions

We studied the activity of 10 neurons (for experiment description see (Barta et al., 2022)), from which we recorded the spontaneous activity for 15 min, then stimulated for 2 s (5 ORNs with pheromone dose 10 pg, 5 ORNs with pheromone does 1 ng) and recorded the activity for another 15 min. The activity of the neurons was elevated even after the stimulus offset (rebound activity) and returned very slowly to the original spontaneous activity.

Both during the spontaneous activity and during the rebound activity, in all recorded neurons the interspike intervals (ISIs) could be clearly separated into intervals within a burst and inter-burst intervals (IBIs) (Fig. 2A). We fit different mixed distributions to the ISI distributions in the general form

$$f(t; \theta_1, \theta_2) = q f_1(t; \theta_1) + (1 - q) f_2(t; \theta_2), \tag{37}$$

where $f_1(t;\theta_1)$ is the probability density function (PDF) of the ISI within a burst, $f_2(t;\theta_2)$ is the PDF of the IBIs, θ_1, θ_2 represent the parameters of the two distributions and q is the ratio of the two distributions. We tried the 9 possible combinations of routinely used, distributions of ISIs: exponential, gamma, and inverse Gaussian. The data were best fitted by a mixture of inverse Gaussian distribution for ISIs within a burst and gamma distribution for the IBIs (Fig. 2B-C).

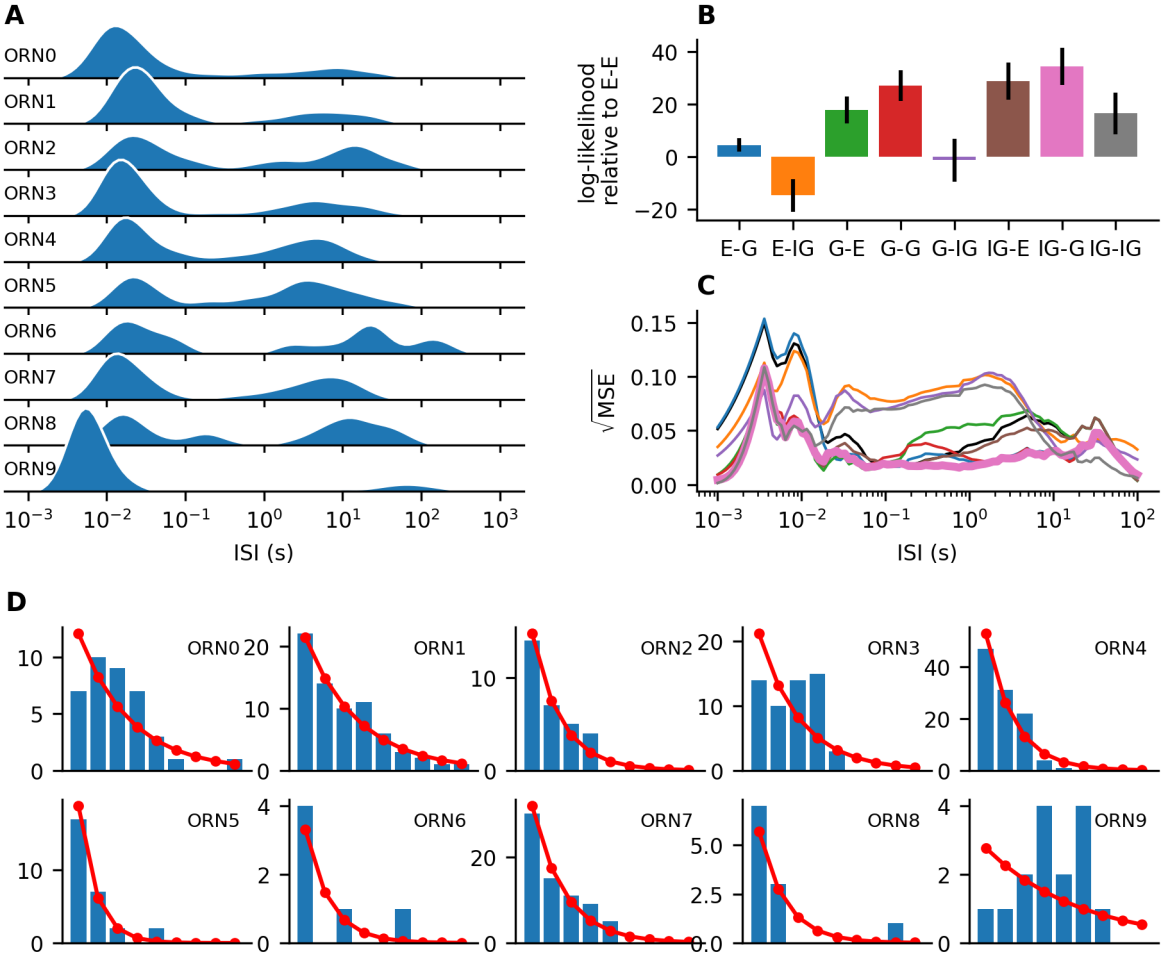

Fig 2. Spontaneous activity of ORNs. The spontaneous activity of 10 different ORNs was recorded for 15 min. The bimodality of their ISI distributions is clearly apparent on the log scale (**A**). Using the maximum likelihood method we fit different mixed distributions to the ISI data. The panel **B** shows the mean value of the log-likelihood of different models (the first letter stands for distribution with shorter ISIs, P - exponential distribution, G - gamma distribution, IG - inverse Gaussian distribution). The averaged values are the values relative to the exponential-exponential distribution for each model, to remove the variability introduced by the inter-neuron variability. The vertical bar indicates the standard error. The best fit was a mix of inverse Gaussian distribution for the bursts and gamma distribution for the inter-burst intervals. **C:** Root of the square error between the CDFs and ECDFs, averaged over the neurons. The colors correspond to **B**, the IG-G model is in bold, and the E-E model is in black. **D:** Distribution of lengths of bursts (shortest possible burst contains two spikes). The red line indicates a geometric distribution with the same mean.

Having separate distributions for the bursts and IBIs allows us to assign a

Table 2. Spontaneous activity of ORNs

	rate (Hz)	⟨IBI⟩ (s)	burst length	⟨burst ISI⟩ (ms)
ORN1	0.18	13.9	3.2	19.5
ORN2	0.36	9.1	3.3	32.8
ORN3	0.13	15.6	2.0	41.7
ORN4	0.27	9.7	2.6	19.7
ORN5	0.44	4.5	2.0	23.5
ORN6	0.16	9.3	1.5	24.8
ORN7	0.03	51.4	1.8	33.3
ORN8	0.31	6.9	2.2	19.2
ORN9	0.09	21.3	1.9	74.5
ORN10	0.09	59.1	5.4	6.8

probability to each ISI, whether it is an IBI or an interval within a burst, and estimate a threshold α between the two modes:

$$qf_1(\alpha;\theta_1) = (1-q)f_2(\alpha;\theta_2). \tag{38}$$

With such a threshold, we can mark each interval as whether it belongs to a burst and analyze the distribution of the number of spikes within a burst. We summarized the statistics of the spontaneous activity (firing rate, average length of the IBI, average number of spikes in one burst, average ISI between two spikes within a burst) in Tab. 2. For most ORNs, the distribution of the number of spikes in a burst is very close to the geometric distribution, indicating that the probability that the next ISI will be short or long is independent of whether the previous ISI was short or long.

2.2 Modeling the rebound activity

The firing rate after the stimulus offset can be fit by a sum of two exponential functions (Barta et al., 2022). Therefore fitted the rebound activity with a mixture of inhomogeneous gamma and inverse Gaussian processes with their intensities is described by a sum of two exponential functions. We evaluated the goodness of fit visually by comparing the observed and expected ISIs with Q-Q plots and concluded that the model fits the data well. Therefore, not only spontaneous activity but also the time-dependent activity of moth ORNs can be modeled with the mixture of the two distributions.

2.3 Origin of the bursting pattern

Using the multi-compartmental model from (Barta et al., 2022) equipped with voltage-gated Na^+ and K^+ channels to produce action potentials, we could reproduce the bursting activity of the ORNs. However, if the spikes are generated due to time correlations in the receptor current, they should lie within a well in the extracellular recordings, as illustrated on the averaged action potential shape from the simulation. However, this is not what we observe in the recordings of the spontaneous activity.

References

R. Barbieri, L. M. Frank, M. C. Quirk, M. A. Wilson, and E. N. Brown. Diagnostic methods for statistical models of place cell spiking activity. *Neurocomputing*, 38-40: 1087–1093, 6 2001a. ISSN 09252312. doi: 10.1016/S0925-2312(01)00450-7.

R. Barbieri, M. C. Quirk, L. M. Frank, M. A. Wilson, and E. N. Brown. Construction and analysis of non-Poisson stimulus-response models of neural spiking activity. *J,*

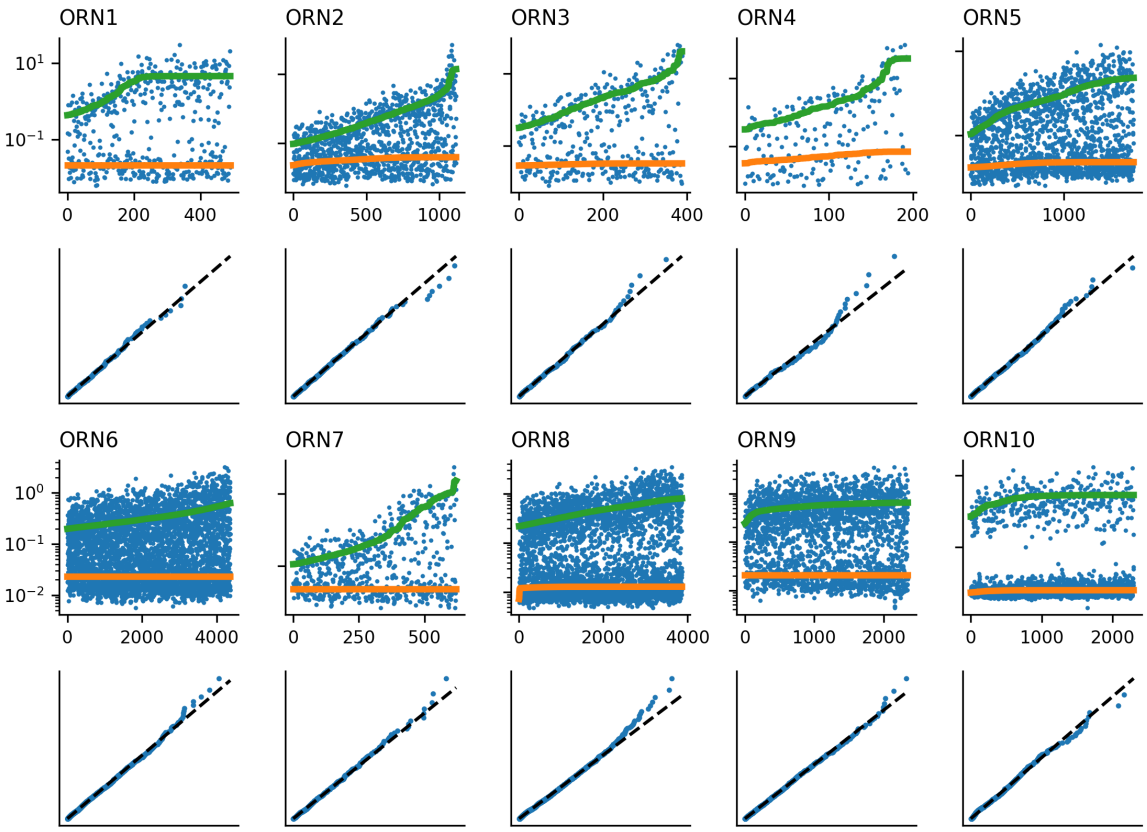

Fig 3. Fit evaluation of ORN rebound activity. Interspike intervals and their predictions (rows 1 and 3) and QQ plots (rows 2 and 4). The x-axis is the index of the ISI (ordered in time) and the y axis is the interspike interval (in seconds). The green color indicates the predicted IBI and the orange color the predicted ISI within a burst. The first two rows are neurons that were stimulated with 10 pg pheromone dose and the second two rows are neurons that were stimulated with a 1 ng dose.

Neurosci. Methods, 105(1):25–37, 1 2001b. ISSN 01650270. doi: 10.1016/S0165-0270(00)00344-7.

T. Barta, C. Monsempès, E. Demondion, A. Chatterjee, L. Kostal, and P. Lucas. Stimulus duration encoding occurs early in the moth olfactory pathway. *bioRxiv*, page 2022.07.21.501055, 7 2022. doi: 10.1101/2022.07.21.501055.

E. N. Brown, R. Barbieri, V. Ventura, R. E. Kass, and L. M. Frank. The Time-Rescaling Theorem and Its Application to Neural Spike Train Data Analysis. *Neural Comput.*, 14(2):325–346, 2 2002. ISSN 0899-7667. doi: 10.1162/08997660252741149.

A. Destexhe, M. Rudolph, J. M. Fellous, and T. J. Sejnowski. Fluctuating synaptic conductances recreate in vivo-like activity in neocortical neurons. *Neuroscience*, 107 (1):13–24, 2001. ISSN 0306-4522.

Y. Gu, P. Lucas, and J.-P. Rospars. Computational Model of the Insect Pheromone Transduction Cascade. *PLoS Comput. Biol.*, 5(3):e1000321, 3 2009. ISSN 1553-7358. doi: 10.1371/journal.pcbi.1000321.

D. Stoyan, W. S. Kendall, and J. Mecke. *Stochastic geometry and its applications.*

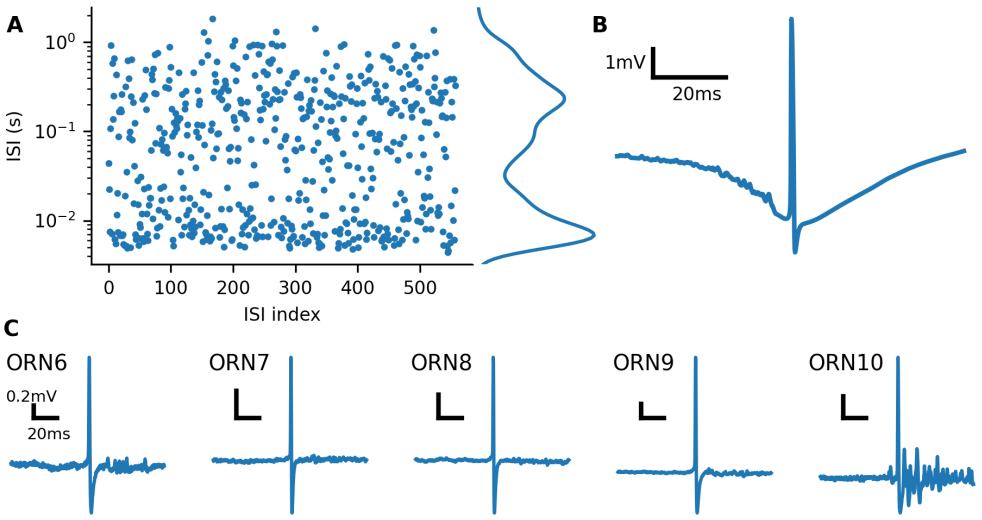

Fig 4. Simulation of ORN model. A: Interspike intervals obtained from a simulation of the ORN model. A clear bimodal structure in the ISI distribution is apparent. **B:** The shape of the average interspike interval (where the recording electrode would be placed, V_{ed}). The action potential sits within a well, as it is evoked by current flow from the sensillar lymph inside the neuron, which decreased V_{ed}. Such a shape is not observed in the experimental recordings (**C**). Both in **B** and **C** we only considered spikes preceded by at least 100 ms without a spike. This did not have a qualitative effect on the shape of the action potentials.

Wiley series in probability and mathematical statistics: Applied probability and statistics. Wiley, 1987. ISBN 9780471905196.

G. E. Uhlenbeck and L. S. Ornstein. On the Theory of the Brownian Motion. *Phys. Rev.*, 36(5):823–841, 9 1930. doi: 10.1103/physrev.36.823.

P. Virtanen, R. Gommers, T. E. Oliphant, M. Haberland, T. Reddy, D. Cournapeau, E. Burovski, P. Peterson, W. Weckesser, J. Bright, S. J. van der Walt, M. Brett, J. Wilson, K. J. Millman, N. Mayorov, A. R. J. Nelson, E. Jones, R. Kern, E. Larson, and C. J. Carey. SciPy 1.0: fundamental algorithms for scientific computing in Python. *Nature Methods*, 17(3):261–272, 3 2020. ISSN 1548-7091. doi: 10.1038/s41592-019-0686-2.